Evaluating Cervical Spine Response and Potential for Injury During Head-First Impact Loading Using a Finite Element Head-Neck Model

by

Marwan Darweesh

A thesis
presented to the University of Waterloo
in fulfillment of the
thesis requirement for the degree of
Master of Applied Science
in
Mechanical and Mechatronics Engineering

Waterloo, Ontario, Canada, 2022

Author's Declaration

I hereby declare that I am the sole author of this thesis. This is a true copy of the thesis, including my required final revisions, as accepted by my examiners.

I understand that my thesis may be made electronically available to the public.

Abstract

Head-first impact (HFI) is caused by events such as rollover motor-vehicle accidents, falls, and sports, and can impose serious and detrimental hard and soft tissue injuries on the cervical spine. HFI is a loading condition which involves direct impact to the head resulting from the person (usually in an inverted position) approaching and subsequently impacting a surface. During HFI loading, the momentum of the following torso coupled with the relatively stationary head impacting a surface act together to compress the cervical spine. Due to the severity of the incurred injuries in addition to the complex kinematics of the cervical spine during HFI, several numerical and experimental studies have been conducted in order to characterize and investigate the response and injury outcome of the cervical spine during HFI loading. However, these experimental and numerical studies have several limitations pertaining to quantitatively analyzing the kinematic response of the cervical spine, studying soft tissue injury risk, and conducting sensitivity studies that identify factors which influence cervical spine response during HFI. Therefore, this study aimed to address these experimental and numerical limitations by achieving two objectives: (1) validating a biofidelic and detailed finite element head-neck model against two sets of experimental data, and (2) conducting a sensitivity study to identify important factors that influence the kinematic, kinetic, and injury response of the cervical spine during HFI. The kinematic results were the buckling behaviour of the cervical spine (quantified by a variable termed the buckling parameter) and the kinetic results were the head contact force and axial neck compressive force histories. The hard tissue injury results entailed the onset time and location of vertebral fracture and the soft tissue injury results entailed identifying ligament rupture and disc avulsion.

HFI parameters (e.g., initial conditions such as cervical spine curvature prior to impact) were identified from literature and varied in a sensitivity study to evaluate the individual effect on cervical spine response relative to a reference baseline model. All model configurations (the two validation models and the sensitivity study models) were simulated in HFI and quantitatively assessed using kinematic response, kinetic response, hard tissue injury, and soft tissue injury. The validation results indicated that there was good agreement for the axial neck compressive force (less than 500 N difference). Good agreement was not predicted for the head contact force (more than 3,500 N difference) because of the different deformation levels observed at the model and

experimental impact interfaces. Good agreement was predicted for the cervical spine kinematic response (less than 7% difference in buckling parameter) because of the same buckling mode and inflection point between the model and the experiments. Moreover, good agreement was observed for the hard and soft tissue injury outcomes in terms of onset time (less than 1 ms difference) and location of injury occurrence (e.g., C3 and C4 laminar and spinous process fractures as well as anterior longitudinal ligament ruptures). The sensitivity study results indicated that the impact velocity of the head and neck prior to impact had the greatest influence on the response of the cervical spine during HFI, followed by the lateral angle of the impact plate and the anteroposterior angle of the head. Quantitatively analyzing the kinematic response of the cervical spine provided guidance and information for investigating the kinetic response and the injury risk. It is recommended that future numerical research investigating HFI focus on the effects of incorporating active and passive musculature on the response of the cervical spine, and to develop a hard tissue failure model suitable for predicting and modelling vertebrae fracture initiation and propagation. Furthermore, it is recommended for future experimental research to consider the effect of freeing the boundary condition applied at the first thoracic vertebra on the resultant response and to consider the lateral angle of the impact plate as an important factor in the behaviour of the cervical spine under HFI.

Acknowledgements

First and foremost, I would like to thank my supervisor, Professor Duane Cronin, for accepting me into his research group and granting me with the opportunity of conducting really interesting and novel biomechanical research. Thank you for always being accommodating and understanding, for always pushing me to keep focused and want more, for your patience and dedication to my research work and objectives, and for being an excellent mentor.

I would like to thank Professor Peter Cripton and Luis Dias from the University of British Columbia for listening to my presentations and always providing valuable feedback. Thank you both for an amazing time in Vancouver and Whistler – by far the best work-related trip I have gone on.

I would also like to thank the University of Waterloo for the financial support, the Canadian Institute for Health Research (CIHR) for funding my research work, and the Global Human Body Models Consortium (GHBMC) for the leadership and access to the FE models.

Thank you to all my colleagues at the Impact Biomechanics and Material Characterization (IMMC) group for the great memories and for making the office fun to work at. A special thank you to Jeffery Barker for his continuous technical support and advice throughout my entire research, to Miguel Corrales for patiently teaching me his reposturing methodology and for co-authoring on my conference papers, and to Prasannaah Hadagali for his help and support throughout my stay at IMMC.

To my fiancée, Hajar – thank you for always being by my side, for being my rock and for constantly pushing me, for being patient whenever I complained, and for being my number 1 supporter. I would not have been able to do this without you, I love you. Thank you to my friends who have kept me sane throughout my research, for always being there for me, and for bearing with me as I wrote my thesis.

Lastly, I am thankful and grateful for my family who have always been there for me from the start. Thank you for your unconditional love and support in everything I did, including this Master program. Thank you for always believing in me and for pushing me to be the best version of myself.

Table of Contents

List of Figures

List of Tables

Chapter 1: Introduction

1.1 Motivation for Research

The cervical spine is mechanically and structurally complex; as such, it is susceptible to a variety of injuries depending on the type of loading. Cervical spine injuries (CSI) (AIS3+) due to head-first impact (HFI) result in a significant individual and financial cost, especially if there is associated spinal cord injury [Allen et al., 1982; Ivancic et al., 2008]. The National Spinal Cord Injury Statistical Centre (NSCISC) reported that there were approximately 17,900 new spinal cord injury cases in 2020 in the United States alone, with associated total annual expenses of $1 million USD [NSCISC, 2021]. During HFI, the cervical spine is compressed due to the momentum of the following torso and the relatively stationary head impacting a surface, potentially leading to life-threatening and debilitating injuries such as quadriplegia [Yoganandan et al., 1989; Nightingale et al., 2015]. HFI can occur from events such as falls and contact sports, but the plurality of CSI occurs due to motor-vehicle accidents (MVA) [Thompson et al., 2009; Hasler et al., 2012]. In the United States, CSI due to MVA account for 45% of total CSI [Sekhon et al., 2001]. HFI that occurs as a result of rollover MVA accounts for 32% of all fatalities in MVA events [Roberts et al., 2018]. Due to the close proximity to vascular, neurological, and respiratory structures, CSI can also be associated with spinal cord injury [Sekhon et al., 2001]. In fact, several studies reported that a high proportion of acute spinal cord injuries occur in the cervical region (55-58%) [Yoganandan et al., 1989; Yadollahi et al., 2016].

Research in HFI has gained traction over the last two decades, and mainly encompasses experimental [Saari et al., 2013; Roberts and Kerrigan, 2015] and numerical studies [Halldin et al., 2000; Nasim et al., 2021]. There have been several published experimental studies in which cadavers were placed in an inverted orientation and dropped on an impact surface. The studies conducted drop tests and usually extracted kinetic results (e.g., cervical spine axial force and contact force between head and impact surface) and injury data post impact. However, due to the associated cost and limited number of specimens, sensitivity/parametric studies have not been conducted on an experimental level. Sensitivity studies are useful in understanding the influence of certain boundary and initial conditions on the response of the cervical spine and have been conducted and reported in some numerical studies [Camacho et al., 1997; Hu et al., 2008]. Numerical studies have presented results on model validation against HFI loading, all of which

were only based on the experimental results reported in the study by Nightingale [Nightingale et al., 1997]. The models previously developed for validation against HFI loading often had the cervical vertebrae modelled as rigid bodies, limiting the models to not being able to predict bone fracture. The previous models were also limited in having a course mesh density (relative to the detailed numerical model used in this study) and not being validated for other loading conditions. Moreover, the results reported in the previous numerical studies did not consider soft tissue injuries and did not quantify the kinematic response of the cervical spine during HFI loading relative to experimental studies. Given the limitations of the previous experimental and numerical HFI studies in addition to the complex dynamics of the cervical spine under HFI loading, a biofidelic and detailed finite element head-neck model was validated against two experimental HFI studies and was used in a sensitivity study as well. This provided relevant knowledge pertaining to the response of the cervical spine and informed further research and improvements to protect the population against HFI events.

1.1 Research Objectives and Approach

The overall goal of this thesis was to validate a detailed finite element head-neck model for HFI loading and to assess the effect of the variation of HFI parameters (i.e., boundary and initial conditions) on the response of the cervical spine throughout the loading. This approach was useful in providing comprehensive data relevant to understanding the behaviour and injury outcome of the cervical spine during HFI loading events.

The first objective of this study was to validate a 50^{th} percentile male detailed finite element head-neck model against experimental results reported in Saari and Nightingale [Nightingale et al., 1997; Saari et al., 2013]. The experimental initial and boundary conditions, such as initial cervical spine curvature and impact velocity, were replicated in the model. The model validation included a comparison of the kinematics and kinetics, and a comparison of the hard and soft tissue injuries predicted by the model with the injuries reported by the experimental studies.

The second objective of this thesis was to perform a sensitivity study in which HFI parameters were individually varied to assess the effect on the response of the cervical spine under HFI loading. The results extracted from each of the simulations in this study were the same as the validation results (kinematics, kinetics, and injury outcome). The study identified the parameters that had the greatest or the least influence on the response and injury risk of the cervical spine.

1.2 Thesis Organization

Chapter 2 outlines and summarizes the fundamental anatomy of the cervical spine, describes the cervical spine injuries and injury mechanisms resultant from HFI, discusses the previous experimental and numerical work that has been done to study HFI, and describes the GHBMC model used for validation and analysis.

Chapter 3 covers the model preparation details necessary to conduct the HFI validation against results from the experimental studies. The chapter also presents the sensitivity study structure and parameters investigated.

Chapter 4 outlines the results describing the response of the cervical spine (kinematic, kinetic, and injury) for the model validation against Saari and Nightingale and the sensitivity study. The chapter also discusses and explains the findings as well as summarizes the sensitivity study results and identifies which parameters had the greatest and least influence on the response of the cervical spine.

Finally, Chapter 5 provides the overall conclusions summarizing the key findings from the validation and sensitivity study. The chapter also provides recommendations for future research in HFI.

Chapter 2: Background

2.1 Anatomy of the Neck

2.1.1 Anatomical Terms

Anatomy is the study concerned with the bodily structure of living things. Anatomical planes and directions are used to divide the body into portions and to define conventional nomenclature regarding anatomical features (Figure 2-1). The anatomical planes are the frontal, transverse, and sagittal planes. The frontal plane divides the body into front and back parts, the transverse plane divides the body into top and bottom parts, and the sagittal plane divides the body into right and left sides. The intersection of the sagittal and frontal planes creates the superior and inferior directions (opposite to each other). The anterior and posterior directions are created by the intersection of the sagittal and transverse planes. The medial and lateral directions, created by the intersection of the transverse and frontal planes, describe the perpendicular direction towards and away from the median, respectively.

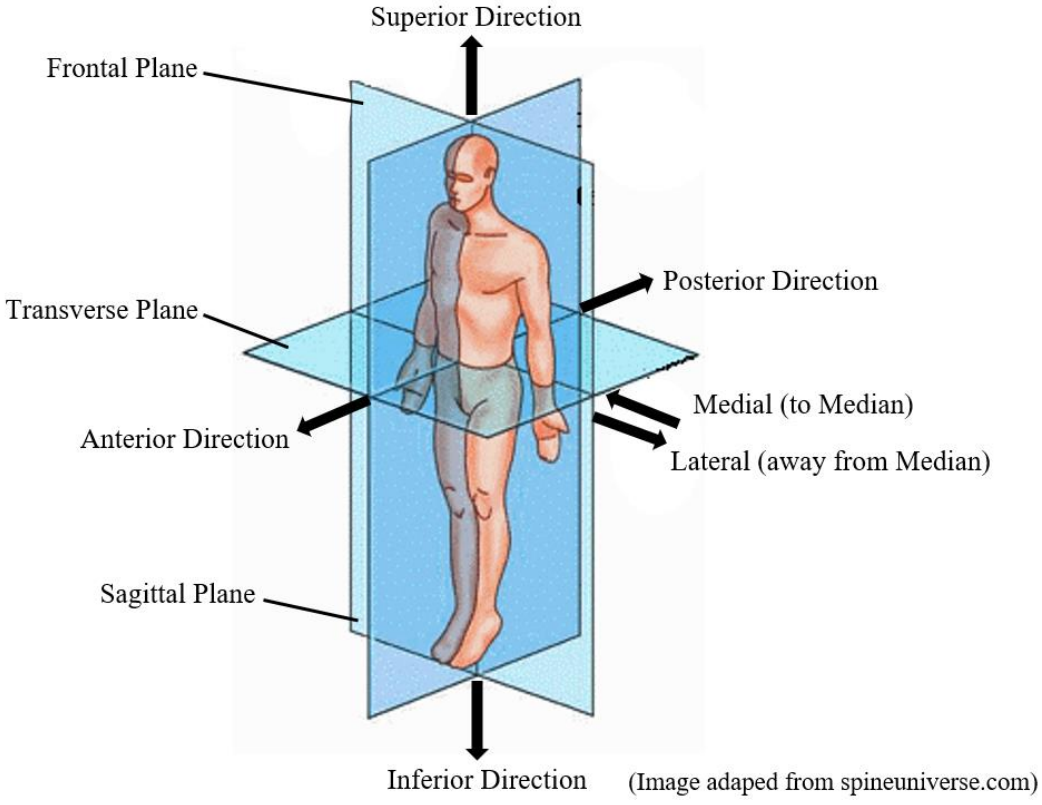

Figure 2-1: Anatomical planes and directions

The anatomical terms used to describe the bending motion of the neck are flexion, extension, lateral bending, and axial rotation (Figure 2-2). Flexion describes the rotation of the head and neck about the lateral axis in the sagittal plane such that the head is ‘looking down’. Alternatively, extension, which is the motion opposite to flexion, describes the rotation of the head and neck (also about the lateral axis in the sagittal plane) such that the head is ‘looking up’. The typical cervical spine range of motion in flexion and extension is 80° to 90°, and 70°, respectively [Swartz et al., 2005]. Lateral bending describes the bending motion of the head and neck towards the right or left side rotating about the anteroposterior axis in the frontal plane, with a typical range of motion of 20° – 45°. Axial rotation entails rotating the head and neck around the superior-inferior axis, with a typical range of motion up to 90° to both sides.

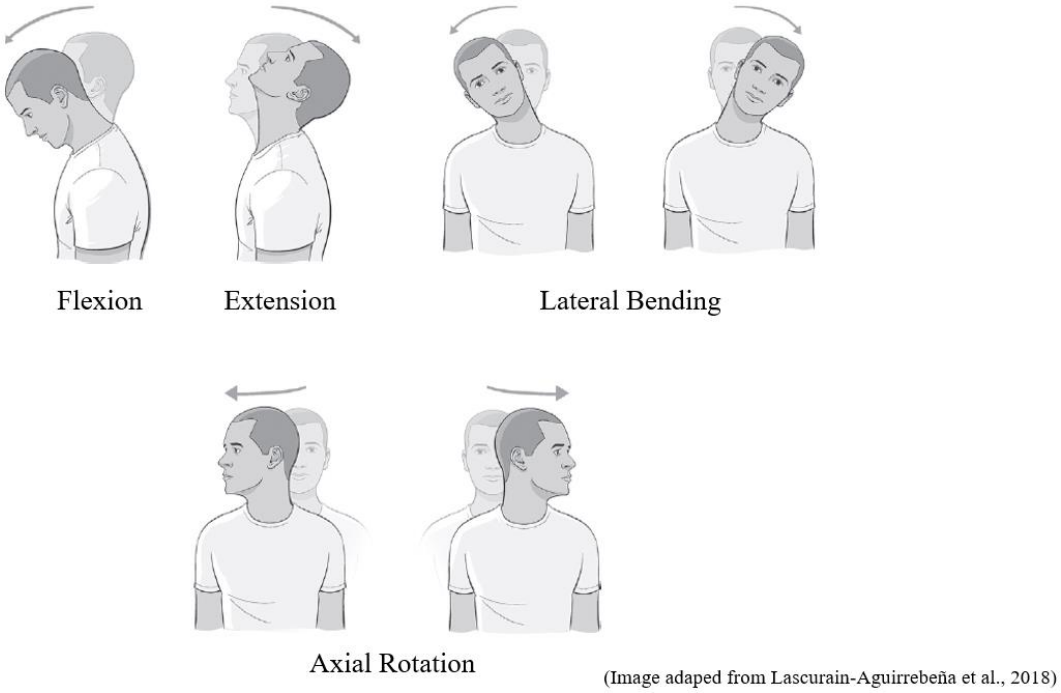

Figure 2-2: Terms describing motion of the head and neck

2.1.2 Cervical Vertebral Anatomy

Vertebrae, which are the series of small bones forming the spinal column, form the spinal column and are divided into three regions: cervical, thoracic, and lumbar. All vertebrae of the spinal column have a centrally located orifice (called the vertebral canal) through which the spinal cord passes. The cervical spine, which is the focus of this thesis, consists of seven vertebrae and is

commonly divided into three sections: upper cervical spine (C1 and C2), the middle cervical spine (C3-C5), and the lower cervical spine (C6-C7) (Figure 2-3) [Cusick and Yoganandan, 2002; Mattucci et al., 2012]. The anatomy of the middle and lower cervical spine vertebrae is similar. The first thoracic vertebra (T1) is often considered alongside the lower cervical spine (specifically for neck models (section 2.4)) it is directly inferior to C7 and consequently forms an intervertebral joint with it. The cervical vertebrae are constructed from a soft and porous inner bone core (trabecular bone) surrounded by a thin and relatively rigid shell (cortical bone) (Figure 2-4). The cortical bone surrounding the vertebral body of the vertebrae is thin (ranging from 0.4 mm to 0.7 mm thick) [Panjabi et al., 2001]. However, it is much thicker around the posterior elements of the vertebrae [Gray, 1918]. The structure of the cortical bone is composed of vertical laminae designed to resist compressive forces [Benzel et al., 2005]. The structure of the trabecular bone is composed of thick vertical columns sustained by thinner horizontal trabeculae [Kopperdahl and Keaveny, 1998].

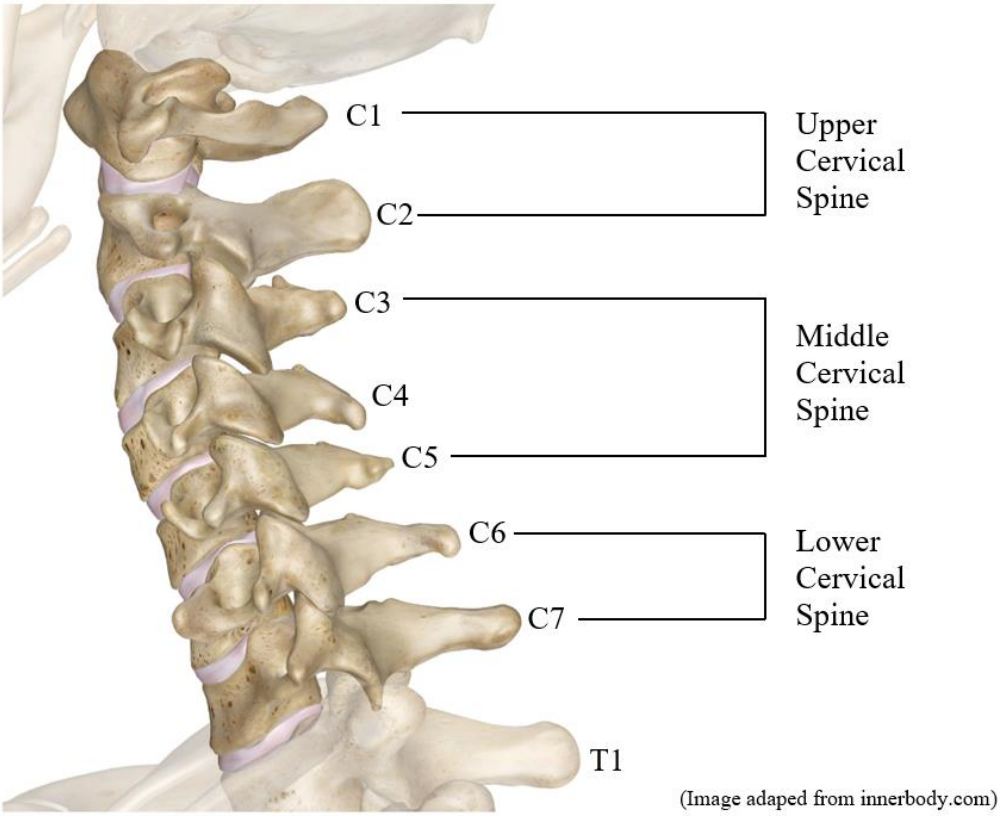

Figure 2-3: Cervical spine division

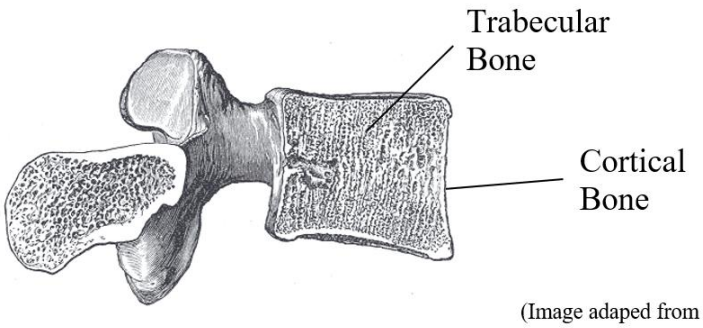

Figure 2-4: Vertebral cortical and trabecular bones [Gray, 1918]

The middle-to-lower cervical spine vertebrae (C3-C7) are comprised of two portions: the anterior portion consisting of the vertebral body, and the posterior portion consisting of the vertebral arch which is made up of the laminae, the pedicles, the facet joints, and seven processes (Figure 2-5). The processes consist of four articular processes, two transverse processes, and one spinous process. The transverse processes and the spinous process serve as attachment points for muscles and ligaments [Benzel et al., 2005].

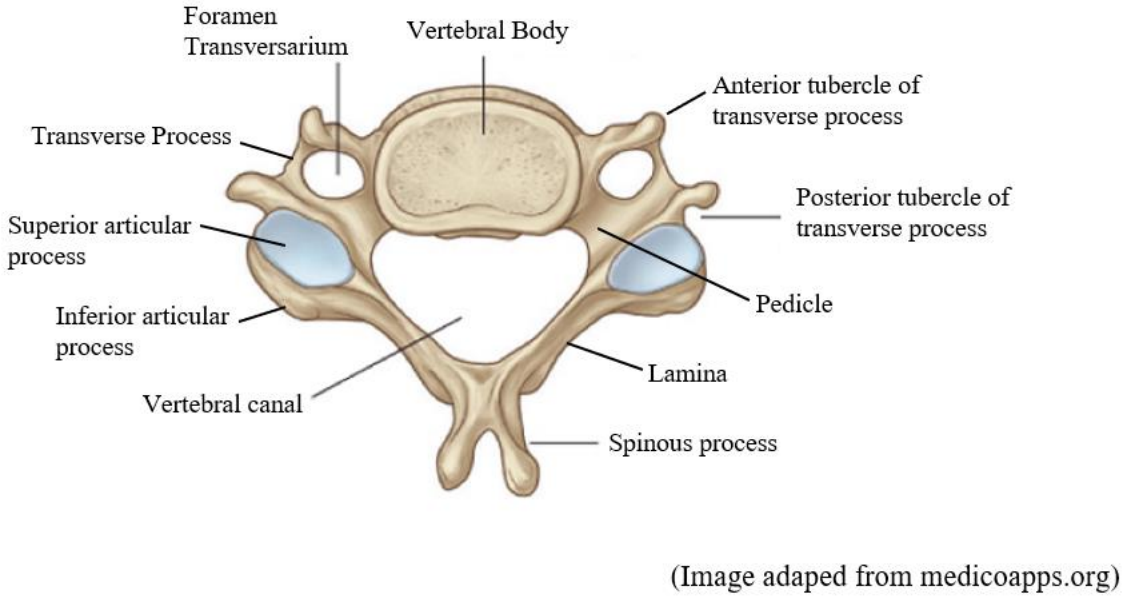

Figure 2-5: Anatomy of the middle-to-lower cervical vertebrae (superior view)

The transverse processes, formed near the union of the pedicle and the vertebral body at either side, contain the transverse foramen, which is a cavity that transmits the vertebral artery. The spinous process is formed from the union of the laminae. There is a set of superior and inferior articular processes at the right and left sides of the cervical vertebrae, and each set is fused by the articular pillar. The surfaces of the articular processes of adjacent vertebrae form facet joints, which are synovial joints important for cervical spine stability [Benzel et al., 2005]. The joints are comprised of cartilage on the articular surfaces and a gap in between containing synovial fluid lubricating the interface (Figure 2-6).

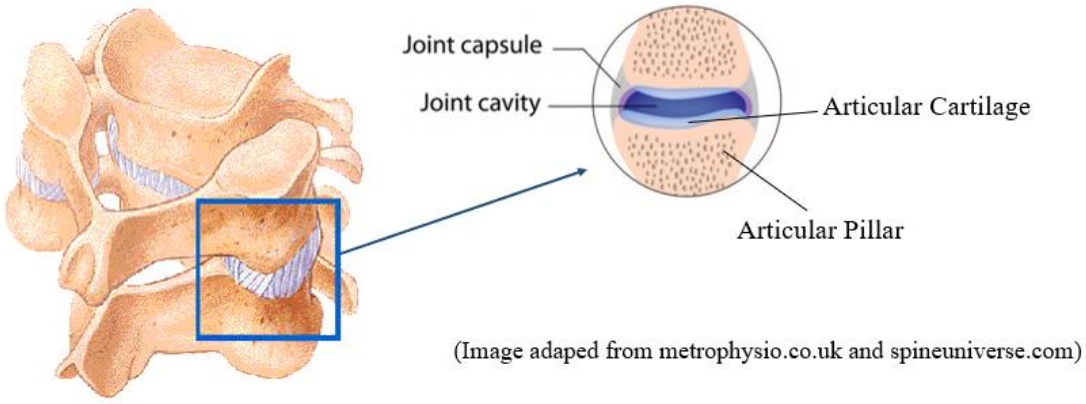

Figure 2-6: Cervical facet joint

The pedicles are short and thick structures that extend dorsolaterally (inferior and lateral direction) from the posterolateral margin of the vertebral body. The laminae are elongated plates directed in the posteromedial direction from the pedicles, to which they are connected, until they are fused to form the spinous process. The posterior elements of the cervical vertebrae are shaped in an arc to form the vertebral foramen (biggest cervical orifice) through which the spinal cord passes. The vertebral body is the largest structure of the cervical vertebrae and is cylindrically shaped. The inferior and superior surfaces of the vertebral body (i.e., endplates) are attached to the intervertebral discs.

The anatomy of the upper cervical spine vertebrae, C1 (atlas) and C2 (axis), are different from the structure of the middle-to-lower cervical spine (Figure 2-7). The atlas is ring-shaped and has no vertebral body or spinous process; it is comprised of anterior and posterior arches and two lateral masses that serve to support the skull (Figure 2-8). There are large concave facets on the superior

surfaces of the lateral masses of the atlas that are connected to the occipital condyles of the skull forming the atlanto-occipital joint. This joint is responsible for the flexion and extension rotation of the head and cervical spine. The facets on the inferior surfaces of the lateral masses of the atlas are large and convex, and they are in contact with the superior articular pillar surfaces of the axis forming the atlanto-axial joint. This joint is responsible for the axial rotation of the head and cervical spine.

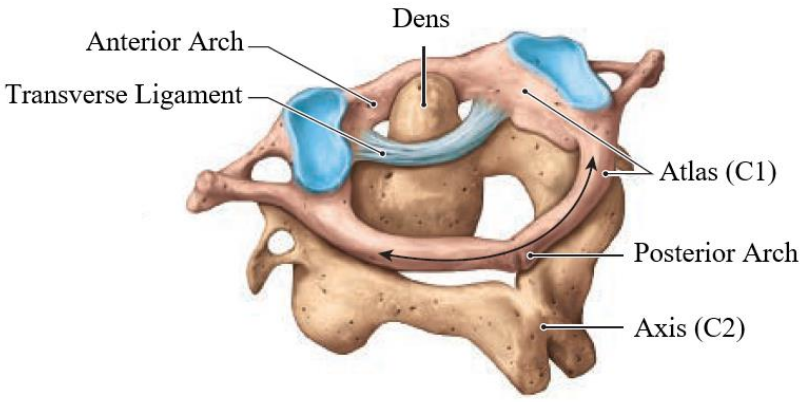

(Image adaped from Martini et al., 2017)

Figure 2-7: Upper cervical spine (C1 and C2) (Martini et al., 2017, used with permission from Pearson)

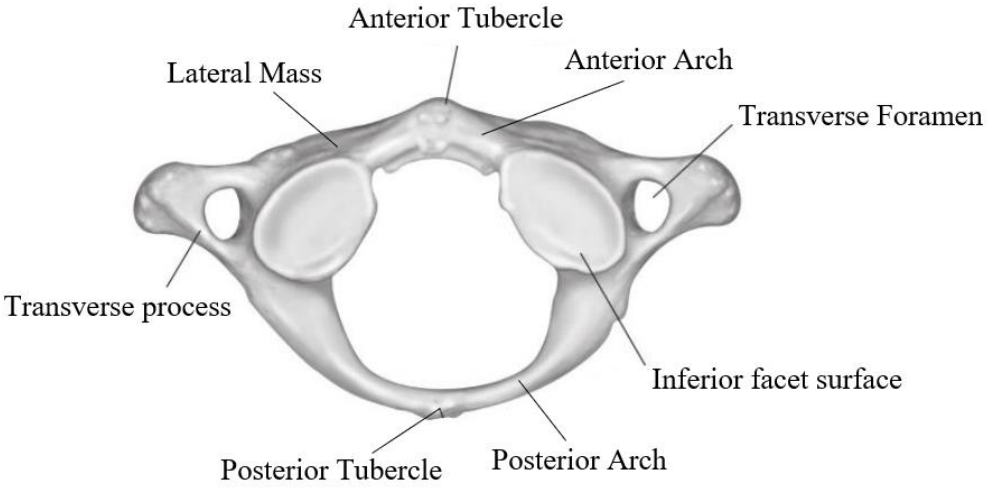

(Image adaped from Benzel, 2012)

Figure 2-8: Anatomy of the atlas (inferior view) (Benzel, 2012, used with permission from Wolters Kluwer)

The axis has a similar structure to the middle-to-lower cervical spine vertebrae (C3-C7) except for an odontoid process (also known as dens) protruding superiorly from the C2 vertebral body (Figure 2-9). There is an articular facet on the anterior surface of the dens for contact with the posterior surface of the anterior arch of the atlas. Additionally, the pedicles, laminae, and spinous process of the axis are larger than those in the middle-to-lower cervical spine [Gray, 1918].

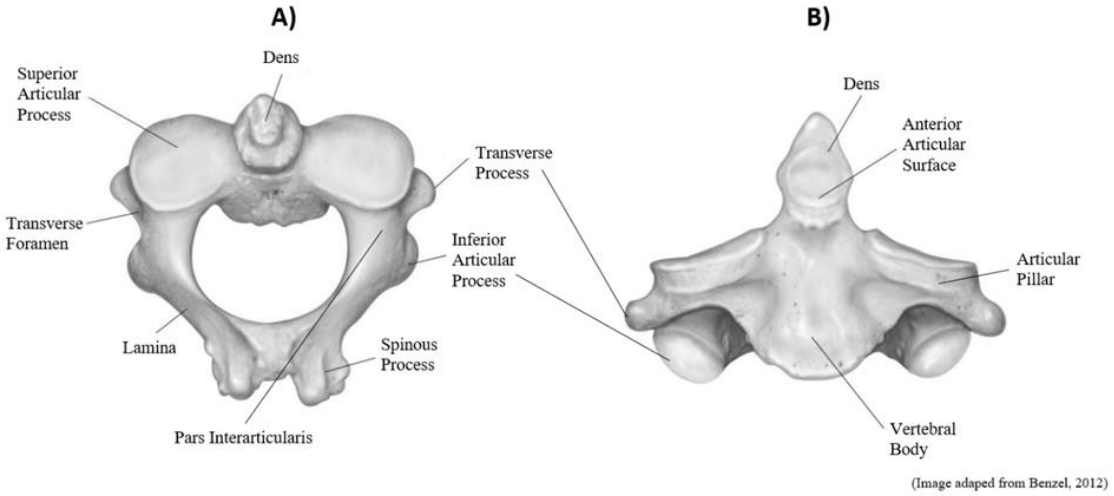

Figure 2-9: Anatomy of the axis, A) superior view, and B) anterior view (Benzel, 2012, used with permission from Wotlers Kluwer)

The cervical spine has a natural curvature called cervical lordosis. Cervical lordosis is the posterior concavity of the cervical spine (from T1 to the foramen magnum (hole in the base of the skull through which the spinal cord passes) and is important in maintaining forward gaze and upright posture of the head [Been et al., 2017]. Moreover, lordosis is crucial for healthy posture and for functions such as breathing control, eye movement, and part of the shock-absorbing mechanism involved in walking and running [Guo et al., 2018]. In fact, loss of cervical lordosis is associated with neck pain and disability. Figure 2-10 shows the lordosis of the cervical spine (in addition to the entire vertebral column) relative to the line of gravity (passing through the dens of the axis) [Benzel et al., 2005]. The line of gravity only serves to illustrate the lordosis curvature of the cervical spine.

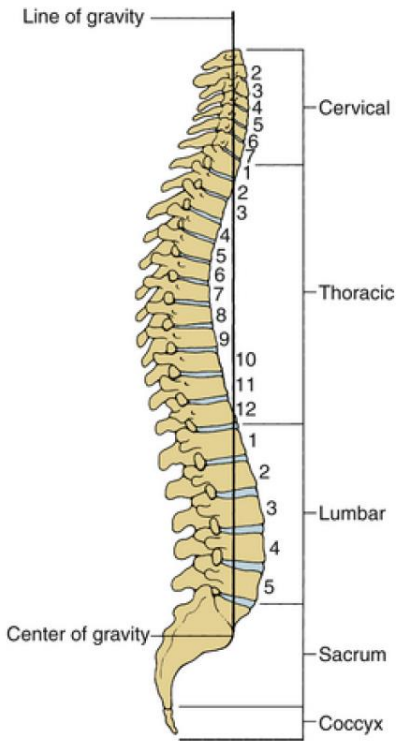

Figure 2-10: Cervical column showcasing the lordosis of the cervical spine relative to the line of gravity (Benzel et al., 2005, used with permission from Elsevier)

2.1.3 Anatomy of the Intervertebral Discs

The intervertebral discs (IVD) are located in between adjacent vertebral bodies (starting at C2-C3) and aid in shock absorption and permit movement between adjacent vertebrae [Moore et al., 2015]. There are three major components in IVD: the annulus fibrosus (made of fibrocartilaginous layer of alternating collagen fibers), cartilaginous end plates, and the nucleus pulposus (Figure 2-11) [Benzel et al., 2005]. At each segment level (e.g., C3-C4 is a segment level), the annulus fibrosus binds the adjacent vertebral bodies. The concentric lamellae in the annulus fibrosus are designed to withstand tension, shear, and torsion loads [Yoganandan et al., 2001]. The nucleus pulposus, consisting of water, proteoglycans (protein chain), collagen, amongst other proteins, is designed to sustain compressive loads [Iatridis et al., 1996].

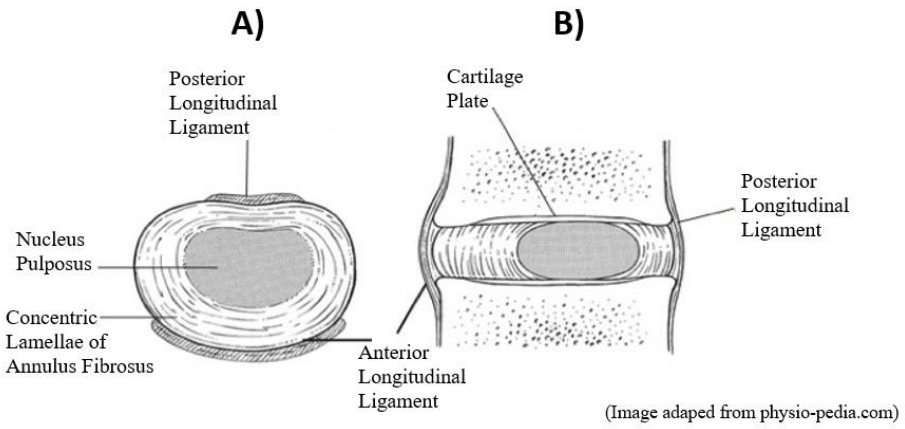

Figure 2-11: IVD anatomy, A) isolated IVD, and B) sagittal cross-section

2.1.4 Anatomy of the Cervical Spine Ligaments

Ligaments are uniaxial structures that only resist tensile forces and connect adjacent vertebrae to each other. They are primarily made of elastin and type I collagen and permit normal spinal motion while preventing excessive motion [Yoganandan et al., 2001; Benzel et al., 2005]. The major ligaments of the cervical spine are the anterior and posterior longitudinal ligaments (ALL and PLL), the ligamentum flavum (LF), the capsular ligament (CL), the interspinous ligament (ISL), and the nuchal ligament (NL).

The ALL is a strong fibrous band that is continuous from the vertebral body of the axis across the entire spinal column and connects the anterolateral aspects of the vertebral bodies and IVD (Figure 2-12) [Benzel et al., 2005, Moore et al., 2015]. The ALL is more effective under extension loading due to the anterior positioning [Yoganandan et al., 2001]. The PLL, similar to the ALL, extends from the axis and continues to span the entire cervical spine. It is slightly weaker than the ALL and is situated within the vertebral canal along the posterior margin of the vertebral bodies and adhering to the IVD (Figure 2-13) [Moore et al., 2015].

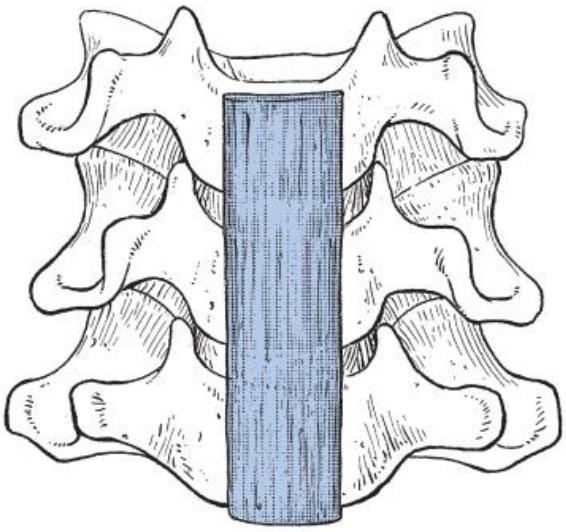

Figure 2-12: Anterior view of the anterior longitudinal ligament (ALL) (Ombregt, 2013, used with permission from Elsevier)

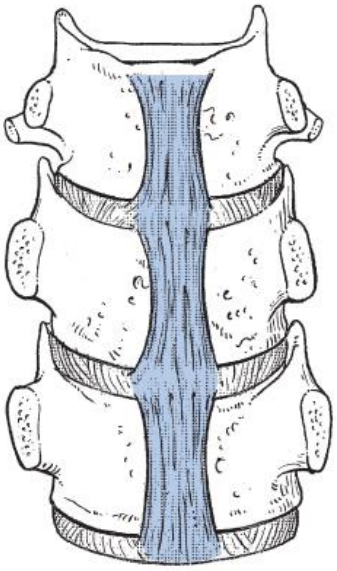

Figure 2-13: Posterior view of the posterior longitudinal ligament (PLL) (Ombregt, 2013, used with permission from Elsevier)

The LF extends from either side of the articular process roots to the point where the laminae fuse to form the spinous process in order to connect the lamina of two adjacent vertebrae (Figure 2-14). It is situated at the posterior wall of the vertebral canal and is the most elastic tissue in the human

body [Benzel et al., 2005]. The CL connects the margins of the articular processes of adjacent vertebrae and surrounds the facet joints (Figure 2-15).

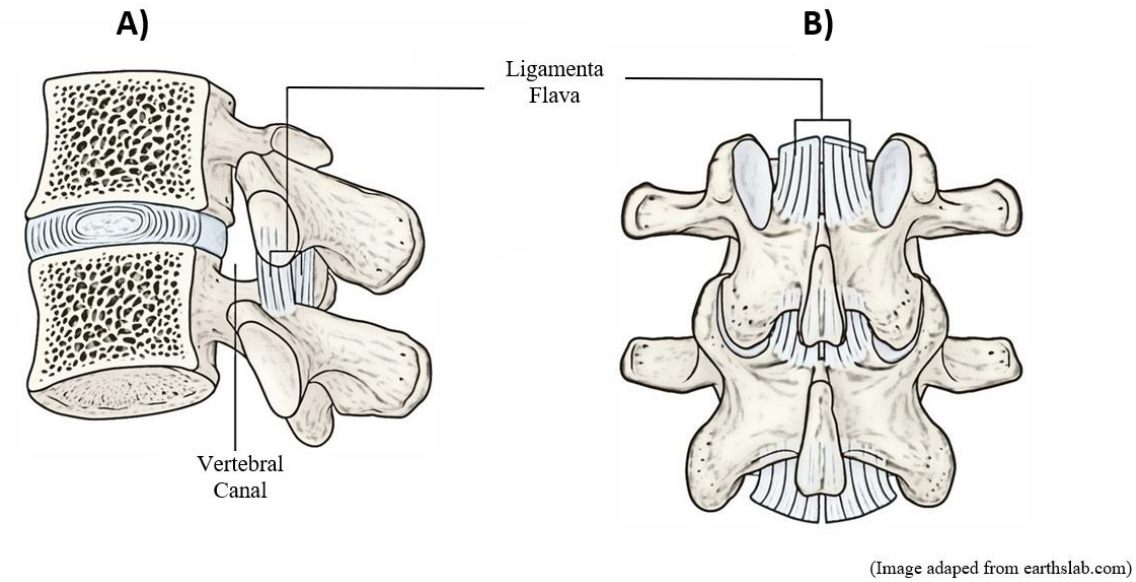

Figure 2-14: Ligamenta flava (LF), A) mid-sagittal cross-section, and B) posterior view

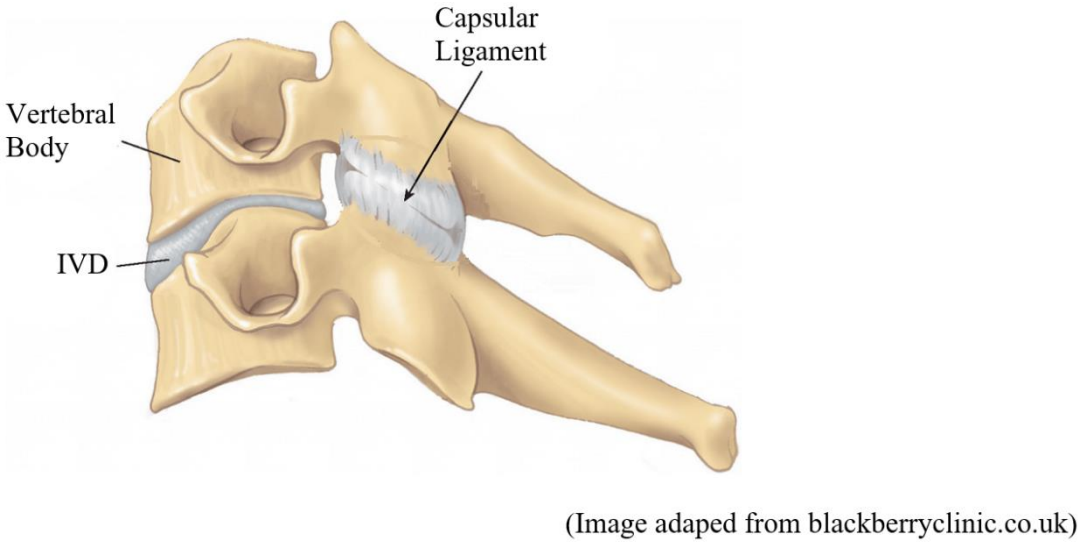

Figure 2-15: Capsular ligament (sagittal view)

The ISL connects the spinous processes of adjacent vertebrae. It is predominantly made of elastin and is relatively weaker than the other ligaments (Figure 2-16) [Yoganandan et al., 2001]. The ISL forms a membrane that merges with the NL at the posterior end. Unlike the ISL, the NL is strong

and made of thickened fibroelastic tissue that extends from the occipital protuberance and posterior border of the foramen magnum to the spinous process of the cervical vertebrae (Figure 2-16) [Moore et al., 2015].

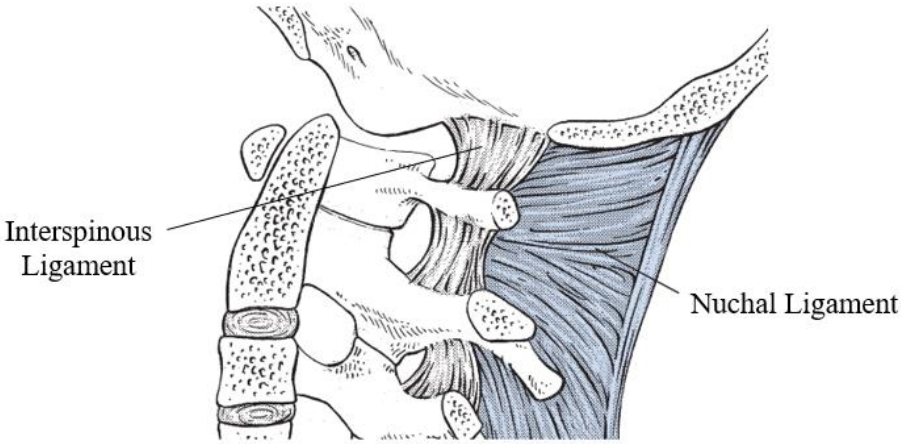

(Image adaped from Ombregt, 2013)

Figure 2-16: Interspinous and nuchal ligaments (Ombregt, 2013, used with permission from Elsevier)

There are additional ligaments at the upper cervical that connect the atlas (C1) to the axis (C2) and the atlas to the base of the skull (Figure 2-17). The anterior and posterior atlanto-occipital membranes are broad and dense ligaments that connect the anterior and posterior arches of C1 to the anterior and posterior margins of the foramen magnum, respectively [Moore et al., 2015]. The ligaments that connect the atlas to the axis are called atlanto-axial ligaments: transverse ligament, cruciate ligament, alar ligament, and tectorial membrane [Moore et al., 2015]. The transverse ligament is the strongest and largest ligament in the cervical spine, and it maintains the contact between the dens and anterior arch of C1. The transverse ligament extends from the medial margins of the lateral masses of C1 to the posterior surface of the dens. The superior and inferior longitudinal bands extend from the transverse ligament to the occipital bone and the vertebral body of C2, respectively. The transverse ligament and the superior and inferior longitudinal bands form the cruciate ligament due to the resemblance to a cross [Moore et al., 2015]. The alar ligaments connect the sides of the dens to the lateral margins of the foramen magnum to prevent excessive rotation at the upper cervical spine. The tectorial membrane extends superiorly from the PLL of the C2-C3 segment level to the internal surface of the occipital bone.

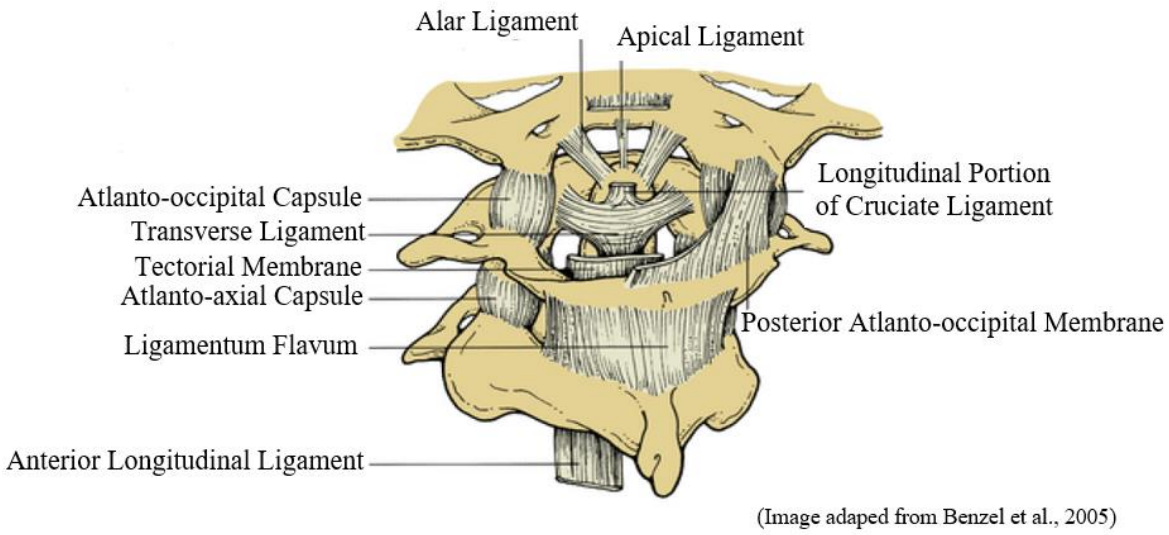

Figure 2-17: Atlanto-occipital and atlanto-axial ligaments (Benzel et al., 2005, used with permission from Elsevier)

2.2 Cervical Spine Injury Due to Head-First Impact

The cervical spine can be subjected to a variety of injuries depending on the loading vector applied. This section describes head-first impact (HFI) injury mechanisms and epidemiological data covering the occurrence and severity of cervical spine injuries resulting from HFI loading.

2.2.1 Cervical Spine Injury Classification and Mechanisms During Head-First Impact

The cervical spine can sustain hard and soft tissue injuries through a variety of mechanisms, where the term mechanism strictly refers to the kinematic behaviour and motion of the cervical spine that leads to injury. Hard tissue injury refers to vertebral injury such as fractures, while soft tissue injury describes injury or damage to the ligamentous or cartilaginous structures of the cervical spine, such as ligament ruptures and disc avulsions. During HFI loading, serious injury (AIS3+) can occur as rapidly as 2 to 30 ms after initial impact between the head and the surface [Swartz et al., 2005; Yoganandan et al., 2016; Maiman et al., 2018]. This short interval occurs well before observable head motion. As the loading progresses and both the head and the impacted surface reach their respective absorptive limits, the head begins accelerating in the inferior direction towards the cervical spine, thereby compressing the neck from the superior direction (via the head)

and the inferior direction (via the following effective torso mass) [Nightingale et al., 1997; Swartz et al., 2005].

Due to the structural and anatomical differences between the upper (C1 and C2) and middle-to-lower cervical spines (C3-C7), the respective hard and soft tissue injuries incurred are different and therefore described separately. The three most common hard tissue injuries sustained by the C1 and C2 vertebrae in the upper cervical spine during compressive loading are Jefferson's fracture, Hangman's fracture, and odontoid fracture [Nightingale et al., 2015]. Jefferson's fracture refers to a 4-part fracture of the atlas: two fracture lines at the anterior arch, and two at the posterior arch (Figure 2-18). It is common for this injury to cause fatality and cervical spine instability, where the term instability entails significant displacement of the vertebra in addition to the fracture.

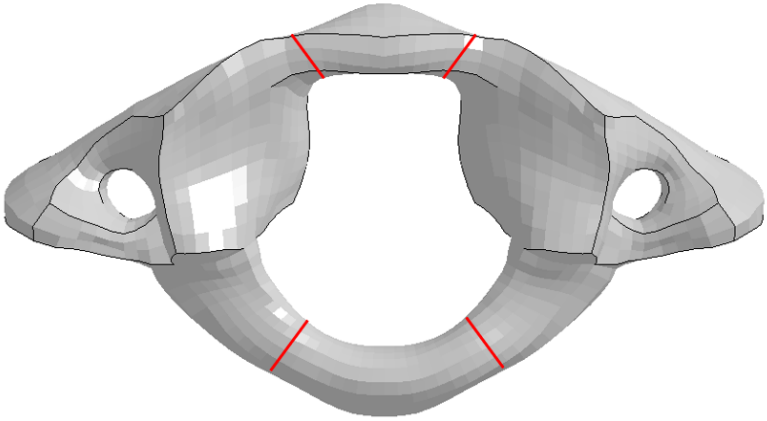

Figure 2-18: Superior view of Jefferson's fracture of the atlas (indicated by the red fracture lines)

Hangman's fracture describes fracture of the pars interarticularis (Figure 2-9) and pedicles of the axis (Figure 2-19). This injury is usually attributed to hyperextension of C2 along with a possibility of rupture of the C2-C3 IVD, indicating the severity of the injury. The odontoid fracture of C2 is another common type of upper cervical spine injury that has the potential for spinal cord impingement (AIS3+) as well. This fracture has three types: Type I odontoid fracture entails fracture to the superior tip of the dens, type II refers to fracture through the main body of the dens, and type III entails fracture of the base of the dens that could potentially extend to the vertebral body of C2 (Figure 2-20). While type I and III odontoid fractures are often stable and clinically manageable, type II fractures have a high associated chance of nonunion (inability for a fracture to heal) that can lead to atlantoaxial dislocation.

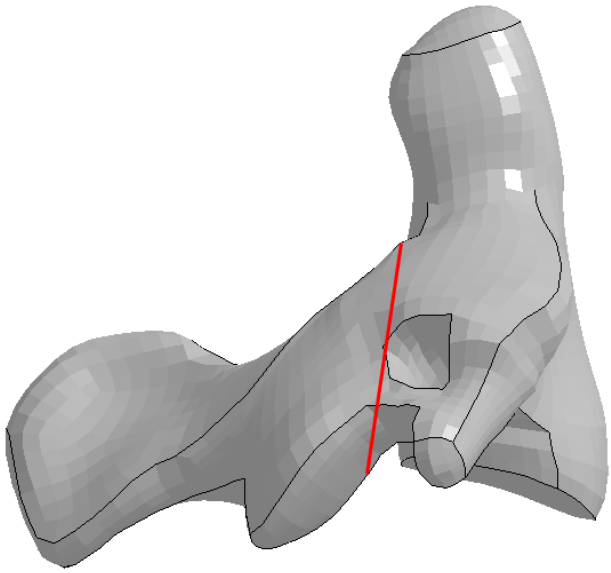

Figure 2-19: Sagittal view of Hangman's fracture of the axis (indicated by the red fracture line)

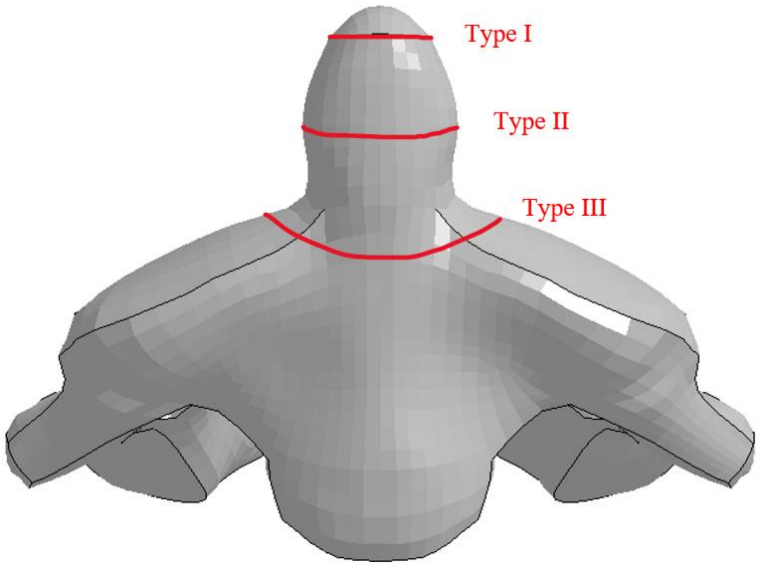

Figure 2-20: Frontal view of odontoid fractures (Types I, II, and III) of the axis (indicated by red fracture lines)

The cervical spine usually undergoes transient deformation, or buckling, during compression, which can impose flexion and extension rotations throughout the loading [Swartz et al., 2005]. During buckling, the cervical vertebrae experience a combination of anterior displacement and either flexion or extension rotation as the cervical spine transitions from one equilibrium configuration to another [Nightingale et al., 1997]. An equilibrium configuration refers to an

instance where the cervical spine does not displace or rotate and reaches a 'locked state'. Cervical spine buckling has several modes that are directly correlated with the load applied. As the load increases, a higher buckling mode is observed. First order (e.g., mode) buckling is the most common under compressive loading and entails extension of the upper-to-middle cervical spine and flexion of the middle-to-lower cervical spine. Moreover, the anterior-most vertebra is the point inferior of which the rotation changes direction from extension to flexion. Higher order buckling, which is more unstable than first order buckling, entails flexion of the upper cervical spine, extension of the middle cervical spine, and flexion of the lower cervical spine. Figure 2-21 shows first order cervical spine buckling along with higher order buckling for comparison.

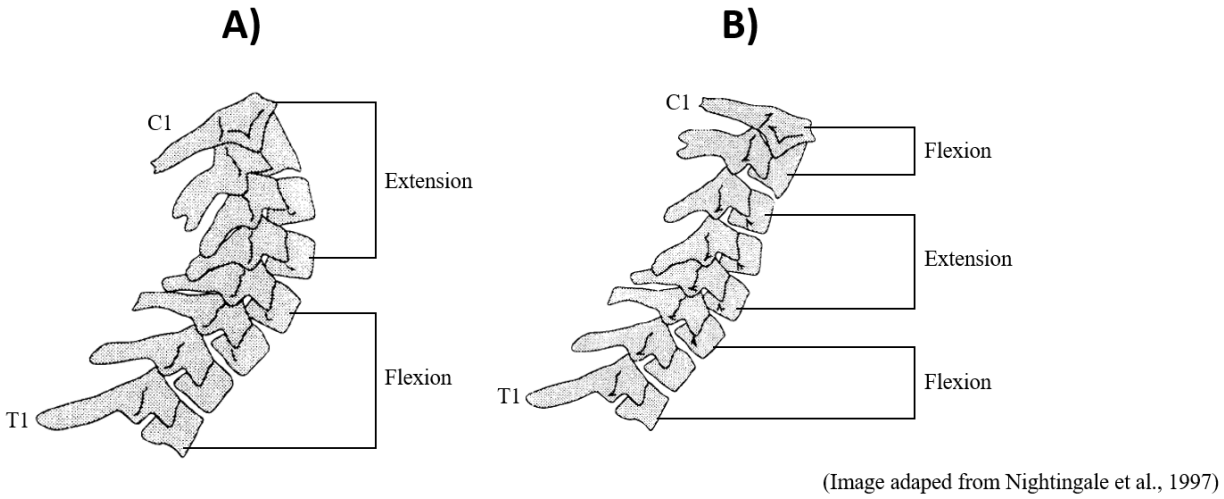

(Image adaped from Nightingale et al., 1997)

Figure 2-21: A) First order buckling with C4 being the anterior-most vertebra, and B) higher (and more unstable) order buckling (Nightingale et al., 2017, used with permission from SAE International)

Compressive loading could be centric or eccentric [Iencean et al., 2013]. The former does not cause significant cervical spine rotation, thereby incurring more hard tissue than soft tissue injuries, especially if there was an absence of cervical lordosis (i.e., natural curvature) prior to impact (Figure 2-22). Eccentric compressive loading leads to cervical spine sagittal rotation (in addition to compression) which causes either vertebral extension or flexion. Therefore, compressive loading can be isolated (i.e., pure vertical compression) or combined with flexion or extension. The severity of these fractures increases when there are associated pedicle and lamina fractures, which leads to instability and higher probability of spinal cord injury as well. When there is associated flexion and extension of the cervical spine, ligamentous (soft tissue) injuries such as

dislocations can occur. Pure dislocations without associated fracture, although rare (accounts for only 5% of spinal cord injuries), can be damaging to the cervical spine [Nightingale et al., 2015]. For example, bilateral facet dislocations, which have a preponderance for the C6-C7 and C7-T1 segment levels, can lead to quadriplegia (Figure 2-23) [Bedbrook, 1979]. Another common injury at the C6-C7 and C7-T1 segment levels is fracture dislocation. Fracture dislocation is characterized by vertebral body fracture along with vertebral displacement (often anterior) (Figure 2-24) [Nightingale et al., 2015].

Figure 2-22: Burst fracture of C5 (red arrow) due to vertical compression (Nightingale et al., 2015, used with permission from Springer)

Figure 2-23: Bilateral facet dislocation at C6-C7 (red arrow) with associated 'teardrop' fragment (Nightingale et al., 2015, used with permission from Springer)

Figure 2-24: Fracture-dislocation of the C7-T1 segment level with translation and vertebral body fracture of C7 (red arrow) (Nightingale et al., 2015, used with permission from Springer)

Due to the multitude of injuries and injury mechanisms that can occur at the middle-to-lower cervical spine due to HFI, there have been several injury classification systems published to provide a comprehensive understanding of the different types of hard and soft tissue injuries that

can be incurred. The classification outlined by Allen et al. summarizes and describes middle-to-lower cervical spine injuries by classifying them according to the mechanism involved [Allen et al., 1982]. The relevant mechanisms are compressive flexion, vertical compression, and compressive extension. Furthermore, each classification is divided into several stages to describe different severity levels.

Compressive flexion stage 1 (CFS1) injury involves the blunting (pushing in) of the anterior-superior margin of the vertebral body to a round contour of the inferior vertebra due to compressive flexion of the superior vertebra. The CFS1 injury entails no failure of the posterior ligamentous complex. CFS2 injury involves vertebral fracture and a deformation of the anterior-inferior corner of the vertebral body in addition to the injuries described in CFS1 (Figure 2-25). CFS3 injury, in addition to what was described above, has a more pronounced oblique fracture of the vertebral body that traverses posteriorly. CFS4 injury involves up to an additional 3 mm posterior displacement of the inferior-posterior vertebral corner into the vertebral canal. Finally, CFS5 injury entails even more posterior displacement of the vertebral body, PLL and posterior ligamentous complex failure (rupture), as well as facet joint separation. This injury mechanism has a preponderance for the middle-to-lower cervical spine segment levels [Allen et al., 1982].

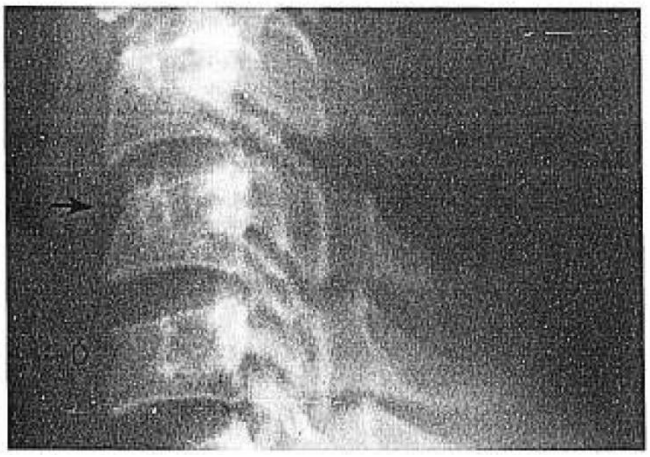

Figure 2-25: Compressive flexion stage 1 injury at the middle cervical spine (Allen et al., 1982, used with permission from Wolters Kluwer)

Vertical compression stage 1 (VCS1) injury entails centric compressive loading without vertebral sagittal rotation and fractures the end plate of either the superior or inferior vertebra without any ligamentous injury. VCS2 injury, in addition to the damage incurred in VCS1, involves fracture

of both end plates in addition to minimal relative displacement at the segment level. Finally, VCS3 injury entails fracture of vertebral body, especially the posterior margin, in addition to a possibility of rupture of the posterior ligamentous complex. The vertical compression mode of injury has a preponderance for the C7-T1 segment level [Allen et al., 1982].

The compressive extension injury has five severity levels. Compressive extension stage 1 (CES1) injury involves unilateral (i.e., on one side of the vertebra) vertebral arch fracture (specifically articular process or lamina) with a possibility of anterior displacement of the vertebral body. CES2 injury entails bilaminar factures at multiple vertebral levels. CES3 injury involves bilateral fracture of the lamina, pedicles, and articular processes without anterior displacement of the vertebral body. CES4 injury exhibits anterior displacement of the vertebral body. Finally, CES5 injury has even more significant anterior displacement of the vertebral body in addition to failure of the anterior and posterior ligamentous complex at two segment levels. The compressive extension injury is reported to most commonly occurs at the C6-C7 segment level [Allen et al., 1982].

2.2.2 Epidemiology

Axial compressive injuries that occur during HFI can have immediate and devastating consequences on the cervical spine. HFI can occur as a result of various events including motor vehicle rollovers, falls, sports, and assault, and can injure the cervical spine more than other isolated mechanisms such as hyperflexion [Falavigna et al., 2018]. A study that investigated 209 football-related cervical spine injuries reported that 52% of the injuries were attributed to axial loading with only 10% and 3% resulting from hyperflexion and hyperextension, respectively [Swartz et al., 2005]. Another study even suggested that the injury incidence due to axial loading in football is greater than 52% [Torg et al., 1987]. Motor vehicle accidents (MVA) are the one of the leading causes of cervical spine injury (CSI) in the United States, accounting for 45% of injuries [Sekhon et al., 2001]. Other studies indicate that almost half (49%) of CSIs occur as a result of MVAs [Thompson et al., 2009; Hasler et al., 2012]. The prevalence of MVAs over other HFI events is often the case for younger CSI patients (below the age of 35); aged CSI patients (65 years or older) incur injuries predominantly from falls (21.7%), followed by MVAs (8.5%) [Fredo et al., 2012; Peck et al., 2018]. The causes of CSIs vary depending on the country, regions within the country, as well as urban versus rural locations. However, on a global level MVAs are responsible for the highest incidence of CSIs (50%) [Sekhon et al., 2001]. Rollover MVAs are of

particular interest given the nature of HFI that occur during the event. Despite rollover crashes only accounting for 1.4% of total crashes in the United States, they result in 32% of all fatalities [Roberts et al., 2018]. In Australia, the fatalities due to rollovers are around 20%, and in Europe the rate is estimated to be around 10% [Young et al., 2007]. Moreover, a study conducted by the National Automotive Sampling System reported that adult, front-row, non-ejected occupants from 2003 to 2007 demonstrated that 55% of all AIS 3+ injuries incurred in pure rollover crashes were primarily to the head and cervical spine, further highlighting the preponderance these accidents have for the cervical spine [Ridella et al., 2008; Roberts et al., 2018]. These CSIs become more serious when spinal cord injury (SCI) is incurred as well.

In addition to rollover crashes damaging and injuring the cervical spine, it was found in several studies that a high proportion of acute SCIs occur in the cervical region (55-58%) [Yoganandan et al., 1989; Yadollahi et al., 2016]. Data from a study investigating spinal trauma patients demonstrated that between 19% and 51% of cases involve injuries to the cervical spine [Clayton et al., 2012; Hasler et al., 2012]. Serious CSIs (i.e., AIS 3+) were found to be approximately 14 times greater than those observed in the thoracolumbar spinal cord in MVAs. The cervical spinal cord can be injured or damaged during HFI as the continuous compression from the following torso could result in significant ligamentous injuries that involve dislocations which could impinge on the spinal column and spontaneously reduce it. In fact, high severity neck trauma (AIS 3+) is 65-77% bone related (hard tissue injury) and 20-23% cervical spinal cord related (soft tissue injury) [Yoganandan et al., 1989].

HFI loading commonly causes hard tissue injury in the cervical spine. Several epidemiological papers report that the middle-to-lower cervical spine is the most susceptible region in HFI events [Yoganandan et al., 1989; Ryan et al., 1992; Koivikko et al., 2004; Foster et al., 2012]. However, the most commonly injured area or region in the cervical spine varies depending on factors such as age for example. Cervical spine hard tissue injuries are reported to be more common in the C5-C7 vertebrae for younger CSI patients (< 50 years), whereas the C1-C3 vertebrae are more susceptible for older CSI patients (> 50 years) [Ryan et al., 1992]. The incidence of C2 fractures increases with age, accounting for 43% of spinal fractures in people over the age of 50. Alternatively, for subjects under the age of 50, it has been found that the C5-C7 vertebrae account for 66% of injuries and that C2 accounts for only 19% of injuries [Winkelstein et al., 1997].

Generally, however, incidence of C4-C5 injuries has been reported to be as high as 61% of total CSIs [Yoganandan et al., 1989]. An equally high incidence of injuries in swimming pool diving (which entails HFI) patients has been reported for the C5-C6 segment level. In contrast, upper cervical spine injuries have been thought to be less common among patients, with an incidence of only 17% of CSIs [Winkelstein et al., 1997]. A similar finding was reported in another paper which studied 65 shallow water diving CSI patients and reported that C5 was the most commonly injured vertebra (56%) followed by C6 (15%) [Aito et al., 2005]. Furthermore, several studies report that the most common type of hard tissue injury was vertebral body fractures [McElhaney et al., 1979; Sekhon et al., 2001; Ridella et al., 2008].

Soft tissue injuries involve injuries such as IVD distractions, ligament ruptures/tears, and cervical spinal cord lesions. A study which investigated 108 hospital patients reported that 32.4% of them had a CSI due to MVA [Martinez-Perez et al., 2014]. The paper reports that the ALL, PLL, and LF were disrupted in 52.8%, 58.3%, and 48.1% of the cases, respectively. The IVD was disrupted in 57.4% of the cases, and the C5-C6 segment level was the most commonly involved in the MVA accidents (28.7%), followed by C6-C7 (22.2%). It was not specified whether those MVAs were exclusive to HFI or not. ALL tears, often associated with extension-type mechanisms, and disc distractions were the most common injuries reported.

2.3 Head-First Impact Experimental and Numerical Studies

This section covers the relevant HFI experimental studies by summarizing and describing the cadaveric and drop test setups and reviewing the results. The focus will be on two specific experimental papers (used for GHBMC model validation in Chapters 3 and 4): Nightingale et al. and Saari et al. [Nightingale et al., 1997; Saari et al., 2013]. This section will also describe the work done in current numerical papers, outline key findings, and discuss the limitations and areas of improvement that were addressed in this thesis.

2.3.1 Head-First Impact Experimental Studies

There are two main categories of cadaveric experiments for HFI: drop tests with whole cadavers and drop tests with whole cervical spines. The former group of experiments entailed unembalmed inverted specimens dropped onto a surface. Culver et al. performed drop tests with 11 unembalmed cadavers impacting a padded surface and found that most injuries occurred in the posterior

vertebral elements and that the initial curvature of the cervical spine influenced the injury mechanism [Culver et al., 1978]. Nusholtz et al. performed drop tests with 12 unembalmed cadavers but using a guided 56 kg impactor (as opposed to the conventional HFI apparatus which drops the specimen on an impact surface) [Nusholtz et al., 1981]. They similarly reported that the initial cervical spine curvature and orientation influenced the dynamic response of the cervical spine and the injuries produced in the specimens, and that head motion was not a good indicator of neck response and injury. Yoganandan et al. conducted drop tests on 16 specimens and reported that cervical fractures were more common when the head maintained contact with the impact surface without significant motion [Yoganandan et al., 1986]. The main limitation identified from these studies was the inability to record the forces throughout the cervical spine as this would entail compromising the integrity of the structure of the specimens.

There were several experimental studies that performed drop tests with whole cervical spines [Myers et al., 1991; Yoganandan et al., 1991; Pintar et al., 1995]. Two experimental studies in particular were isolated for their complete datasets pertaining to kinetic, kinematic, and injury results [Nightingale et al., 1997; Saari et al., 2013]. The experimental study performed by Saari et al. entailed drop tests with 12 cervical spine specimens. All specimens contained the vertebrae from the occiput to T2 and were frozen prior to the experiments. All musculature and the natural spinal cord were removed from the specimens. The T1 and T2 vertebrae were potted in dental stone such that the C7-T1 intervertebral joint was unrestricted. The drop track apparatus used in the experiments constrained the T1 vertebra in all degrees of freedom except for vertical translation. An effective torso mass of 15 kg was attached to the mount cup of the specimens to which the T1 and T2 vertebrae were potted. All specimens were attached to a surrogate head at the occiput and placed in an inverted orientation above a steel platen impact plate (Figure 2-26). The surrogate head was made of an aluminum frame with the top consisting of softwood with a layer of leather to emulate human skin. Details on the specific geometry and mechanical properties of the top of the surrogate head were not available.

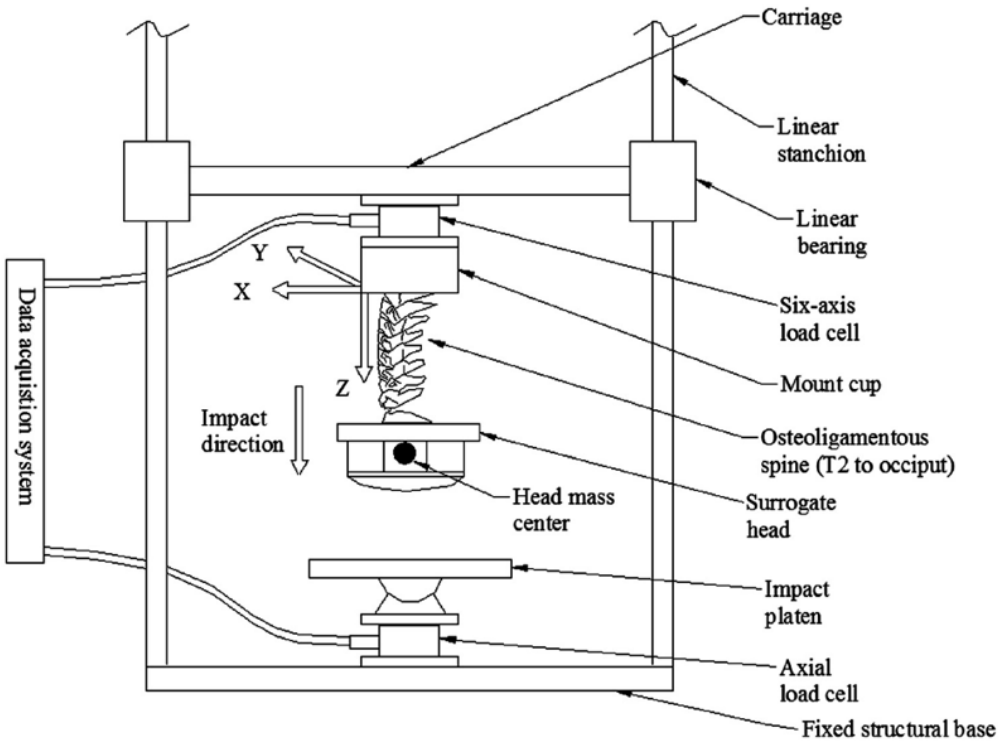

Figure 2-26: Experimental HFI setup by Saari et al. (Saari et al., 2013, used with permission from ASME)

Six of the 12 specimens had a follower load used to simulate in vivo compressive muscle force, and the other six did not have a follower load. Follower loads were included in order to evaluate the effect of muscle compression (hypothesized to influence cervical spine response) on the response and injury of the cervical spine in inverted HFI loading. The non-follower load (NFL) specimens were the focus of this thesis and were used for model validation (Chapters 3 and 4). The average impact velocity of the six NFL specimens was 2.75 m/s. The individual impact velocities of the specimens along with their corresponding sex and age are outlined in Table 2-1. A 6-axis load cell was placed at the T1-T2 mount cup in order to measure the cervical spine axial force history (labelled in Figure 2-26). Similarly, an axial 3-axis load cell was placed below the impact surface in order to measure the head contact force with the steel platen impact plate (labelled in Figure 2-26). Figure 2-27 and Figure 2-28 show the head contact force and axial neck compressive force history plots of the six NFL specimens, respectively.

Table 2-1: Age, gender, and impact velocity of NFL specimens (data adapted from Saari et al., 2013)

Saari NFL Specimen	Age	Gender	Impact Velocity (m/s)
H1062	87	M	2.8
H1092	75	F	2.7
H1094	77	M	2.8
H1095	73	F	2.8
H1099	79	M	2.8
H1101	-	-	2.6

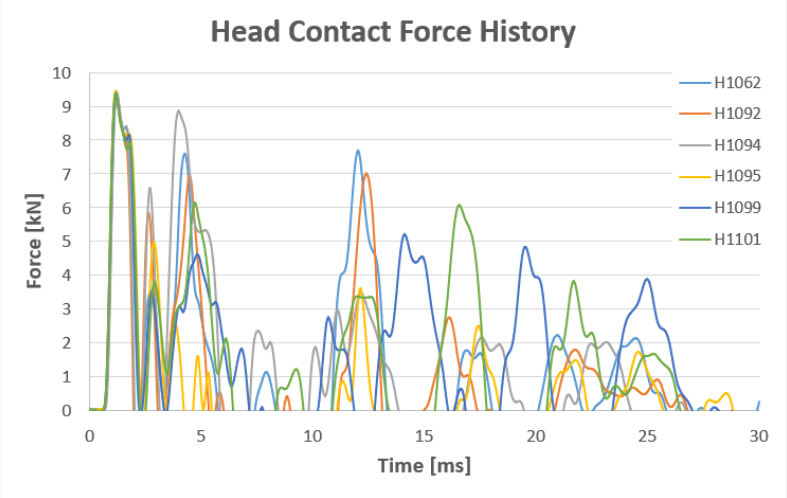

Figure 2-27: Head contact force history plots of Saari et al. NFL specimens (data adapted from Saari et al., 2013)

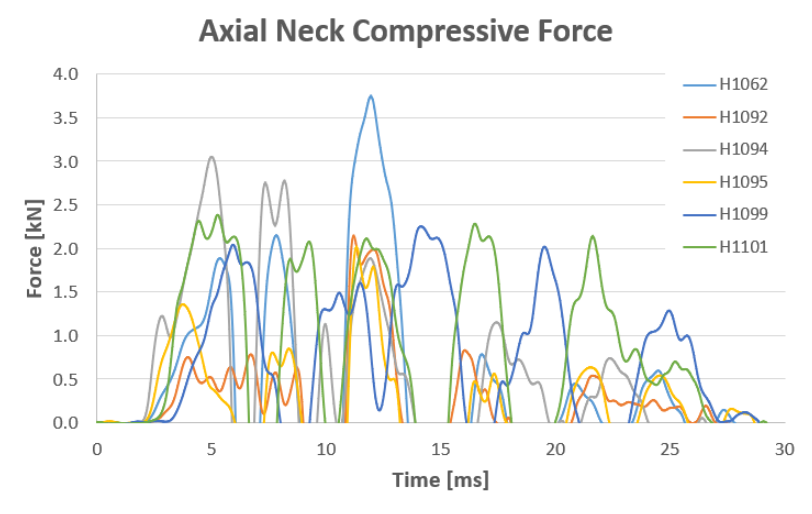

Figure 2-28: Axial neck compressive force history plots of Saari et al. NFL specimens (data adapted from Saari et al., 2013)

The cervical vertebrae were instrumented with 4 photo-reflective markers used to track the kinematic motion of the respective vertebrae throughout the loading. Three markers were placed on the vertebral body, while the 4th marker was placed on the lateral mass/articular pillar. The specific location on the vertebral body (e.g., anterior-inferior corner) of the three markers placed on the vertebral bodies was not reported. However, the anterior-most marker was selected by the experimentalists to trace the cervical spine vertebral positions in the sagittal plane. These cervical spine vertebral positions were useful in quantifying the cervical spine curvature of the specimens and were provided for the entire 30 ms interval of loading (Chapter 3). Figure 2-29 shows the cervical spine traces of the six NFL specimens, in addition to the calculated average curve, from 0-7 ms. Furthermore, high-speed videos (1000 frames per second) of the specimens impacting the steel platen were provided by one of the authors of the study. The hard and soft tissue injuries sustained in the specimens post impact are summarized in Table 2-2.

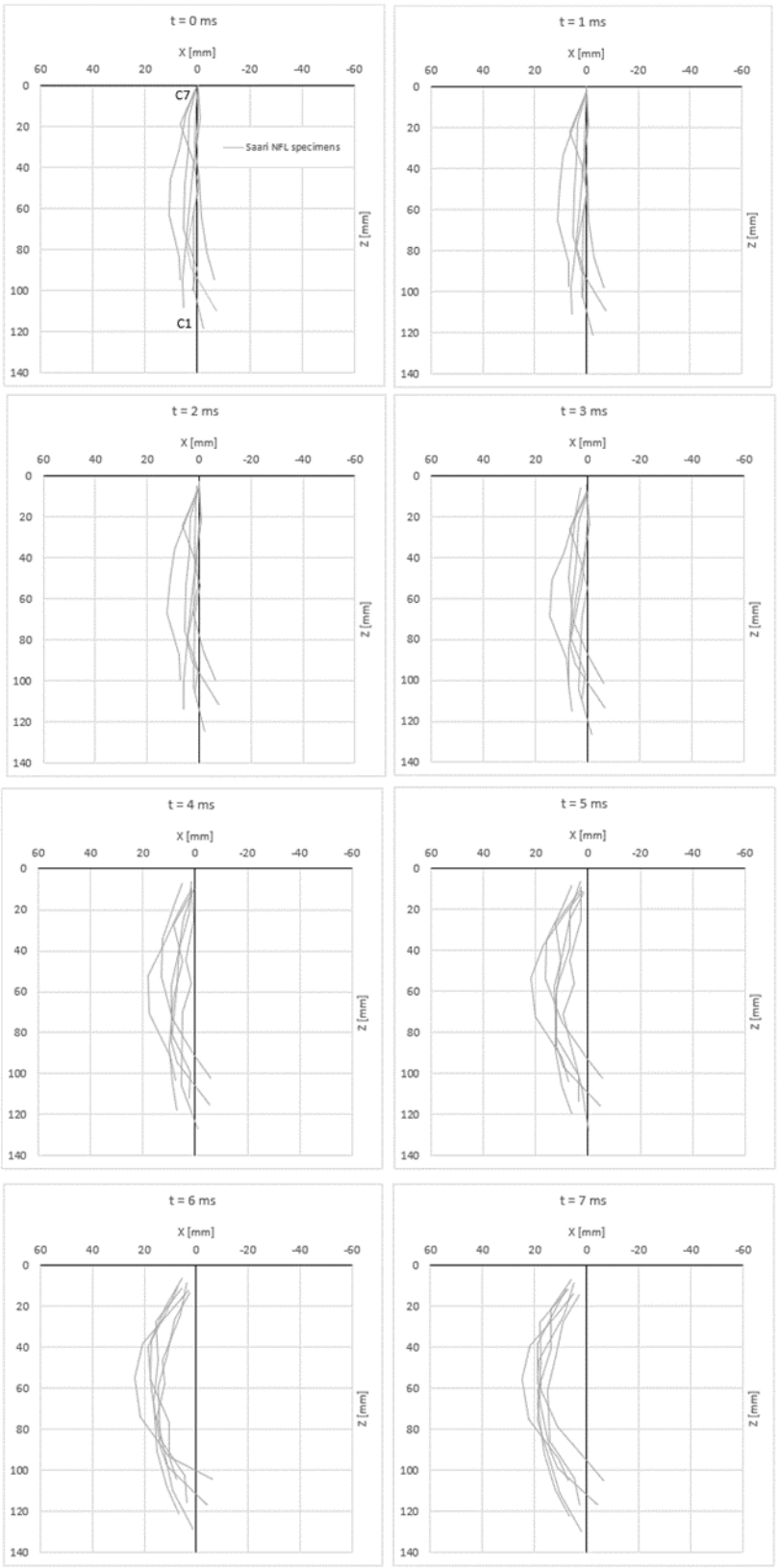

Figure 2-29: Cervical spine sagittal traces of NFL specimens (data adapted from Saari et al., 2013)

Table 2-2: Hard and soft tissue injuries of Saari NFL specimens (data adapted from Saari et al., 2013)

NFL specimens	Hard Tissue Injury	Soft Tissue Injury
H1062	Occipital condyle bilateral fracture	- C1-C2 joint capsule bilateral capsule - C1-C2 subluxation
H1092	Injury data not reported for this specimen	Injury data not reported for this specimen
H1094	- C4 spinous process fracture - C4 anterior inferior extension avulsion fracture - C4-C5 right facet capsule	- C4-C5 right facet capsule - C4-C5 ISL damage - C4-C5 ALL damage
H1095	- C3 anterior inferior avulsion fracture - C4 anterior inferior avulsion extension fracture	- C1-C2 joint capsule bilateral rupture - C3-C4 ALL rutpure - C3-C4 ISL damage
H1099	- C3 bilateral laminar fractures - C3 left inferior facet fracture - C4 anterior superior and anterior inferior extension avulsion fractures	- C3-C4 ALL rupture - C3-C4 right facet capsule rupture - C3-C4 ISL damage - C6-C7 left facet capsule and left LF rupture
H1101	- C4 spinous process fracture - C5 anterior superior extension avulsion fracture	- C4-C5 ALL rupture - C4-C5 ISL damage - C5 right superior uncinate process

The experimental drop test performed by Nightingale et al. involved 18 head-neck specimens. The specimens were comprised of ligamentous spines (occiput to T1) with the human skull, and the musculature and natural spinal cord removed (similar to Saari) (Figure 2-30). The purpose of the study was to evaluate the effect of rigid vs. padded impact surfaces, and to evaluate the effect of sagittal plane orientation of the impact plate on the response of the cervical spine.

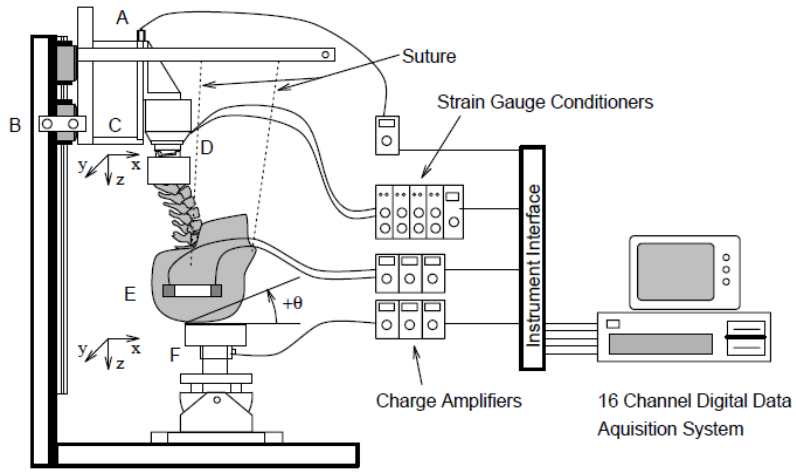

Figure 2-30: Drop test apparatus from Nightingale et al. A: accelerometer on torso mass, B: optical velocity sensor, C: carriage and torso mass, D: six-axis load cell, E: head accelerometer, and F: impact plate and three-axis load cell (Nightingale et al., 1997, used with permission from SAE International)

Nine of the 18 specimens impacted a rigid and frictionless surface (steel plate with a 3 mm layer of Teflon on top), while the remaining nine specimens impacted a padded surface (5 cm of a highly deformable, open-cell polyurethane foam). In each of these two groups, three of the specimens had the impact plate oriented at 0° in the sagittal plane (vertex impact), three with a plate orientation of 15° (anterior impact to the head), and three with a plate orientation of -15° (posterior impact to the head). The three specimens impacting the rigid (Teflon) plate with a sagittal orientation of 0° were the focus of the model validation (Chapters 3 and 4).

The T1 vertebra was potted to a mount cup and were constrained in all degrees of freedom except for vertical translation. An effective torso mass of 16 kg was attached to the mount cup of the specimens. The average impact velocity of the three specimens was 2.96 m/s, and the individual impact velocities of the specimens along with their corresponding sex and age are summarized in Table 2-3. A data acquisition system was used to obtain the contact force of the head impacting the Teflon surface and the axial neck force measured at the mount cup to which T1 was potted. Figure 2-31 and Figure 2-32 show the head contact force and axial neck compressive force history plots of the three specimens, respectively.

Table 2-3: Age, gender, and impact velocity of relevant Nightingale specimens (data adapted from Nightingale et al., 1997)

Nightingale Specimen	Age	Gender	Impact Velocity (m/s)
N22	71	M	3.26
N24	62	M	3.20
N26	65	M	2.43

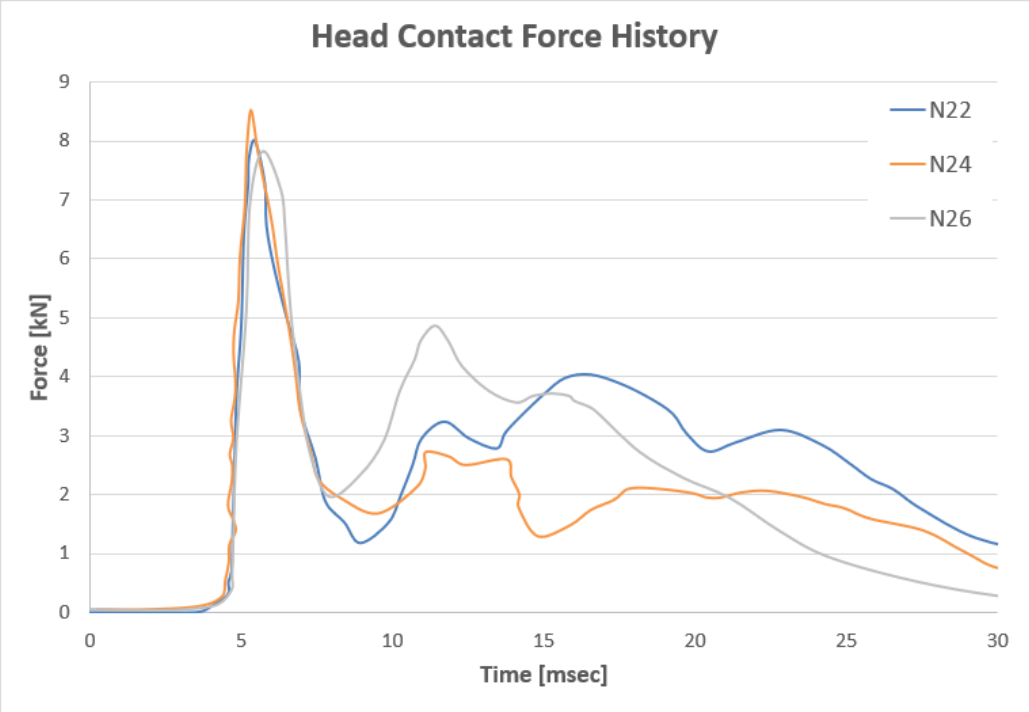

Figure 2-31: Head contact force history plots of Nightingale specimens N22, N24, and N26 (data adapted from Nightingale et al., 1997)

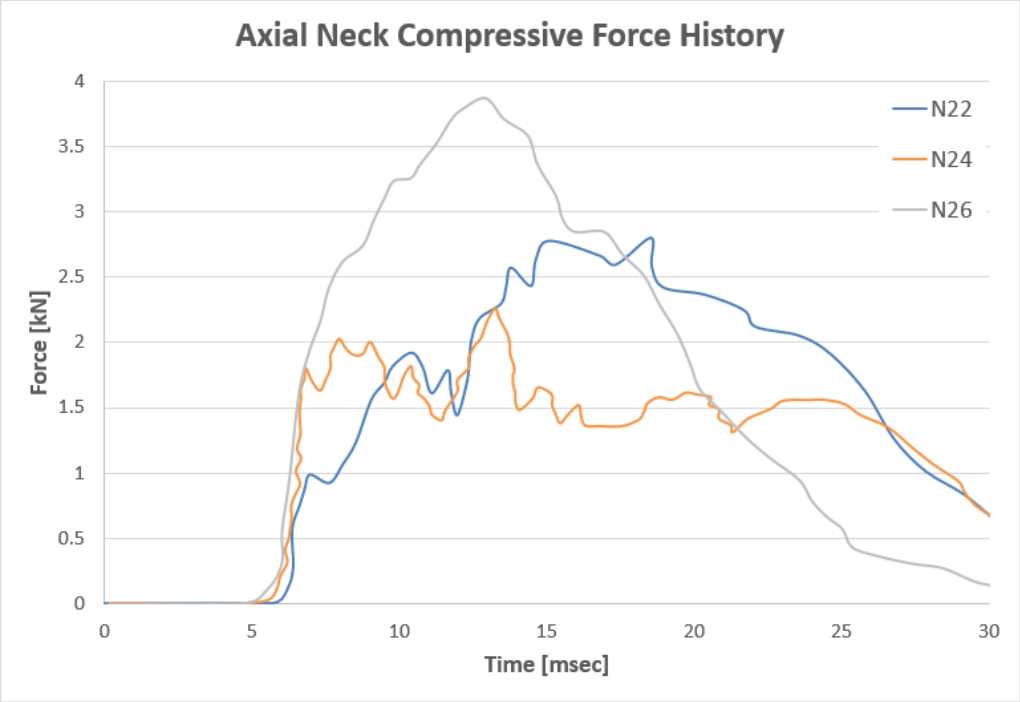

Figure 2-32: Axial neck compressive force history plots of Nightingale specimens N22, N24, and N26 (data adapted from Nightingale et al., 1997)

The sagittal plane angle of the C7-T1 IVD of the specimens was 25°. This was the only data reported pertaining to the initial cervical spine posture of the specimens. Table 2-4 summarizes the hard tissue injuries sustained in the three specimens. Soft tissue injuries were not reported, and specimen N26 did not incur any injuries.

Table 2-4: Hard tissue injuries of Nightingale relevant specimens (data adapted from Nightingale et al., 1997)

Nightingale Specimen	Hard Tissue Injury
N22	C1 3-part comminuted fracture
N24	- C1 2-part posterior arch fracture - C2 Hangman's fracture
N26	Specimen did not incur any injuries

Initial cervical spine posture (curvature) was hypothesized by several experimental studies to influence the response of the cervical spine during HFI loading [Culver et al., 1978; Nusholtz et al., 1981; Yoganandan et al., 2018]. Therefore, it is important to identify literature that quantified cervical spine posture in inverted HFI positions; this information was later used in assessing the effect of varying the curvature on the cervical spine response and injury outcome. An experimental study by Newell et al. determined vertebral alignment and posture when upside down [Newell et al., 2013]. This inverted orientation occurs during rollover crashes which are responsible for the majority of HFI (subsection 2.2.2). The data reported in this study was important in obtaining the range of cervical spine initial postures when upside down to use for model analysis and validation (Chapters 3 and 4). The study quantified the posture of nine volunteers in three conditions: upright and relaxed posture, inverted and relaxed posture, and inverted and looking forward posture. The inverted and relaxed posture was the most representative for HFI analysis. Cervical spine posture was quantified using two metrics: the sagittal plane angle of C7, and the curvature index (CI), calculated as a percentage (Figure 2-33).

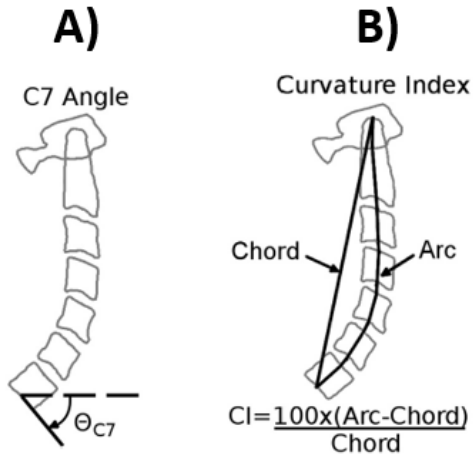

Figure 2-33: Cervical spine quantification metrics from Newell et al. A) C7 angle, and B) curvature index (Newell et al., 2013, used with permission from PERGAMON)

The C7 angle was measured between the line collinear with the superior mid-sagittal surface of the C7 vertebral body and the true horizontal. A positive angle indicated flexion. The curvature index was calculated as a percentage difference between the arc and chord lengths of the cervical spine. The arc length is the sum of the straight-line segments passing through the superior and inferior midpoints at the mid-sagittal plane of adjacent vertebral bodies from C2 to C7, and the

chord length is the distance from the tip of the dens to the inferior mid-point at the mid-sagittal plane of the C7 vertebral body. The study reported, for an average of nine volunteers, that the C7 angle was 25.3° ± 6.5° for an inverted and relaxed posture. The study also reported (for the same nine volunteers) that the curvature index was 3.0% ± 1.4% for an inverted and relaxed posture. In addition to measuring the cervical spine curvature, the study quantified the sagittal head orientation by measuring the head angle using the Frankfort plane (Figure 2-34).

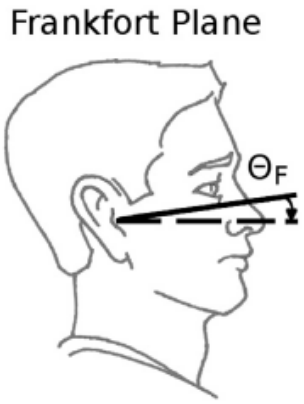

Figure 2-34: Head angle measurement via the Frankfort plane as described in Newell et al. (Newell et al., 2013, used with permission from PERGAMON)

The Frankfort plane is defined by a line passing though the tragion and the inferior margin of the orbit [Cheng et al., 2012]. Newell reported that the Frankfort plane angle (measured between the Frankfort plane and the true horizontal) was -25.2° ± 10.5° for an inverted and relaxed posture. The negative sign on the angle corresponded to extension motion of the head.

2.3.2 Head-First Impact Numerical Studies

Finite element (FE) models in numerical studies can be a useful tool in further describing the intricate response of the cervical spine under certain loading conditions (including HFI). Table 2-5 outlines seven numerical HFI studies previously conducted to investigate HFI loading through developing FE head-neck models.

Table 2-5: Summary of numerical HFI studies identified from literature

Summary of Numerical HFI Studies		
Study	**Model Description**	**Study Details**
Camacho et al., 1997	- Ligamentous cervical spine - Rigid vertebrae - Full human head	- HFI validation against Nightingale (1997) study - Sensitivity study with vertebral and head stiffness and damping parameters
Yang et al., 1998	- Ligamentous cervical spine with beam passive muscle elements - Full human head	- HFI validation against Nightingale (1997) study - Validation for rear impact and frontal impact with pre-deployed airbag
Halldin et al., 2000	- Ligamentous cervical spine - Full human head	- HFI validation against Nightingale (1997) study - Validation for segment level compression, extension, flexion, torsion, shear, and lateral bending - Proposed modified car roof design to reduce injury from axial loading
Zhang et al., 2005	- Ligamentous cervical spine - Rigid vertebrae - Full human head	- HFI validation against Nightingale (1997) study - Assessed range of motion under physiological loading
Hu et al., 2008	- Ligamentous cervical spine with beam muscle elements - Full human head	- HFI validation against Nightingale (1997) study - Sensitivity study with interface friction, padding stiffness, impact velocity, AP surface angle, and lateral surface angle parameters
Nightingale et al., 2016	- Ligamentous cervical spine with beam active muscle elements - Full human head - Portion of torso	- HFI validation against Nightingale (1997) study - Sensitivity study with muscle activation, torso constraints, and pre-flexion angle parameters
Nasim et al., 2021	- Ligamentous cervical spine with beam muscle elements - Hybrid III head	- HFI validation against Nightingale (1997) study - Assessed range of motion under physiological loading

A study by Camacho et al. developed a FE model and validated it for HFI against the experimental drop tests performed by Nightingale [Nightingale et al., 1997; Camacho et al., 1997]. The FE model in this study had rigid vertebrae with anthropometric properties (mass, mass moment of inertia, etc.) representative of a 50th male (Figure 2-35).

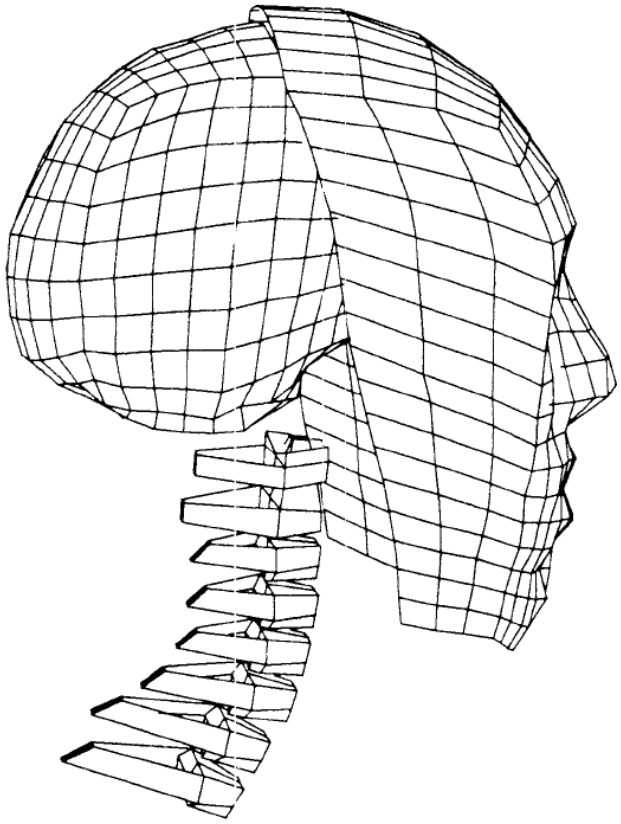

Figure 2-35: FE model developed by Camacho et al. for HFI validation (Camacho et al., 1997, used with permission from SAE International)

The resultant buckling behaviour was qualitatively compared (e.g., visual comparison of buckling modes (first vs. higher order buckling)) against the specimen cervical spines for the HFI simulations. Good agreement was obtained for the neck force and head contact force histories. Additionally, the authors identified that the axial neck force was highly sensitive to changes in cervical spine flexion-extension properties, and less sensitive to changes in head mass and stiffness. However, the study was limited in not quantitatively analyzing the kinematic response (i.e., cervical buckling) and in not identifying and extracting the potential for hard and soft tissue injuries. These limitations were addressed in this study.

Yang et al. developed a FE model to perform validation for HFI loading against the experimental results by Nightingale [Yang et al., 1998]. The head-neck model was based on a 50^{th} male, and the boundary and initial conditions were applied in accordance with the ones reported in the study by Nightingale. The head model had a total 7,351 elements, and the neck model had 11,498 solid

elements, 3,071 shell elements, and 108 spring elements. This mesh density was relatively course compared to the model used in this study. The model had good kinetic (head contact force and axial neck compressive force histories) and kinematic (observing buckling behaviour qualitatively) agreement with the respective experimental results. However, there were several limitations identified from the study. First, the study reported that there were no guarantees that the constitutive laws and material properties of the hard and soft tissues in the model were selected accurately. Moreover, the ligament thickness was assumed to be uniform for all ligaments, compressive and tensile properties of the intervertebral discs were considered to be constant at all levels, and passive muscles were modelled with beam elements. These limitations are addressed in the biofidelic model used in this study. Lastly, the study did not quantitatively analyze the kinematic response and did not investigate soft tissue injury risk, whereas the work presented in this study analyzed these two result metrics.

The HFI validation process conducted by Halldin et al. entailed qualitative analysis of the buckling response, extracting the kinetic response (head contact force and axial neck compressive force histories), and predicting the location of hard tissue injury. Additionally, alternate roof structures designed to reduce neck load and injury were considered. The neck model consisted of 4,560 solid elements, 3,572 shell elements, and 230 spring elements (Figure 2-36). Figure 2-37 shows the model of the head with a relatively course mesh.

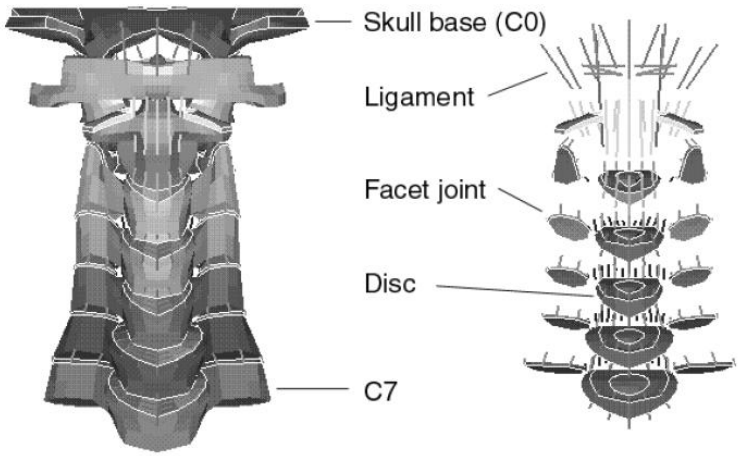

Figure 2-36: FE neck model developed by Halldin et al. (Halldin et al., 2000, used with permission from SAE)

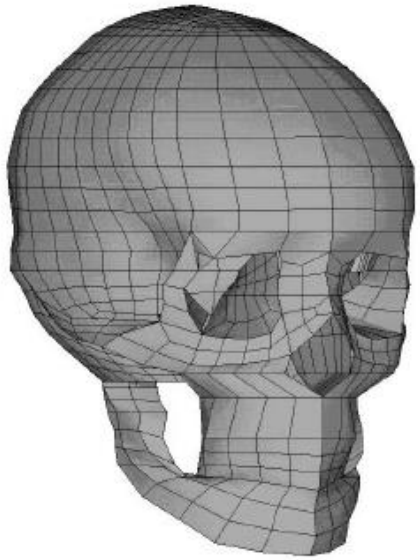

Figure 2-37: FE head model developed by Halldin et al. (Halldin et al., 2000, used with permission from SAE)

There was good agreement for the kinetic response as the FE model plots were within the reported experimental corridors. A good correlation was found between the horizontal velocity of C3 and C4 (the anterior-most vertebrae throughout the buckling) and the axial force at T1. As the horizontal velocity of the C3 and C4 vertebrae reached a peak value, the T1 axial force was at a maximum as well; that was used to predict the onset of buckling. Hard tissue injury was quantified using maximum effective stress and it was found that the pedicles of C2 had the highest stress which corresponded to Hangman's fracture, an injury reported experimentally [Nightingale et al., 1997]. However, similar to the previous numerical studies, this study did not quantitively analyze the kinematic response or investigate the potential for soft tissue injury (ligament rupture, dislocation, etc.).

Zhang et al. developed a FE model to validate against the Nightingale experimental results and consisted of a total 22,094 elements and 28,638 nodes (Figure 2-38) [Zhang et al., 2005]. Similar to previous results, there was good agreement for the kinetic plots and qualitatively extracted buckling behaviour. The study also showed good agreement for the range of motion of the neck under physiological loading. However, this study did not quantitatively analyze the kinematic response of the cervical spine or the hard and soft tissue injury outcome during HFI.

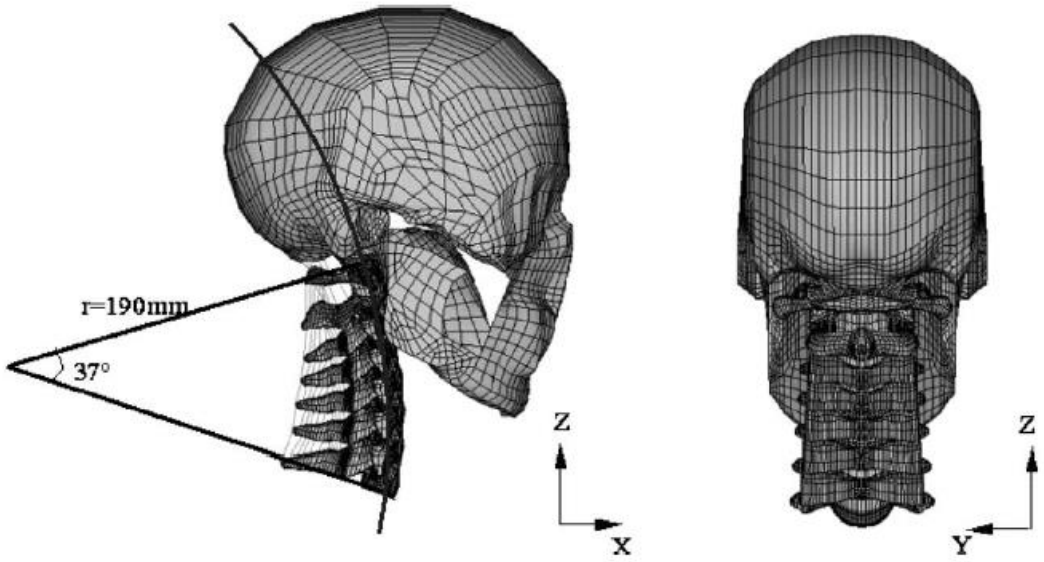

Figure 2-38: FE model developed by Zhang et al. for HFI validation (Zhang et al., 2005, used with permission from ASME)

Hu et al. developed a FE model to validate against experiment results by Nightingale, and to assess the effects of changing the coefficient of friction (COF) between the head and the impact plate, impact velocity, padding material thickness and stiffness, anteroposterior impact surface angle, and lateral impact surface angle [Hu et al., 2008]. The full head-neck model consisted of 32,135 elements and 23,933 nodes (Figure 2-39).

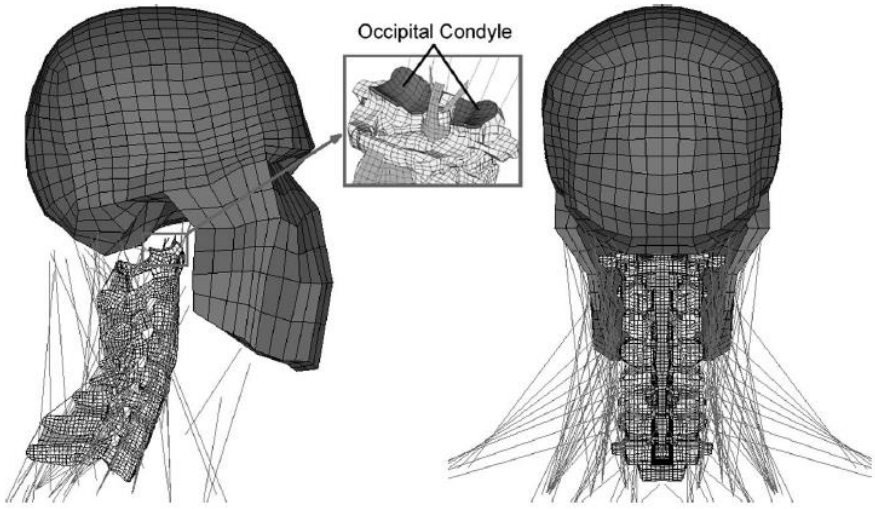

Figure 2-39: FE model developed by Hu et al. for HFI validation (Hu et al., 2008, used with permission from Wolters Kluwer)

The model demonstrated good kinetic agreement for the head contact force and axial neck compressive force histories. The study reported a Design of Experiments parametric study which revealed that the impact velocity was the most important factor in determining the risk of cervical spine fracture. Decreasing the COF decreased the risk of cervical spine injury because it allowed the head to escape the axial load path, thereby reducing the compression on the cervical spine. Increasing the thickness and decreasing the stiffness of the impact surface reduced the neck fracture risk. Although the result published several key findings pertaining to cervical spine response under HFI, it had the same limitations as the previous numerical studies.

A numerical study by Nightingale et al. developed a FE model to assess the effect of three HFI parameters: muscle activation, torso constraints, and pre-flexion angle of the cervical spine [Nightingale et al., 2016]. The numerical model used was an improved upon version of the FE model developed by Camacho et al., but a rigid body formulation was still used to model the cervical vertebrae (Figure 2-40) [Camacho et al., 1997].

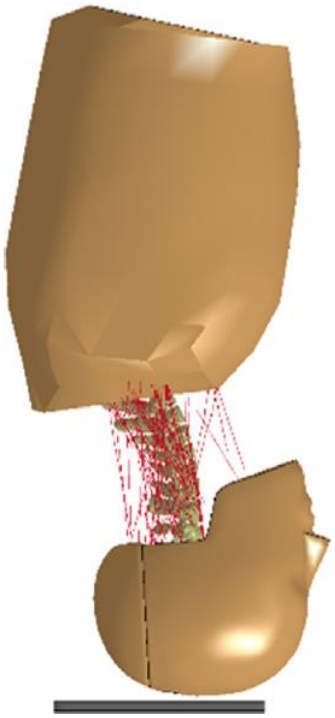

Figure 2-40: FE model developed by Nightingale et al. for HFI validation (Nightingale et al., 2016, used with permission from PERGAMON)

The study reported that the simulations with active musculature (relative to simulation without active musculature) had higher compressive forces (32%) and greater shear forces (25%) at T1. Constraints on torso motion during the early interval of loading increased the average neck compression force by only 5%. Moreover, it was found that the peak force and buckling modality were very sensitive to changes in pre-flexion angles of the neck; as the pre-flexion angle increased, the axial peak and buckling modality increased. Similar to the previous numerical studies, this study was limited in not quantitatively analyzing the kinematic response and injury outcome.

Finally, a recent study by Nasim et al. developed a FE neck model along with a Hybrid III head to validate for HFI loading (Figure 2-41) [Nasim et al., 2021]. There was good agreement for the buckling results (qualitative) and kinetic plots (quantitative) with the respective experimental results. In addition to the Hybrid III head not being a biofidelic representation of the human head in terms of material properties and the vast variety of hard and soft tissues it contains, the study, similar to the previous numerical studies, did not investigate the kinematic response quantitatively and did not investigate the potential for soft tissue injuries.

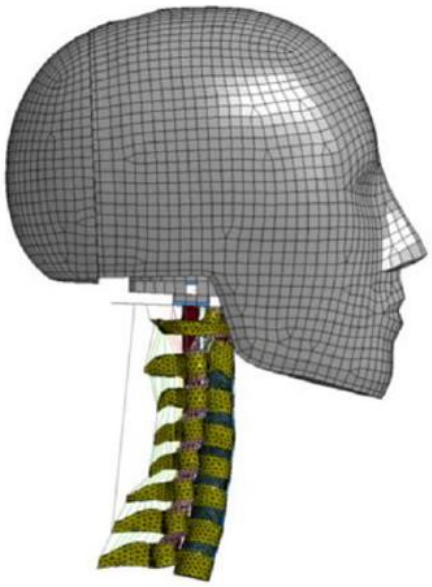

Figure 2-41: FE model developed by Nasim et al. for HFI validation [Nasim et al., 2021]

2.4 The GHBMC Model

The Global Human Body Models Consortium (GHBMC) model is a biofidelic finite element models which has been validated at the full body and cervical spine levels [Barker and Cronin, 2021]. The 50th percentile young (26-year-old) male (M50) human body model (Version 5.0) (focus of this thesis) was geometrically based on magnetic resonance imaging and computed tomography of a specific male subject: 26 years old, 78 kg body weight, 174.9 cm tall, with a body mass index of 25.7 [Gayzik et al., 2011]. Research and validation against HFI through work in numerical studies (subsection 2.3.2) has increased over the last decade. However, the numerical studies had limitations and areas of improvement which were addressed through the model validation using the GHBMC model.

The full head-neck model, extracted from the full body model, has all the hard and soft tissues of the human head and neck up to and including the first thoracic vertebra (T1) (Figure 2-42), and has been validated with various load cases including flexion, extension, axial rotation, and lateral bending [Barker et al., 2017]. The full head-neck model has a total 395,803 solid (3D) elements, 132,283 shell (2D) elements, 4,457 beam (1D) elements, and 508,740 nodes. The soft tissues are the flesh and skin of the head and neck, passive musculature, tendons, intervertebral discs, ligaments, cartilage found in the joints of the head and neck, and the brain components. The hard tissues of the model are the bones such as the vertebrae and the skull. All tissues of the full head-neck model have been assigned representative constitutive models and failure criteria.

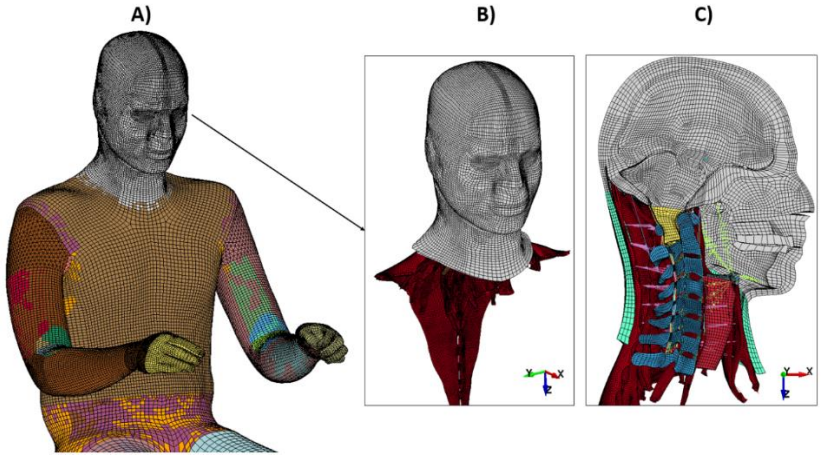

Figure 2-42: A) GHBMC M50 full body model, B) GHBMC M50 full head-neck model (extracted from A), and C) mid-sagittal view of GHBMC M50 full head-neck model shown in B

2.4.1 Cervical Vertebrae of the GHBMC Model

The trabecular and cortical bones were modelled using solid and shell elements, respectively (Figure 2-43). The constitutive model properties assigned to the trabecular and cortical bones are summarized in Table 2-6 [Khor, 2018].

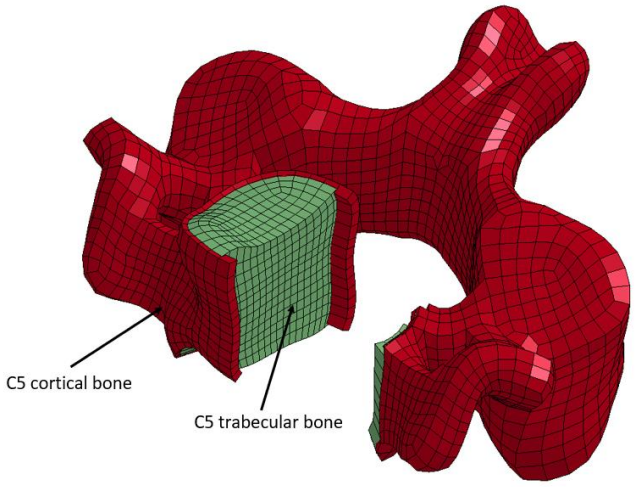

Figure 2-43: C5 cortical and trabecular bones (portion of vertebral body removed for visualization)

Table 2-6: Mechanical properties of the trabecular and cortical bones of the cervical vertebrae

Property	Cervical Vertebrae	
	Trabecular bone	Cortical bone
Density (kg/m^3)	1000	2000
Young's modulus 11 direction (MPa)	0.7	17.9
Young's modulus 22 direction (MPa)	0.3	10.4
Young's modulus 12 direction (MPa)	0.2	0.0
Young's modulus 23 direction (MPa)	0.1	0.0
Shear modulus (MPa)	0.3	4.0

The constitutive model that was assigned to the trabecular bone was transversely isotropic, crushable, and of low density with no significant Poisson effect (*MAT TRANSVERSELY_ISOTROPIC_CRUSHABLE_FOAM). This material model is suitable for

energy-absorbing structures such as trabecular bone (subsection 2.1.2). The material model used for the cortical bone was orthotropic elastic plastic with an anisotropic yield criterion (*MAT_ORTHO_ELASTIC_PLASTIC).

An additional element erosion card (*MAT_ADD_EROSION) can be used in order to activate element erosion once the failure effective plastic strain values for trabecular and cortical bones were reached (9.17% and 3.43%, respectively) [Khor, 2018]. With this failure option (i.e., hard tissue failure turned on), fracture was indicated by the eroded trabecular (solid) and cortical (shell) elements. This failure option is limited because element erosion is not a biofidelic representation of bone fracture initiation and propagation; bone fracture does not entail bone fragments eroding/deleting. Alternatively, hard tissue failure can be turned off by omitting this card and subsequently identifying fracture by observing the trabecular and cortical bone elements that surpassed the respective failure effective plastic strain values. However, this failure option is limited because model results and response after the first element reaches the respective failure strain cannot be used due to the strain accumulation that occurs.

2.4.2 Soft Tissues of the GHBMC Model

The main cervical spine ligaments (Figure 2-44 -Figure ***2-46***) in the GHBMC M50 full head-neck model are ALL, PLL, LF, ISL, CL, as well as the atlanto-axial and atlanto-occipital upper cervical spine ligaments. All ligaments had the same non-linear tension-only material formulation (*MAT_ELASTIC_SPRING_DISCRETE_BEAM), and each ligament was assigned a tensile displacement at failure to define progression element erosion (Figure 2-47) [Mattuci et al., 2012; Mattuci and Cronin, 2015].

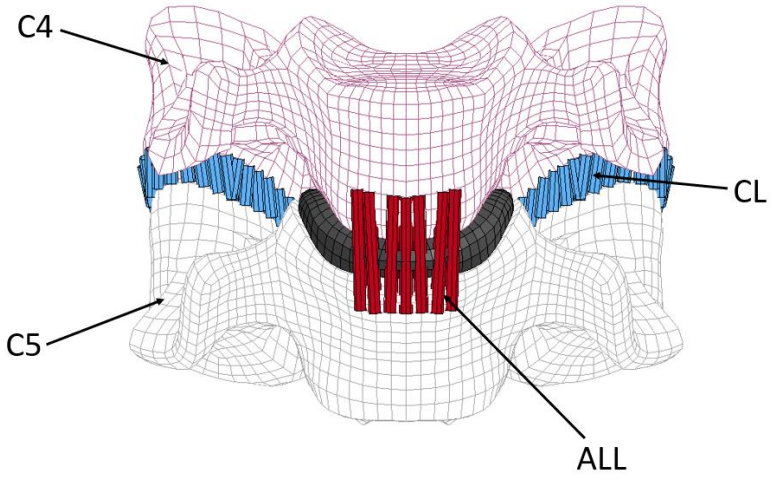

Figure 2-44: Frontal view of ALL and CL shown at the C4-C5 segment level. Beam elements thickened for visualization

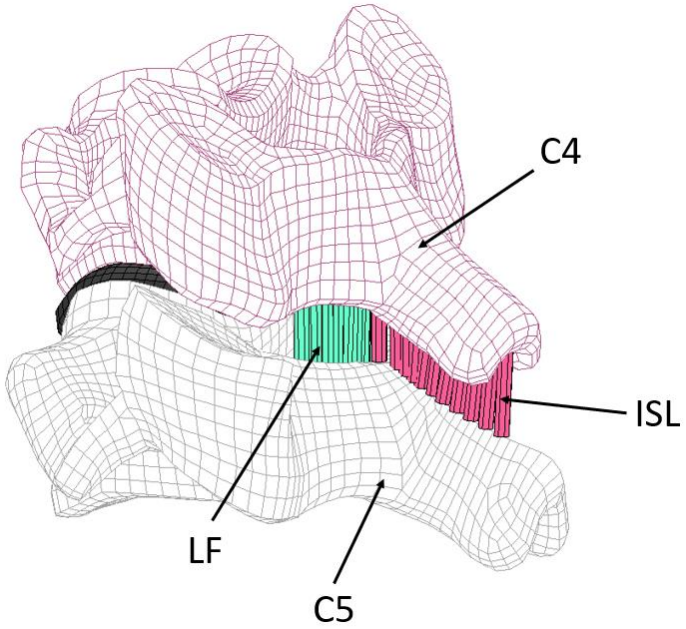

Figure 2-45: Posterolateral view of ISL and LF shown at the C4-C5 segment level. Beam elements thickened for visualization

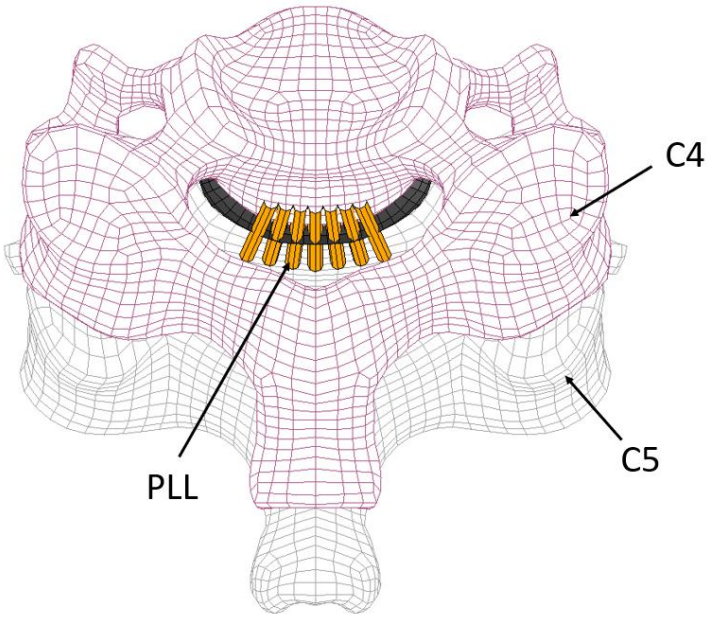

Figure 2-46: Superior view of PLL at the C4-C5 segment level. Beam elements thickened for visualization

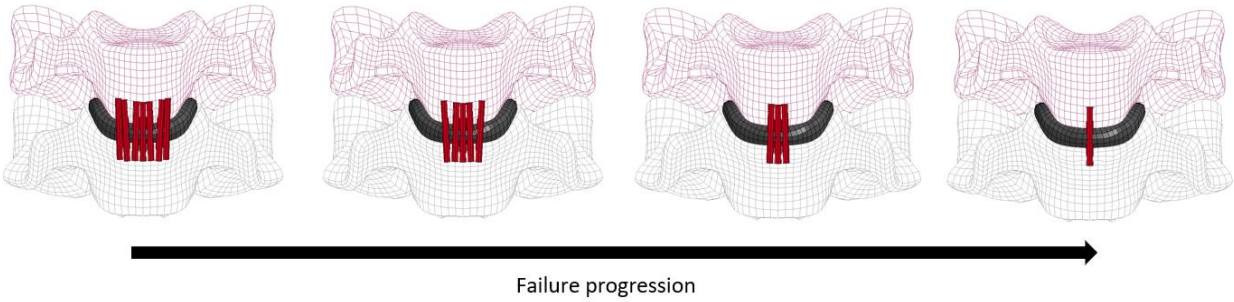

Figure 2-47: Ligament failure progression (ALL shown as an example)

The IVD consisted of two components: the annulus fibrosus and the nucleus pulposus (Figure 2-48). The annulus fibrosus is a composite with the fibre being the annulus fibrosus fibre and the matrix is the ground substance. The annulus fibrosus fibres were modelled as five concentric layers of quadrilateral shell elements using an orthotropic elastic fabric material formulation (*MAT_FABRIC) [Ebara et al., 1996; Holzapfel et al., 2005]. The ground substance was modelled with quadrilateral solid elements using a highly compressible foam material formulation (*MAT_HILL_FOAM) that took Poisson's ratio effectsinto account [Fujita et a., 1997; Kasra et al., 2004]. The nucleus pulposus was modelled with quadrilateral solid elements using an elastic fluid material formulation (*MAT_ELASTIC_FLUID) [Yang and Kish, 1988; Iatridis et al.,

1996]. Disc avulsion was defined by a critical stress failure criterion at the interface between the disc and the vertebral body [DeWit and Cronin, 2012].

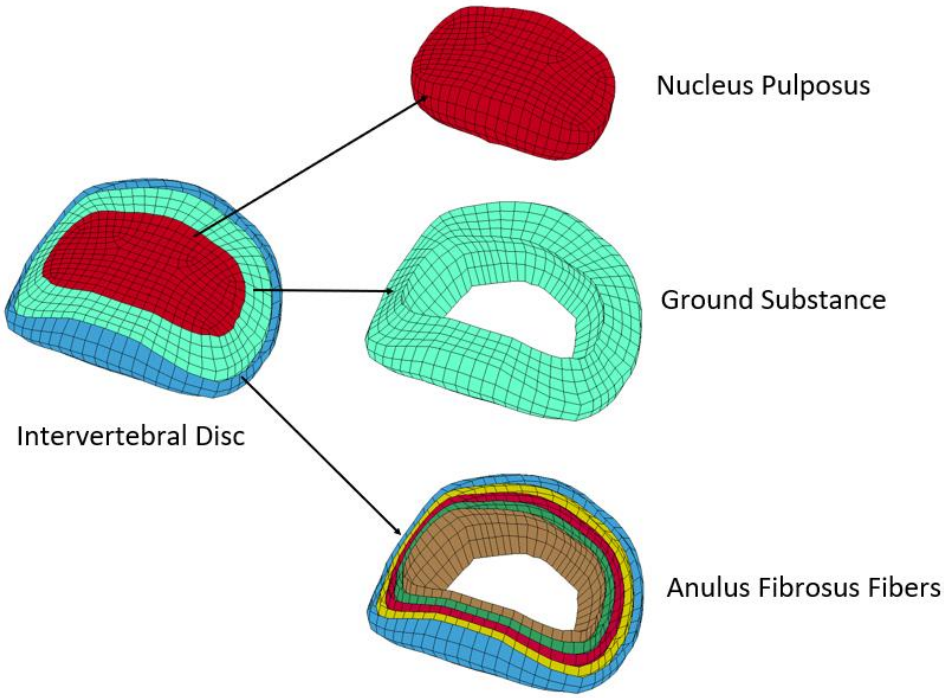

Figure 2-48: Intervertebral disc components in GHBMC M50 model

Chapter 3: Methods

3.1 GHBMC Model Positioning and Boundary Conditions for Head-First Impact (HFI)

The GHBMC M50 model (version 5-0d) was assessed for Head-First Impact (HFI) loading, and the model response was assessed in a sensitivity study where HFI parameters (i.e., boundary and initial conditions) were varied in order to evaluate the resultant effect on cervical spine behaviour. The model assessment against the experimental studies by Saari and Nightingale (covered in sections 3.2 and 3.3) entailed applying the respective initial and boundary conditions reported in the studies and subsequently comparing the model response to the respective experimental results. The sensitivity study (covered in section 3.4) entailed varying one HFI parameter at a time while keeping the rest constant to assess the individual effect on cervical spine response and injury.

Setting up the GHBMC full head-neck model (extracted from the GHBMC M50 model as described in section 2.4) for a HFI configuration involved first removing some of the tissues in order to match the specimen preparation details outlined in the experimental studies. The neck flesh, active and passive muscles, tendons, hyoid bone and attachments, and active muscle attachments were all removed from the GHBMC full head-neck model (Figure 3-1) because Saari and Nightingale removed these tissues from their cadaver specimens.

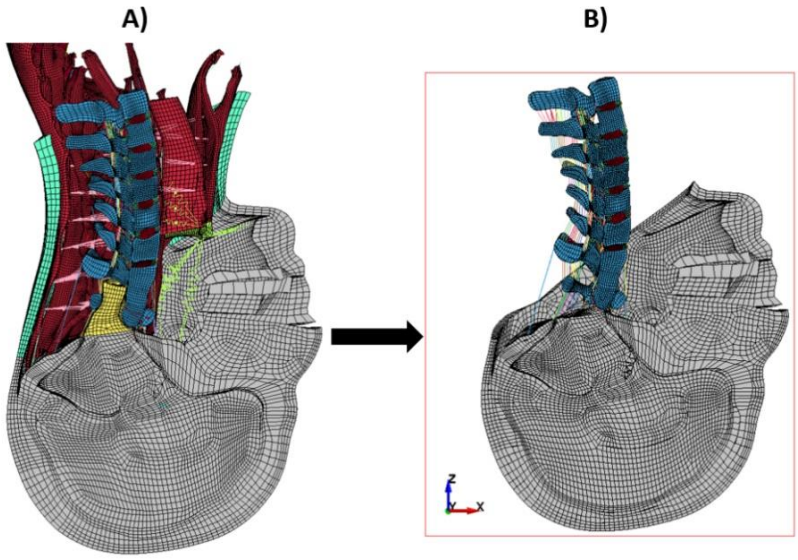

Figure 3-1: A) GHBMC full head and neck model, including spinal cord (yellow), neck adipose tissue (turquoise), muscles (red), active attachments (pink), and hyoid bone (green). B) GHBMC full head and neck model with the tissues mentioned in A) removed

Two model configurations were created to match the boundary and initial conditions of the Saari and Nightingale studies. Both configurations were based on the same extracted GHBMC head-neck model (Figure 3-1B), and the term 'configuration' strictly refers to a unique set of boundary and initial conditions (head position, spinal curvature). The two experimental papers reported a set of initial and boundary conditions: initial cervical spine curvature, impact velocity, effective torso mass, and impact interface details, which were applied to the head and neck finite element model (Figure 2). As described in subsection 2.3.1, each of the two studies specifically reported how their specimen cervical spine curvatures were measured, and these curvatures were accordingly reproduced in the corresponding GHBMC model configurations. In both experimental studies, the specimens were dropped with certain impact velocities, and the average impact velocities were then calculated and applied to the corresponding GHBMC model configurations. The experimental setups added a mass to the T1 vertebra in order to simulate effective torso mass, and the same mass was implemented in the model configurations by increasing the mass of the T1 vertebra. Additionally, the drop track apparatus used in both experimental tests only allowed for vertical translation of the T1 vertebra. This constraint was applied to both GHBMC model configurations by assigning a rigid body formulation (*MAT_RIGID) to the T1 vertebra in order to restrict its motion to vertical translation only. Finally, the impact interface was re-created for each study. Each of the experimental studies had different impact interface details such as material properties

of the impact plate, and those were modelled in the corresponding GHBMC model configurations. The four HFI configuration parameters applied to the GHBMC model are summarized in Figure 3-2. In addition to these initial and boundary conditions, the acceleration due to gravity of 9.81 m/s^2 was applied to both configurations in the downward (negative z) direction (*LOAD_BODY_Z option in LS-DYNA) to the entire model.

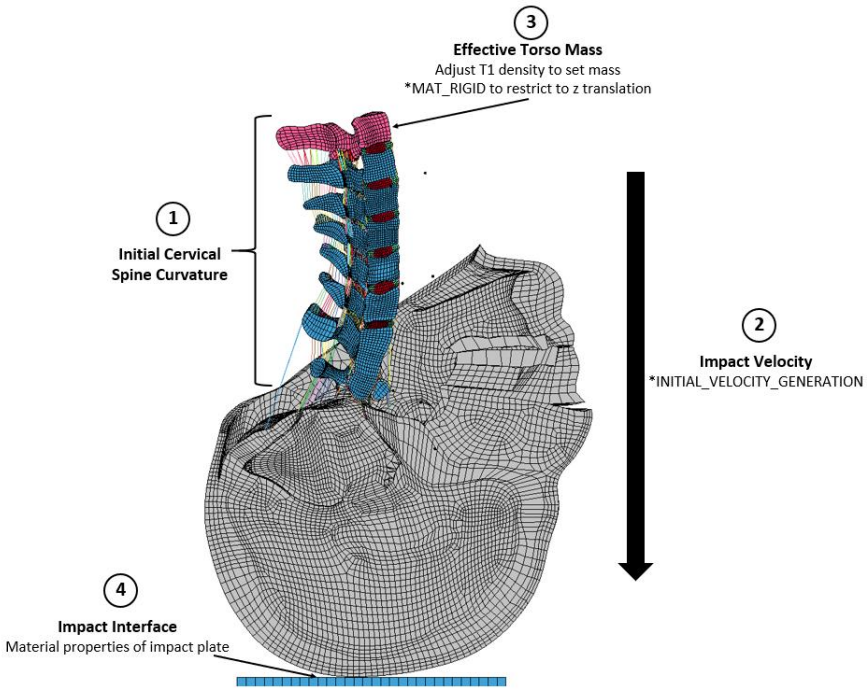

Figure 3-2: Four HFI configuration parameters applied to the GHBMC model: 1) initial cervical spine curvature, 2) impact velocity, 3) effective torso mass, and 4) impact interface

3.2 GHBMC Model Assessment and Boundary Conditions Based on Saari (2013) Experimental Study

A GHBMC model configuration, which will henceforth be referred to as GHBMC_Saari, was created in order to model the boundary and initial conditions reported in the experimental setup by Saari for the non-follower load (NFL) specimens. The GHBMC_Saari model configuration (Figure 3-2) included the experimental boundary and initial conditions (labelled in Figure 3-2) outlined in the experimental study.

As described in subsection 2.3.1, the raw kinematic data (photo-reflective marker coordinates) was used to quantify and represent the initial cervical spine curvature of the specimens in the sagittal

plane. The anterior-most markers on the vertebral bodies of the vertebrae were selected in order to trace the cervical spine in the sagittal plane. The initial cervical spine curvature from GHBMC M50 was traced in the sagittal plane by selecting a node at the mid-sagittal plane at each of the vertebrae from C1 to C7. These seven nodes were each selected to be on the anterior-most margin of the vertebral body and were roughly the same distance away from the inferior edge of the respective vertebral bodies (Figure 3-3). This node selection was done in order to match the experimental procedure where the anterior-most photo-reflective markers were selected to trace the specimen cervical spines in the sagittal plane. After the x (anteroposterior) and z (superior-inferior) coordinates of the nodes were extracted, the cervical spine from GHBMC M50 at t = 0 ms was plotted and overlaid on top of the specimen data for each of the cervical spines from the experimental study (Figure 3-4) in order to compare the curvatures. The anteroposterior (x) and inferior-superior (z) distances between the nodes and the corresponding photo-reflective marker positions at each vertebral level from Figure 3-4 are outlined in Table 3-1.

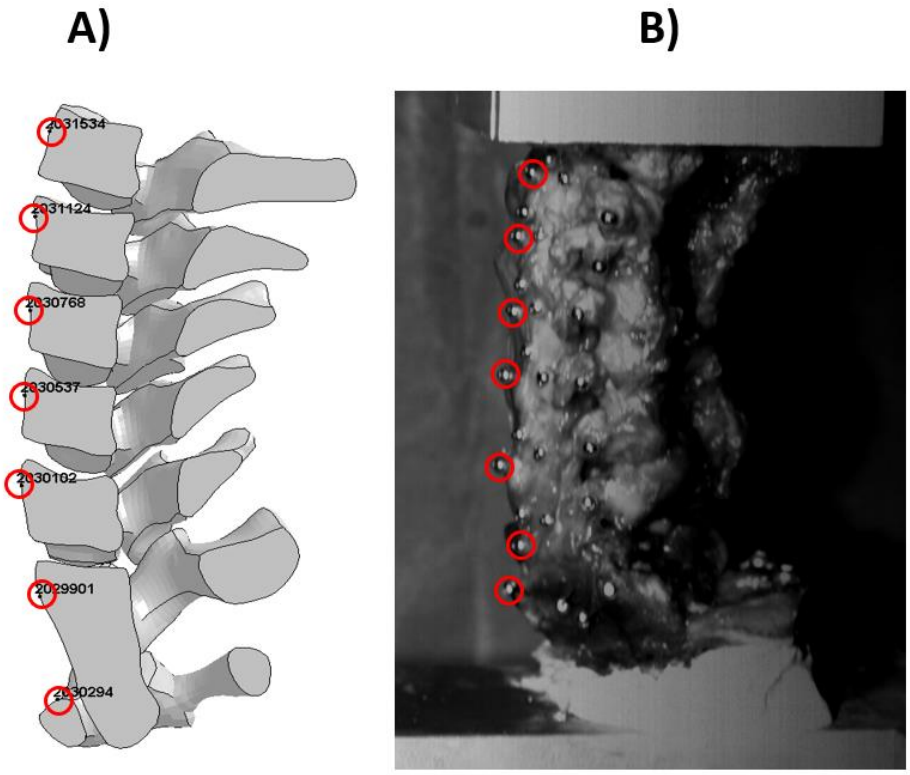

Figure 3-3: A) GHBMC M50 mid-sagittal node selection (C2-C7) producing sagittal cervical spine trace at t = 0 ms, and B) photo-reflective markers on Saari NFL specimen H1062 - markers selected for cervical spine trace are circled in red [Saari et al., 2013]

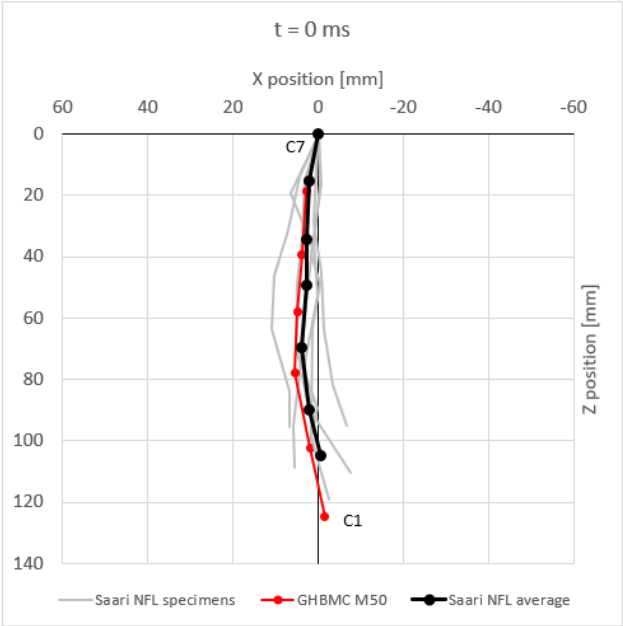

Figure 3-4: Initial (t = 0 ms) cervical spine sagittal (x-z) trace of NFL specimens (grey) and average curvature (black) and GHBMC M50 model based on node selection (red)

Table 3-1: X (anteroposterior) and Z (superior-inferior) difference between GHBMC M50 model nodes and corresponding vertebral photo-reflective markers from average Saari NFL curve

X and Z Difference between GHBMC M50 curve and Saari NFL average curve		
Vertebra	**x (mm)**	**z (mm)**
C1	1.04	20.03
C2	0.31	12.51
C3	1.40	8.26
C4	2.00	8.61
C5	1.15	5.21
C6	0.52	3.27
C7	0.00	0.00

The GHBMC M50 cervical spine was longer than any of the specimen cervical spines (and consequently longer than the average spinal length of the specimens) (third column in Table 3-1). However, the initial posture of the GHBMC M50 cervical spine was similar to the average experimental initial posture (second column in Table 3-1). The x and z coordinates of the model and experimental plots were normalized by their respective initial spinal z-lengths in order to better visualize the initial postural agreement. For example, the x and z coordinates of all seven vertebral points of GHBMC M50 were divided by the initial spinal z-length of GHBMC M50 of 124.8 mm (calculated by subtracting the C7 z coordinate from the C1 z coordinate). The normalized plots of the model and experiment, overlaid on top of each other in the same graph, are shown in Figure 3-5. Table 3-2 illustrates the good initial postural agreement between the normalized plots by outlining the updated x and z differences between the corresponding vertebral points.

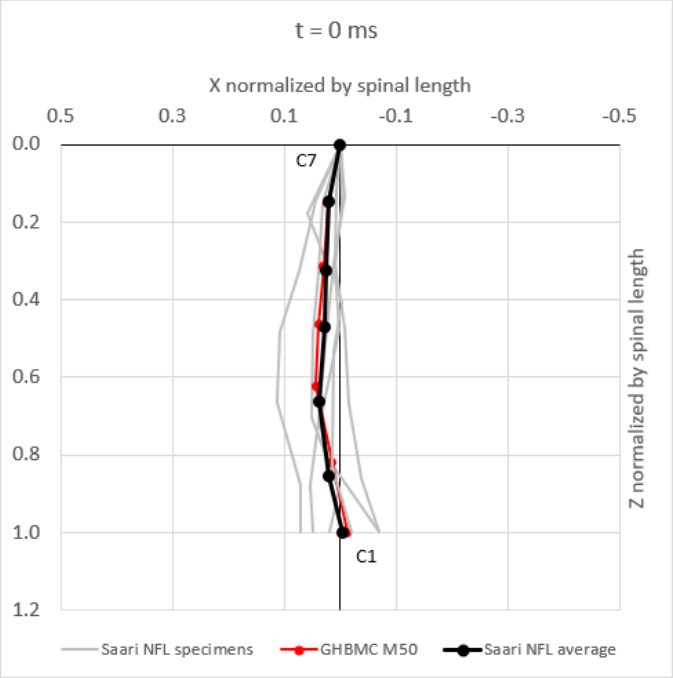

Figure 3-5: Initial (t = 0 ms) normalized cervical spine sagittal traces of Saari NFL specimens (and average) as well as GHBMC M50

Table 3-2: X (anteroposterior) and Z (superior-inferior) difference between GHBMC M50 model nodes and corresponding vertebral photo-reflective markers from average Saari NFL curve following normalization

Normalized X and Z difference between GHBMC M50 and Saari NFL average curves		
Vertebra	**X**	**Z**
C1	0.01	0.00
C2	0.01	0.04
C3	0.01	0.04
C4	0.01	0.01
C5	0.01	0.01
C6	0.00	0.00
C7	0.00	0.00

The initial impact velocity boundary condition was applied to the head and neck model (*INITIAL_VELOCITY_GENERATION option in LS-DYNA) with a vertically downward (-z) velocity of 2.75 m/s (average velocity of the six NFL specimens). The effective torso mass boundary condition was applied by modifying the density of the rigid T1 vertebra in the GHBMC M50 model. The experimental setup reported that an effective torso mass of 15 kg was attached to the mount cup to which the T1 vertebra was potted. Consequently, the density of the rigid T1 vertebra was increased to a calculated value of 72.95×10^{-5} kg/mm^3 to account for that mass. Lastly, the impact interface boundary condition was addressed by modelling the impact plate material and selecting the appropriate coefficient of friction. The experimental study used a surrogate head (Figure 2-26) that consisted of an aluminum frame incorporating an impact surface of softwood (e.g., pine or spruce) covered with a layer of leather to emulate human skin. There was not enough information available regarding the mechanical properties and geometry of the surrogate head in order to accurately model it, therefore the GHBMC model head was used for the model and the impact interface was designed to provide similar head kinematics to that reported in the experimental study. This was the only experimental detail that was not accounted for in

GHBMC_Saari, and as a result it was taken into consideration for result analysis and comparison during model validation (Chapter 4). The impact plate used in the experimental setup was a steel platen and was initially modeled (meshed in a commercial pre-processing software (Hypermesh 2019, Altair)) as such using the mechanical properties of mild steel. However, a large amount of head rebound (i.e., head completely bouncing off the impact plate) was observed after the initial impact, which was not reported in the experimental study (Figure 3-6).

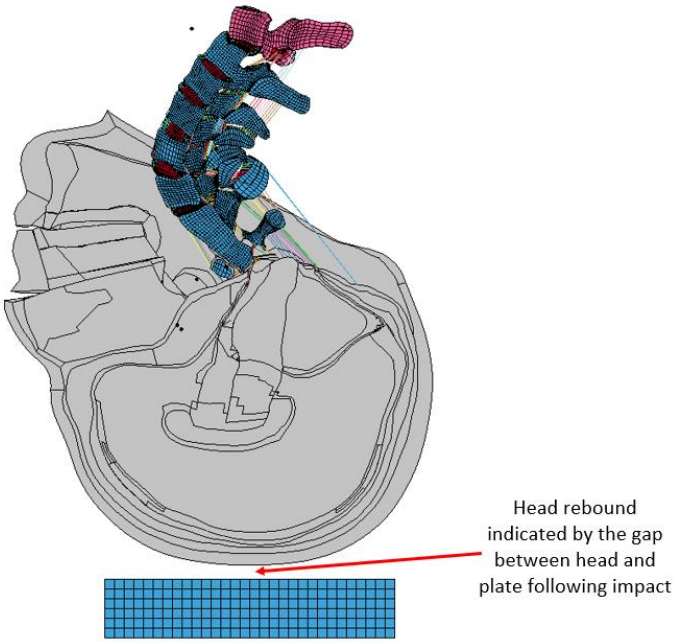

Figure 3-6: GHBMC_Saari 8 ms after impacting steel impact plate, gap between head and plate corresponds to head rebound

The high-speed videos of the experimental test specimens indicated that there was little to no head rebound experienced by the experimental surrogate heads. Unfortunately, detailed information on the surrogate head materials was not available, and so an additional impact layer was modelled (also meshed in Hypermesh) and added to the impact surface that represented the combination of softwood and leather on the physical surrogate head. An assumption was made to use orthotropic red pine softwood (a common type) and generic leather properties in an elasto-plastic material formulation (*MAT_PIECEWISE_LINEAR_PLASTICITY) with an elastic perfectly-plastic stress vs. strain curve [Salman et al., 2020; Kretschmann, 2010; Kennedy, 1965; Kanagy et al., 1943]. The density used was a calculated average of red pine and leather densities. The addition

of the new leather-wood layer provided head kinematics comparable to those measured from the high-speed video of the experiments (Figure 3-7).

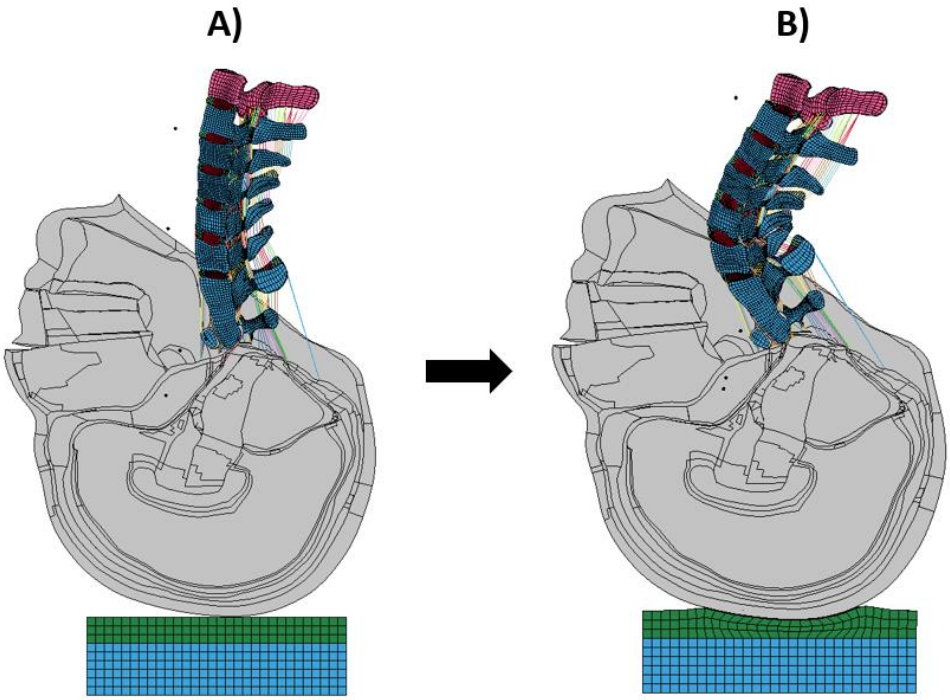

Figure 3-7: A) GHBMC_Saari setup with additional wood-leather layer (green) on top of initial steel plate (blue) at t = 0 ms, and B) GHBMC_Saari at t = 8 ms to showcase that head rebound was eliminated by adding the wood-leather which introduced plastic deformation

The surrogate head kinematics were quantitatively obtained by digitizing the high-speed videos of the NFL specimens using a freely available tracking software (Tracker, version 5.1.5, Open Source Physics). In order to quantitatively compare the head kinematics of GHBMC M50 and the experimental surrogate heads, the same point (Point A, Figure 3-8) was tracked in the experimental high-speed videos and the model. Point A was chosen to be located on the inferior edge of the surrogate head directly superior to the lateral mass marker of C1 (Figure 3-8). This selection was replicated in GHBMC M50 as well (Figure 3-9).

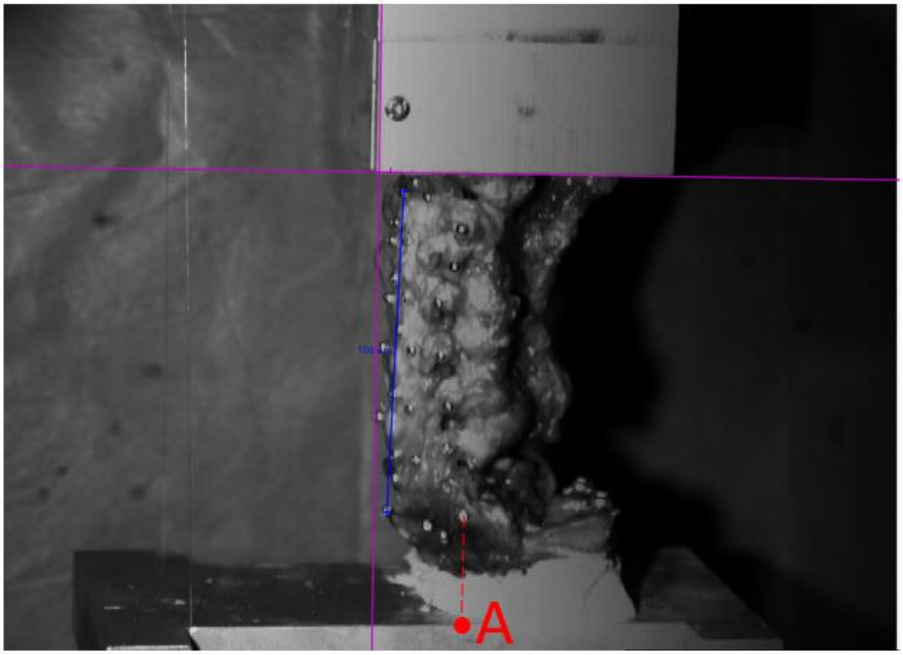

Figure 3-8: Saari specimen H1062 high-speed video frame as seen in Tracker. Axes (purple) with origin coincident on the anterior-superior corner of the mount cup. Calibration stick (blue) to establish scale. Point A (red) on the inferior edge of surrogate head directly superior (red dashed line) to C1 lateral mass photo-reflective marker [Saari et al., 2013]

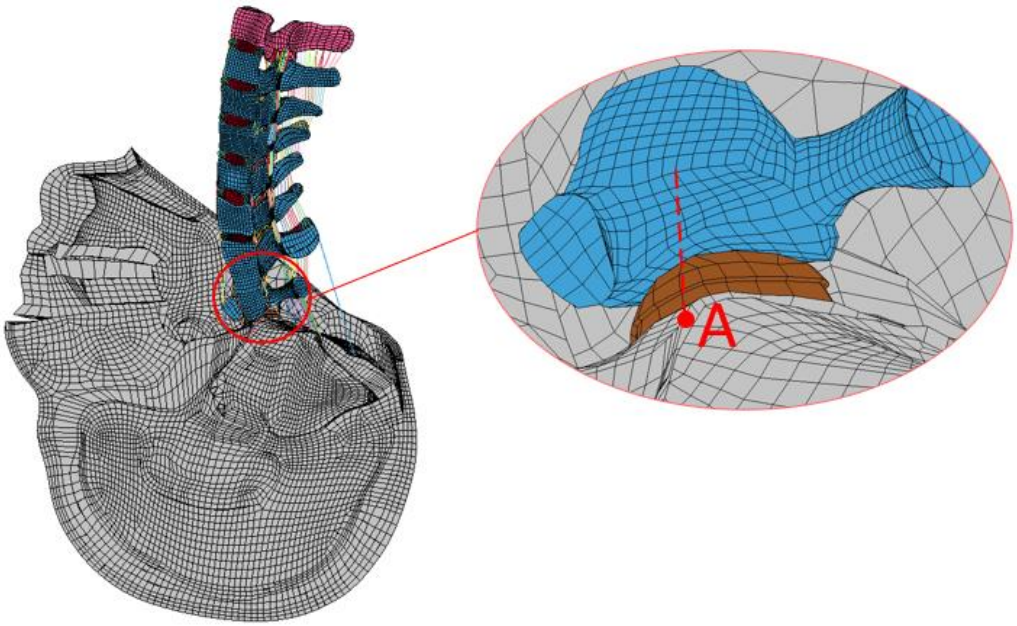

Figure 3-9: GHBMC M50 point A (red) shown on the close-up on the right directly superior to the lateral mass of C1 (blue). Occipital condyle (brown) shown for reference

The Tracker software user interface shown in Figure 3-8 also indicated the x-z axes with the origin coincident with the anterior-superior corner of the mount cup. This was consistent with what was reported in the experimental setup and data acquisition details. In addition, a calibration stick (blue) was used in Tracker software in order to establish the correct scale in the provided high-speed video frames. For specimen H1062 in Figure 3-8, that distance of 100.3 mm was obtained through the available photo-reflective marker coordinates. It was ensured that this initial setup process in Tracker for head kinematic extraction was performed on the high-speed video frame corresponding to the onset of head impact. Following the setup process, the z (vertical) displacement was extracted from the NFL specimens (using Tracker software) and GHBMC M50 (using commercial finite element software (LS-PrePost, LSTC)). The head kinematic results are discussed in Chapter 4.

The coefficient of friction (μ) at the interface between the head and the impact plate (i.e., impact interface) was based on a published value (μ = 0.6) of leather on steel [Fuller, 1984]. Figure 3-10 summarizes the boundary and initial conditions applied to GHBMC_Saari.

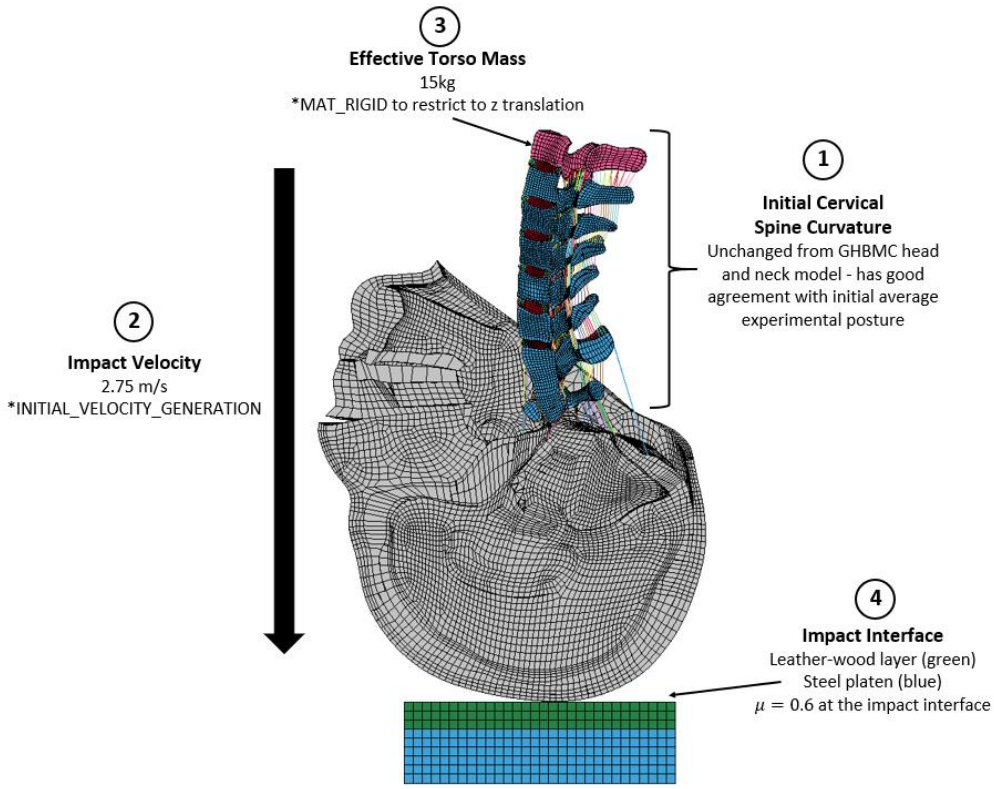

Figure 3-10: Four HFI configuration parameters applied to the GHBMC_Saari model: 1) initial cervical spine curvature, 2) impact velocity, 3) effective torso mass, and 4) impact interface

The GHBMC_Saari model had hard tissue failure turned off. With this failure option applied, there was no element erosion that occurred once the solid (trabecular bone) and shell elements (cortical bone) reached their respective failure thresholds (effective plastic strain values of 9.17% and 3.43%, respectively); thereby accumulating plastic strain following the onset of hard tissue injury. This failure option was considered an upper bound for real-life hard tissue failure (bone fracture) because it was limited in not being able to represent bone fracture propagation; the elements just accumulated plastic strain. Alternatively with hard tissue failure turned on, element erosion occurred once the solid and shell elements reached their respective failure effective plastic strain values. This failure option was considered a lower bound for real-life hard tissue failure because element erosion, which is not analogous to real-life vertebral fracture propagation, significantly transected the axial load path following the first element deletion. Both failure options were considered for the model validation in order to bound the response: GHBMC_Saari with hard tissue failure turned off, and GHBMC_Saari_failON with hard tissue failure turned on. Both model configurations were identical with the only difference being the failure option applied.

The model validation against the Saari experimental results compared the HFI progression (qualitative) and kinematic, kinetic, and injury results. The results were extracted from GHBMC_Saari and GHBMC_Saari_failON model configurations.

The HFI progression entailed visual observation of the mid-sagittal view of the model configurations from 0-15 ms (e.g., at 5 ms intervals) in order to qualitatively describe the general response of the cervical spine during HFI loading. The kinematic results consisted of the x and z coordinates of the vertebral body nodes (Figure 3-3) from 0 ms to 7 ms. Moreover, a proposed kinematic metric, termed the buckling parameter, was used to further quantify the buckling behaviour of the cervical spine during HFI loading. The buckling parameter, calculated as a percentage, was the ratio of the sagitta to the chord length. The sagitta is the difference between the x coordinate (anteroposterior) of the anterior-most vertebral node and the x coordinate of the C7 vertebral node, and the chord length is the difference between the z coordinate of the C7 vertebral node and the z coordinate of the C1 vertebral node. This is shown in Equation 1 and illustrated in Figure 3-11. The term ‘CX’ in Equation 1 represented the vertebra that had the greatest anterior distance from the C7 vertebra at a given time during the impact. The kinetic results were the axial contact force between the head and impact plate vs. time, and the axial neck force

(measured at C7) vs. time. Additionally, the peak neck and head contact forces, the slope of the neck and head contact force rise time, the time from head impact to the peak neck force, and the time from head impact to the point where the neck force started to increase were extracted from the plots in order to further quantify the kinetic response. The trends in the plots were analyzed to understand their relation to the kinematic and injury response. Finally, the hard and soft tissues injuries were extracted and compared to reported experimental injuries. Hard tissue injury was quantified by extracting the onset times of vertebral fracture across all vertebral levels from GHBMC_Saari and GHBMC_Saari_failON, and by identifying the location of hard tissue failure within each vertebra (e.g., spinous process, pedicles, etc.) in the models. Soft tissue injury was quantified by extracting the onset times of ligament failure (rupture) across all segment levels, identifying which ligaments failed across all segment levels (e.g., ALL, CL, etc.), and identifying the occurrence of disc avulsion across the C2-C3 to C7-T1 segment levels. Soft tissue injury was defined the same way for both model configurations: ligament rupture was defined by the tensile displacement at failure, whereas disc avulsion was indicated by the normal failure stress.

$$Buckling\ parameter = \frac{(CX - C7)_x}{(C7 - C1)_z} \times 100\% \quad (1)$$

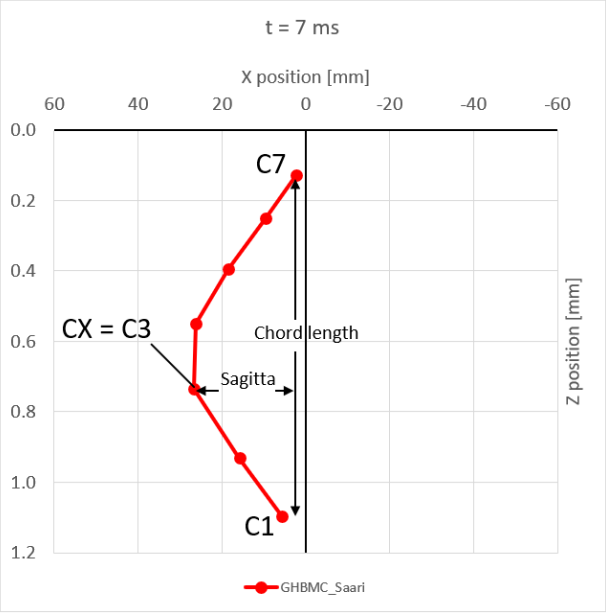

Figure 3-11: Kinematic plot illustrating how the buckling parameter was calculated

3.3 GHBMC Model Assessment and Boundary Conditions Based on Nightingale (1996) Experimental Study

A GHBMC model configuration, which will henceforth be referred to as GHBMC_Nightingale, was created in order to replicate the boundary and initial conditions described in the experimental setup outlined in the study by Nightingale.

The cervical spine curvature of the specimens was represented in GHBMC_Nightingale. The specimen curvatures were quantified in the experimental study through the sagittal plane orientation of the C7-T1 intervertebral discs. This was done by ensuring that the AP angle of the discs (with respect to the true horizontal) was 25° for all specimens. Unlike the procedure carried out to represent the Saari specimen cervical spine curvatures in GHBMC_Saari (section 3.2), there was no raw data provided in order to trace the model cervical spine in the sagittal plane and compare it to the Nightingale specimens; the only posture information available was the AP angle of the C7-T1 disc. The GHBMC M50 model had a C7-T1 disc AP angle of 13°. The AP angle was measured at the mid-sagittal plane of the disc. The desired angle of 25° was achieved through the use of simulation-based reposturing (Figure 3-12). This was done by first applying a boundary condition to fix the head and applying an angular displacement to the T1 vertebra. Specifically, the angular displacement was an angle (in degrees) assigned based on the desired disc sagittal orientation. Therefore, an angle of 12° (e.g., 25° subtract 13°) was assigned in the curve in order to rotate the T1 vertebra (and consequently the C7-T1 disc) in flexion by the desired amount. This flexion rotation was applied for a duration one second. Following that, the model was allowed to settle for a duration of 1 second. Settling ensured that the model had achieved equilibrium. The output cervical spine posture following the reposturing simulation was then extracted and used as the stress-free initial posture for the HFI simulation in GHBMC_Nightingale.

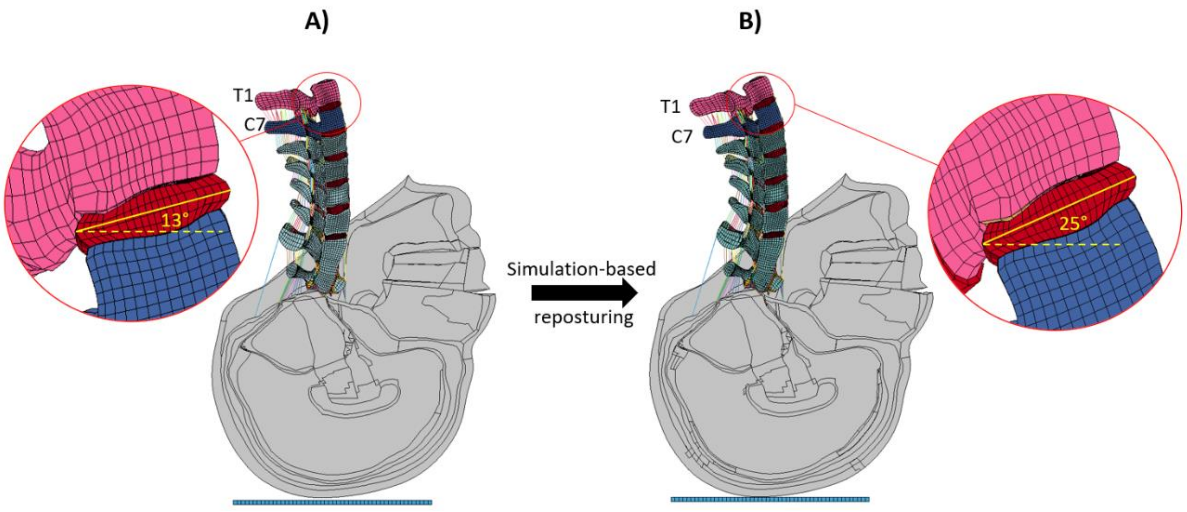

Figure 3-12: A) Mid-sagittal view of GHBMC M50 model C7-T1 disc orientation (solid yellow line) of 13° with respect to the true horizontal (dashed yellow line). B) Mid-sagittal view of GHBMC_Nightingale with the repostured C7-T1 disc orientation of 25° with respect to the true horizontal

The impact velocity boundary condition was applied using the *INITIAL_VELOCITY_GENERATION card and a vertically downward (-z) velocity of 2.96 m/s (average velocity of the 3 relevant specimens) was applied on the entire model. The experimental setup reported that an effective torso mass of 16 kg was attached to the mount cup to which the T1 vertebra was potted. The density of the rigid T1 vertebra was accordingly increased to a calculated value of 72.945×10^{-4} kg/mm^3 in order to account for that mass.

The experimental setup reported the use of a 3 mm-thick Teflon layer on top of the steel impact plate. The Teflon layer (made of solid elements) was meshed in Hypermesh with the desired 3 mm thickness. The steel layer (made of shell elements), which was positioned directly below the Teflon layer, was also modelled in Hypermesh. The Teflon material model was then applied in LS-DYNA using mechanical properties obtained from literature [Rae & Dattelbaum, 2004]. The rigid steel plate was assigned a rigid body formulation (*MAT_RIGID) in LS-DYNA. All of the boundary conditions and HFI setup details that were accounted for in GHBMC_Nightingale are summarized in Figure 3-13.

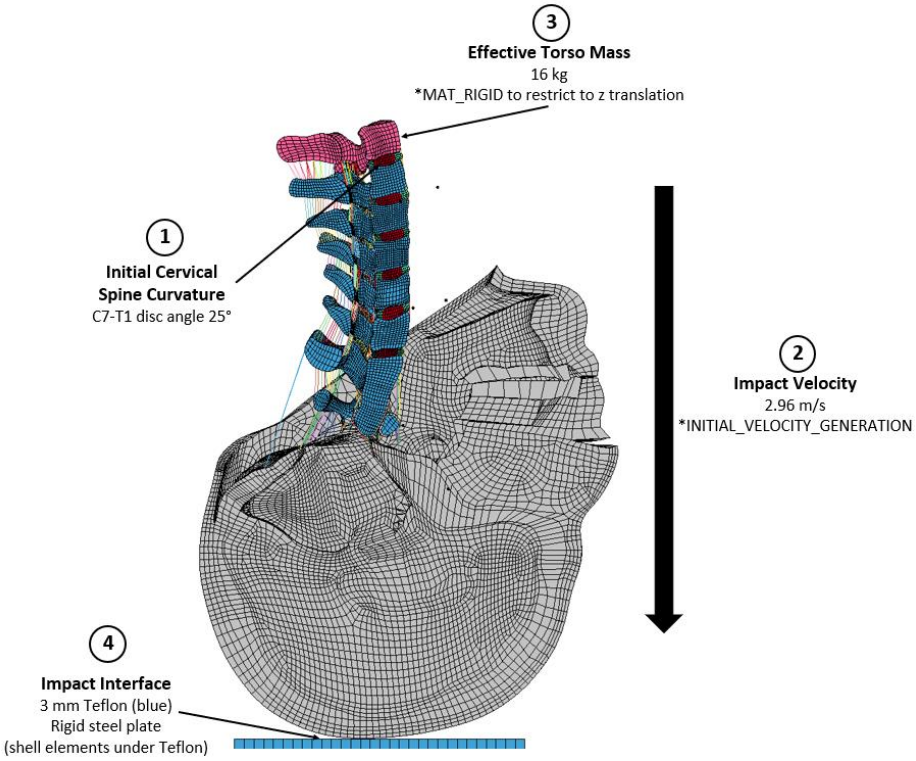

Figure 3-13: Four HFI configuration parameters applied to the GHBMC_Nightingale model: 1) initial cervical spine curvature, 2) impact velocity, 3) effective torso mass, and 4) impact interface

The model validation against the Nightingale experimental results included HFI progression (qualitative) as well as comparisons of kinetic and injury results. Similar to the validation process described for the Saari experimental results (section 3.2), the results were extracted from GHBMC_Nightingale and GHBMC_Nightingale_failON (hard tissue failure off and on, respectively) in order to compare the response, discuss the respective limitations, and subsequently select an appropriate failure option to apply for the sensitivity study. Moreover, kinematic results were not extracted for the validation against Nightingale because there was no raw data provided that enabled a quantitative kinematic analysis of the cervical spine to better understand the buckling behaviour. The kinetic results included the axial contact force between the head and impact plate vs. time, the axial neck force (measured at C7) vs. time, as well as the kinetic metrics (extracted from the kinetic plots) discussed at the end of section 3.2. The trends in the aforementioned plots were analyzed to understand their relation to the kinematic and injury response. Finally, the hard and soft tissue injuries were extracted and compared to the reported experimental injuries.

3.4 Sensitivity Study of Head-First Impact Parameters using the GHBMC_Saari Model

There were several parameters (i.e., initial and boundary conditions) reported in experimental studies that influence the response of the cervical spine in terms of kinetics (forces observed), kinematics (buckling observed), and injury during HFI. Those parameters were initial cervical spine curvature (posture), impact velocity, the anteroposterior (AP) plate angle, the lateral plate angle, the coefficient of friction between the head and the impact plate, and the AP head angle. In this sensitivity study, one parameter was varied at a time (Figure 3-14) to assess the individual effect on cervical spine response during HFI. The model used for this sensitivity study was the GHBMC_Saari model (with hard tissue failure turned off) because the Saari experiments (unlike Nightingale) included kinematic data at each vertebral body level, which allowed for a quantitative kinematic analysis used to better explain the kinetic response and injury outcome of the models. The hard tissue failure was turned off for the sensitivity study after the limitations and influence on model response were compared against the failure on option (covered in Chapter 4). For each of the parameter variations in the sensitivity study, the kinematic, kinetic, and injury results, and HFI progressions were extracted from the respective models. As previously discussed (section 3.2), the kinematic results were the sagittal cervical spine traces from 0-7 ms in addition to the buckling parameters, and the kinetic results were the head contact force and axial neck compressive force history plots in addition to the extracted kinetic metrics. The hard tissue injury results entailed comparing the onset times of vertebral fracture across all vertebral levels and identifying the location of injury within the vertebrae (e.g., spinous process, pedicles, etc.). The soft tissue injuries were quantified by extracting the onset times of ligament failure (rupture) across all segment levels, identifying which ligaments failed across all segment levels (e.g., ALL, CL, etc.), and identifying the occurrence of disc avulsion across the C2-C3 to C7-T1 segment levels.

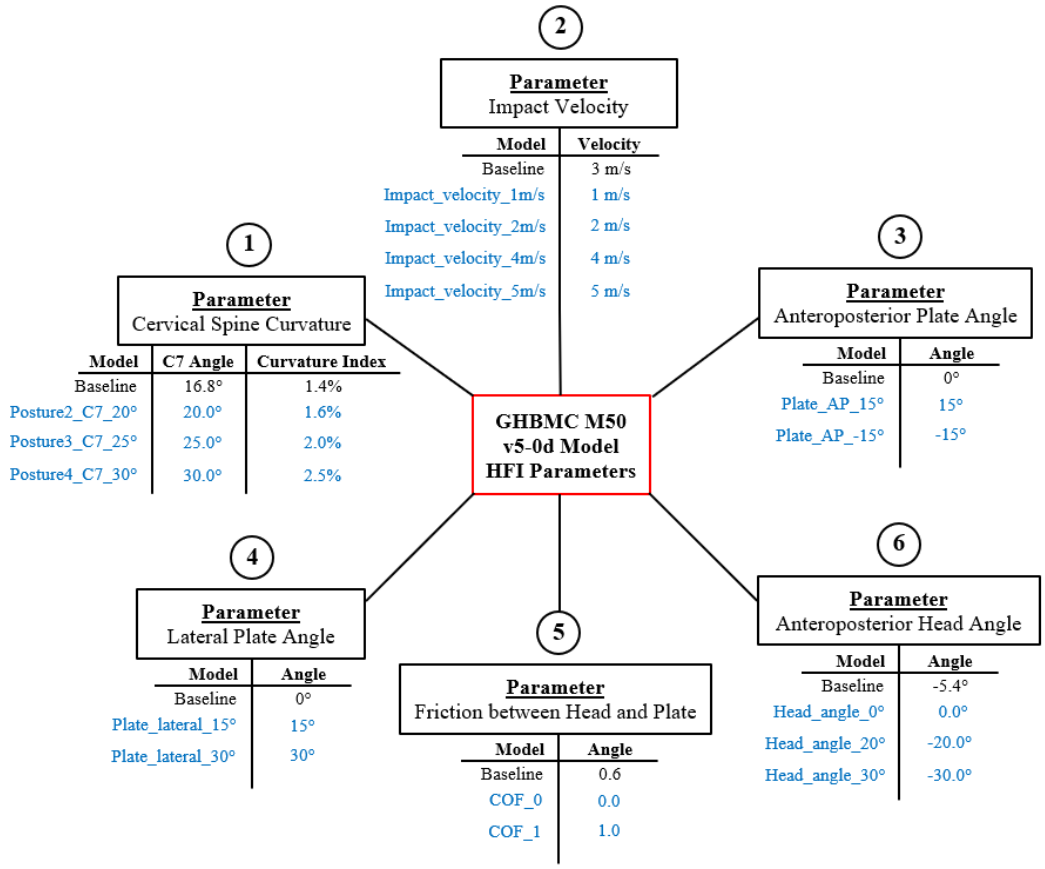

Figure 3-14: Sensitivity study simulation chart

3.4.1 Initial Cervical Spine Curvature

The metrics that were used to quantify cervical spine curvature, as outlined in the volunteer experimental study by Newell (subsection 2.3.1), were the curvature index and C7 angle [Newell et al., 2013]. The curvature index of the baseline model was 1.4% and the C7 angle was 16.8°. The study by Newell reported that, for an average of 9 volunteers, the curvature index was 3.0% $\pm$ 1.4% for an inverted-relaxed posture. The baseline curvature index of 1.4% was slightly less than the lower bound of the reported range. For the same 9 volunteers, the C7 angle was 25.3° $\pm$ 6.5° for an inverted-relaxed posture, where the positive sign of the angle corresponded to flexion. Similar to the curvature index, the baseline C7 angle of 16.8° was slightly less than the lower bound of the reported range. Based on this information, three additional C7 angles were considered: 20°, 25°, and 30°. The reasoning behind incrementing the C7 angles by 5° was to sufficiently cover the range of C7 angles of inverted-relaxed occupants as reported in the study by

Newell. Therefore, the C7 angle was accordingly varied using simulation-based reposturing (similar to what was implemented in GHBMC_Nightingale).

Simulation-based reposturing was performed on the baseline model to obtain different model configurations with varying curvatures that possess higher C7 angles and, as a result, higher curvature indexes. Given the baseline model C7 angle of 16.8° relative to the range of angles reported in the study by Newell, three additional postures were created. Each of the newly created postures corresponded to a unique model; the models along with the baseline model are outlined in Table 3-3 with their corresponding C7 angles and calculated curvature indexes.

Table 3-3: C7 angles and curvature indexes of baseline model and models with C7 angle variation

GHBMC Model	C7 Angle (°)	Curvature Index (%)
Baseline	16.8	1.4
Posture2_C7_20°	20.0	1.6
Posture3_C7_25°	25.0	2.0
Posture4_C7_30°	30.0	2.5

A boundary condition was applied to fix the head and C1 in all degrees of freedom (*BOUNDARY_SPC_SET in LS-DYNA). A loading condition was applied to C7 in order to rotate it in the sagittal plane by prescribing an angular displacement which defined the amount, in degrees, C7 must rotate in order to achieve the desired angle. For example, an angular displacement of 8.2° of flexion rotation was applied to the baseline model (with a C7 angle of 16.8°) to yield the Posture3_C7_25° model. The boundary and loading conditions were applied for a duration of 1 second, followed by a duration of 1 second where the model was allowed to settle. This latter settling duration ensured that the model had achieved equilibrium. Following the reposturing simulation, the desired orientation (i.e., cervical spine posture) was extracted from the last output file of the simulation which contained the updated nodal positions that were to be used as stress-free initial orientation positions for the subsequent HFI simulations. Figure 3-15 shows the models in mid-sagittal view side-by-side for visual comparison.

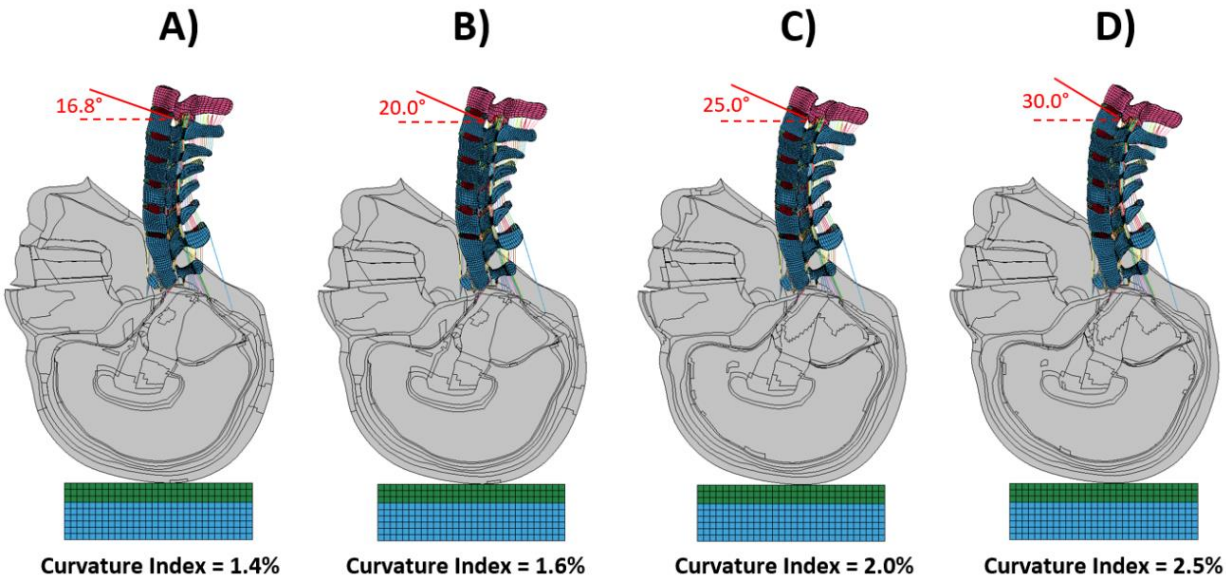

Figure 3-15: A) Baseline model, B) Posture2_C7_20° model, C) Posture3_C7_25° model, and D) Posture4_C7_30° model, all with C7 angles and curvature indexes labelled

3.4.2 Impact Velocity

In rollover crashes, which are the leading cause of cervical spine injuries due to HFI according to epidemiology (subsection 2.2.2), impact velocities between the head and the car roof can be anywhere between 1 m/s and 5 m/s [Bahling et al., 1990; Hu et al., 2008; Viano et al., 2008]. As a result, it was important to consider impact velocity as a factor that could influence the extent of hard and soft tissue injuries sustained, as well as cervical spine kinetic and kinematic response during HFI loading. The baseline model, as described in GHBMC_Saari (subsection 3.2), had an impact velocity of 2.75 m/s. Impact velocities of 1 m/s, 2 m/s, 4 m/s, and 5 m/s were considered in order to sufficiently cover the range reported in the aforementioned literature studies. The new models along with the baseline model are outlined in Table 3-4 with their corresponding impact velocities indicated.

Table 3-4: Impact velocities of the baseline model and newly created models with velocity variations

GHBMC Model	Impact Velocity (m/s)
Baseline	2.75
Impact_velocity_1m/s	1.00
Impact_velocity_2m/s	2.00
Impact_velocity_4m/s	4.00
Impact_velocity_5m/s	5.00

3.4.3 Anteroposterior Impact Plate Angle

The AP angle of the impact plate could have an effect on the cervical spine response in terms of kinematics, kinetics, and injury risk during HFI loading. It was found that there was a good probability of the head impacting a surface at an angle in a real-life scenario of HFI, especially during rollover crashes [Bahling et al., 1990]. Moreover, the experimental study conducted by Nightingale found that varying the AP angle of the impact plate influenced the response of the cervical spine due to the head motion being affected. Therefore, the AP angle of the impact plate was considered important in this sensitivity study. The baseline model was setup such that vertex HFI (which corresponded to an AP angle of 0°) was occurring. Two additional AP angles were considered: 15° and -15°. These angles were chosen to match what was done in the experimental study by Nightingale. As a result, two new models were created with the 15° and -15° AP angles: Plate_AP_15° and Plate_AP_-15°, respectively. Figure 3-16 shows these models alongside the baseline model for reference.

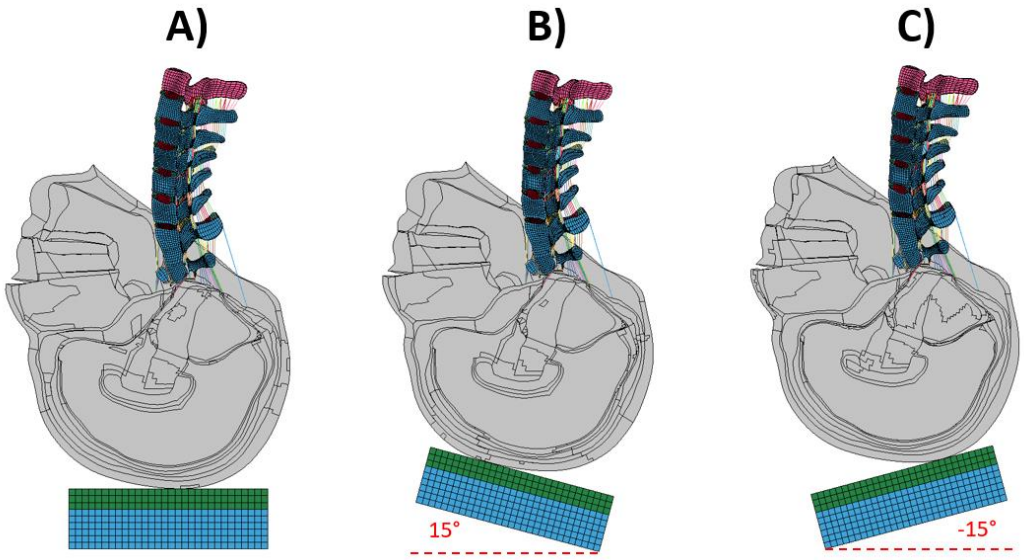

Figure 3-16: A) Baseline model, B) Plate_AP_15° mode, and C) Plate_AP_-15° model

3.4.4 Lateral Impact Plate Angle

The lateral angle of the impact plate can have an effect on the cervical spine response during HFI that is similar to varying the AP angle of the plate. In fact, during rollover crashes, the head can impact the roof of the car at a lateral angle that is not necessarily 0° [Bahling et al., 1990]. A lateral

plate angle of 0° corresponded to a horizontal orientation in the frontal plane. Moreover, a numerical study (subsection 2.3.2) performed a sensitivity analysis with varying the lateral angle (e.g., angles of 15° and 30°) of the impact plate as one of the modelling parameters owing to the significance of the angle and reported how it had a notable effect on the behaviour of the cervical spine during HFI loading [Hu et al., 2008]. As a result, the lateral angle of the impact plate was considered as a HFI parameter in this sensitivity study.

The baseline model had a lateral impact plate angle of 0°. The two additional lateral angles that were considered in this study were 15° and 30° (identical to the numerical study by Hu). Due to the anatomical symmetry of the GHBMC model about the sagittal plane, the lateral angle variations were only applied to one side of the model (Figure 3-17).

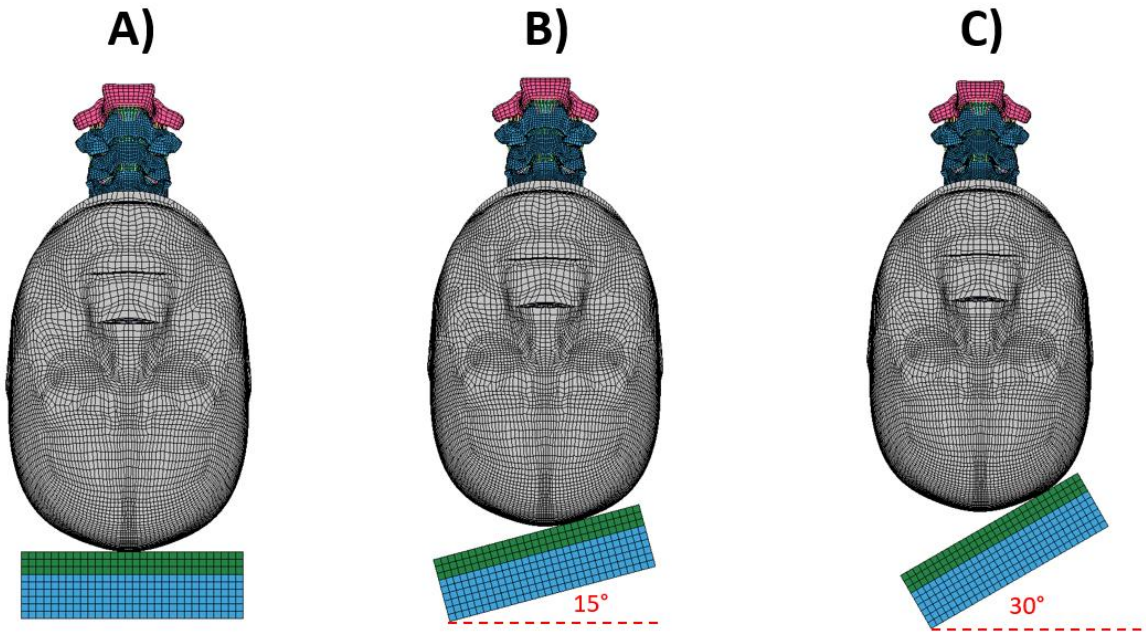

Figure 3-17: A) Baseline model, B) Plate_lateral_15° model, and C) Plate_lateral_30° model

3.4.5 Coefficient of Friction between Head and Impact Plate

The friction between the head and the impact plate could play a role in affecting the response and injury risk of the cervical spine during HFI because friction had a direct effect on the motion of the head, which was reported to influence the behaviour of the cervical spine under compression [Nightingale et al., 1997]. For instance, a high friction at the interface (e.g., $\mu = 1$) can impede the

motion of the head and restrict it more than a frictionless interface (e.g., μ = 0). As a result, the friction between the head and the plate was considered as a HFI modelling parameter in this sensitivity study.

As previously described in GHBMC_Saari (subsection 3.2), the friction between the head and the leather layer of the baseline model was 0.6. Two new models were created, COF_0 and COF_1, by changing the friction at the impact interface to 0 and 1, respectively. The models were created in order to account for impact interfaces with lower and higher friction values (relative to the baseline).

3.4.6 Anteroposterior Head Angle

During HFI scenarios such as rollover, people can have different pre-impact postures and head orientations. Therefore, the AP angle of the head, defined by the Frankfort plane, could play an important role in affecting the cervical spine response during HFI loading.

The Frankfort plane was defined by a line passing through the tragion and the inferior margin of the orbit (Figure 3-18). Newell reported that the Frankfort plane angle (measured between the Frankfort plane and the true horizontal) was -25.2° $\pm$ 10.5° for an inverted-relaxed posture. The negative sign on the angle corresponded to extension motion of the head. According to the sign convention of the Frankfort plane angle outlined in the study, a 0° Frankfort plane angle meant the Frankfort plane was parallel to the anatomical transverse plane (or the line created by the Frankfort plane was parallel to the true horizontal) (Figure 3-19). The baseline model had a Frankfort plane angle of -5.4°. This angle was less than the range reported in the study, and therefore GHBMC model orientations with Frankfort plane angles of -20° and -30° were considered. An additional lower bound angle of 0° was also considered. These angles were achieved through the use of simulation-based reposturing.

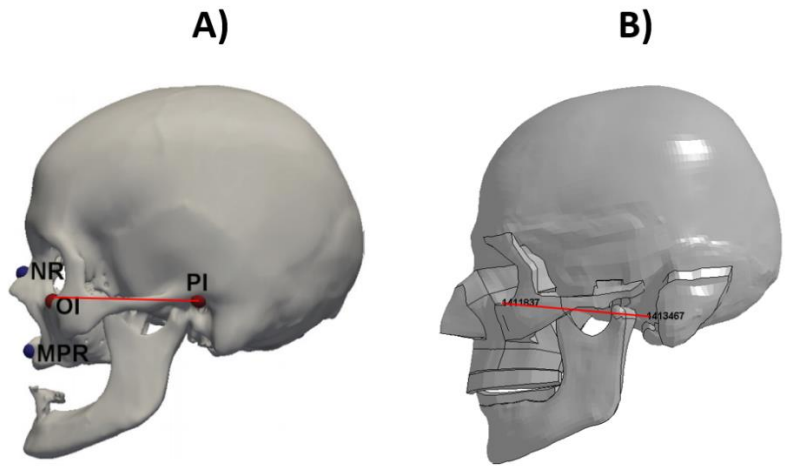

Figure 3-18: A) Skull showing the orbital landmark (OI), the tragion landmark (PI), and the Frankfort plane (red line), adapted from [Cheng et al., 2012], and B) GHBMC model with nodes identifying the orbital and tragion landmarks along with Frankfort plane (red line)

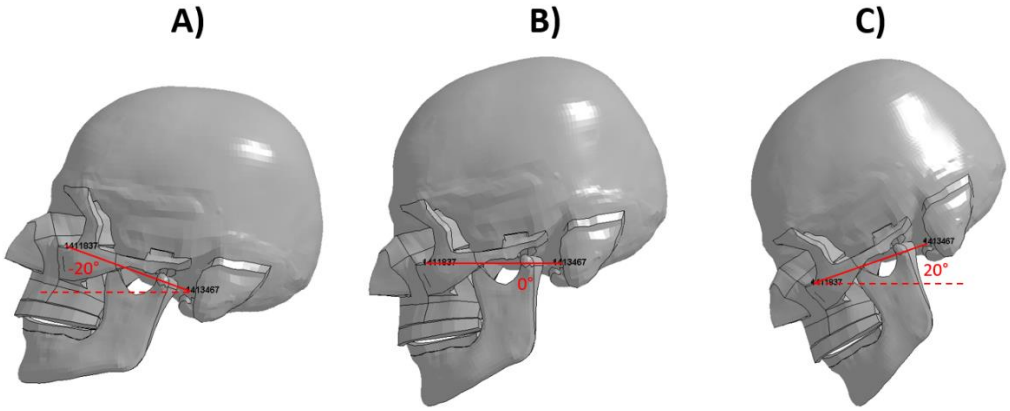

Figure 3-19: GHBMC head in different orientations to showcase Frankfort plane angle sign convention adopted by [Newell et al., 2013]. A) Frankfort plane angle -20°, B) Frankfort plane angle 0°, and C) Frankfort plane angle 20°

The implementation of simulation-based reposturing to achieve the desired Frankfort plane angles was similar to what was used in GHBMC_Nightingale, as well as the models with differing cervical spine curvatures outlined in subsection 3.2.1. A boundary condition was applied to T1 in order to fix it in all degrees of freedom (i.e., no translation or rotation in x, y, z). The loading condition was applied to the head in the form of an angular displacement curve prescribing rotation about the medial-lateral axis (i.e., sagittal rotation). The rotation values, in degrees, defined in the angular displacement curves were calculated based on the desired orientation. For example, an

angle of 5.4° was prescribed in the angular displacement curve in order to achieve the 0° Frankfort plane angle from the baseline Frankfort plane angle of -5.4°. Similar to previous implementations of simulation-based reposturing, the loading conditions were applied for a duration of 1 second, followed by a 1 second settling period in order to establish model equilibrium. The final posture was extracted from this reposturing simulation as the initial stress-free posture for the HFI simulation. As a result of rotating the head in flexion (e.g., going from baseline -5.4° to 0°), the cervical spine curvature was reduced, causing a decrease in the curvature index. Alternatively, rotating the head in extension (e.g., going from baseline -5.4° to -20° or -30°) resulted in a more curved cervical spine with a higher curvature index. Table 3-5 outlines the newly created models that corresponded to the Frankfort plane angles of 0°, -20°, and -30°, along with their curvature indexes, and Figure 3-20 shows these models in mid-sagittal view side-by-side for a visual comparison.

Table 3-5: Frankfort plane angles and curvature indexes of the baseline model and newly created models with varying head inclination

GHBMC Model	Frankfort Plane Angle (°)	Curvature Index (%)
Baseline	-5.4	1.4
Head_angle_0°	0.0	1.4
Head_angle_20°	-20.0	1.6
Head_angle_30°	-30.0	2.2

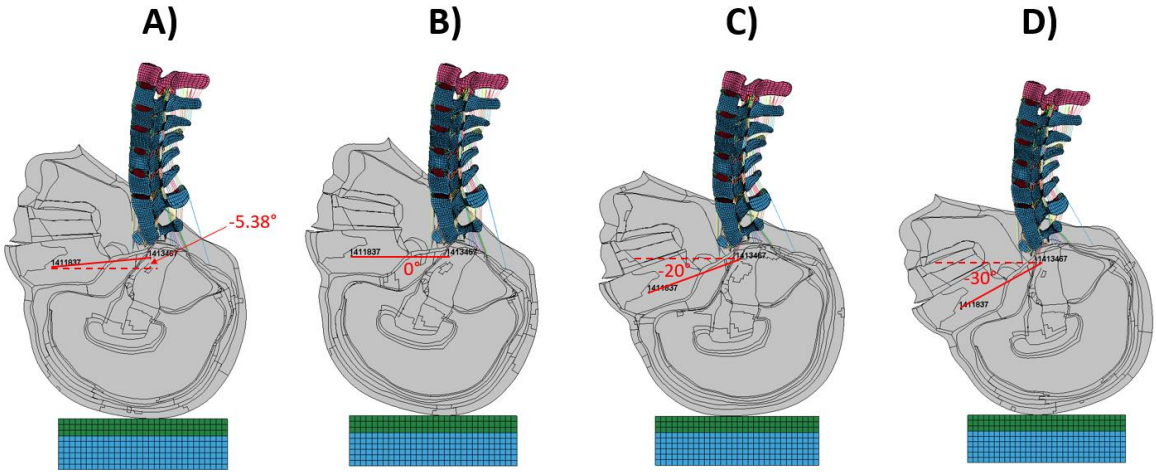

Figure 3-20: A) Baseline mode, B) Head_angle_0° model, C) Head_angle_20° model, and D) Head_angle_30° model

Chapter 4: Results and Discussion

4.1 Model Validation Against Saari (2013) Experimental Results

As described in section 3.2, head rebound was eliminated from GHBMC_Saari through the addition of the leather-wood layer. The head rebound was eliminated to match the experimental response, which showed that head rebound was absent from the NFL specimens (proven through the use of Tracker to digitize the high-speed videos). In order to illustrate that head rebound was occurring with the initially modelled steel layer and was eliminated from GHBMC_Saari after the addition of the leather-wood layer, the z displacement of point A (Figure 3-9) was extracted to compare the model head kinematics to the experimental surrogate head kinematics. Figure 4-1 shows the z displacement vs. time plots of point A of all six NFL specimens, the average of the NFL specimens, as well as GHBMC_Saari using the initially modelled steel plate (depicted in Figure 3-6). Figure 4-2 shows the same plot but using the additional leather-wood layer that was modelled to eliminate head rebound.

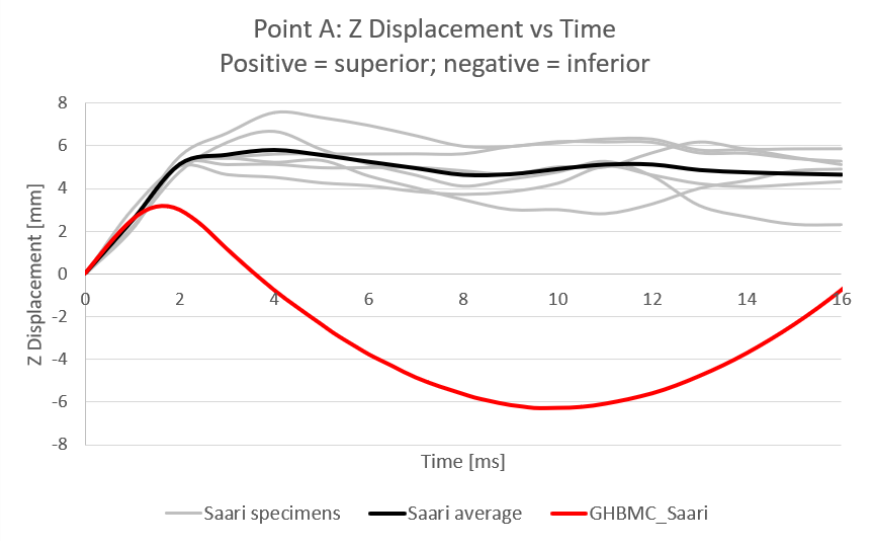

Figure 4-1: Point A z displacement of NFL Saari specimens, (with average shown in black) vs. GHBMC_Saari with the initially modelled steel layer only

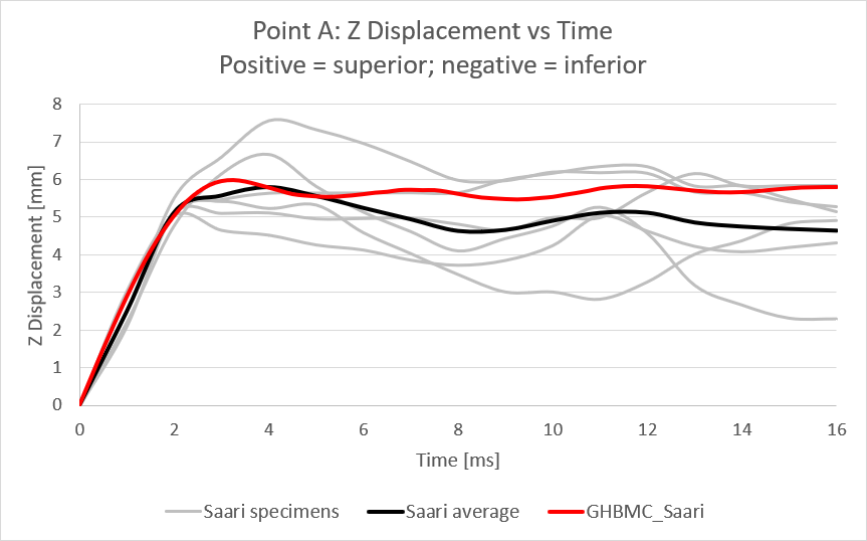

Figure 4-2: Point A z displacement of NFL Saari specimens (with average shown in black) vs. GHBMC_Saari with the addition of the wood-leather layer

The z displacement plot of point A from GHBMC_Saari (Figure 4-1) demonstrated a different response than the experimental plots due to the head rebound that occurred. The head rebound response differed greatly from what was seen in point A from the NFL surrogate heads; the head deformed axially during the first 3 ms, followed by a plateau region, which indicated that the surrogate head was experiencing no rebound. However, in Figure 4-2 the z displacement of point A in GHBMC_Saari now plateaued, which indicated that no head rebound occurred. The head rebound was eliminated from GHBMC_Saari because the leather-wood layer deformed plastically, which in turn resulted in an increased head vertical displacement into the layer. The deformation of the leather-wood layer continued until the perfectly-plastic zone (as defined in the material model) was reached and the head vertical motion was relatively restricted. The kinematic response of the GHBMC_Saari model head with the leather-wood layer was in better agreement (relative to the model with the steel plate modelled initially) with the digitized head kinematics of the NFL surrogate heads.

Kinematic, kinetic, and injury results were extracted from the GHBMC_Saari model (hard tissue failure turned off) and the GHBMC_Saari_failON model (hard tissue failure turned on). As discussed in Chapter 3, results were studied for both configurations to assess the impact the respective limitations of the failure options had on the model response. Subsequently, an

appropriate failure option (failure off or on) was applied in the sensitivity study that was better suited for predicting hard and soft tissue injuries.

HFI Progression

The HFI progressions of the GHBMC_Saari and GHBMC_Saari_failON model configurations from 0 ms to 15 ms are shown in Figure 4-3 and Figure 4-4, respectively.

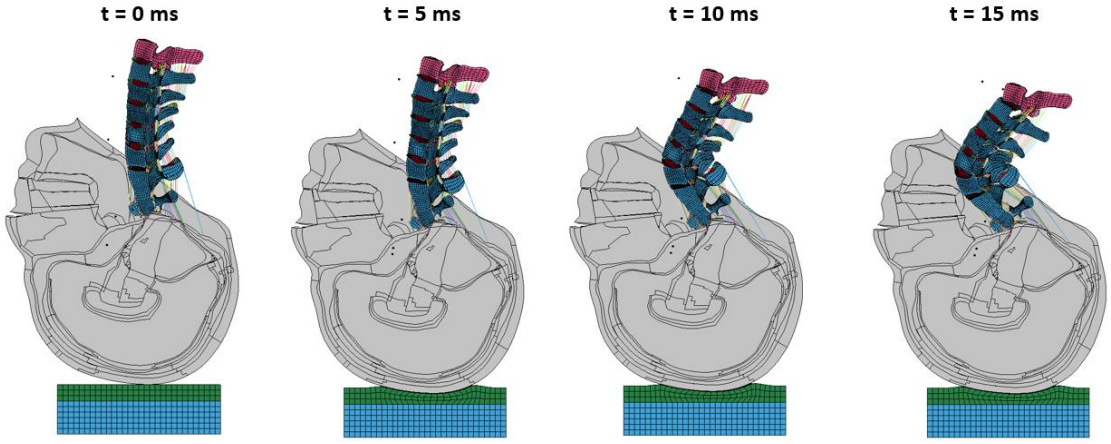

Figure 4-3: HFI progression of GHBMC_Saari from 0 ms to 15 ms

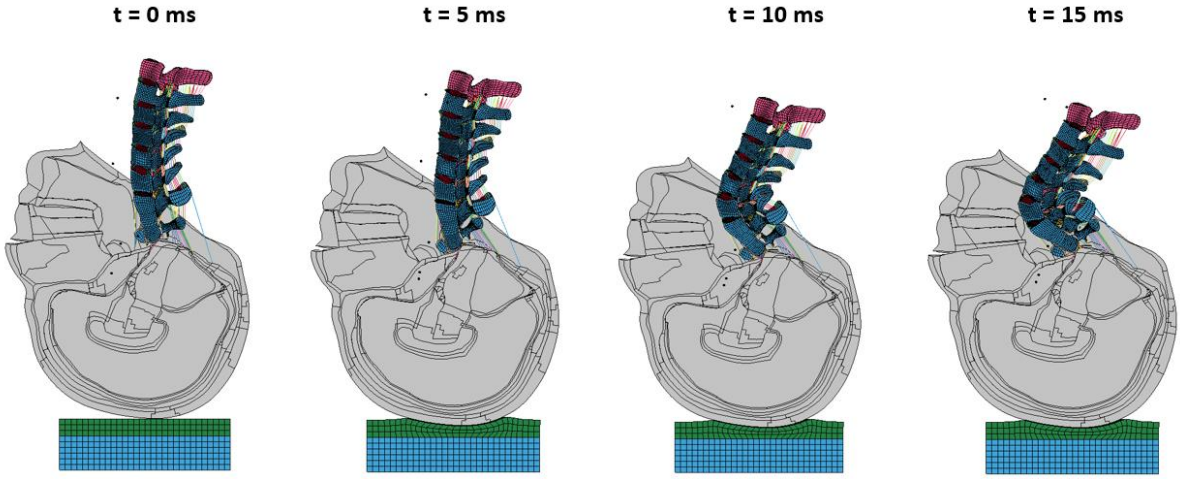

Figure 4-4: HFI progression of GHBMC_Saari_failON from 0 ms to 15 ms

During the first 5 ms of the HFI progression of the model configurations, the head plastically deformed the leather-wood layer, resulting in vertical head displacement into the layer and negligible cervical spine deformation (this was later quantified through the kinematic results).

Between 5 and 10 ms, cervical spine buckling was observed where C1-C3 rotated in extension, and C4-C7 rotated in flexion. The T1 vertebra did not rotate due to the imposed boundary condition, and as a result, disc avulsion occurred at the C7-T1 segment level. The rate of change of buckling was the highest between 5-10 ms, indicating that most of the buckling occurred during that interval. Furthermore, the buckling, as quantified through anterior displacement of the vertebrae, was concentrated at the C3 vertebra (i.e., C3 was the inflection point). This concentration was due to the direction of rotation of the vertebrae throughout the loading. The C3 vertebra initially (first 3 ms) rotated in flexion followed by extension. The extension that occurred in the upper cervical spine paired with the mixed rotation of C3 made C3 the vertebra at which the rotation switched direction. At around 5 ms after head impact, solid and shell elements in GHBMC_Saari_failON (corresponding to the vertebrae trabecular and cortical bones, respectively) were eroded due to hard tissue failure at the pedicles and dens of C2.

Kinematic Results

The GHBMC_Saari and GHBMC_Saari_failON kinematic results, which entailed cervical spine sagittal traces from 0-7 ms, were compared against the average experimental trace from the Saari specimens in Figure 4-5. The buckling parameter increase throughout the first 7 ms of loading, which identified how gradually or abruptly the cervical spine exhibited buckling, is summarized in Table 4-1.

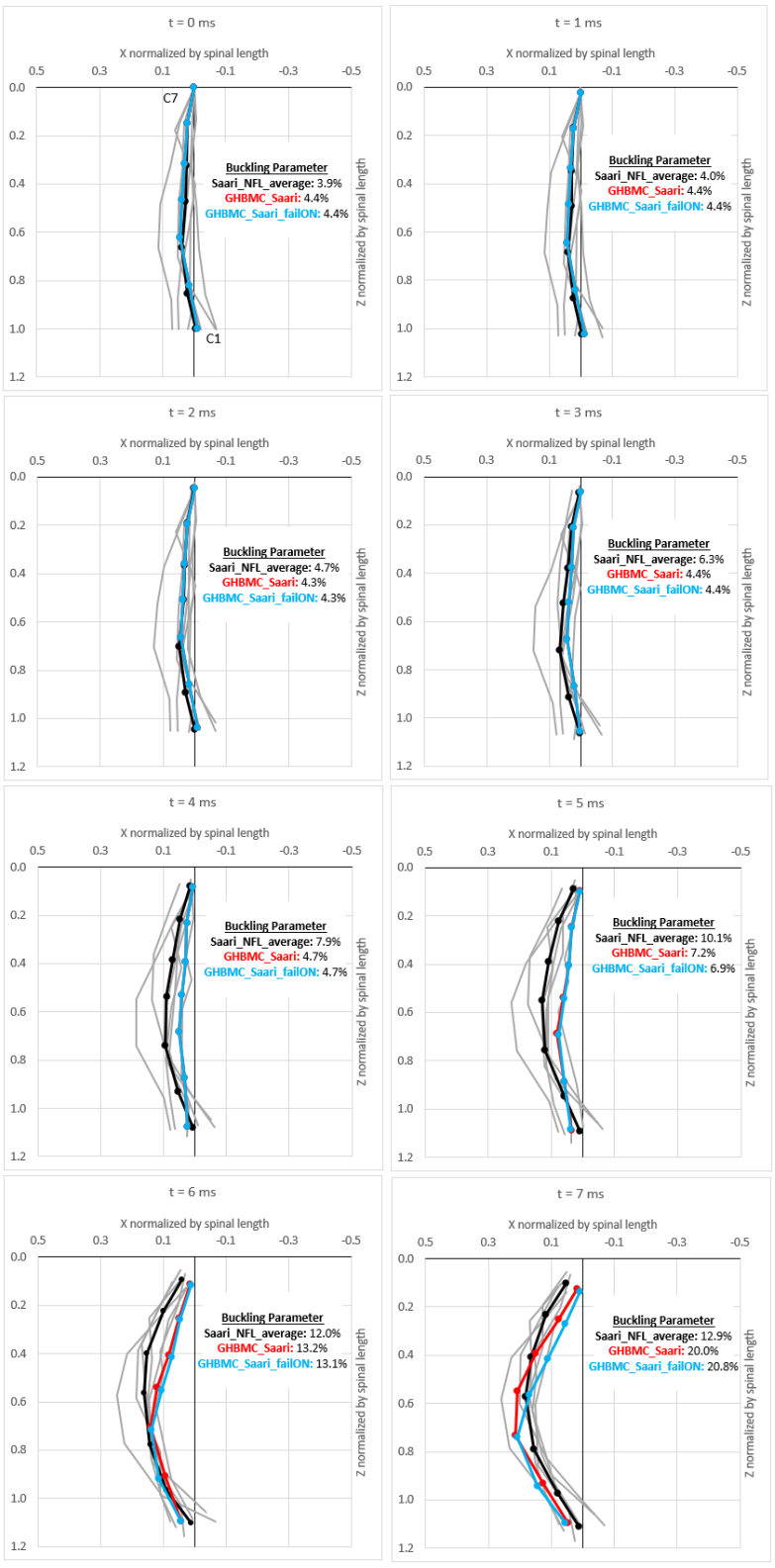

Figure 4-5: Cervical spine sagittal kinematic plots from 0 ms to 7 ms of GHBMC_Saari, GHBMC_Saari_failON, and average Saari NFL specimens, with specimen curves shown in grey

Table 4-1: Buckling parameter increase throughout the first 7 ms of loading for GHBMC_Saari and GHBMC_Saari_failON models, as well as Saari NFL average and Saari NFL specimen H1062

Buckling Parameter Increase Throughout First 7 ms of Loading			
Model	Average of buckling parameter increases (%)	Greatest buckling parameter increase (%)	Time interval corresponding to greatest increase (ms)
GHBMC_Saari	2.2	6.8	6-7
GHBMC_Saari_failON	2.3	7.7	6-7
Saari NFL Average	1.2	2.1	4-5

From 0 ms to 4 ms, the cervical spines of both model configurations experienced negligible buckling. The negligible buckling was indicated from the buckling parameter values and comparing their progression during the first 4 ms of loading. During this period, the leather-wood layer was plastically deformed while the head translated downwards, and the load was not yet fully transmitted throughout the cervical spine (this was shown in the kinetic results later in the section). The GHBMC models had similar values corresponding to the average of buckling parameter increases throughout 7 ms of loading (e.g., 2.2% and 2.3%). The cervical spine sagittal traces of the two model configurations started to deviate after 4 ms following head impact, which coincided with hard tissue failure initiation in the models (covered later in the section). Due to the element erosion that occurred predominantly at the upper cervical spine of the GHBMC_Saari_failON model, the C2 vertebral point corresponding to that model translated more anteriorly relative to the GHBMC_Saari model during the 4-7 ms interval. Additionally, the lower cervical spine of GHBMC_Saari_failON did not buckle (anteriorly displace) as much as in GHBMC_Saari due to the element erosion predominantly occurring at the upper cervical spine of GHBMC_Saari_failON. Due to the higher degree of buckling observed in the GHBMC_Saari_failON model, the greatest buckling parameter increase value was higher than that of the GHBMC_Saari model (7.7% > 6.8%). The greatest buckling parameter increase occurred during the same interval (6-7 ms) for both model configurations.

The buckling sustained in both models was abrupt relative to the average experimental response as all the buckling occurred during the last 3 ms of the interval (i.e., 4-7 ms). Alternatively, the buckling sustained in the average experimental response was more gradual as the buckling parameter increased consistently throughout the 7 ms of loading. The average of buckling

parameter increases as well as the greatest buckling parameter increase corresponding to the models were both higher than the respective average experimental values (Table 4-1). Moreover, the average experimental time interval corresponding to the greatest buckling parameter increase was 4-5 ms (compared to the 6-7 ms interval for the models). This experimental interval (4-5 ms) further signified the consistent and gradual increase of the buckling parameter of the specimens throughout the loading. Due to the elastic head deformation and plastic leather-wood layer deformation that occurred during the first 4 ms after head impact in the models, the cervical spine buckling was evident only during the 4-7 ms interval. The buckling was abrupt due to the significant extension rotation of the upper cervical spine (C1 and C2) that accentuated the buckling at the middle cervical spine (specifically C3). Alternatively, the relatively rigid surrogate head attached to the specimens experienced presumably minimal elastic deformation and therefore the axial force transmission to the cervical spine was faster. Moreover, the upper cervical spines of the specimens did not experience significant extension rotation as was the case in the models. As a result, experimental cervical spine buckling was more gradual and occurred over the 7 ms span of loading considered.

Kinetic Results

The GHBMC_Saari and GHBMC_Saari_failON kinetic results, which entailed investigating head contact force and axial neck compressive force history traces, were compared against the corresponding experimental force traces. Kinetic metrics such as initial peak force and the slope of the initial force rise time were extracted to quantitively study the kinetic response of the cervical spine throughout the loading. The head contact and axial neck force history plots are shown in Figure 4-6 and Figure 4-7, and the kinetic metrics extracted from the plots are summarized in Table 4-2 and Table 4-3.

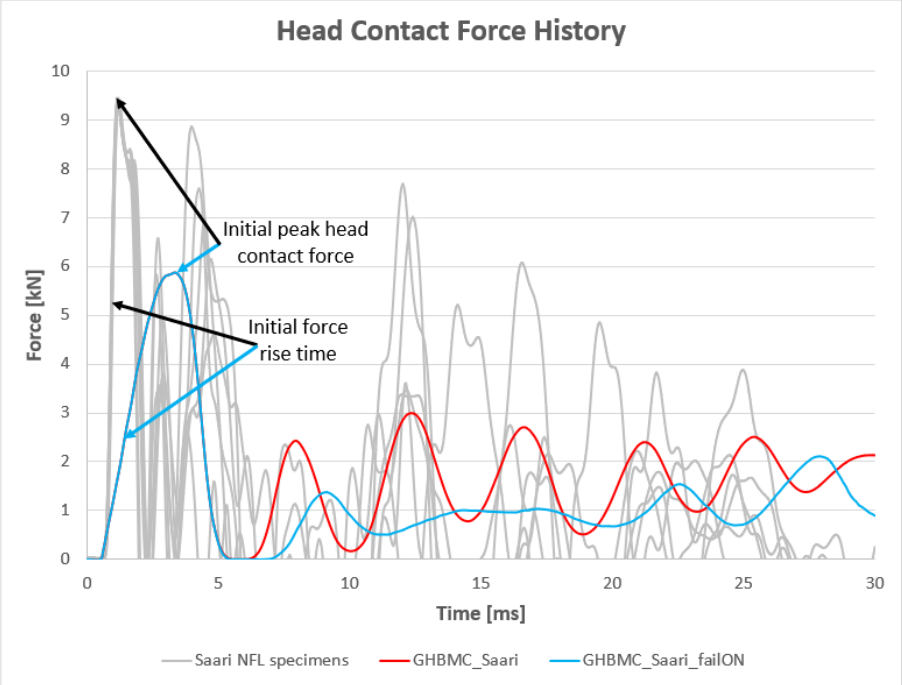

Figure 4-6: Head contact force history plots of GHBMC_Saari, GHBMC_Saari_failON, and Saari NFL specimens, with initial peak head contact force and initial force load-up labelled

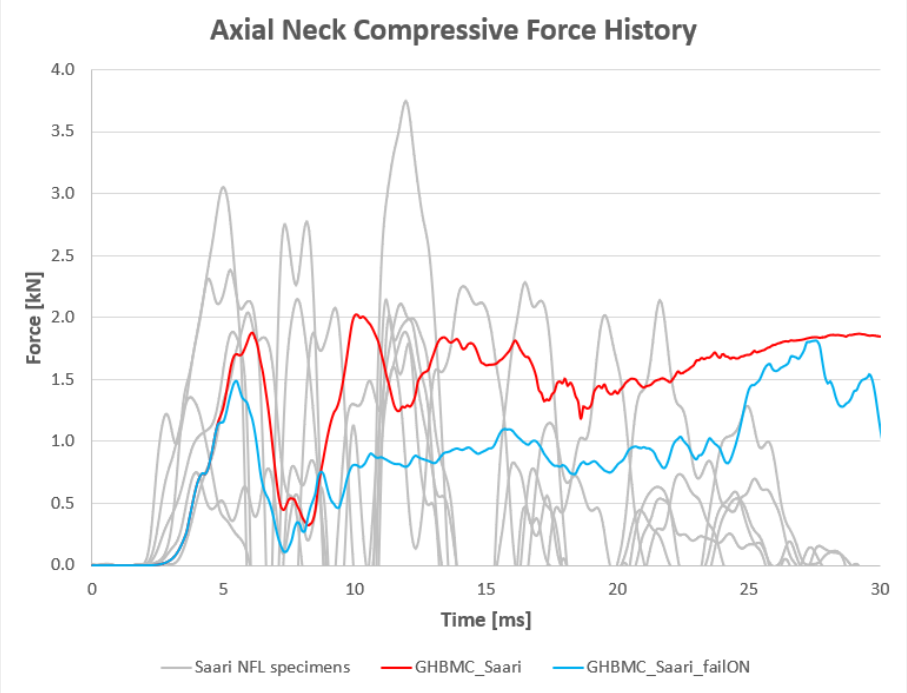

Figure 4-7: Axial neck compressive force history plots of GHBMC_Saari, GHBMC_Saari_failON, and Saari NFL specimens

Table 4-2: Head contact force metrics for GHBMC_Saari, GHBMC_Saari_failON, Saari NFL specimens, and Saari average NFL response

Head Contact Force Metrics		
	Initial peak head contact force (kN)	Slope of initial head contact force rise time (kN/ms)
GHBMC Model		
GHBMC_Saari	5.9	2.1
GHBMC_Saari_failON	5.9	2.1
Saari (2013)		
H1062	9.4	17.1
H1092	9.4	18.4
H1094	9.4	16.9
H1095	9.4	18.7
H1099	9.3	18.0
H1101	9.4	18.3
Average	9.4	17.9

Table 4-3: Axial neck compressive force metrics for GHBMC_Saari, GHBMC_Saari_failON, Saari NFL specimens, and Saari average NFL response

Axial Neck Compressive Force Metrics				
	Initial peak axial force (kN)	Slope of initial neck force rise time (kN/ms)	Time from head impact to initial peak axial neck force (ms)	Time from head impact to neck force rise time (ms)
GHBMC Model				
GHBMC_Saari	1.9	0.5	5.6	2.1
GHBMC_Saari_failON	1.5	0.5	5.0	2.1
Saari (2013)				
H1062	1.9	0.6	4.7	1.5
H1092	0.7	0.5	3.3	1.7
H1094	3.1	1.4	4.3	1.3
H1095	1.4	0.8	3.1	1.4
H1099	2.0	0.5	5.3	1.1
H1101	2.3	1.1	3.8	1.6
Average	1.9	0.8	4.1	1.4

The GHBMC model configurations had the same initial peak head contact force value of 5.9 kN and the same slope of initial force rise time of 2.1 kN/ms. Both models reached the peak force value 3 ms after head impact. During this initial period, the kinetic response of the models was identical because element erosion did not yet occur in the GHBMC_Saari_failON model. The model force traces temporarily, and very briefly, reached zero around 5.5-6.0 ms after head impact (which was after element erosion took place in GHBMC_Saari_failON). The period when the force traces were momentarily zero coincided with when deviation was observed in the model traces: the GHBMC_Saari trace had a value of zero for a duration of 1 ms and the GHBMC_Saari_failON model for a duration of 2 ms. Following that, the deviation continued

where the GHBMC_Saari trace plateaued around 1.5 kN, while the GHBMC_Saari_failON trace plateaued relatively uniformly around 1 kN.

The plots showed that, on average, the experimental force traces had much steeper initial slopes following the onset of head impact (e.g., 17.9 kN/ms > 2.1 kN/ms) and higher initial peaks (e.g., 9.4 kN > 5.9 kN) than both GHBMC model configurations. Moreover, the experimental specimen curves showed more sharp and consecutive increases and decreases in force. The steeper slopes and higher peaks corresponding to the experimental traces could be a result of the surrogate heads experiencing less (if not negligible) plastic deformation upon impact with the plate. The level of plastic deformation of the surrogate heads, however, was not conclusive as the high-speed videos of the experiments did not have the top of the head or the impact interface in the frame of the videos, and therefore any deformation that may have occurred at the interface could not be observed. The consecutive force increases and decreases in the experimental trace was a possible indication that the surrogate heads experienced several consecutive head rebounds at a rapid rate. This finding was not conclusive, however, because the high-speed videos did not have the impact interface included in the frame. Another reason for the difference in trends is the significant plastic deformation (~ 6 mm) of the leather-wood layer which dampened the impact, thereby reducing the peak force and initial slope.

The GHBMC_Saari_failON axial neck compressive force trace had a lower peak (e.g., 1.5 kN < 1.9 kN) than the GHBMC_Saari model. The former model had a lower peak force because the upper cervical spine experienced element erosion around 5 ms after head impact. The element erosion reduced the axial stiffness of the cervical spine, thereby not allowing it to sustain as much axial load at the upper cervical spine. As a result, the remainder of the cervical spine (including C7 where the force was measured) registered a lower peak force. The model configurations showcased a similar trend for the axial neck force history plots where there was an initial rise time leading to a peak force, followed by a sharp decrease, a slight increase, and then a plateau.

During the initial interval of force rise time, the cervical spine axial force increased due to the compression of the effective torso mass. The force increase continued for both model configurations until the peak force values were reached at 5.0 ms for the GHBMC_Saari model and at 5.6 ms for the GHBMC_Saari_failON model. The subsequent force decrease coincided with when the extension rotational velocity of C1 plateaued, the extension rotational velocity of C2

began to increase, and the anterior velocity of C3 began to reach a peak value. The kinematics of these specific vertebrae were investigated because C1 and C2, being the first two vertebrae of the cervical spine, experienced significant extension rotation which initiated the buckling, and C3 was the anterior-most vertebra throughout the buckling. This series of simultaneous rotations and translations at the upper-to-middle cervical spine indicated that buckling started to occur in the cervical spine. Therefore, the force decrease that occurred in the models coincided with when the upper-to-middle cervical spine experienced buckling, thereby reducing the axial stiffness of the spine, which led to a lower axial force at C7 where the force was measured. The subsequent period where the force increased coincided with when the anterior velocity of C3 began to rapidly decrease. This decrease in anterior velocity indicated that the buckling was slowing down, thereby increasing the axial stiffness of the cervical spine and increasing the measured axial force at C7.

The slopes of the initial rise times of the two GHBMC model configurations (0.5 kN/ms) had a good agreement with the reported experimental values (0.8 kN/ms $\pm$ 0.4 kN/ms). The initial peak axial force of GHBMC_Saari (1.9 kN) was equal to the average initial peak axial force of the Saari NFL specimens. The times from head impact to the point where the neck force started to increase and to the peak axial force corresponding to the model configurations were higher than the respective average experimental values. The delay values of the model configurations were higher than the experimental values because the surrogate heads could be more rigid than the GHBMC heads and therefore not experience as much elastic deformation, which would lead to faster axial force transmission to the lower cervical spine than observed in the models.

Hard Tissue Injury Risk

Hard tissue injury in GHBMC_Saari (failure OFF) was defined by the effective plastic strain reaching a value of 9.17% for trabecular bone (solid elements), and 3.43% for cortical bone (shell elements). For GHBMC_Saari_failON, hard tissue injury was identified by observing the deleted solid (trabecular) and shell elements (cortical). Figure 4-8 shows the time of hard tissue failure initiation in GHBMC_Saari_failON and Table 4-4 shows the location of hard tissue injury (e.g., vertebral body, spinous process, etc.) in GHBMC_Saari_failON. These hard tissue metrics were not extracted for GHBMC_Saari because, following the onset of first hard tissue injury, the model configuration was not a biofidelic representation of vertebral failure progression (Chapter 3).

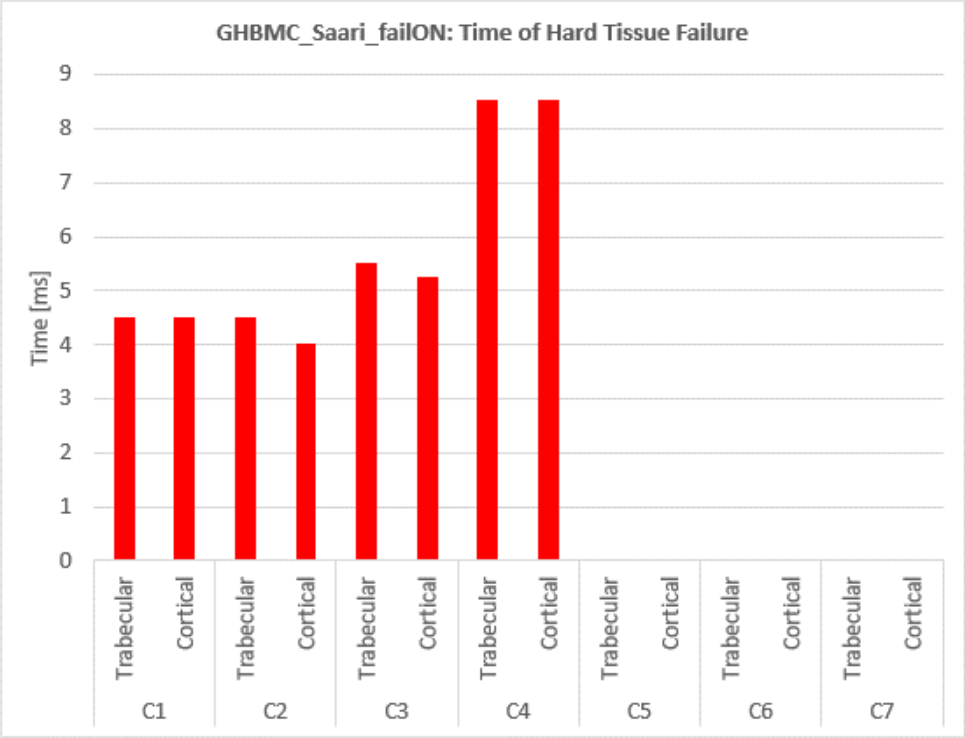

Figure 4-8: Time of hard tissue failure initiation in GHBMC_Saari_failON

Table 4-4: Location of hard tissue injury for GHBMC_Saari_failON

Location of Hard Tissue Failure		
		GHBMC_Saari_failON
C1	Trabecular	Anterior arch, posterior arch
	Cortical	Anterior arch, posterior arch
C2	Trabecular	Tip of dens, pars interarticularis, pedicles, spinous process
	Cortical	Tip of dens, pars interarticularis, pedicles, spinous process
C3	Trabecular	Pedicles, transverse processes, spinous process, vertebral body, lamina
	Cortical	Pedicles, transverse processes, spinous process, lamina, vertebral body
C4	Trabecular	Pedicles, transverse processes, lamina
	Cortical	Pedicles, transverse processes, spinous process, lamina
C5	Trabecular	
	Cortical	
C6	Trabecular	
	Cortical	
C7	Trabecular	
	Cortical	

The GHBMC model configurations had different hard tissue injury progressions because of their failure options (i.e., failure on vs. off), but both started with failure at the cortical bone of C2 4.0 ms after head impact. Following that onset of hard tissue failure, the GHBMC_Saari_failON model predicted failure at the trabecular bones of C1 and C2 as well as the cortical bone of C1 (4.5 ms), the cortical bone of C3 (5.25 ms), the trabecular bone of C3 (5.5 ms), and the trabecular and cortical

bones of C4 (8.5 ms). The GHBMC_Saari_failON model predicted earlier hard tissue failure times at the upper cervical spine than at the middle cervical spine due to the significant element erosion at the upper cervical spine. The time corresponding to the onset of hard tissue failure in both GHBMC model configurations (4.0 ms) was in good agreement with the reported experimental onset of first injury occurrence of the NFL specimens (4.9 ms $\pm$ 1.1 ms). The reported experimental hard tissue injury results indicated that C3 and C4 were the most commonly fractured vertebrae with extension avulsion fracture (associated with ALL rupture) as well as laminar and spinous process fractures being the most common injury types. Keeping the element erosion limitations associated with the failure on option in mind, GHBMC_Saari_failON produced comparable results because C3 and C4 were predicted to fracture as well. Moreover, the model predicted laminar and spinous process fractures at C3 and C4 but did not predict vertebral body fracture. The extension avulsion fractures were not predicted in the model because when the ALL ruptured (covered later in this section), the beam elements were simply deleted and did not induce stress at the vertebral body.

Soft Tissue Injury Risk

Soft tissue injury, which entailed ligament ruptures and disc avulsions, was defined the same way for both GHBMC model configurations. Ligament rupture was defined by the tensile displacement at failure, whereas disc avulsion was defined by normal failure stress. Figure 4-9 shows a bar graph comparing time of ligament failure in GHBMC_Saari and GHBMC_Saari_failON, Table 4-5 outlines which ligaments failed at every segment level from C1-C2 to C7-T1, and Table 4-6 outlines which intervertebral disc avulsed from the C2-C3 segment level to the C7-T1 segment level.

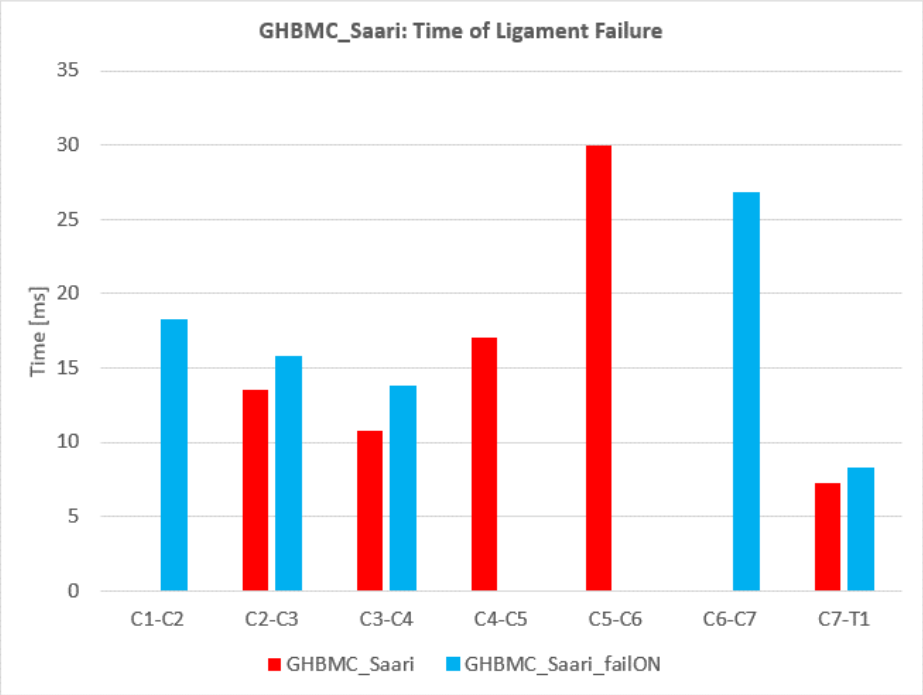

Figure 4-9: Time of ligament failure at every segment level (C1-C2 to C7-T1) of GHBMC_Saari and GHBMC_Saari_failON

Table 4-5: Outline of ligament failure at every segment level for GHBMC_Saari and GHBMC_Saari_failON

Ligament Failure		
Level	GHBMC_Saari	GHBMC_Saari_failON
C1-C2		CL
C2-C3	CL	ALL, CL
C3-C4	ALL, CL	CL
C4-C5	ALL	
C5-C6	ALL	
C6-C7		ISL
C7-T1	ISL, LF, CL, PLL	ISL

Table 4-6: Outline of disc avulsion at the segment levels C2-C3 to C7-T1 for GHBMC_Saari and GHBMC_Saari_failON

Disc Failure		
Level	GHBMC_Saari	GHBMC_Saari_failON
C2-C3		Avulsion
C3-C4		
C4-C5		
C5-C6		
C6-C7		
C7-T1	Avulsion	

For the GHBMC_Saari model configuration, the ligaments at C7-T1 failed first at 7.25 ms, followed by ligaments at C3-C4 (10.75 ms), C2-C3 (13.5 ms), C4-C5 (17 ms), and C5-C6 (30 ms). Most of the ligaments at the C7-T1 segment level ruptured due to the imposed boundary condition at T1, which restricted its motion to vertical (z) translation only. The C7 vertebra rotated in flexion throughout the loading, and as a result there was a large amount of relative rotation between T1 and C7, which imposed high levels of tension on the ligaments between those vertebrae and causing them to rupture. This significant relative rotation between the vertebrae continued until disc avulsion occurred later on at that segment level. The next segment level that experienced ligament failure (C3-C4) also had significant relative rotation between the involved vertebrae (e.g., C3 rotated in extension while C4 rotated in flexion). No ligaments were predicted to fail at the C1-C2 and C6-C7 segment levels. For the GHBMC_Saari_failON model configuration, the C7-T1 segment level, like GHBMC_Saari, experienced ligament failure first (8.25 ms after head impact), followed by C3-C4 (13.75 ms), C2-C3 (15.75 ms), C1-C2 (18.25 ms), and C6-C7 (26.75 ms). However, disc avulsion was predicted at the C2-C3 segment level (as opposed to the C7-T1 segment level). The C2-C3 disc avulsion happened because of the element erosion that occurred at the tied contact surface between the superior surface of the vertebral body of C3 and the C2-C3 disc. For this model configuration, there was no predicted ligament failure at the C4-C5 and C5-C6 segment levels.

For the GHBMC_Saari_failON model, ALL rupture at the upper cervical spine (C2-C3) occurred because C2 and C3 rotated in extension. Although the vertebrae in the middle and lower cervical spines rotated in flexion, ALL rupture was still predicted at the middle cervical spine in GHBMC_Saari. ALL rupture occurred in the middle cervical spine because the vertebrae did not rotate in flexion by the same amount, thereby causing a relative rotation between consecutive vertebrae. For example, at 10 ms after head impact, C4 had rotated in flexion by 17° while C5 rotated 29°. Due to the inferior vertebra (C5) rotating more than the superior one (C4), the ALL was subjected to tension, which ultimately led to ligament rupture.

The reported experimental soft tissue injury results indicated that the most common injury was ALL and ISL rupture at the C3-C4 and C4-C5 segment levels. The soft tissue injuries predicted by GHBMC_Saari were comparable with these experimental results as it also produced ALL rupture at the C3-C4 and C4-C5 segment levels; this was not predicted by GHBMC_Saari_failON. Moreover, the model configurations predicted CL rupture at the upper-to-middle segment levels (i.e., C1-C2, C2-C3, and C3-C4) – a soft tissue injury not observed in the specimens.

Summary of Results and Discussion for Validation Against Saari

The GHBMC_Saari and GHBMC_Saari_failON models demonstrated an abrupt increase in the buckling parameter that occurred during the 4-7 ms interval of loading. The abrupt buckling parameter increase corresponding to the models differed from the gradual and consistent increase in buckling sustained in the experimental specimens, which occurred over the entire 7 ms interval of loading. The difference in buckling could be attributed to the difference at the impact interface due to the specimens having a surrogate head that presumably did not experience as much elastic deformation, thereby transmitting the axial load faster to the cervical spine. Moreover, the significant plastic deformation of the leather-wood layer in the models dampened the impact and slowed down the axial load transfer to the cervical spine.

The upper cervical spine of the GHBMC_Saari_failON model led to more anterior displacement (~ 2 mm) than in GHBMC_Saari due to the element erosion that occurred in the former. Due to the concentrated buckling at the upper cervical spine of GHBMC_Saari_failON, the lower cervical spine did not experience as much buckling, did not register as much force/load, and did not sustain as much hard/soft tissue injury. C3 was the anterior-most vertebra (i.e., buckling transition point) throughout the buckling in both model configurations, whereas C4 was the anterior-most vertebra

throughout the buckling in the experimental specimens. It was then found that the anterior velocity of C3 was a useful tool in understanding and measuring the buckling behaviour. As the anterior velocity of C3 increased, the cervical spine experienced buckling, and the axial force measured at C7 decreased due to the reduced axial stiffness of the cervical spine. Alternatively, when the anterior velocity of C3 decreased, the buckling slowed down to an eventual 'locked' state of the cervical spine, thereby increasing the axial stiffness and the measured axial force at C7.

For the axial neck compressive force history, both GHBMC model configurations had a good agreement in terms of initial peak force as well as the slope of the initial neck force rise time. However, the delay from head impact to the initial peak axial neck force and to the onset of neck force rise time corresponding to the models were greater than those corresponding to the experiment. The longer delay observed in the model response was attributed to the significant plastic deformation of the leather-wood layer during the loading, which dampened the impact. For the head contact force history, the initial peak head contact force as well as the slope of the initial head force rise time of the models were lower than the respective experimental values. The difference of the slope and peak head contact force between the models and experiment was attributed to the surrogate head and how it experienced a different level of deformation at the impact interface relative to the model head.

Both models had good agreement with the reported experimental range of the onset time of hard tissue injury. The GHBMC_Saari_failON model predicted lamina and spinous process fractures at C3 and C4, which were reported experimentally as well. Similar to the soft tissue injuries sustained in the experimental specimens, both models predicted ALL rupture at the C3-C4 and C4-C5 segment levels. The models also predicted CL rupture across several segment levels; an injury not observed in the experimental specimens.

4.2 Model Validation Against Nightingale (1996) Experimental Results

HFI Progression

The HFI progressions of the GHBMC_Nightingale and GHBMC_Nightingale_failON model configurations from 0 ms to 15 ms are shown in Figure 4-10 and Figure 4-11, respectively.

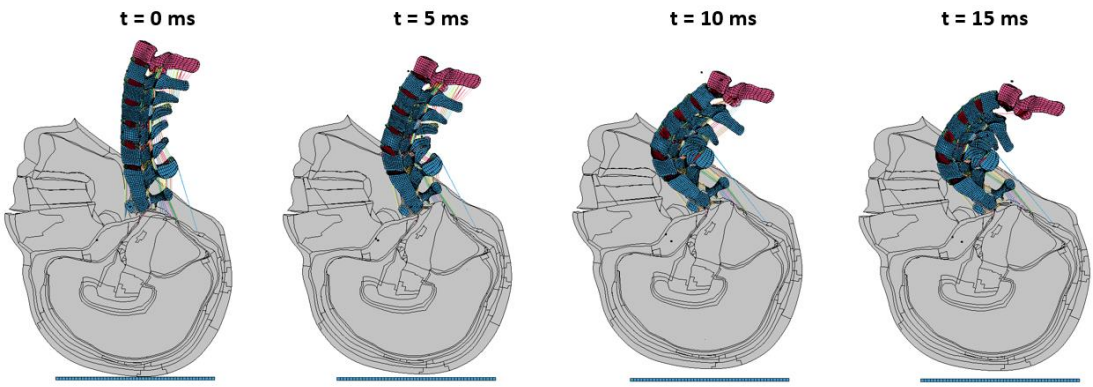

Figure 4-10: HFI progression from 0 ms to 15 ms of GHBMC_Nightingale

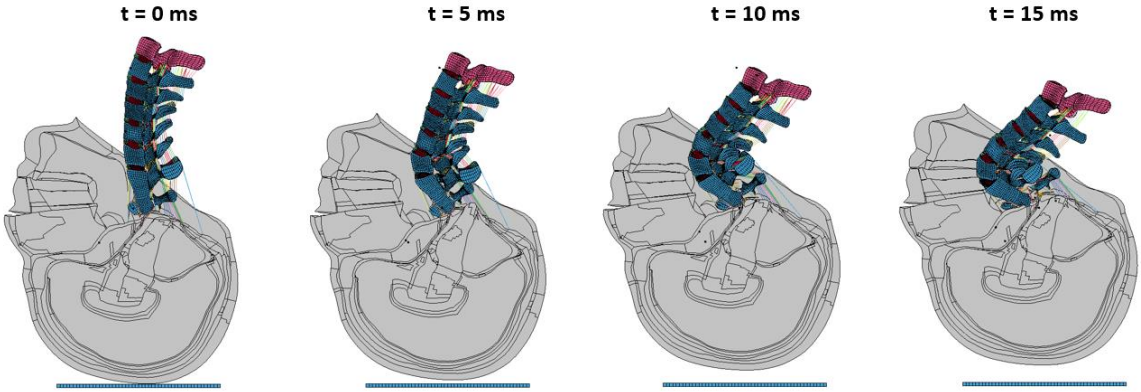

Figure 4-11: HFI progression from 0 ms to 15 ms of GHBMC_Nightingale_failON

For GHBMC_Nightingale, the general buckling response of the cervical spine entailed C1 and C2 rotating in extension, C3 initially (0-4 ms) rotating in flexion followed by extension, and C4-C7 rotating in flexion. The head started to rebound 4 ms after impact with the Teflon plate and buckling at the upper-to-middle to cervical spine initiated at 5 ms. The rebound occurred mainly due to the elastic energy stored in the head upon impact with the relatively high stiffness Teflon layer and steel backing plate. The buckling, which was concentrated (in terms of anterior displacement) at the C3 vertebra, was accentuated as the head continued to rebound vertically from 5-10 ms. During the 10-15 ms interval, the head reached its maximum rebound height and started translating back towards the impact plate while the cervical spine continued to buckle. The C7-T1 intervertebral disc experienced avulsion at 15 ms.

For GHBMC_Nightingale_failON, the general buckling response entailed C1 and C2 rotating in extension, and C3-C7 rotating in flexion. The cervical spine experienced buckling and the head started to rebound off the impact plate during the first 5 ms. The cervical buckling was accentuated from 5-10 ms as the head continued to rebound vertically away from the Teflon plate, with minimal visible displacement and deformation occurring in the middle-to-lower cervical spine (C4-C7). With hard tissue failure initiating around 5 ms, the 10 ms image of GHBMC_Nightingale_failON showed element erosion focused on the upper-to-middle cervical spine; specifically; the C2 and C3 vertebrae. Cervical spine buckling continued as the loading progressed to 15 ms following head impact, and the head continued to rebound vertically away from the impact plate as well. The head rebounded to a maximum height almost twice that sustained by the head in GHBMC_Nightingale. The significant element erosion which occurred at the upper cervical spine of GHBMC_Nightingale_failON reduced the axial stiffness of the cervical spine directly inferior to the head. As a result, there was more upper cervical spine buckling (quantified through anterior displacement) in the GHBMC_Nightingale_failON model than in the GHBMC_Nightingale model. The increased buckling in the former did not restrict the vertical motion of the head as much as in the latter, therefore the head rebounded with a greater displacement off the impact plate in GHBMC_Nightingale_failON. Moreover, due to the significant element erosion that occurred at the upper cervical spine resulted in a straighter lower cervical spine with minimal buckling in GHBMC_Nightingale_failON. Unlike the prediction in GHBMC_Nightingale, GHBMC_Nightingale_failON did not predict disc avulsion at the C7-T1 segment level.

Kinetic Results

Figure 4-12 and Figure 4-13 show the head contact force and axial neck compressive force history plots, respectively, and Table 4-7 and Table 4-8 summarize the kinetic data obtained from the history plots.

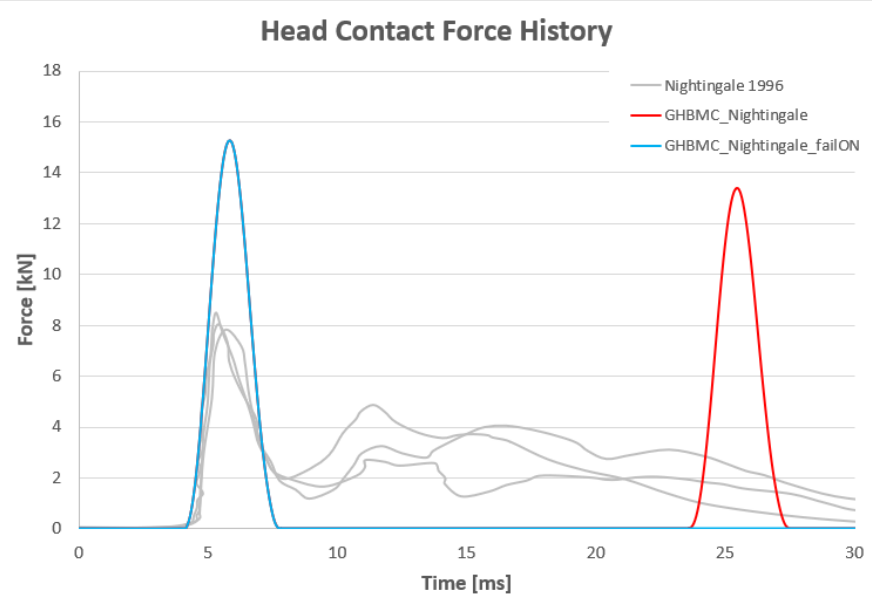

Figure 4-12: Head contact force history plot including GHBMC_Nightingale, GHBMC_Nightingale_failON, and experimental results [Nightingale et al., 1996]

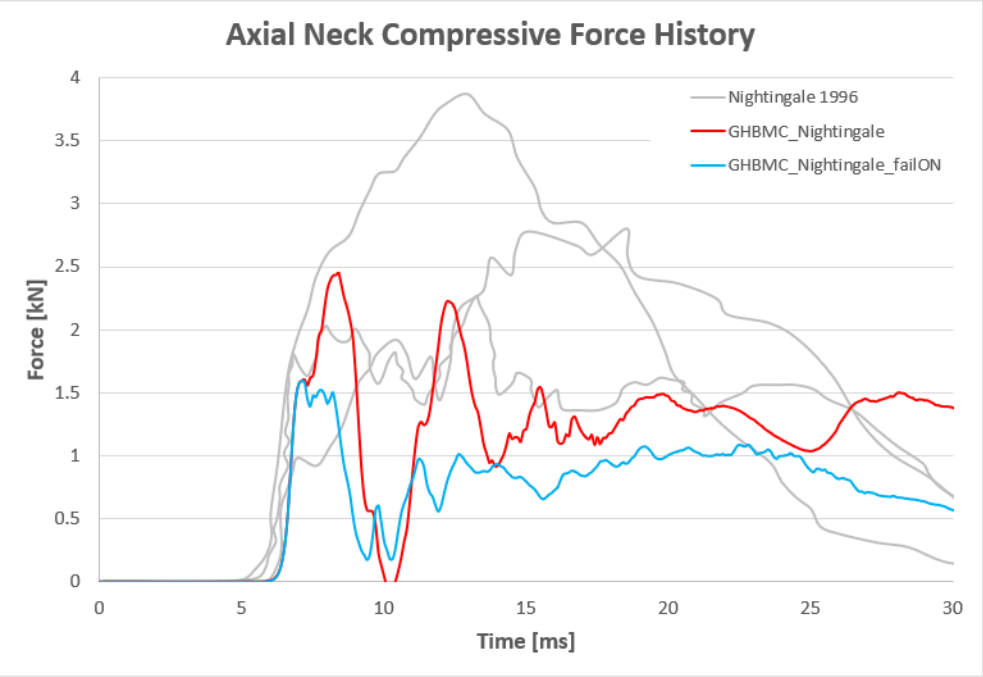

Figure 4-13: Axial neck compressive force history plot including GHBMC_Nightingale, GHBMC_Nightingale_failON, and experimental results [Nightingale et al., 1996]

Table 4-7: Head contact force metrics for GHBMC_Nightingale, GHBMC_Nightingale_failON, Nightingale specimens, and Nightingale average response

Head Contact Force Metrics		
	Initial peak head contact force (kN)	Slope of initial head contact force rise time (kN/ms)
GHBMC Model		
GHBMC_Nightingale	15.2	9.4
GHBMC_Nightingale_failON	15.2	9.4
Nightingale (1996)		
N22	8.0	10.0
N24	8.5	11.2
N26	7.8	10.3
Average	8.1	10.5

Table 4-8: Axial neck compressive force metrics for GHBMC_Nightingale, GHBMC_Nightingale_failON, Nightingale specimens, and Nightingale average response

Axial Neck Compressive Force Metrics				
	Initial peak axial force (kN)	Slope of initial neck force rise time (kN/ms)	Time from head impact to initial peak axial neck force (ms)	Time from head impact to neck force rise time (ms)
GHBMC Model				
GHBMC_Nightingale	2.1	1.6	4.3	1.9
GHBMC_Nightingale_failON	1.6	1.6	3.1	1.9
Nightingale (1996)				
N22	2.0	1.0	5.6	1.6
N24	1.8	2.0	2.2	0.9
N26	3.9	1.5	8.2	1.3
Average	2.6	1.5	5.3	1.3

Both GHBMC model configurations had the same slope of the initial head contact force rise time (9.4 kN/ms) and initial peak head contact force (15.2 kN). Due to the head rebound that occurred in the GHBMC model configurations, the model head contact force traces went to zero after the initial peak force was reached. The second peak observed in GHBMC_Nightingale (red curve) corresponded to when the head fell back onto the Teflon plate. A second peak in the GHBMC_Nightingale_failON head contact force trace was not observed as the head did not make second contact with the impact plate within the given loading interval (30 ms).

The initial peak head contact force corresponding to the models (15.2 kN) was greater than average (8.1 kN $\pm$ 0.4 kN) experimental results. The slope of the initial head contact force rise time, as predicted by the GHBMC model configurations (9.4 kN/ms), was slightly less than the individual and average (10.5 kN/ms $\pm$ 0.6 kN/ms) experimental results. Head rebound was not observed in

the experimental curves as there was a non-zero plateau following the initial peak. Although the experimental results did not report whether the experimental specimens rebounded off the plate during testing, the kinetic results suggested that rebound did not occur. The similar slopes of the initial head contact force rise time between the models and the experiment indicated a similar level of stiffness at the impact interfaces. However, the significantly higher initial peak forces associated with the models suggested the presence of high elastic energy, which resulted in the model noticeably rebounding off the impact plate.

For the axial neck compressive force history traces of the GHBMC model configurations, the same trend was observed: an initial peak, followed by a sharp force decrease, a second force increase, and finally a plateau. The mechanics of the cervical spine that defined this trend were identical to the mechanics observed in the validation of GHBMC_Saari and was explained in section 3.2. The initial peak axial neck force of GHBMC_Nightingale was greater than that of GHBMC_Nightingale_failON (2.1 kN > 1.6 kN); however, both models have the same slope of the initial neck force rise time (1.6 kN/ms). The rate of force transmission was the same for both models until 3 ms following head impact where element erosion initiated at the cortical bone of C2 in the GHBMC_Nightingale_failON model. The element erosion at the upper cervical spine of that model reduced the axial stiffness of the cervical spine and cut off the load transmission to C7 where the axial force was measured. As a result, the force decreased in the model following that point but continued to increase in GHBMC_Nightingale due to the absence of element erosion. Furthermore, the time from head impact to the initial peak axial neck force was expectedly less for the GHBMC_Nightingale_failON model due to the lower initial peak force. Both models, however, had the same time from head impact to the onset of the neck force rise time as this preceded the initiation of element erosion.

Specimen N26 did not experience any injury, therefore the axial neck compressive force trace corresponding to the specimen did not have the same trend compared to specimens N22 and N24, and as a result had a noticeably higher initial peak and a greater time from head impact to that initial peak. The absence of injury from specimen N26 was important to consider as it increased the average experimental results for those metrics. The initial peak axial neck force of the GHBMC model configurations (2.1 kN and 1.6 kN) had a good agreement with the average experimental value (2.6 kN $\pm$ 1.2 kN). The slope of the initial neck force rise time of the models (1.6 kN/ms)

had a good agreement with the respective average experimental results (1.5 kN/ms ± 0.5 kN/ms). The delay between head impact and the initial rise in peak axial neck force of the models (4.3 ms and 3.1 ms) had a good agreement with the average result of all three experimental specimens (5.3 ms ± 3 ms). Moreover, the delay from head impact to onset of axial neck force load-up of the models (1.9 ms) was slightly greater than the average experimental results (1.3 ms ± 0.4 ms).

Hard Tissue Injury Risk

Figure 4-14 shows the time of hard tissue failure initiation in GHBMC_Nightingale_failON and Table 4-9 shows the location of hard tissue injury (e.g., vertebral body, spinous process, etc.) in GHBMC_Nightingale_failON. These hard tissue metrics were not extracted for GHBMC_Nightingale because following the onset of first hard tissue injury, the model configuration was not a biofidelic representation of vertebral failure progression (Chapter 3).

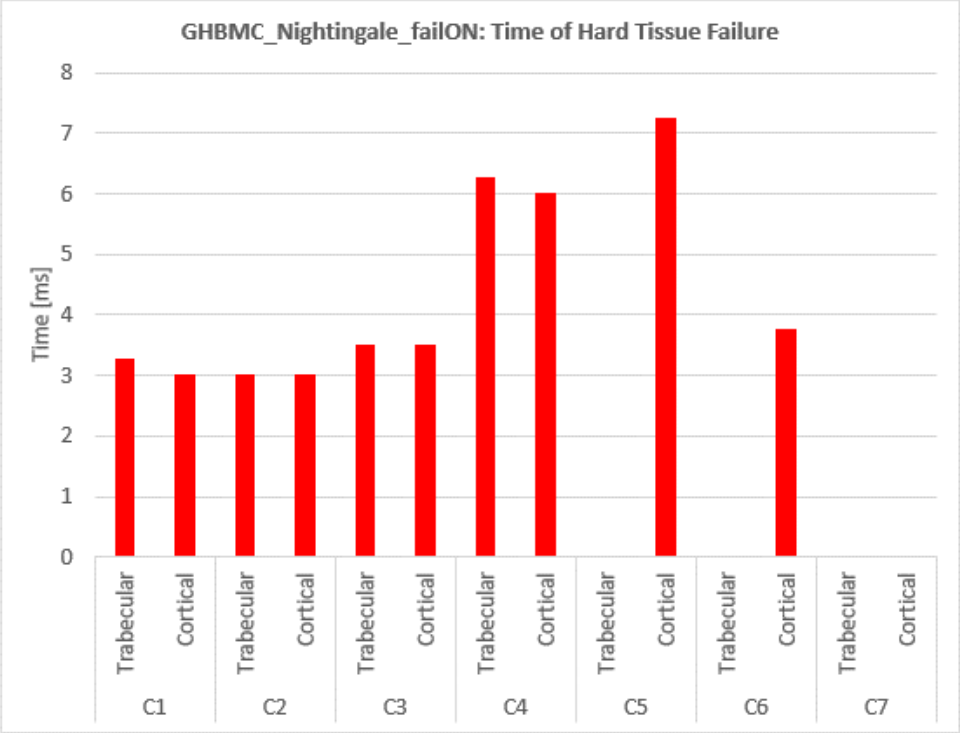

Figure 4-14: Onset times of hard tissue failure for GHBMC_Nightingale and GHBMC_Nightingale_failON

Table 4-9: Location of hard tissue failure of GHBMC_Nightingale and GHBMC_Nightingale_failON

Location of Hard Tissue Failure		
		GHBMC_Nightingale_failON
C1	Trabecular	Anterior arch
	Cortical	Anterior arch, posterior arch
C2	Trabecular	Tip of dens, transverse process, pedicles
	Cortical	Tip of dens, pedicles, pars interarticularis, transverse processes, spinous process
C3	Trabecular	Pedicles, transverse processes, spinous process
	Cortical	Pedicles, transverse processes, spinous process
C4	Trabecular	Pedicles, transverse processes
	Cortical	Pedicles
C5	Trabecular	
	Cortical	Pedicles
C6	Trabecular	
	Cortical	Right pedicle
C7	Trabecular	
	Cortical	

Similar to the analysis for the validation against Saari (section 4.1), the GHBMC model configurations had different hard tissue injury progressions because of their failure options, but both had the same onset of hard tissue failure at the cortical bone of C2 3.0 ms after head impact. Following the onset of hard tissue failure, the GHBMC_Nightingale_failON model predicted failure at the cortical bone of C1 (3.0 ms), the trabecular bone of C2 (3.0 ms), the trabecular bone of C1 (3.25 ms), the trabecular and cortical bones of C3 (3.5 ms), the cortical bone of C6 (3.75 ms), the trabecular bone of C4 (6.25 ms), and the cortical bone of C5 (7.25 ms). The

GHBMC_Nightingale_failON model predicted earlier hard tissue failure times at the upper cervical spine than at the middle-to-lower cervical spine due to the element erosion at the upper cervical spine.

The time corresponding to first hard tissue injury in the models (3.0 ms) was in between the reported experimental times to injury (2.2 ms for specimen N24 and 6.5 ms for specimen N22). Moreover, keeping the limitations of element erosion in mind, the hard tissue injuries predicted by GHBMC_Nightingale_failON were comparable with the reported experimental injuries as the experimental specimens predominantly had C1 comminuted fractures as well as C2 pedicle fractures (Hangman's).

Soft Tissue Injury Risk

The soft tissue injury metrics that were extracted from the GHBMC model configurations were the onset times of ligament failure at all the segment levels (i.e., C1-C2 until C7-T1) and which intervertebral discs experienced avulsion at the C2-C3 to C7-T1 segment levels. Figure 4-15 shows the onset times of ligament failure, Table 4-10 summarizes the location of ligament failure (i.e., which segment level), and Table 4-11 summarizes the location of disc avulsion (i.e. segment level).

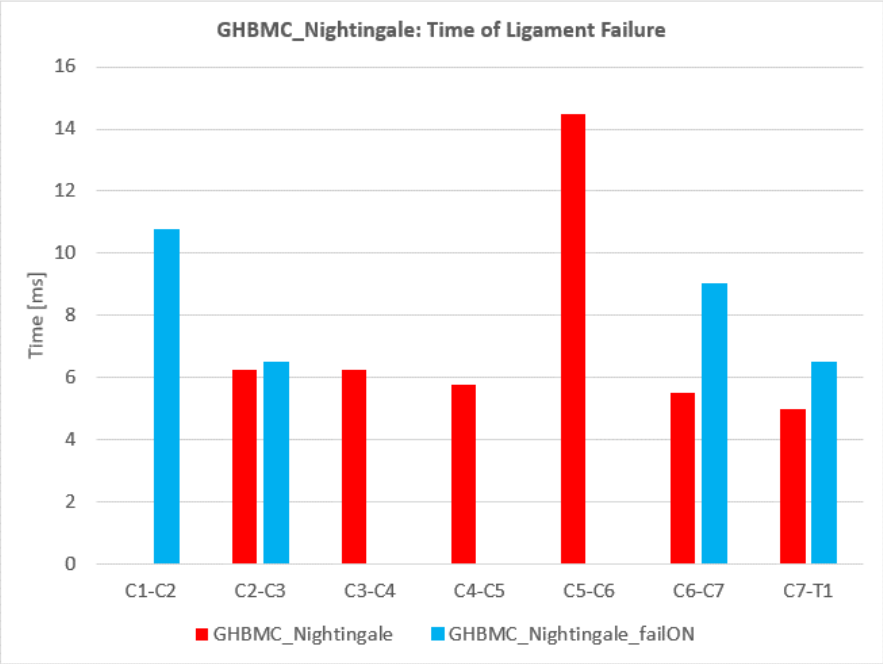

Figure 4-15: Onset times of ligament failure at every segment level for GHBMC_Nightingale and GHBMC_Nightingale_failON

Table 4-10: Location of ligament failure of GHBMC_Nightingale and GHBMC_Nightingale_failON

Ligament Failure		
Level	GHBMC_Nightingale	GHBMC_Nightingale_failON
C1-C2		CL
C2-C3	ALL, CL	ALL, CL
C3-C4	ALL, CL	
C4-C5	ALL	
C5-C6	ALL	
C6-C7	ISL	ISL
C7-T1	ISL, LF, CL, PLL	ISL, LF, CL, PLL

Table 4-11: Location of disc failure (avulsion) of GHBMC_Nightingale and GHBMC_Nightingale_failON

Disc Failure		
Level	GHBMC_Nightingale	GHBMC_Nightingale_failON
C2-C3		
C3-C4		
C4-C5		
C5-C6		
C6-C7		
C7-T1	Avulsion	

Similar to hard tissue injury, the sequence of soft tissue injury was different for each of the two model configurations due to the differing failure options embedded. However, both model configurations experienced the first ligament failure at the C7-T1 segment level, with

GHBMC_Nightingale predicting an earlier failure time (e.g., 5 ms < 6.5 ms). The GHBMC_Nightingale_failON model predicted a later ligament failure time for the C7-T1 segment level because of the lower load transmission to the lower cervical spine due to the significant element erosion at the upper cervical spine (specifically C2). Therefore, the C7-T1 segment level was more intact in that model and disc avulsion was not predicted. Moreover, the model also predicted a later ligament failure time at the C6-C7 segment level (lower cervical spine) for the same aforementioned reason. The model did not predict ligament failure at the C3-C4 to C5-C6 segment levels. However, due to the element erosion at the upper cervical spine, the model predicted ligament failure at the C1-C2 segment level. The GHBMC_Nightingale model, on the other hand, predicted ligament failure at all segment levels except for C1-C2. The model predicted ALL rupture at the C2-C3 to C5-C6 segment levels, and ISL rupture at the C6-C7 and C7-T1 segment levels. Additionally, the model predicted CL rupture at the C2-C3 and C3-C4 segment levels. The cervical spine mechanism responsible for ALL rupture was explained in GHBMC_Saari (section 3.3): when considering two adjacent vertebrae (e.g., C3 and C4), ALL rupture occurred either when the superior vertebra rotated with more flexion than the inferior vertebra (C3-C4 to C5-C6), or when the superior vertebra rotated in extension while the inferior one rotated in flexion (C2-C3). These relative motions acted to increase the anterior gap between the adjacent vertebral bodies, thereby imposing tension on the ALL and rupturing them once the critical tension value was reached. Alternatively, also when considering two adjacent vertebrae, ISL rupture occurred when the opposite motions took place. For example, ISL rupture occurred at the C6-C7 segment level because C6 (the superior vertebra) had more flexion rotation than C7 (the inferior vertebra); at 10 ms, C6 rotated 28° while C7 rotated 15°. ISL rupture occurred at the C7-T1 segment level of both models because C7 rotated in flexion and T1 did not rotate in flexion or extension (due to the imposed boundary condition).

Summary of Results and Discussion for Validation Against Nightingale

The GHBMC model configurations exhibited head rebound during HFI loading. The head in GHBMC_Nightingale_failON experienced greater rebound off the impact plate because of the significant element erosion that occurred at the C2 vertebra. The element erosion in GHBMC_Nightingale_failON reduced the axial stiffness of the upper-to-middle cervical spine, thereby increasing the extension rotation of C1 and C2 (relative to GHBMC_Nightingale) and

providing greater translational freedom for the head to rebound off the impact plate. Unlike the analysis for GHBMC_Saari (section 4.1), head rebound was not eliminated from GHBMC_Nightingale because the Nightingale impact interface details (unembalmed head with flesh and a 3 mm Teflon impact surface) were completely modelled and represented in GHBMC_Nightingale.

The element erosion reduced axial force transmission to the lower cervical spine, and as a result the lower cervical spine registered a lower initial peak axial force, exhibited less deformation, and sustained fewer hard and soft tissue injuries. For the comparison of the model and experimental axial neck compressive force history plots, there was a good agreement between the initial peak axial force, the slope of the initial neck force rise time, and the time from head impact to the initial peak axial neck force. The time from head impact to the onset of neck force rise time corresponding to the models was greater than the respective experimental values. It should be noted that the experimental values that were considered for analysis and comparison were those corresponding to specimens N22 and N24; specimen N26 did not experience injury and as a result did not exhibit a similar trend in the axial neck compressive force. For the head contact force history plots, there was good agreement between the models and the experimental values in terms of the slope of the initial head contact force rise time. The initial peak head contact force of the models, however, was significantly greater than the experimental values. The greater peak head contact force corresponding to the models indicated higher elastic energy at the interface in the models. Moreover, due to the head rebound that occurred in the models and not in the experiments, the model kinetic response was different than the experimental kinetic response as the model head contact force trace went to zero following head impact as the head rebounded off the impact plate.

There was good agreement between the models and the experiment in terms of hard tissue injury because the models predicted the onset of first hard tissue injury to be 3 ms, which was between the reported experimental times of 2.2 ms and 6.5 ms. Furthermore, the GHBMC_Nightingale_failON model predicted C1 and C2 fracture as well as Hangman's fracture as sustained in the experimental specimens. Soft tissue injuries were not reported in the experimental results, and both models had different predicted outcomes. The GHBMC_Nightingale_failON model had less middle-to-lower cervical spine ligament failure (due

to the element erosion at the upper cervical spine) and did not predict disc avulsion at the C7-T1 segment level as was the case for the GHBMC_Nightingale model.

4.3 Sensitivity Study Results of Head-First Impact Parameters

All the sensitivity study simulations were run with hard tissue failure turned off. The absence of element erosion in the failure off option (upper bound of bone fracture prediction) did not significantly affect the kinematics of the cervical spine during the time interval of interest (0-7 ms). However, the failure off option could not be used to predict hard tissue failure after the first element (trabecular or cortical) reached the respective failure effective plastic strain value. Alternatively with upper cervical spine element erosion in the failure on option (lower bound of bone injury prediction), the kinematic response of the cervical spine was affected such that the middle-to-lower cervical spine remained relatively intact, and experienced less anterior displacement and sustained fewer soft tissue injuries following the onset of hard tissue injury. Given the importance of the kinematic results in analyzing the kinetic results and hard and soft tissue injury outcomes, the hard tissue failure off option was implemented in the sensitivity study simulations.

Similar to the analysis presented in the model validation, the HFI progressions, kinematic, kinetic, and injury results were extracted from all the sensitivity study simulations in addition to the baseline model. As previously discussed, the kinematic results described and quantified the buckling behaviour of the cervical spine, and the kinetic results described the head contact and axial neck compressive force vs. time response of the models. Given that failure was turned off for the simulations, hard tissue failure prediction following the onset of injury was not presented as the failure option is not a biofidelic representation of injury progression post the first occurrence of fracture. As a result, the hard tissue injury results entailed identifying the vertebra, bone type, and vertebral region where injury first occurred (e.g., dens of cortical bone of C2), and presenting the effective plastic strain contours of that vertebra at the onset of hard tissue injury. Soft tissue injury results entailed identifying which ligaments failed and discs avulsed (e.g., ALL rupture at C3-C4 segment level).

4.3.1 Initial Cervical Spine Curvature: Results and Discussion

HFI Progression

The HFI progressions from 0-15 ms, depicted through the mid-sagittal view of the head and cervical spine impacting the plate, for the baseline, Posture2_C7_20°, Posture3_C7_25°, and Posture4_C7_30° models are shown in Figure 4-16 Figure 4-19, respectively.

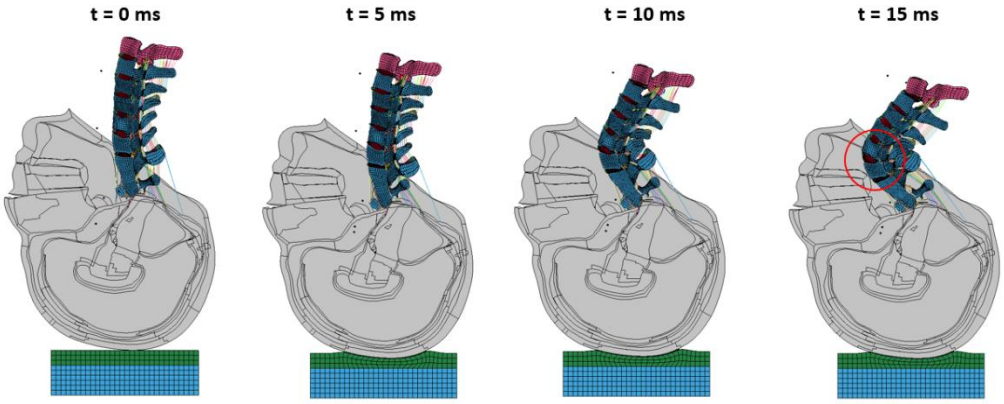

Figure 4-16: HFI progression from 0-15 ms of Baseline model with buckling transition point (C3) circled in red

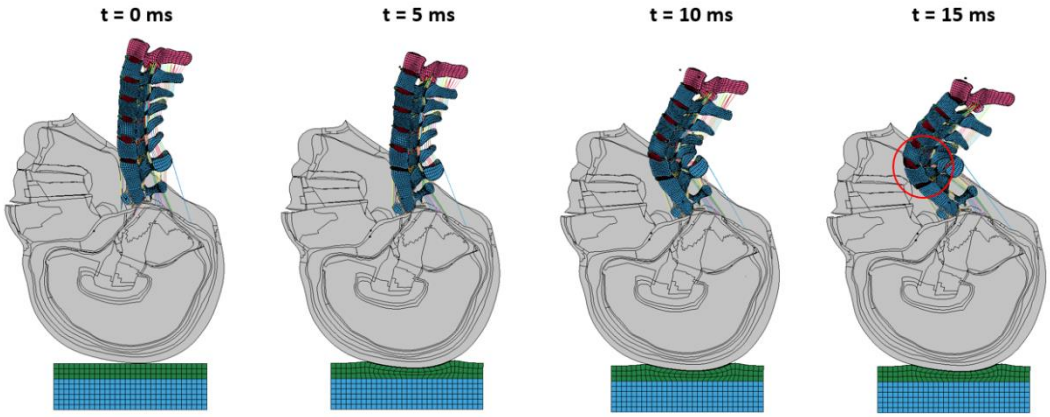

Figure 4-17: HFI progression from 0-15 ms of Posture2_C7_20° model with buckling transition point (C3) circled in red

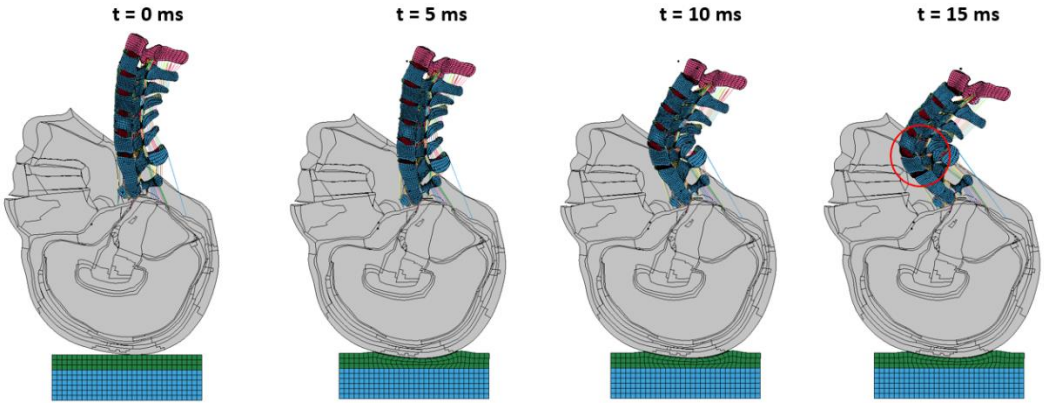

Figure 4-18: HFI progression from 0-15 ms of Posture3_C7_25° model with buckling transition point (C3) circled in red

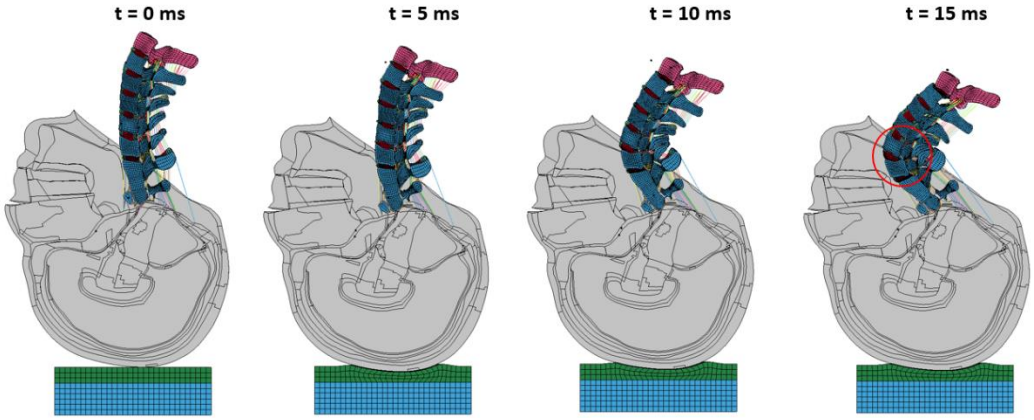

Figure 4-19: HFI progression from 0-15 ms of Posture4_C7_30° model with buckling transition point (C3) circled in red

The HFI progression of the baseline model (also Figure 4-3) showed that from 0-5 ms, the cervical spine experienced little to no deformation while the head plastically deformed the leather-wood layer in the vertical direction. The other GHBMC model configurations experienced minimal cervical spine deformation as well as plastic deformation of the leather-wood layer. During the time interval of 5-10 ms, cervical spine buckling, concentrated at the C3 vertebra in terms of anterior displacement, was observed as the head was restricted by the leather-wood layer for all model configurations. During the 10-15 ms time interval, cervical spine buckling continued and relative deformation at the C7-T1 segment level was observed. All models demonstrated the same general kinematic cervical spine response: C1-C3 rotated in extension (with C3 initially, but very

briefly, rotating in flexion followed by extension), and C4-C7 rotated in flexion. Increasing the cervical spine curvature had no visual (qualitative) effect on the general kinematic response of the cervical spine throughout HFI loading.

Kinematic Results

As previously discussed in section 4.1, the cervical spine of the baseline model experienced negligible anterior displacement during the first 4 ms. The other model configurations also experienced a similar initial response. Moreover, the majority of the buckling occurred during the last 3 ms of loading (i.e., 4-7 ms) for all models. Increasing the cervical spine curvature had a negligible effect on the overall buckling response of the cervical spine; all models exhibited relatively similar buckling throughout the 7 ms of loading (buckling parameter increased by 15.7% for all models). Increasing the cervical spine curvature did not significantly affect the kinematic response because the cervical spine curvature change was more concentrated at the lower cervical spine (i.e., varying the C7 angle) and therefore the overall cervical spine kinematic response was unaffected by the change in curvature.

Kinetic Results

Figure 4-20 and Figure 4-21 show the head contact force and axial compressive neck force histories, respectively. Table 4-12 summarizes the axial compressive neck force metrics obtained from the axial neck force history plots.

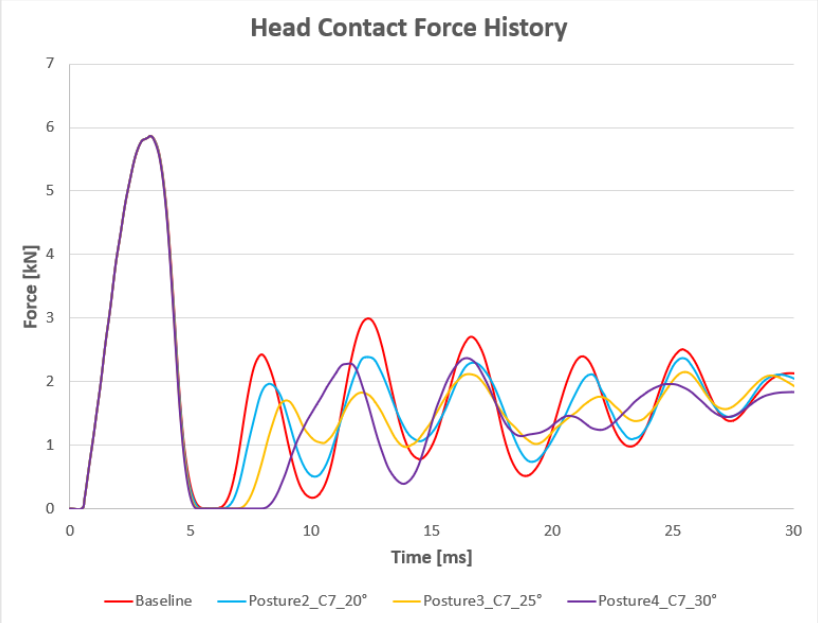

Figure 4-20: Head contact force history plots of the baseline, Posture2_C7_20°, Posture3_C7_25°, Posture4_C7_30° models

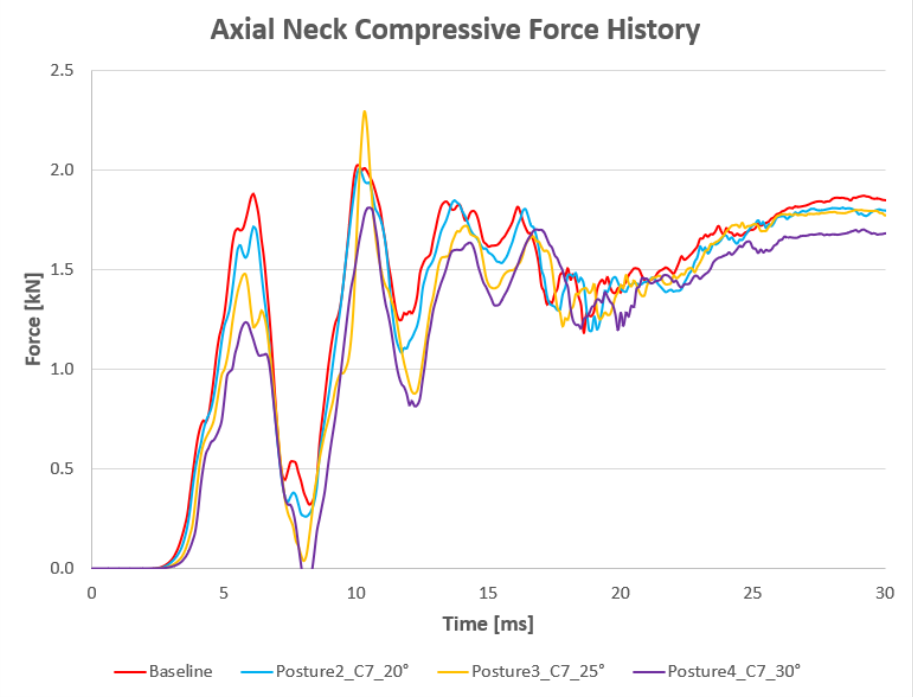

Figure 4-21: Axial neck compressive force history plots of baseline, Posture2_C7_20°, Posture3_C7_25°, Posture4_C7_30° models

Table 4-12: Axial neck compressive force metrics for the baseline, Posture2_C7_20°, Posture3_C7_25°, and Posture4_C7_30° models

Axial Neck Compressive Force Metrics				
GHBMC Model	Initial peak axial force (kN)	Slope of initial neck force rise time (kN/ms)	Time from head impact to initial peak axial neck force (ms)	Time from head impact to neck force rise time (ms)
Baseline	1.9	0.5	5.6	2.1
Posture2_C7_20°	1.7	0.5	5.6	2.2
Posture3_C7_25°	1.5	0.5	5.3	2.3
Posture4_C7_30°	1.2	0.5	5.3	2.5

The initial cervical spine posture had no effect on the initial peak head contact force nor on the slope of the initial head contact force rise time. However, the head rebound (corresponding to the period where the head contact force is 0 kN) time period increased as the cervical spine curvature increased. The head rebound period increased because as the curvature increased, the axial force from the cervical spine (particularly T1 where the effective torso mass is) to the head decreased. The reduced axial force associated with the higher cervical curvature imposed less compression on the head; therefore, the head rebound increased.

As the cervical spine curvature increased, the initial peak axial force decreased. The slope of the initial neck force rise time of all the GHBMC model configurations (0.5 kN/ms) was unaffected by the change in cervical spine curvature. The decrease in the initial peak axial force was associated with the relatively lower axial stiffness at the lower cervical spine. The stiffness was reduced because of the increased curvature, which in turn increased the lateral (x) component of the force at C7 and reduced the axial component. The slope of the initial neck force rise time was unaffected because the change in curvature at the upper-to-middle cervical spine was minimal, thereby not impeding or influencing the rate of axial load transfer to C7. The time from head impact to initial peak axial neck force of the GHBMC model configurations generally decreased as the cervical spine curvature increased. The times corresponding to the baseline model and Posture2_C7_20° model were equal (5.6 ms), and the same was true for the Posture3_C7_25° and Posture4_C7_30° models (5.3 ms). The time from head impact to neck force rise time of the GHBMC model configurations increased as the cervical spine curvature increased. The delay increased because of the reduced rate of axial load transmission to the lower cervical spine due to the reduced axial stiffness associated with the higher curvatures. Finally, the same trend was observed in the axial neck compressive force history plots of all the GHBMC model configurations. The trend involved an increase in force until the initial peak axial neck force,

followed by a sharp force decrease, a sharp force increase, and finally a plateau around 1.5 kN. This trend was previously explained in section 4.1.

Hard Tissue Injury Risk

The onset of failure for all GHBMC model configurations, including the baseline model, was at the cortical bone of C2 located at the tip of the dens. Hard tissue injury initiated at the tip of the dens due to the impact between the tip and base of the skull resulting from the early extension rotation of C2. This is an artifact of the model as this injury has not been reported in epidemiological studies. Figure 4-22 shows the effective plastic strain fringe plots of the cortical bone of C2 at the onset of injury of all model configurations alongside the baseline model for reference.

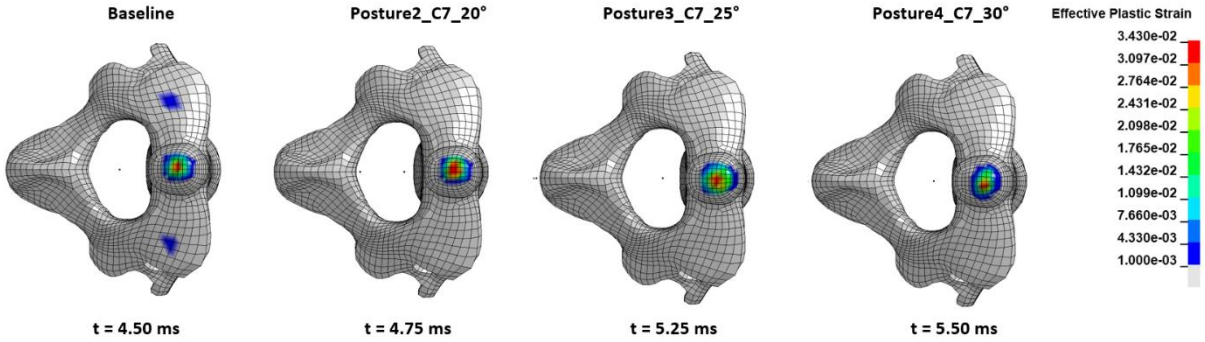

Figure 4-22: Effective plastic strain fringe plots (superior view) of Baseline, Posture2_C7_20°, Posture3_C7_25°, and Posture4_C7_30° models

As the C7 angle increased, the onset of hard tissue injury was delayed. Hard tissue injury was delayed due to the reduced axial load associated with the higher cervical spine curvature (Figure 4-21). The injury location (i.e., tip of the dens of the cortical bone of C2) was not affected by the increased cervical spine curvature because the increased curvature was primarily concentrated at the lower cervical spine (e.g., C7).

Soft Tissue Injury Risk

Figure 4-23 shows the times corresponding to ligament failure initiation for the models as the cervical spine curvature was increased, and Table 4-13 outlines the location of ligament failure in addition to which ligaments failed.

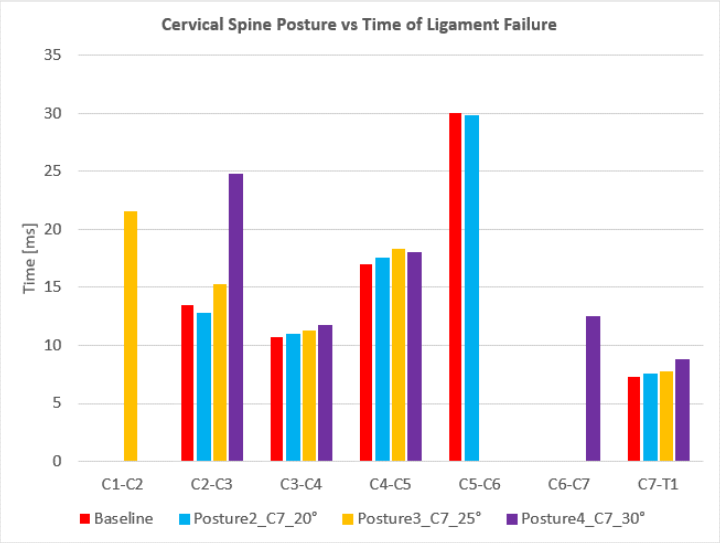

Figure 4-23: Onset times of ligament failure at every segment level for baseline, Posture Posture2_C7_20°, Posture3_C7_25°, and Posture4_C7_30° models

Table 4-13: Location of ligament failure of baseline, Posture2_C7_20°, Posture3_C7_25°, and Posture4_C7_30° models

Ligament Failure				
Level	Baseline	Posture2_C7_20°	Posture3_C7_25°	Posture4_C7_30°
C1-C2			ISL	
C2-C3	CL	CL	CL	CL
C3-C4	ALL, CL	ALL, CL	ALL, CL	ALL, CL
C4-C5	ALL	ALL	ALL	ALL
C5-C6	ALL	ALL		
C6-C7				ISL
C7-T1	ISL, LF, CL, PLL	ISL, LF, CL, PLL	ISL, LF, CL, PLL	ISL, LF, CL, PLL

As the cervical spine curvature increased, the ligament failure initiation time increased at the C2-C3, C3-C4, C4-C5, and C7-T1 segment levels. Additionally, the models with the highest curvatures (Posture3_C7_25° and Posture4_C7_30°) did not predict injury at the C5-C6 segment level. The Posture3_C7_25° model was the only one that predicted ligament failure (ISL) at the C1-C2 segment level. ISL failure was predicted at that segment level because the relative extension

rotation between C1 and C2 was the greatest in that model. Similarly, the Posture4_C7_30° model was the only one that predicted ligament failure (ISL) at the C6-C7 segment level. For the segment levels where all of the models predicted ligament failure, the delayed onset of soft tissue injury was due to the reduced axial stiffness associated with the greater curvature, which led to a decreased axial force and level of injury. However, all of the models predicted the same ligaments (ALL, PLL, ISL, CL, and LF) to fail at these segment levels (C2-C3 to C4-C5, and C7-T1). Additionally, all models predicted disc avulsion at the C7-T1 segment level.

Summary of Results and Discussion for Cervical Spine Curvature Variation

As the cervical spine curvature increased, the buckling response (as quantified by anterior displacement and the buckling parameter) was not affected; all models experienced negligible cervical deformation during the first 4 ms of loading and exhibited buckling during the 4-7 ms interval. Moreover, the increased cervical spine curvature had no effect on the initial peak head contact force and the slope of the initial head contact force rise time. However, the head rebound period (associated with when the head contact force was zero following the initial peak) increased as the cervical spine curvature increased. The head rebound increased because of the increased translational freedom the head experienced as a result of the increased curvature. The increased curvature meant that the vertebrae were more anterior, which allowed the head to rebound more in the inferior direction. Moreover, due to the increased cervical spine curvature, the initial peak axial neck force decreased. The axial neck force decreased due to the reduced axial stiffness of the lower cervical spine associated with the increased curvature. The reduced axial load associated with the higher cervical spine curvature delayed the onset of hard and soft tissue injury in the vertebrae.

4.3.2 Impact Velocity: Results and Discussion

HFI Progression

The HFI progressions from 0-15 ms, depicted through the mid-sagittal view of the head and cervical spine impacting the plate, for the Impact_velocity_1m/s, Impact_velocity_2m/s, Impact_velocity_4m/s, and Impact_velocity_5m/s models are shown in Figure 4-24 -Figure ***4-27***, respectively.

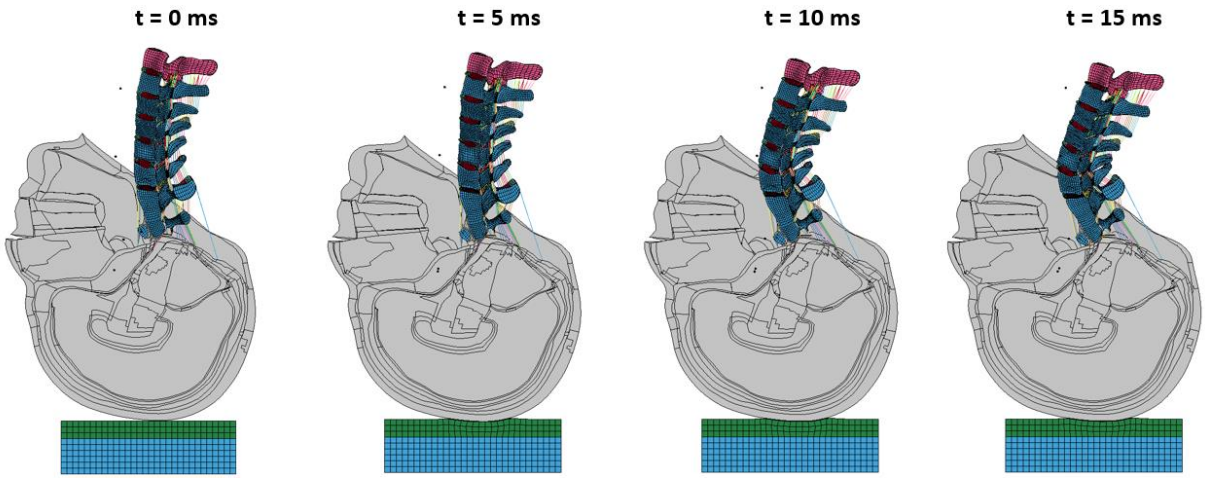

Figure 4-24: HFI progression from 0-15 ms of Impact_velocity_1m/s model

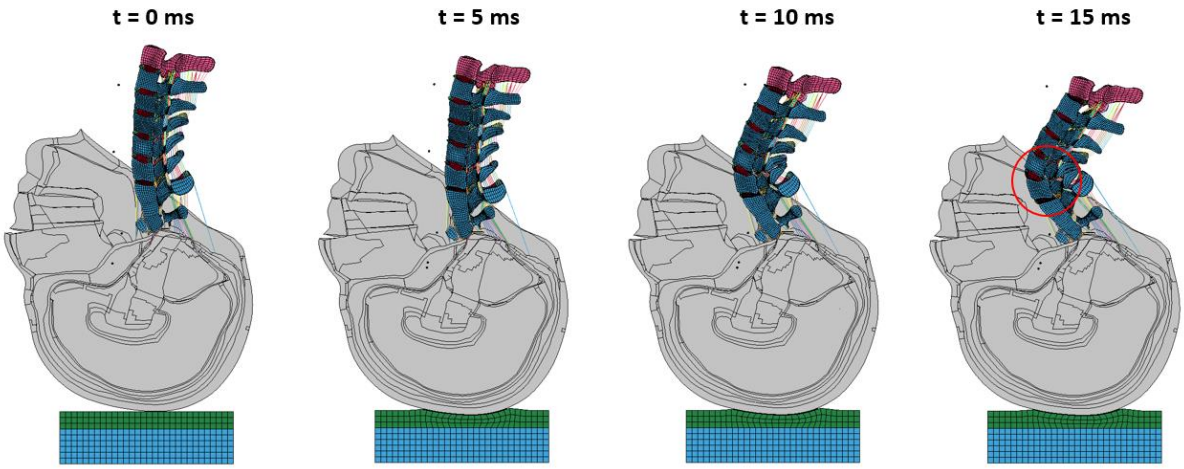

Figure 4-25: HFI progression from 0-15 ms of Impact_velocity_2m/s model with buckling transition point (C3) circled in red

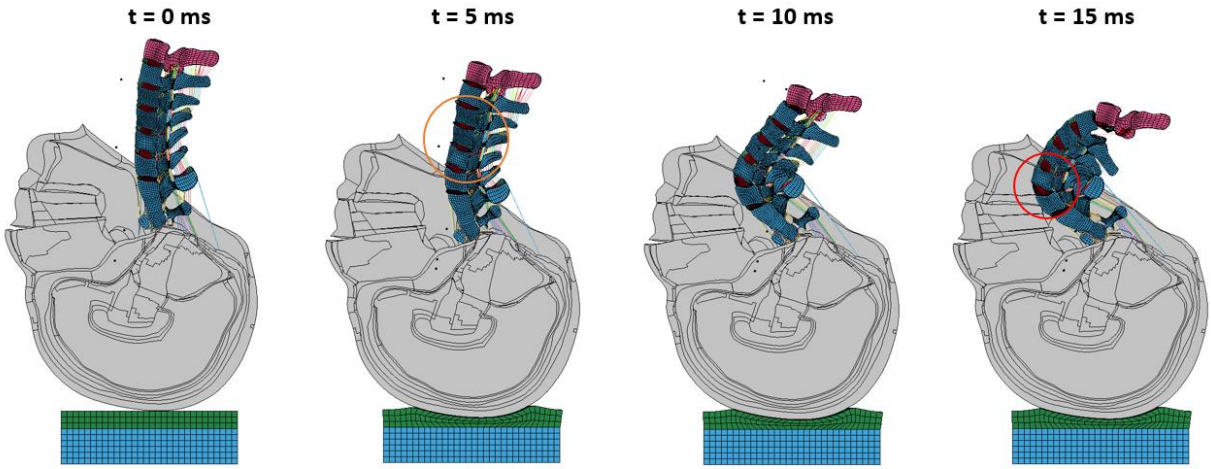

Figure 4-26: HFI progression from 0-15 ms of Impact_velocity_4m/s model with s-shape buckling mode circled in orange and buckling transition point (C4) circled in red

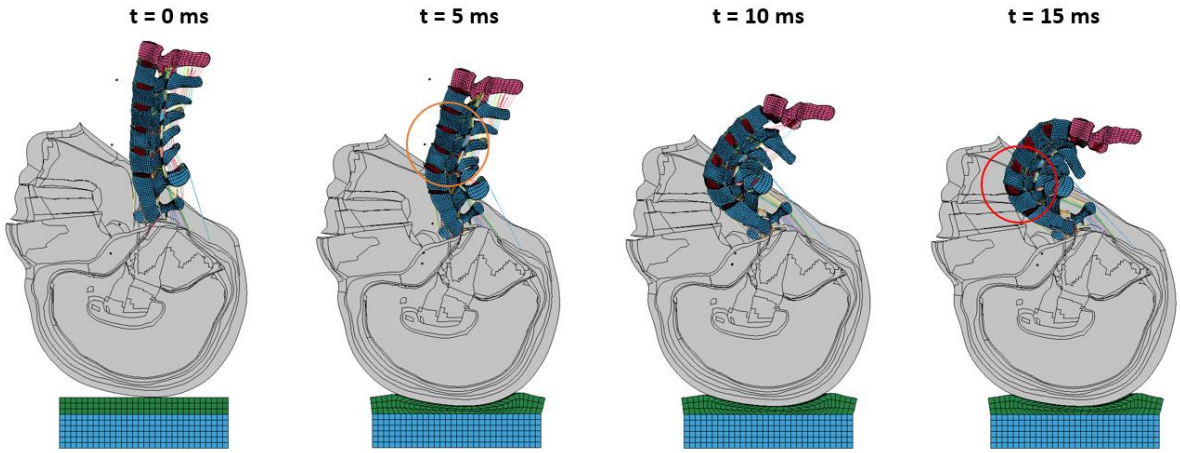

Figure 4-27: HFI progression from 0-15 ms of Impact_velocity_5m/s model with s-shape buckling mode circled in orange and buckling transition point (C4) circled in red

As the impact velocity increased, the buckling (e.g., anterior displacement) of the cervical spine and the plastic deformation of the leather-wood layer increased. When the impact velocity was 1 m/s (e.g., Impact_velocity_1m/s), the cervical spine experienced very minimal anterior displacement around the C3 vertebra. When the impact velocity was increased to 2 m/s, the cervical spine buckling became visually more noticeable around the C3-C4 segment level 10 ms after head impact. The HFI progression of the baseline model, with an impact velocity of 2.75 m/s, has been described in subsection 4.3.1. When the impact velocity was 4 m/s, the buckling mode observed 5 ms after head impact resembled an s-shape with the C4 vertebra being displaced

relatively more posterior. The buckling at 10 ms was more pronounced, and the C7-T1 disc experienced avulsion at 15 ms. The highest impact velocity of 5 m/s resulted in more cervical spine buckling, and earlier disc avulsion (10 ms instead of 15 ms).

Kinematic Results

Figure 4-28 shows the cervical spine sagittal traces from 0 ms to 7 ms for all GHBMC model configurations along with the corresponding buckling parameters. Table 4-14 indicates the buckling parameter increase throughout the first 7 ms of loading for the models.

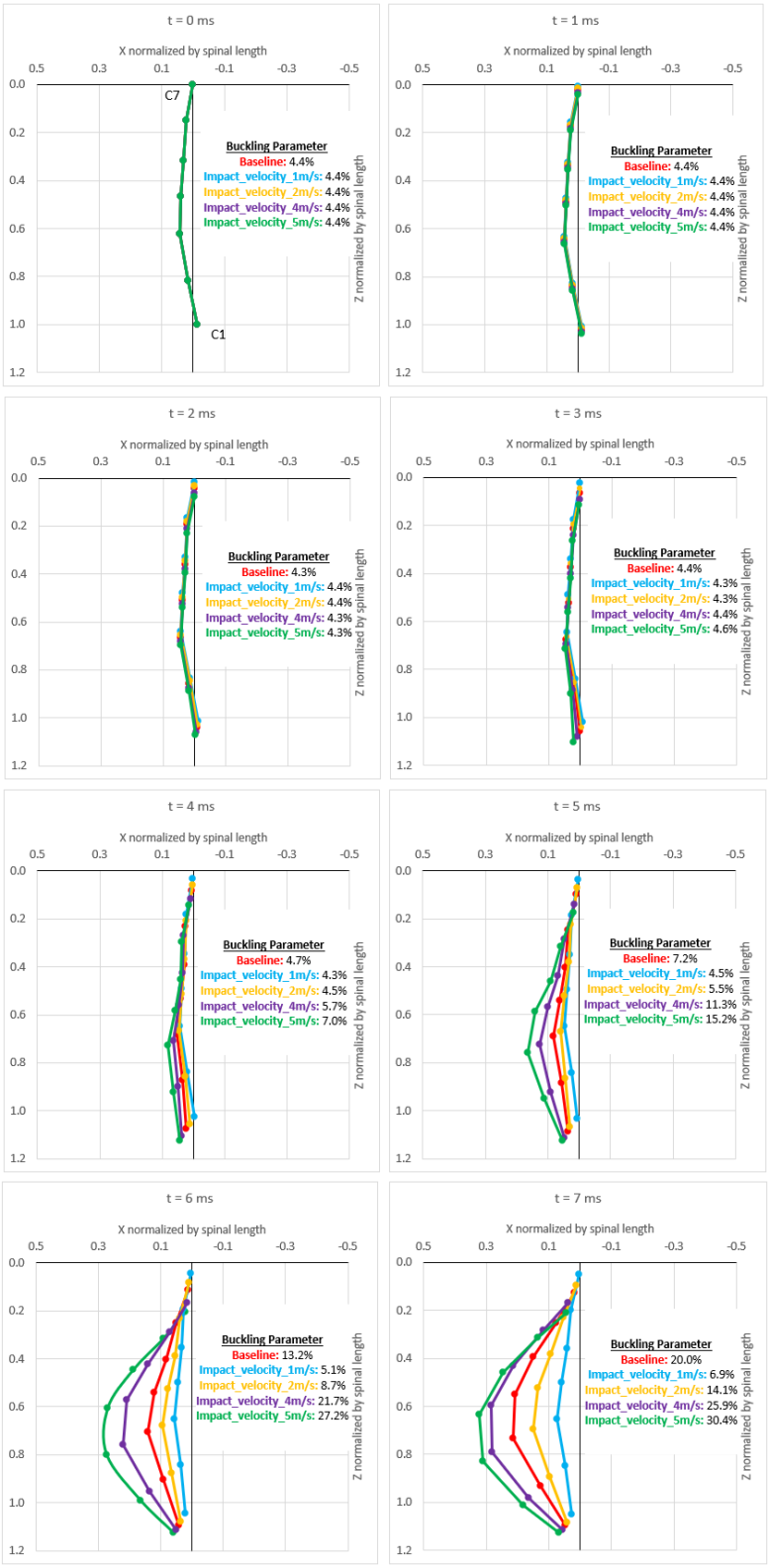

Figure 4-28: Cervical spine sagittal kinematic plots from 0 ms to 7 ms of Baseline, Impact_velocity_1m/s, Impact_velocity_2m/s, Impact_velocity_4m/s, and Impact_velocity_5m/s models

Table 4-14: Buckling parameter increase throughout the first 7 ms of loading for baseline, Impact_velocity_1m/s, Impact_velocity_2m/s, Impact_velocity_4m/s, and Impact_velocity_5m/s models

Buckling Parameter Increase Throughout First 7 ms of Loading			
Model	Average of buckling parameter increases (%)	Greatest buckling parameter increase (%)	Time interval corresponding to greatest increase (ms)
Baseline	2.2	6.8	6-7
Impact_velocity_1m/s	0.4	1.8	6-7
Impact_velocity_2m/s	1.4	5.4	6-7
Impact_velocity_4m/s	3.1	10.4	5-6
Impact_velocity_5m/s	3.7	12.0	5-6

During the first 2 ms after head impact, all GHBMC model configurations experienced no deformation or buckling. During the first 3 ms after head impact, only the Impact_velocity_5m/s model started to buckle due to the higher energy; the rest of the models still experienced no deformation. As the impact velocity increased, the cervical spine buckling experienced more deformation and buckling. As the impact velocity increased, there was an increase in the average of the buckling parameter increases. The increase in impact velocity also increased the value of the greatest buckling parameter increase. Moreover, the time interval corresponding to the greatest buckling parameter increased changed from 6-7 ms to 5-6 ms for the higher impact velocity models (Impact_velocity_4m/s and Impact_velocity_5m/s). For the Impact_velocity_1m/s model, the C1-C2 vertebrae rotated in extension, the C3 vertebra rotated in flexion for the first 7 ms after head impact followed by extension, and the C4-C7 vertebrae rotated in flexion. For the rest of the models, the C1-C3 vertebrae rotated in extension while the C4-C7 vertebrae rotated in flexion.

Kinetic Results

Figure 4-29 and Figure 4-30 show the head contact force history and axial neck compressive force history, respectively. Table 4-15 and Table 4-16 summarize head contact force and axial neck compressive metrics extracted from the aforementioned plots.

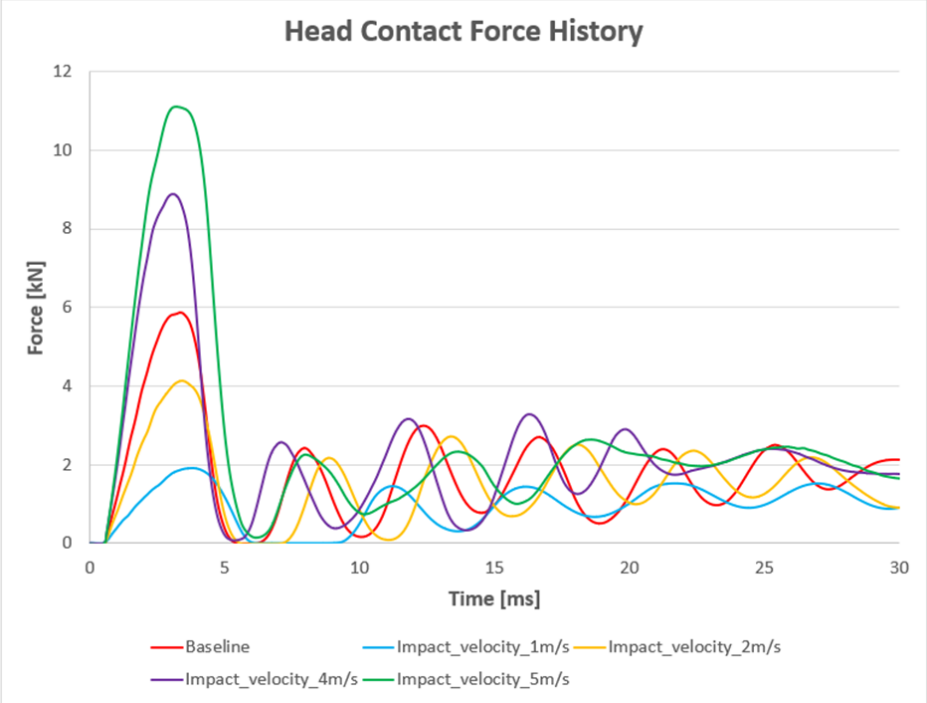

Figure 4-29: Head contact force history plots of baseline, Impact_velocity_1m/s, Impact_velocity_2m/s, Impact_velocity_4m/s, and Impact_velocity_5m/s models

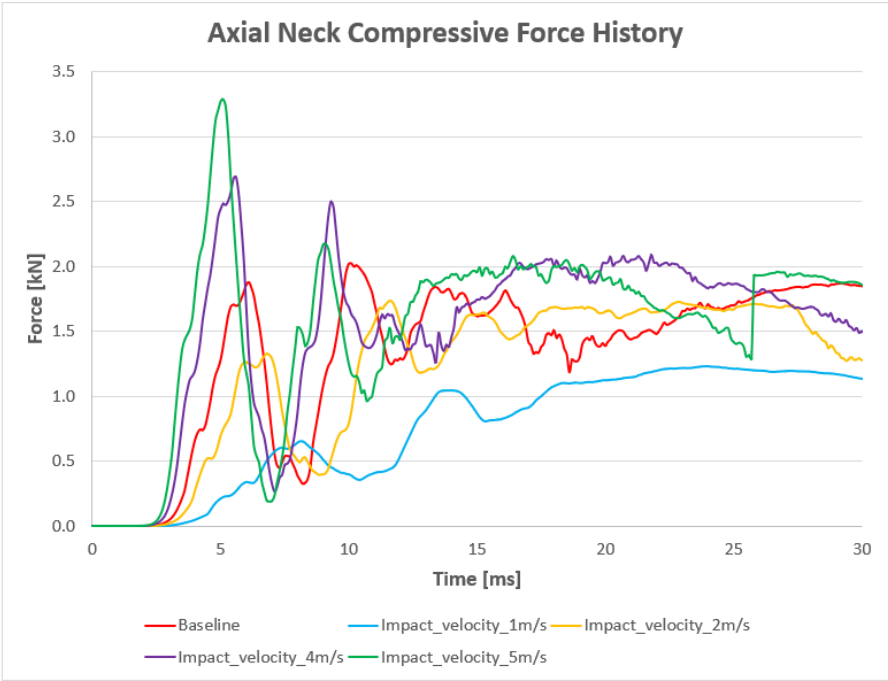

Figure 4-30: Axial neck compressive force history plots of baseline, Impact_velocity_1m/s, Impact_velocity_2m/s, Impact_velocity_4m/s, and Impact_velocity_5m/s models

Table 4-15: Head contact force metrics of baseline, Impact_velocity_1m/s, Impact_velocity_2m/s, Impact_velocity_4m/s, and Impact_velocity_5m/s models

Head Contact Force Metrics		
GHBMC Model	Initial peak head contact force (kN)	Slope of initial head contact force rise time (kN/ms)
Baseline	5.9	2.1
Impact_velocity_1m/s	1.9	0.6
Impact_velocity_2m/s	4.1	1.4
Impact_velocity_4m/s	8.9	3.6
Impact_velocity_5m/s	11.1	4.1

Table 4-16: Axial neck compressive force metrics of baseline, Impact_velocity_1m/s, Impact_velocity_2m/s, Impact_velocity_4m/s, and Impact_velocity_5m/s models

Axial Neck Compressive Force Metrics				
GHBMC Model	Initial peak axial force (kN)	Slope of initial neck force rise time (kN/ms)	Time from head impact to initial peak axial neck force (ms)	Time from head impact to neck force rise time (ms)
Baseline	1.9	0.5	5.6	2.1
Impact_velocity_1m/s	0.7	0.1	7.6	2.7
Impact_velocity_2m/s	1.3	0.3	6.3	2.3
Impact_velocity_4m/s	2.7	0.8	5.1	1.8
Impact_velocity_5m/s	3.3	1.2	4.6	1.7

As the impact velocity increased, the initial peak contact force decreased, and the time of head rebound (associated with when the head contact force reaches 0 kN) decreased. The head rebound period decreased because as the impact velocity increased, the plastic deformation of the leather-wood layer (from the impact of the head) increased due to the higher energy. The increased plastic deformation meant the head translated more into the layer and had more material surrounding it, which impeded and restricted the translation even more. The trend of the plots, however, remained the same for all impact velocities: a peak followed by a plateau around 2 kN. Moreover, when the impact velocity increased, the slope of the initial head contact force rise time increased. The slope increased due to the higher impact energy, which transmitted the load at a higher rate.

The trends observed in the axial neck compressive force history plots were similar for all the models except for Impact_velocity_1m/s: an initial peak, followed by a sharp force decrease, a force increase, and a plateau around 1.75 kN. The Impact_velocity_1m/s model showed a trend, which involved a slow force increase followed by a plateau at 1.25 kN. The slow force increase was because the cervical spine of the Impact_velocity_1m/s model experienced the least buckling, thereby not influencing the axial force transmission across the cervical spine. As the impact

velocity increased the initial peak axial force decreased, and the slope of initial neck force rise time increased. Furthermore, when the impact velocity increased, the time from head impact to initial peak axial neck force and the time from head to neck force rise time both decreased due to the higher impact energy.

Hard Tissue Injury Risk

The onset of failure for all GHBMC model configurations was at the cortical bone of C2 located at the tip of the dens. As previously discussed (subsection 4.3.1), the tip of the dens experienced failure due to the impact with the base of the skull. Figure 4-31 shows the effective plastic strain fringe plots of the cortical bone of C2 at the onset of injury of all model configurations alongside the baseline model for reference.

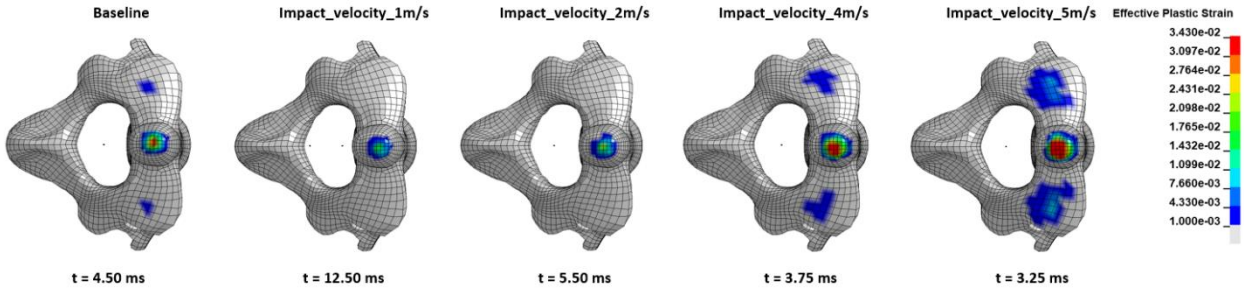

Figure 4-31: Effective plastic strain fringe plots (superior view) of Baseline, Impact_velocity_1m/s, Impact_velocity_2m/s, Impact_velocity_4m/s, and Impact_velocity_5m/s models

As the impact velocity increased, the onset of hard tissue injury was delayed. The delay was due to the reduced axial load associated with the decreased velocity and energy. The injury location (i.e., tip of the dens of the cortical bone of C2) was not affected by the increased impact velocity; however, the elements generally experienced greater effective plastic strains (indicated by the bigger red and blue zones in the strain plots).

Soft Tissue Injury Risk

Figure 4-32 shows the failure onset time of ligaments at all segment levels, Table 4-17 outlines which ligaments failed at each segment level, and Table 4-18 outlines the occurrence of disc avulsion at the C2-C3 to C7-T1 segment levels.

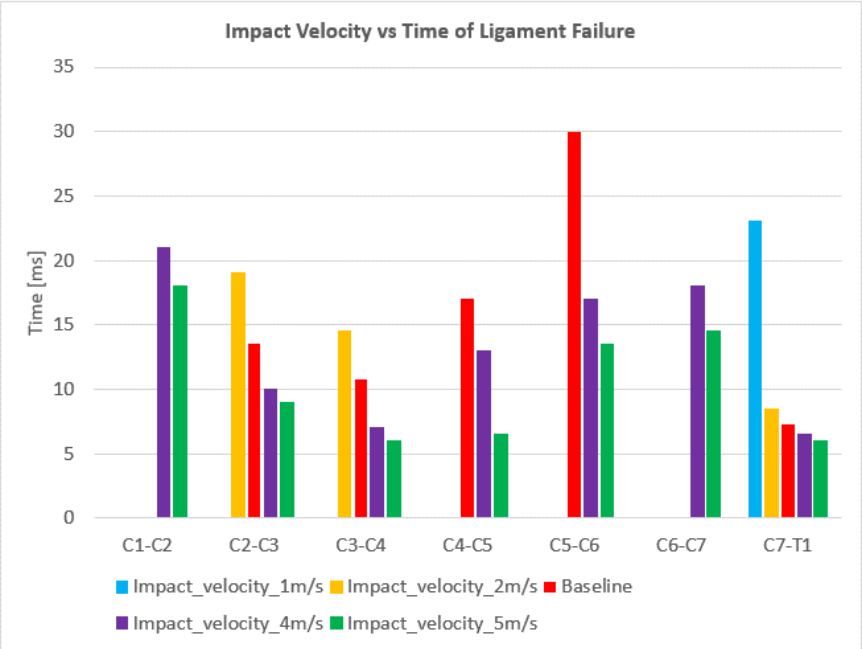

Figure 4-32: Onset times of ligament failure at every segment level for baseline, Impact_velocity_1m/s, Impact_velocity_2m/s, Impact_velocity_4m/s, and Impact_velocity_5m/s models

Table 4-17: Location of ligament failure at every segment level for baseline, Impact_velocity_1m/s, Impact_velocity_2m/s, Impact_velocity_4m/s, and Impact_velocity_5m/s models

Ligament Failure					
Level	Baseline	Impact_velocity_1m/s	Impact_velocity_2m/s	Impact_velocity_4m/s	Impact_velocity_5m/s
C1-C2				ISL	ISL
C2-C3	CL		CL	CL	ALL, CL
C3-C4	ALL, CL		ALL, CL	ALL, CL	ALL, CL
C4-C5	ALL			ALL	ALL
C5-C6	ALL			ALL	ALL
C6-C7				ALL	ALL, ISL
C7-T1	ISL, LF, CL, PLL	ISL	ISL, LF, CL, PLL	ISL, LF, CL, PLL	ISL, LF, CL, PLL

Table 4-18: Location of disc avulsion at C2-C3 to C7-T1 segment levels of baseline, Impact_velocity_1m/s, Impact_velocity_2m/s, Impact_velocity_4m/s, and Impact_velocity_5m/s models

Disc Failure					
Level	Baseline	Impact_velocity_1m/s	Impact_velocity_2m/s	Impact_velocity_4m/s	Impact_velocity_5m/s
C2-C3					
C3-C4					
C4-C5					
C5-C6					
C6-C7					
C7-T1	Avulsion			Avulsion	Avulsion

As the impact velocity increased, the onset times of ligament failure increased. Relative to the baseline model (which predicted ligament failure at all segment levels except for C1-C2 and C6-C7), the higher impact velocity models predicted ligament failure at all segment levels. Moreover, the ligaments predicted to fail in the baseline, Impact_velocity_4m/s, and Impact_velocity_5m/s models were mostly the same. For the C1-C2 segment level, the Impact_velocity_4m/s and Impact_velocity_5m/s models were the only ones that predicted ligament failure (ISL). For the C2-C3 segment level, the three models predicted CL failure and the Impact_velocity_5m/s model also predicted ALL failure. For the C3-C4 to C5-C6 segment levels, the three models had the same ligament failure predictions. For the C6-C7 segment level, the baseline model did not predict ligament failure, the Impact_velocity_4m/s model predicted only ALL failure, and the Impact_velocity_5m/s predicted ALL and ISL failures. The same ligament failure prediction was observed at the C7-T1 segment level for the baseline, Impact_velocity_4m/s, and Impact_velocity_5m/s models. Moreover, the three aforementioned models all sustained disc avulsion at the C7-T1 segment level. Alternatively, the lower impact velocity models predicted ligament failure at less segment levels. The Impact_velocity_2m/s model predicted ligament failure only at the C2-C3, C3-C4, and C7-T1 segment levels, and the Impact_velocity_1m/s model predicted ligament failure only at the C7-T1 segment level. None of the two lower impact velocity models predicted ligament failure at the C1-C2 segment level. The ligament failure predictions were the same for the C2-C3 (CL) and C3-C4 (ALL and CL) segment levels in the baseline and

Impact_velocity_2m/s models; the Impact_velocity_1m/s model did not predict ligament failure at those levels.

Summary of Results and Discussion for Impact Velocity Variation

As the impact velocity increased, the cervical spine exhibited more deformation and buckling throughout the loading and the leather-wood layer experienced greater plastic deformation due to the higher energy. The increase in impact velocity also led to a decrease in the head rebound period because the head translated more into the leather-wood layer due to the higher energy. Moreover, the initial peak head contact force and initial peak axial neck force both increased. Due to the increased load and deformation of the cervical spine, more hard and soft tissue injuries were sustained with relatively faster onset times of first hard and soft tissue injury occurrence.

4.3.3 Anteroposterior Impact Plate Angle: Results and Discussion

HFI Progression

Figure 4-33 and Figure 4-34 show the HFI progressions of the Plate_AP_15° and Plate_AP_-15° models, respectively. During the first 5 ms, the cervical spine in both models experienced minimal deformation and buckling. Noticeable buckling occurred between 5 ms and 10 ms for both models as well as the baseline model (Figure 4-3). The head in the Plate_AP_15° model slightly rotated in flexion (4.3° after 15 ms), and the head in Plate_AP_-15° slightly rotated in extension (6.2° after 15 ms). For the Plate_AP_15° model, the C1-C3 vertebrae rotated in extension, while the C4-C7 vertebrae rotated in flexion. For the Plate_AP_-15° mode, the C1 and C2 vertebrae rotated in extension, while the C3-C7 vertebrae rotated in flexion.

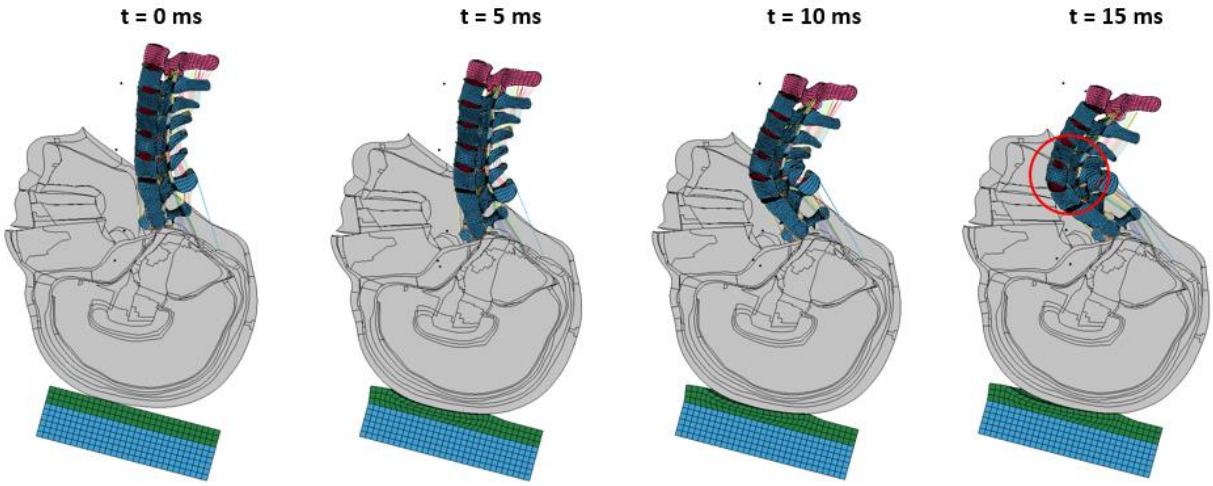

Figure 4-33: HFI progression from 0-15 ms of Plate_AP_15° with buckling transition point (C4) circled in red

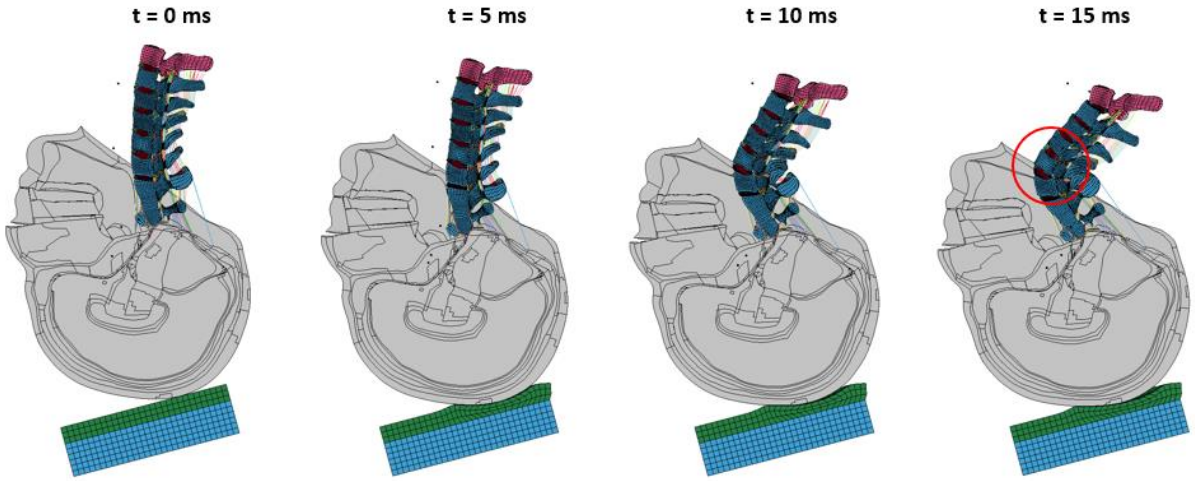

Figure 4-34: HFI progression from 0-15 ms of Plate_AP_-15° with buckling transition point (C3) circled in red

Kinematic Results

Figure 4-35 shows the kinematic plots from 0-7 ms of all the GHBMC model configurations along with their corresponding buckling parameters. The buckling parameter increases throughout the first 7 ms of loading were extracted from the kinematic plots and are summarized in Table 4-19.

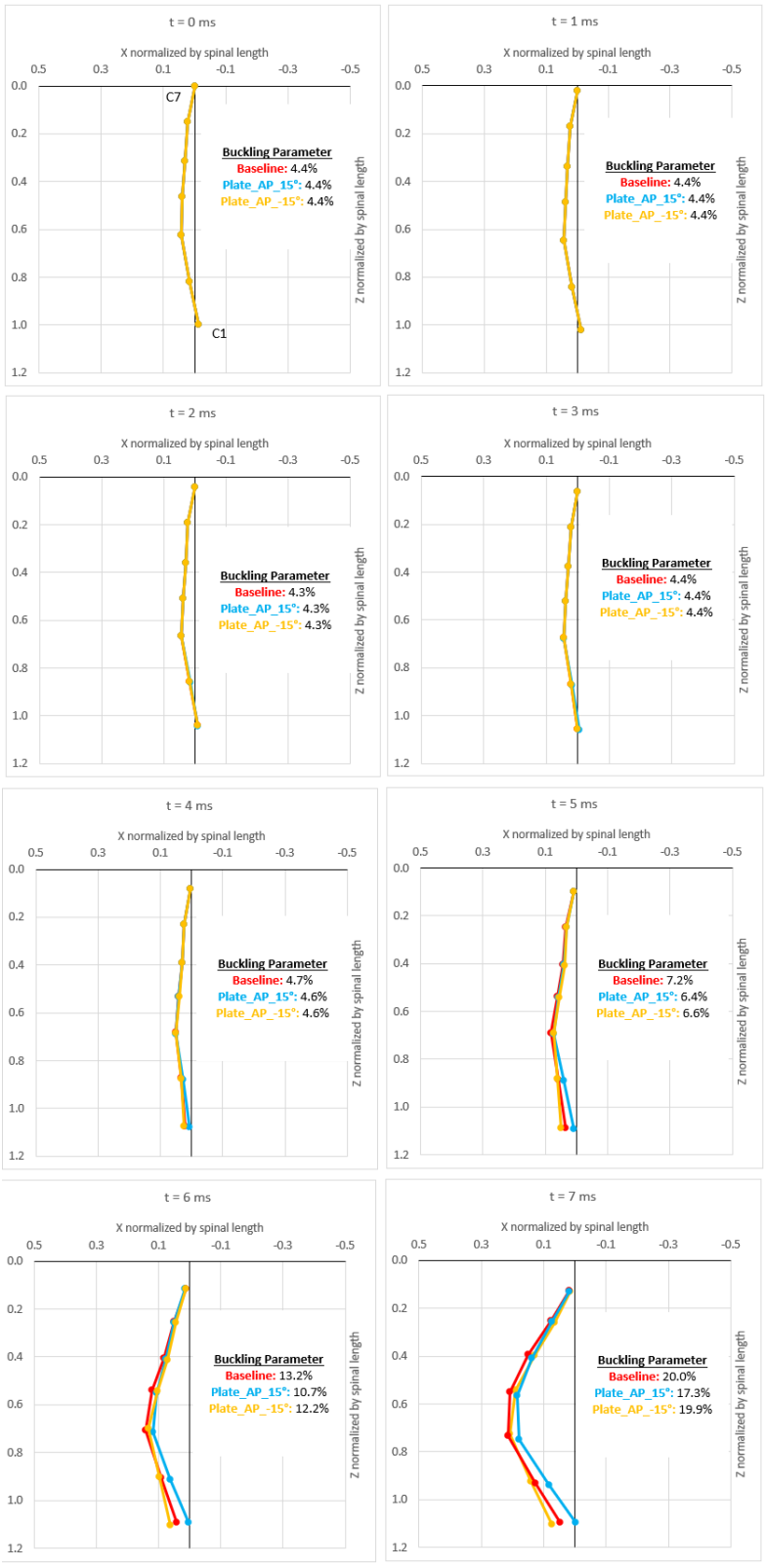

Figure 4-35: Cervical spine sagittal kinematic plots from 0 ms to 7 ms of Baseline, Plate_AP_15°, and Plate_AP_-15° models

Table 4-19: Buckling parameter increase throughout the first 7 ms of loading for baseline, Plate_AP_15°, and Plate_AP_-15° models

Buckling Parameter Increase Throughout First 7 ms of Loading			
Model	Average of buckling parameter increases (%)	Greatest buckling parameter increase (%)	Time interval corresponding to greatest increase (ms)
Baseline	2.2	6.8	6-7
Plate_AP_15°	1.8	6.6	6-7
Plate_AP_-15°	2.3	7.7	6-7

During the first 4 ms, all three models experienced minimal cervical spine buckling (as was visually observed through HFI progression). During the 4-7 ms interval, the Plate_AP_15° model exhibited the least buckling while the other two models exhibited nearly similar levels of buckling. The difference in buckling was attributed to the rotation of the head and upper cervical spine, in addition to the anterior velocity of C3 (buckling transition point). The head in the Plate_AP_15° model rotated in flexion, which opposed the extension rotation of the upper cervical spine (C1 and C2). As a result, the C1 vertebra rotated in extension less than the baseline and Plate_AP_-15° models during the 7 ms interval and the anterior velocity of C3 in Plate_AP_15° was less than the other models as well. Therefore, due to the head opposing the direction of rotation of the upper cervical spine (which initiated the buckling), the overall buckling was less in Plate_AP_15°.

Kinetic Results

The head contact force Figure 4-36 and axial neck compressive force histories Figure 4-37 were extracted from the models, respectively. Table 4-20 and Table 4-21 summarize head contact force and axial neck compressive force metrics extracted from the aforementioned plots, respectively.

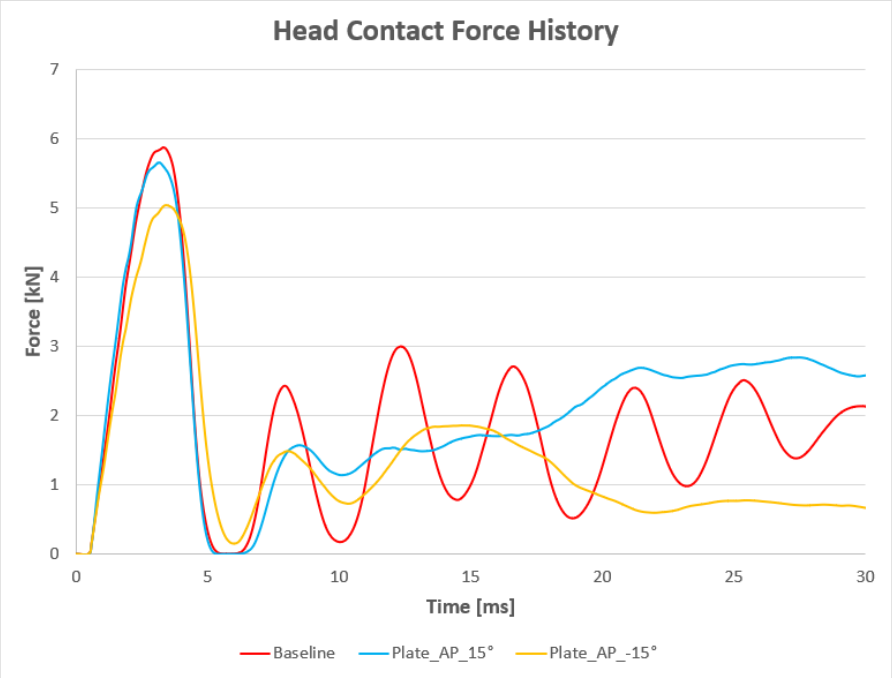

Figure 4-36: Head contact force history plots of baseline, Plate_AP_15°, Plate_AP_-15° models

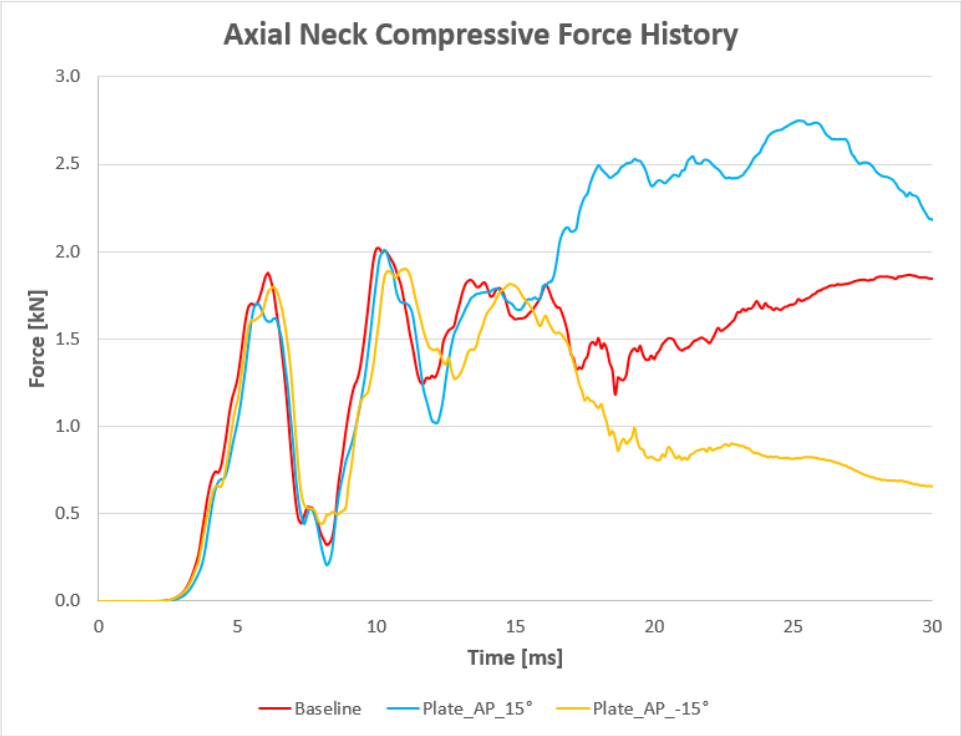

Figure 4-37: Axial neck compressive force history plots of baseline, Plate_AP_15°, Plate_AP_-15° models

Table 4-20: Head contact force metrics of baseline, Plate_AP_15°, and Plate_AP_-15° models

Head Contact Force Metrics		
GHBMC Model	Initial peak head contact force (kN)	Slope of initial head contact force rise time (kN/ms)
Baseline	5.9	2.1
Plate_AP_15°	5.7	2.1
Plate_AP_-15°	5.0	1.7

Table 4-21: Axial neck compressive force metrics of baseline, Plate_AP_15°, and Plate_AP_-15° models

Axial Neck Compressive Force Metrics				
GHBMC Model	Initial peak axial force (kN)	Slope of initial neck force rise time (kN/ms)	Time from head impact to initial peak axial neck force (ms)	Time from head impact to neck force rise time (ms)
Baseline	1.9	0.5	5.6	2.1
Plate_AP_15°	1.7	0.6	5.2	2.2
Plate_AP_-15°	1.8	0.5	5.8	2.1

The trend observed in the head contact force history plots for the three models was the same: a force rise time leading to an initial peak, followed by a force decrease and a plateau around 1.5 kN. When the impact plate was rotated 15° (i.e., Plate_AP_15°), the initial peak force was slightly lower relative to the baseline model (e.g., 5.7 kN < 5.9 kN). However, the slope of the initial head contact force rise time was the same for those two models. The slope was the same because both models experienced similar head vertical displacement into the leather-wood layer (5.5 mm). When the impact plate was rotated -15° (i.e., Plate_AP_-15°), the initial peak force was the lowest out of the three models (e.g., 5.0 kN < 5.7 kN < 5.9 kN). The slope of the initial head contact force rise time also decreased (e.g., 1.7 kN/ms < 2.1 kN/ms). The decrease in force and slope were associated with the greater vertical displacement into the leather-wood layer that resulted in more plastic deformation. Moreover, due to that increased displacement into the layer, the head rebound period of Plate_AP_-15° was less than that corresponding to the baseline and Plate_AP_15° models.

The trend observed in the axial neck compressive force history plots was the same for all three models. Changing the AP angle of the impact plate did not have a significant effect on the axial neck force metrics. However, the initial peak axial neck force corresponding to the Plate_AP_15° model was slightly less than the other models. Due to the reduced extension rotation of C1 in

Plate_AP_15°, the C2 vertebra extension rotation increased (relative to the two other models). The rotation increased because the odontoid (which was in contact with the anterior arch of C1) experienced less extension, which led to slightly more C2 extension. This increased rotation caused slightly more middle-cervical spine flexion rotation, which reduced the axial force component at C7 where the force was measured.

Hard Tissue Injury Risk

The onset of failure for all GHBMC model configurations was at the cortical bone of C2 located at the tip of the dens. Figure 4-38 shows the effective plastic strain fringe plots of the cortical bone of C2 with the time corresponding to the onset of hard tissue injury of all the model configurations.

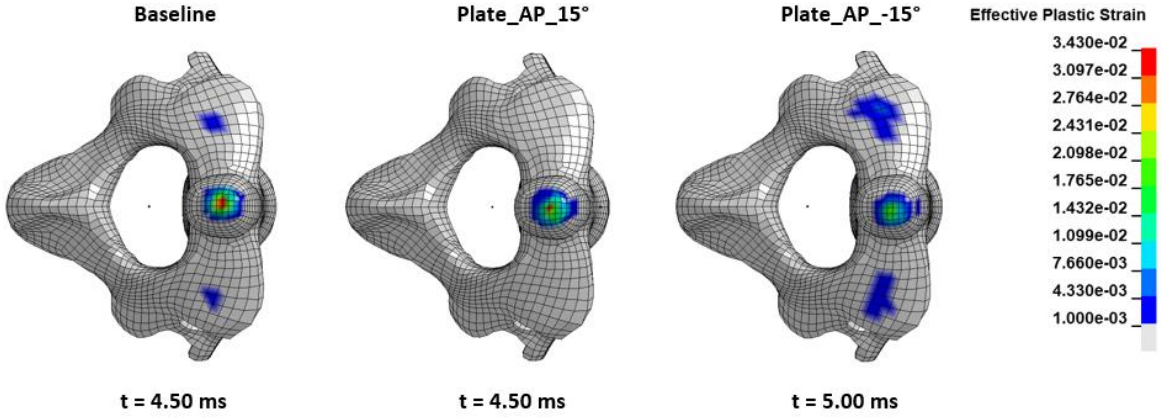

Figure 4-38: Effective plastic strain fringe plots (superior view) of Baseline, Plate_angle_15°, and Plate_angle_-15° models

As the AP angle of the impact plate increased from -15° to 0° the onset of hard tissue injury was delayed. However, increasing the angle from 0° to 15° did not affect the onset of hard tissue injury. The Plate_AP_-15° model predicted a relatively delayed onset of hard tissue injury because the head and upper cervical spine rotated more in extension, which slightly alleviated the load at the upper cervical spine and resulted in a minimal delay of the onset of injury. The injury location (i.e., tip of the dens of the cortical bone of C2) was not affected by the increased AP plate angle because, despite the change in AP orientation of the plate, the general kinematic and buckling response of the cervical spine (C1-C3 rotated in extension, C3 transition point, and C4-C7 rotated in flexion) was not affected.

Soft Tissue Injury Risk

Figure 4-39 shows the onset time of ligament failure for segment levels of the three models, and Table 4-22 identifies which ligaments failed at every segment level.

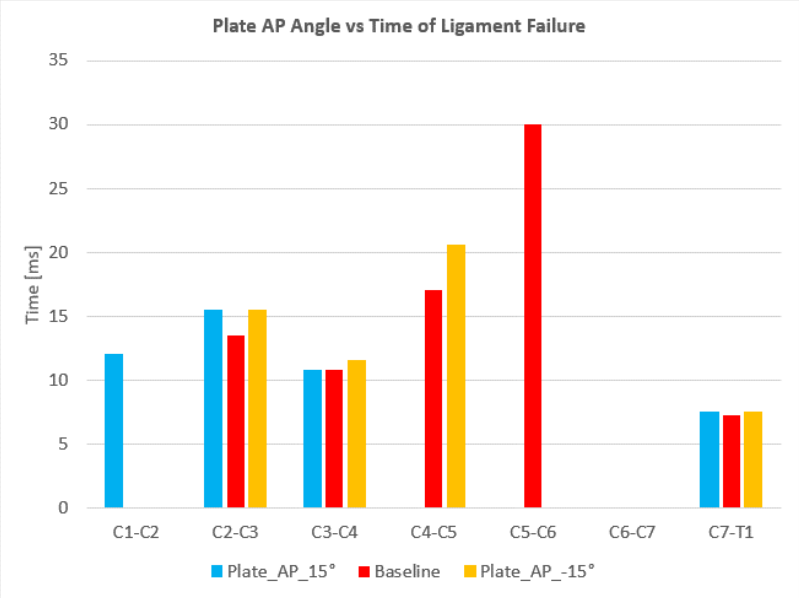

Figure 4-39: Onset times of ligament failure at every segment level for baseline, Plate_AP_15°, and Plate_AP_-15° models

Table 4-22: Location of ligament failure at every segment level for baseline, Plate_AP_15°, and Plate_AP_-15° models

Ligament Failure			
Level	**Baseline**	**Plate_AP_15°**	**Plate_AP_-15°**
C1-C2		ISL	
C2-C3	CL	CL	CL
C3-C4	ALL, CL	ALL, CL	ALL
C4-C5	ALL		ALL
C5-C6	ALL		
C6-C7			
C7-T1	ISL, LF, CL, PLL	ISL, LF, CL, PLL	ISL, LF, CL, PLL

The time of ligament failure predicted in the three models at the C7-T1 segment level (the first level that experienced ligament failure) very slightly increased in the Plate_AP_15° and Plate_AP_-15° models relative to the baseline model (7.5 ms vs. 7.25 ms). However, the ligaments that failed at that level were the same for all three models. The Plate_AP_15° model was the only one that did not predict disc avulsion at the C7-T1 segment level. Disc avulsion was not observed because the model mainly predicted upper cervical spine soft (and hard) tissue failure (e.g., it was the only one to predict ISL failure at the C1-C2 segment level). ISL failure at the C1-C2 segment level was predicted due to the head rotating in flexion, opposite to the direction of rotation of the upper cervical spine. As a result of that relative rotation, higher strains could have been imposed at the upper cervical spine, thereby subjecting it to more hard and soft tissue injury. For the C3-C4 segment level (which experienced ligament failure right after the C7-T1 segment level), the baseline and Plate_AP_15° models had the same onset time of ligament failure (10.75 ms) whereas the Plate_AP_-15° model had a slightly delayed time relative to the two other models (11.5 ms). Moreover, the Plate_AP_-15° model predicted only ALL failure whereas the other two models (baseline and Plate_AP_15°) predicted ALL and CL failure at the C3-C4 segment level. All three models predicted ligament failure (CL) at the C2-C3 segment level, with the Plate_AP_15° and Plate_AP_-15° models delaying the onset time of ligament failure (15.5 ms) relative to the baseline model (13.5 ms). For the C4-C5 segment level, only the baseline and Plate_AP_-15° models predicted ligament failure (ALL), wit the latter delaying the onset time of ligament failure relative to the baseline (20.5 ms > 17 ms). Finally, none of the three models predicted ligament failure at the C6-C7 segment level. Overall, the Plate_AP_15° and Plate_AP_-15° models predicted less soft tissue injury across all segment levels relative the baseline model.

Summary of Results and Discussion for AP Plate Angle Variation

It was found that the direction of rotation of the head influences the response of the cervical spine throughout loading. In the Plate_AP_15° model, the head rotated in flexion, and in the Plate_AP_-15° model it rotated in extension. The cervical spine in the Plate_AP_15° model exhibited the least overall buckling due to the head rotating in a direction opposite to the extension rotation of the upper cervical spine, which initiated the buckling. The cervical spine of the baseline and Plate_AP_-15° models exhibited similar overall buckling. The reduced buckling predicted in Plate_AP_15° resulted in a slightly lower initial peak axial force; the other two models having

similar values for the peak axial force. The plot trend, however, was the same for all three models. The Plate_AP_-15° had the lowest initial peak head contact force due to the greater head vertical displacement into the leather-wood layer, which resulted in more plastic deformation and a shorter head rebound period. Due to the relatively greater extension rotation of the head and upper cervical spine in Plate_AP_-15°, the load was slightly alleviated at the upper cervical spine and as a result the onset of injury was delayed relative to the other models (baseline and Plate_AP_15°). The Plate_AP_15° and Plate_AP_-15° models delayed the onset of ligament rupture but did not affect the occurrence of disc avulsion.

4.3.4 Lateral Impact Plate Angle: Results and Discussion

HFI Progression

Figure 4-40 and Figure 4-41 show the sagittal view of the HFI progressions from 0-15 ms (at 5 ms intervals) of the Plate_lateral_15° and Plate_lateral_30° models, respectively. Additionally, Figure 4-42 and Figure 4-43 show the frontal views of the aforementioned HFI progressions.

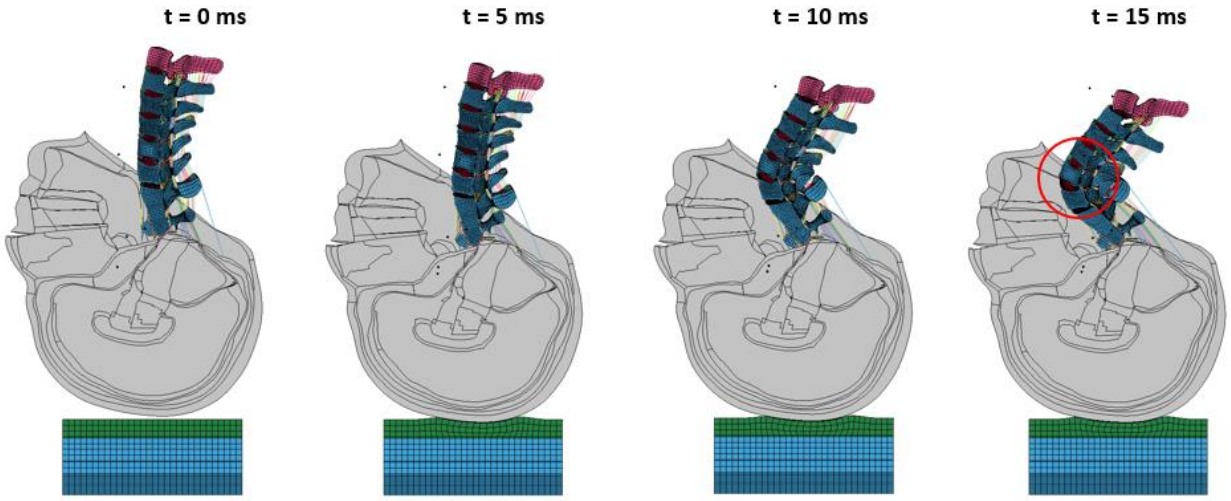

Figure 4-40: Sagittal view of the HFI progression from 0-15 ms of the Plate_lateral_15° model with buckling transition point (C3) circled in red

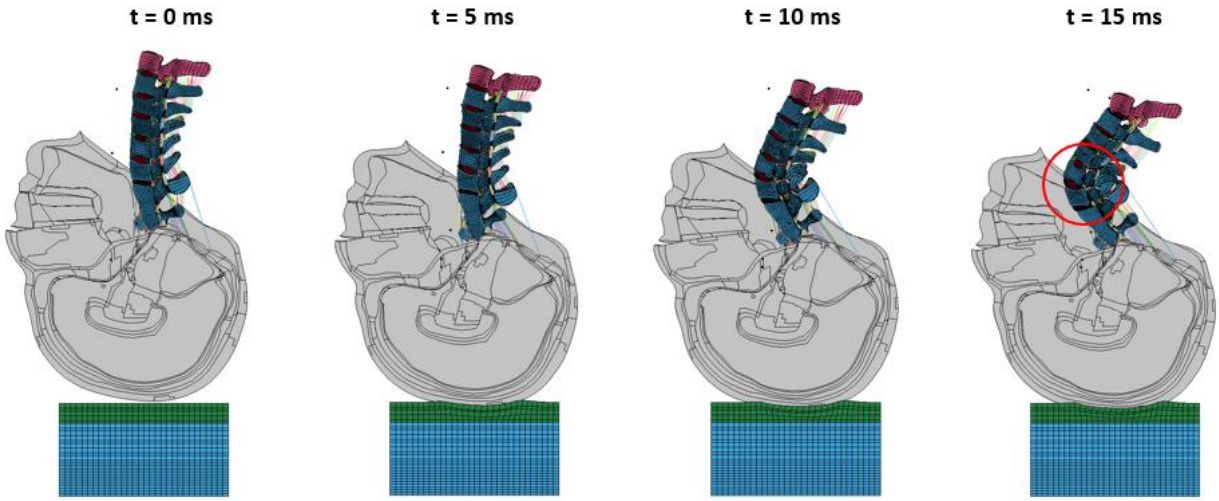

Figure 4-41: Sagittal view of the HFI progression from 0-15 ms of the Plate_lateral_30° model with buckling transition point (C3) circled in red

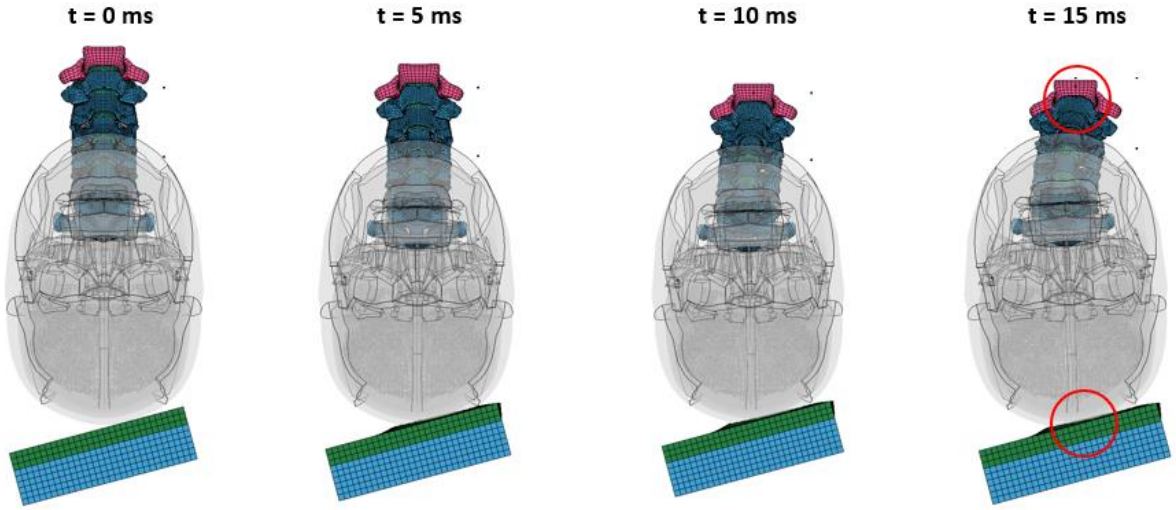

Figure 4-42: Frontal view of the HFI progression from 0-15 ms of the Plate_lateral_15° model with lateral offset between T1 and head vertex (circled in red) illustrated in 15 ms image

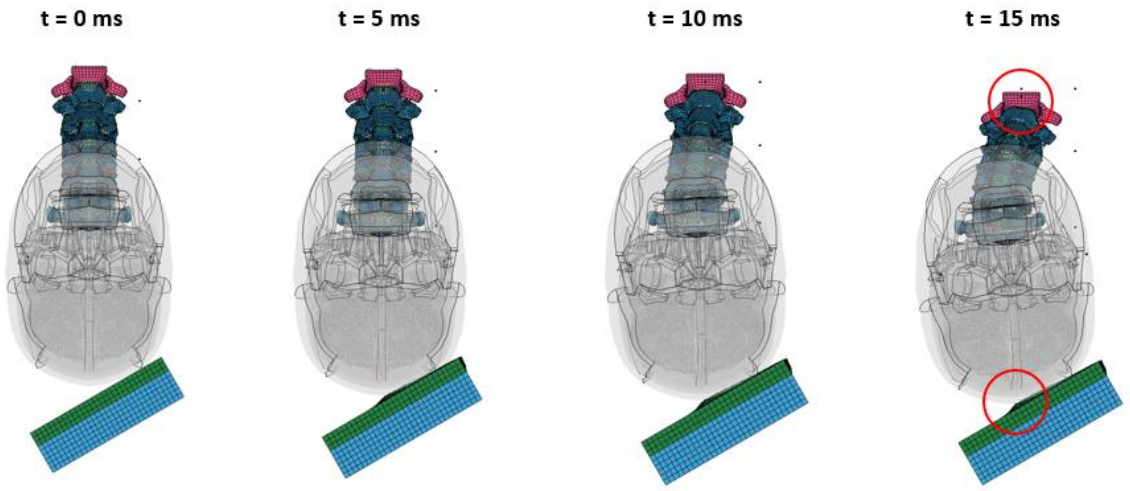

Figure 4-43: Frontal view of the HFI progression from 0-15 ms of the Plate_lateral_30° model with lateral offset between T1 and head vertex (circled in red) illustrated in 15 ms image

The sagittal view of the HFI progression of the Plate_lateral_15° model was similar to that of the baseline model: the cervical spine experienced minimal deformation and buckling during the first 5 ms while the head plastically deformed the leather-wood surface. The cervical spine experienced buckling during the 5-10 ms and 10-15 ms intervals, while the head remained relatively stationary as it deformed the leather-wood layer. The frontal view of the Plate_lateral_15° model indicated that the head slightly rotated counterclockwise during the 10-15 ms interval. As a result, there was a lateral offset between the T1 vertebra and the head. The sagittal view of the HFI progression of the Plate_lateral_30° model demonstrated the same behaviour as observed in the other two models; however, the overall cervical spine buckling was less relative to the two other models. The frontal view of the HFI progression of the Plate_lateral_30° model demonstrated more counterclockwise head rotation due to the steeper incline of the impact plate. As a result, there was more lateral offset between the T1 vertebra and the head. Moreover, the cervical spine experienced axial rotation and lateral bending in the Plate_lateral_15° and Plate_lateral_30° models. In fact, the lateral angle of the impact plate was the only parameter where cervical spine rotation in planes other than the sagittal plane was observed.

Kinematic Results

Figure 4-44 shows the kinematic cervical spine plots from 0-7 ms of the three models overlaid on the same graph. Table 4-23 summarizes the extracted buckling parameter increases throughout the first 7 ms of loading.

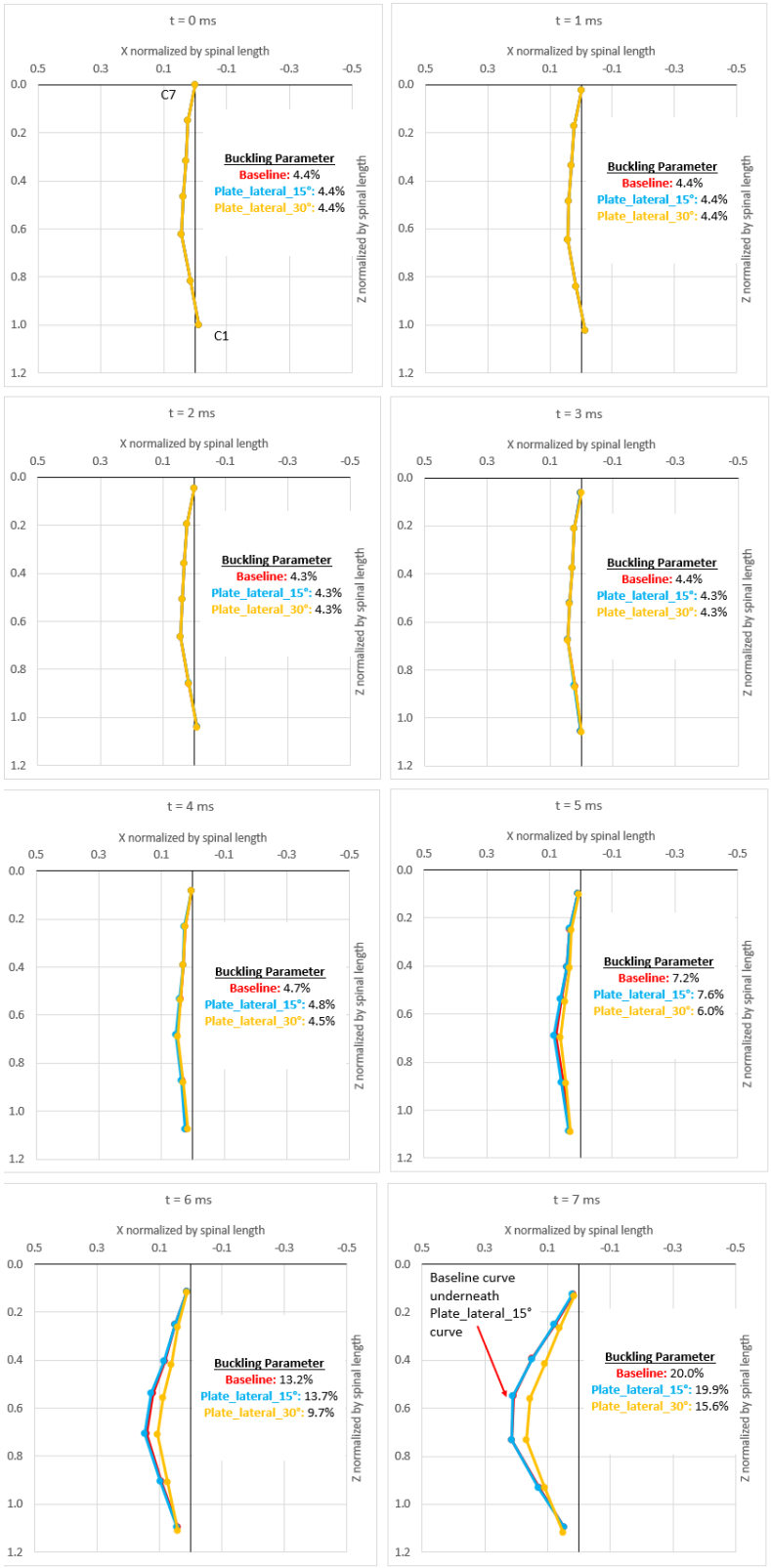

Figure 4-44: Cervical spine sagittal kinematic plots from 0 ms to 7 ms of baseline, Plate_lateral_15°, and Plate_lateral_30° models

Table 4-23: Buckling parameter increase throughout the first 7 ms of loading for baseline, Plate_lateral_15°, and Plate_lateral_30° models

Buckling Parameter Increase Throughout First 7 ms of Loading			
Model	Average of buckling parameter increases (%)	Greatest buckling parameter increase (%)	Time interval corresponding to greatest increase (ms)
Baseline	2.2	6.8	6-7
Plate_lateral_15°	2.2	6.2	6-7
Plate_lateral_30°	1.6	5.9	6-7

During the first 4 ms of HFI loading, the three models experienced negligible cervical spine buckling as indicated visually from the plots and quantitatively from the corresponding buckling parameter values. This outcome was consistent with the qualitative findings from the HFI progression. During the 4-7 ms interval, it can be noticed that increasing the lateral angle of the impact plate to 15° (from the baseline 0°) did not reduce the buckling of the cervical spine; the cervical spine buckling of the baseline and Plate_lateral_15° models was the same during that interval. Moreover, the average of the buckling parameter increases was the same for both models (2.2%), but the greatest buckling parameter increase was slightly less for the Plate_lateral_15° model (6.2% < 6.8%). However, increasing the lateral angle of the impact plate to 30° (i.e., Plate_lateral_30°) reduced the buckling during the 4-7 ms interval. The buckling was reduced due to the significant incline causing lateral deformation of the cervical spine, which alleviated the sagittal buckling exhibited (Figure 4-43). The average of the buckling parameter increases and the greatest buckling parameter increase were also reduced (e.g., 1.6% < 2.2%, and 5.9% < 6.2% < 6.8%). All three models experienced the greatest buckling parameter increase during the 6-7 ms interval.

Kinetic Results

Figure 4-45 and Figure 4-46 show the head contact force and axial neck compressive force plots of the three models, respectively. Table 4-24 and Table 4-25 show the head contact force and axial neck compressive force metrics that were extracted from the aforementioned plots, respectively.

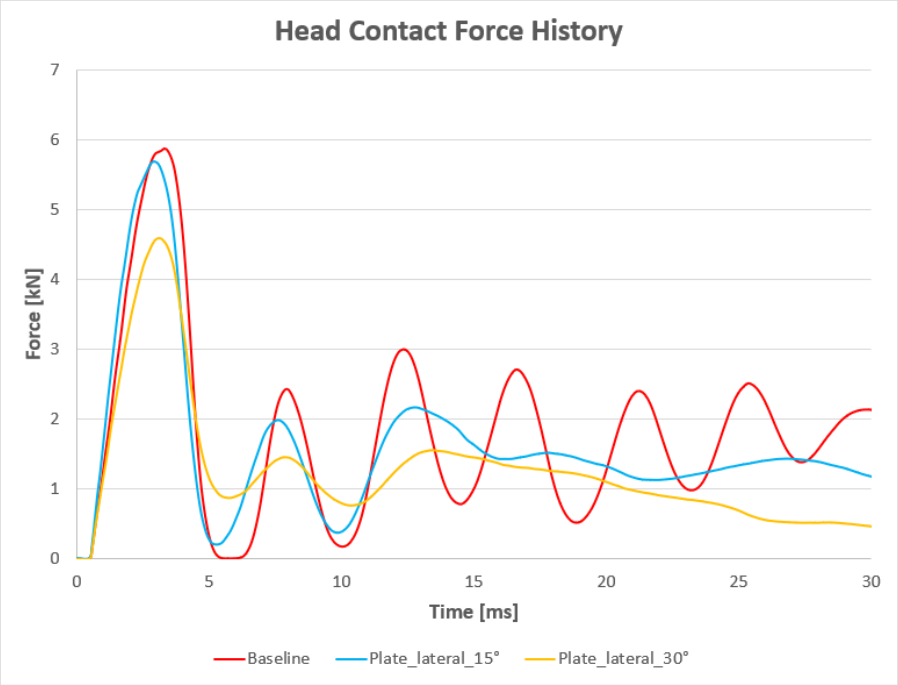

Figure 4-45: Head contact force history plots of baseline, Plate_lateral_15°, and Plate_lateral_30° models

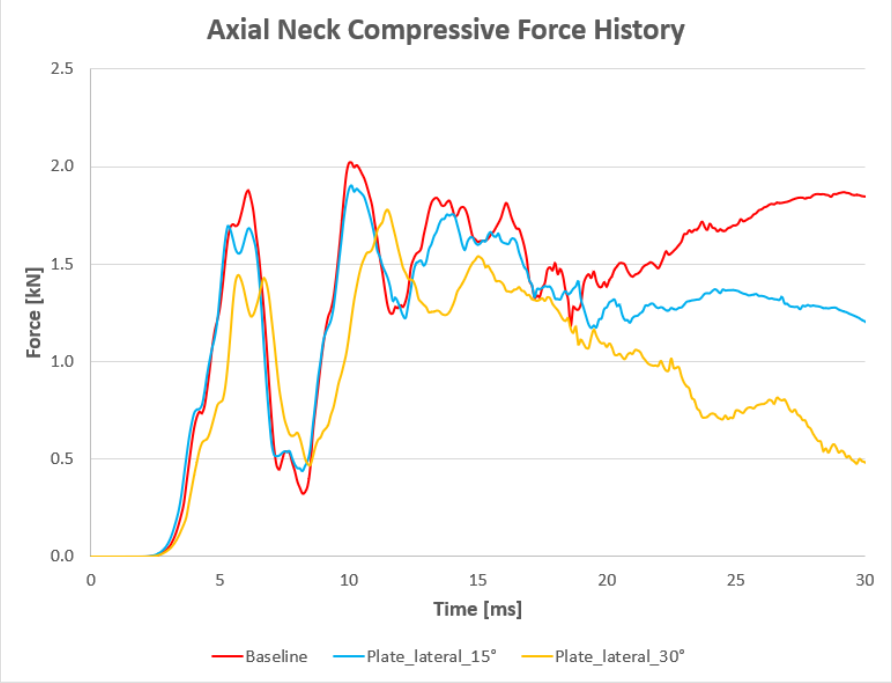

Figure 4-46: Axial neck compressive force history plots of baseline, Plate_lateral_15°, and Plate_lateral_30° models

Table 4-24: Head contact force metrics for baseline, Plate_lateral_15°, and Plate_lateral_30° models

Head Contact Force Metrics		
GHBMC Model	Initial peak head contact force (kN)	Slope of initial head contact force rise time (kN/ms)
Baseline	5.9	2.1
Plate_lateral_15°	5.7	2.4
Plate_lateral_30°	4.6	1.8

Table 4-25: Axial neck compressive force metrics for baseline, Plate_lateral_15°, and Plate_lateral_30° models

Axial Neck Compressive Force Metrics				
GHBMC Model	Initial peak axial force (kN)	Slope of initial neck force rise time (kN/ms)	Time from head impact to initial peak axial neck force (ms)	Time from head impact to neck force rise time (ms)
Baseline	1.9	0.5	5.6	2.1
Plate_lateral_15°	1.7	0.6	4.8	2.0
Plate_lateral_30°	1.4	0.5	5.2	2.1

As the lateral angle of the impact plate increased from 0° to 15° to 30°, the initial peak head contact force decreased (e.g., 4.6 kN < 5.7 kN < 5.9 kN). The slope of the initial head contact force rise time slightly increased when the lateral angle increased from 0° to 15° (e.g., 2.4 kN/ms > 2.1 kN/ms) and decreased when the lateral angle was increased to 30° (e.g., 1.8 kN/ms < 2.4 kN/ms and 1.8 kN/ms < 2.1 kN/ms). Moreover, following the initial head contact force peak, as the lateral angle was increased, the head rebound period decreased and the plateau region became less sinusoidal. However, all models still plateaued at around 1.5 kN. With the increased lateral angle, the shear (lateral) force increased and the normal force (superior-inferior) force decreased, thereby decreasing the head contact force. Additionally, due to the increased surface contact area with the increased lateral angle of the plate, more of the head contacted the impact plate, which reduced the head rebound period.

As the lateral angle increased, the initial peak axial neck force decreased (e.g., 1.4 kN < 1.7 kN < 1.9 kN). This decrease was associated with the increased incline of the impact plate, which caused lateral deformation of the cervical spine that reduced the sagittal buckling exhibited. The slope of the initial neck force rise time was similar for all three. When the lateral angle was increased from 0° to 15°, the time from head impact to initial peak axial neck force decreased (4.8 ms < 5.6 ms). The time from head impact to initial peak axial neck force corresponding to the Plate_lateral_30°

model was slightly greater than that corresponding to the Plate_lateral_15° model (5.2 ms > 4.8 ms) but less than that corresponding to the baseline model (5.2 ms < 5.6 ms). The times from head impact to neck force rise time corresponding to the baseline and Plate_lateral_30° models were equal (2.1 ms), but the time corresponding to the Plate_lateral_15° model was slightly less (e.g., 2.0 ms < 2.1 ms). The trend observed in the axial neck compressive force history plots was the same for all models.

Hard Tissue Injury Risk

The onset of failure for all GHBM model configurations was at the cortical bone of C2 location at the tip of the dens. Figure 4-47 shows the effective plastic strain fringe plots of the cortical bone of C2 at the onset of injury of all model configurations.

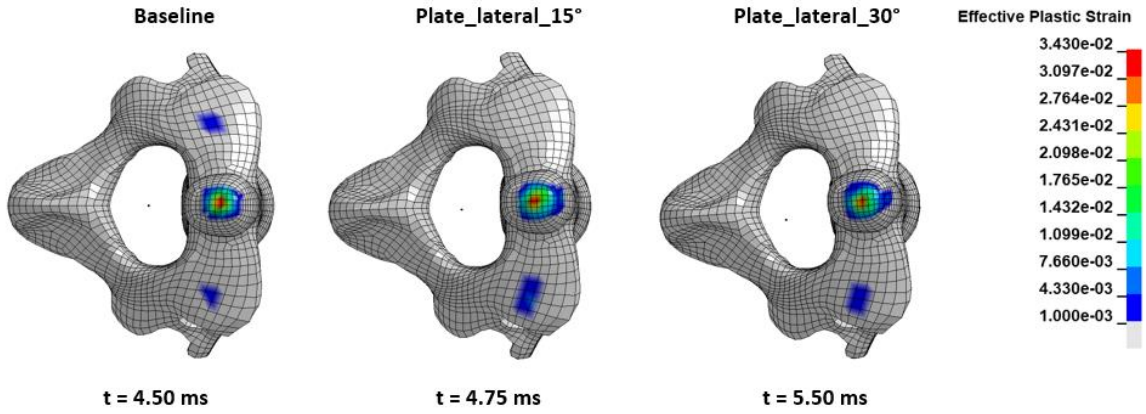

Figure 4-47: Effective plastic strain fringe plots (superior view) of Baseline, Plate_lateral_15°, and Plate_lateral_30° models

As the lateral angle of the impact plate increased, the onset of hard tissue injury was delayed. The delay was due to the reduced axial load that was associated with the increased lateral force component. The injury location (i.e., tip of the dens of the cortical bone of C2) was not affected by the increased lateral angle of the impact plate.

Soft Tissue Injury Risk

Figure 4-48 shows the onset times of ligament failure for all segment levels of the three models, and Table 4-26 identifies which ligaments failed at every segment level.

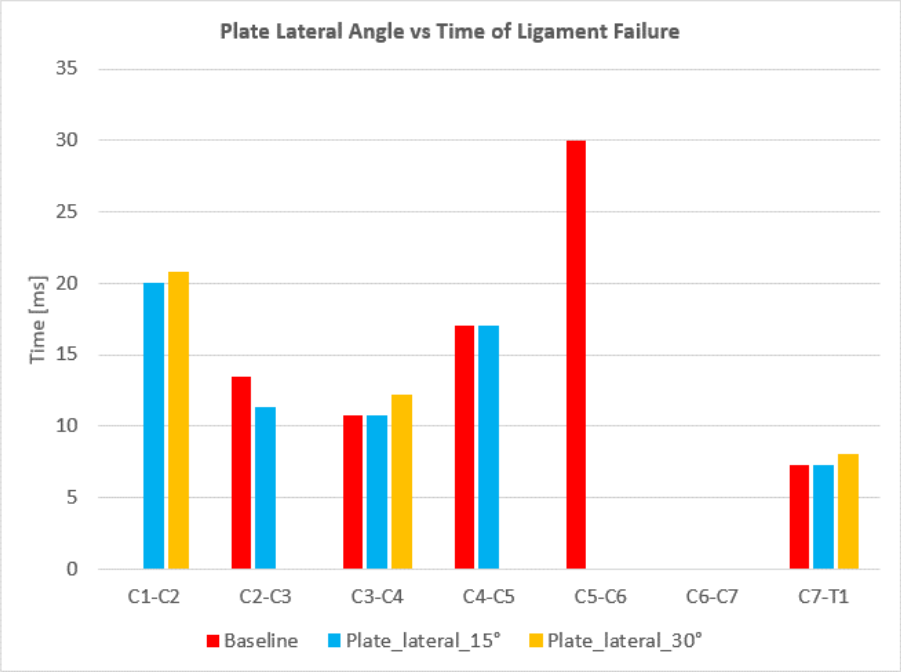

Figure 4-48: Onset times of ligament failure at every segment level for baseline, Plate_lateral_15°, and Plate_lateral_30° models

Table 4-26: Location of ligament failure at every segment level for baseline, Plate_lateral_15°, and Plate_lateral_30° models

Ligament Failure			
Level	**Baseline**	**Plate_lateral_15°**	**Plate_lateral_30°**
C1-C2		ISL	ISL
C2-C3	CL	CL	
C3-C4	ALL, CL	ALL, CL	ALL
C4-C5	ALL	ALL	
C5-C6	ALL		
C6-C7			
C7-T1	ISL, LF, CL, PLL	ISL, LF, CL, PLL	ISL, LF, CL, PLL

The Plate_lateral_30° model predicted the least soft tissue injury relative to the two other models (e.g., Plate_lateral_30° model predicted soft tissue failure at 3 of the 7 segment levels). The C7-T1 segment level was the first one to experience soft tissue ligament failure in all three models.

As the lateral angle increased from 0° to 15° to 30°, the onset of ligament failure was delayed at that segment level. Similarly, the onset of ligament failure was delayed at the C3-C4 segment level as the lateral angle increased. The Plate_lateral_15° and the Plate_lateral_30° models predicted ligament failure at the C1-C2 segment level (ISL). ISL failure was predicted at the C1-C2 segment level due to the addition of lateral bending that the upper cervical spine experienced, which subjected the ISL at the C1-C2 segment level to more tension, causing it to rupture. ISL rupture at the C1-C2 segment level was not predicted in the baseline model because the lateral bending that occurred was negligible. In addition to the Plate_lateral_30° delaying the onset of ligament failure and reducing the overall occurrence, the model also predicted less ligament failure at the C3-C4 segment level (ALL vs. ALL and CL for the Plate_lateral_15° and baseline models). All models predicted disc avulsion at the C7-T1 segment level.

Summary of Results and Discussion for AP Plate Angle Variation

As the lateral plate angle increased, the lateral offset between the head and T1 increased. The increase in the lateral angle of the impact plate caused lateral bending, which alleviated buckling of the spine, specifically observed in the Plate_lateral_30° model. Moreover, as the lateral angle increased, the shear force between the head and the impact plate increased and the normal force between the head and the impact plate (head contact force) decreased. The increased surface area associated with the higher lateral angle of the impact plate reduced the head rebound period. The initial peak axial neck force also decreased due to the increased lateral load and deformation, which reduced the axial load. The reduced load associated with the greater lateral angle reduced the overall occurrence of hard and soft tissue injuries. Furthermore, the onset time of hard and soft tissue injury was delayed. The Plate_lateral_15° and Plate_lateral_30° models, unlike the baseline model, predicted upper cervical spine ligament failure (ISL at C1-C2 segment level) due to the added lateral bending, which imposed more tension on the ligaments causing them to rupture.

4.3.5 Friction Between Head and Impact Plate: Results and Discussion

HFI Progression

Figure 4-49 and Figure 4-50 show the HFI progression from 0-15 ms of the COF_0 and COF_1 models, respectively. There was no distinguishable qualitative difference in the behaviour of the three models during the first 15 ms of HFI. All cervical spines experienced minimal deformation

and buckling during the first 5 ms, and the buckling was more evident during the 5-15 ms interval while the head plastically deformed the leather-wood layer. The C1-C3 vertebrae of all models rotated in extension (with C3 being the buckling transition point), while the C4-C7 vertebrae rotated in flexion.

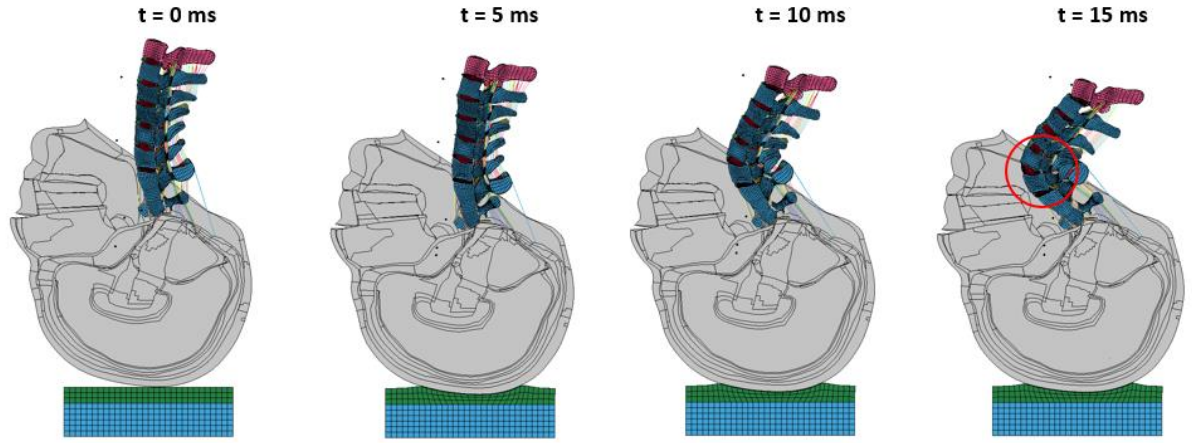

Figure 4-49: HFI progression from 0-15 ms of the COF_0 model with buckling transition point (C3) circled in red

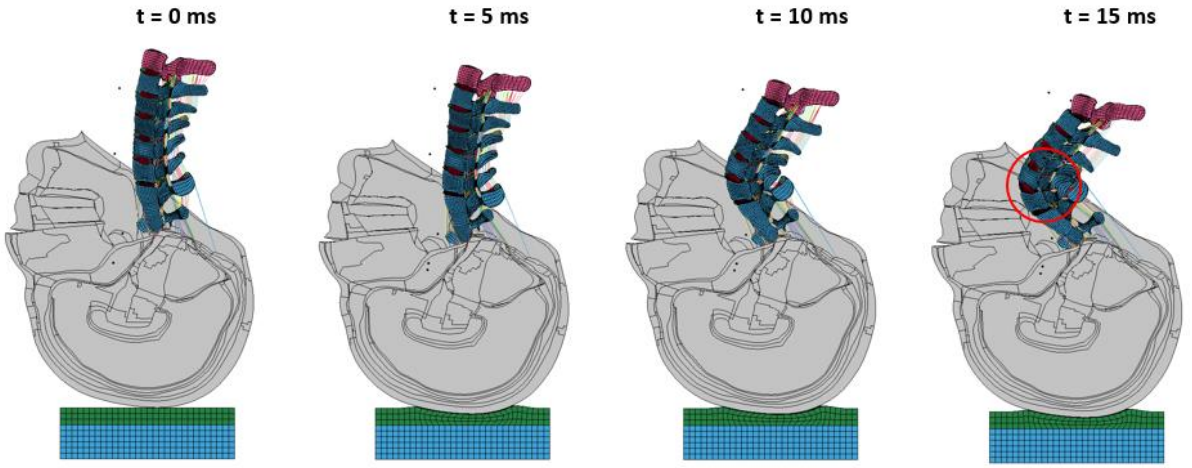

Figure 4-50: HFI progression from 0-15 ms of the COF_1 model with buckling transition point (C3) circled in red

Kinematic Results

During the first 4 ms, the model cervical spines experienced minimal buckling. During the 4-7 ms interval, the COF_1 and baseline models experienced identical buckling behaviour (i.e., the respective vertebrae translated anteriorly by the same amount), but the COF_0 model experienced slightly less buckling during that interval. The COF_0 model experienced less buckling because the head in the model rotated more in extension, which resulted in it translating posteriorly (as opposed to anterior translation for the other two models). The posterior translation of the head resulted in less anterior translation of C1 and C2 and less extension rotation C2, which led to reduced overall buckling of the cervical spine. All three models experienced abrupt buckling (most of the buckling occurred during the 5-7 ms interval).

Kinetic Results

Figure 4-51 shows the head contact force history plots, and Table 4-27 summarizes the head contact force metrics extracted from the plots.

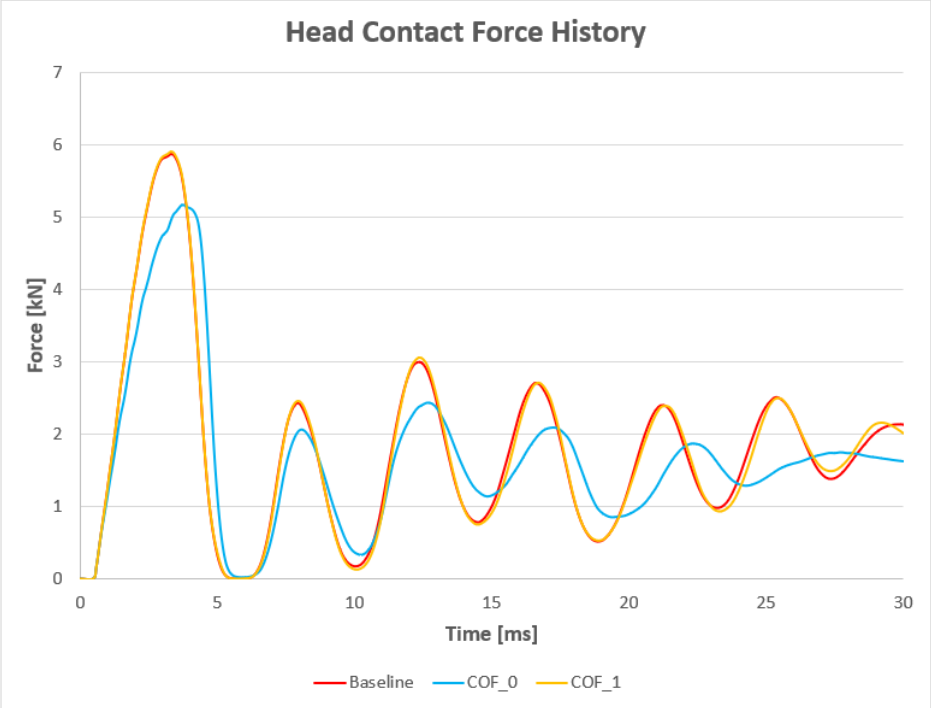

Figure 4-51: Head contact force history plots of baseline, COF_0, and COF_1 models

Table 4-27: Head contact force metrics corresponding to baseline, COF_0, and COF_1 models

Head Contact Force Metrics		
GHBMC Model	**Initial peak head contact force (kN)**	**Slope of initial head contact force rise time (kN/ms)**
Baseline	5.9	2.1
COF_0	5.2	1.6
COF_1	5.9	2.1

The head contact force plots of the baseline and COF_1 models were identical: both models had the same initial peak head contact force (5.9 kN), slope of initial head contact force rise time (2.1 kN/ms), and the same trend. The same trend was observed because the difference between the coefficient of friction at the impact interface between the two models was not significant, therefore the head kinematics were similar, which resulted in almost identical head contact force plots. The trend entailed an initial peak force followed by a force decrease and a sinusoidal force plateau around 1.5 kN. The COF_0 model had a lower initial peak head force (5.2 kN < 5.9 kN) and a lower initial head contact force rise time slope (1.6 < 2.1). The lower force and slope were due to the lower friction at the impact interface of COF_0 providing more translational freedom to the head; the head in COF_0 had more vertical displacement into the leather-wood layer. With the increased displacement into the layer, the contact surface increased, which in turn decreased the slope of the force rise time (due to the higher plastic deformation) and decreased the initial peak head contact force.

Changing the friction at the impact interface had a minimal effect on the initial peak axial force. Moreover, all three models had the same trend, slope of initial axial neck force rise time, and time from head impact to the onset of neck force rise time. However, the COF_0 model had a slightly lower time from head impact to initial peak axial force (relative to the other two models), which can be associated with the reduced overall buckling.

Hard Tissue Injury Risk

The onset of failure for all GHBMC model configurations was at the cortical bone of C2 located at the tip of the dens. Figure 4-52 shows the effective plastic strain fringe plots of the cortical bone of C2 at the onset of injury of all model configurations alongside the baseline model for reference.

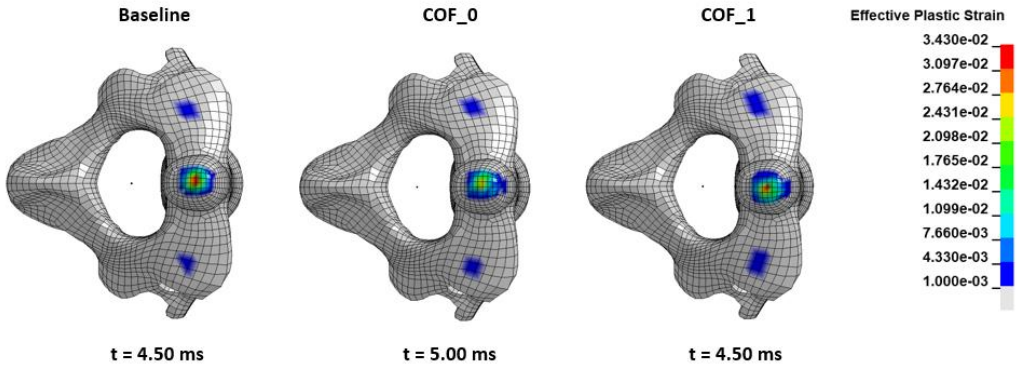

Figure 4-52: Effective plastic strain fringe plots (superior view) of Baseline, COF_0, and COF_1 models

As the friction at the interface increased from 0 (COF_0) to 0.6 (Baseline), the onset of hard tissue injury occurred earlier. The earlier injury occurrence was attributed to the slightly lower axial force across the cervical spine, which resulted in less stress and injury. As the friction was increased further from 0.6 to 1.0 (COF_1), the onset of hard tissue failure was unaffected due to the similar kinetic response predicted in both (Baseline and COF_1).

Soft Tissue Injury Risk

The C7-T1 and C3-C4 segment levels were the first ones that experienced ligament failure in all three models. The COF_0 model slightly delayed the onset of ligament failure at these two segment levels relative to the two other models (7.5 ms > 7.0 ms). All models predicted the same ligaments to fail at all segment levels, and all predicted disc avulsion at the C7-T1 segment level. Overall, changing friction at the impact interface did not have a significant effect on the occurrence and timing of ligament failure and disc avulsion.

Summary of Results and Discussion for Coefficient of Friction between Head and Plate Variation

As friction at the impact interface increased from 0 to 1, the gross kinematic behaviour of the cervical spine was unaffected. However, the COF_0 model exhibited slightly less overall buckling relative to the other two models. The model experienced less buckling due to the posterior translation of the head, which reduced the extension rotation of the upper cervical spine, thereby slightly reducing the buckling across the entire cervical spine. There was more plastic deformation of the leather-wood layer observed in the COF_0 model, which decreased the slope of the head contact force rise time and decreased the initial peak head contact force. The head contact force

response of the COF_1 and baseline models were identical. For the axial neck compressive force, varying the friction at the interface only reduced the time from head impact to the initial peak axial neck force of the COF_0 model relative to the two other models. The time was reduced due to the slightly reduced buckling, which altered the axial load transfer across the cervical spine. Moreover, due to the slightly lower initial peak axial force, the COF_0 model slightly delayed the onset of hard tissue injury. Varying the friction at the interface did not affect the prediction of soft tissue occurrence and onset at all segment levels. Additionally, all three models predicted disc avulsion at the C7-T1 segment level.

4.3.6 Anteroposterior Head Angle: Results and Discussion

HFI Progression

Figure 4-53 -Figure ***4-55*** show the HFI progressions from 0-7 ms of the Head_angle_0°, Head_angle_20°, and Head_angle_30° models, respectively. There was no distinguishable qualitative difference between the HFI progressions of the aforementioned models. The C1-C3 vertebrae rotated in extension (with the C3 vertebra being the buckling transition point) and the C4-C7 vertebrae rotated in flexion for all models. During the first 5 ms, the cervical spines experienced minimal buckling while the heads plastically deformed the leather-wood layer. During the 5-15 ms interval, cervical spine buckling was more evident (especially around C3) in all three models as well as the baseline model.

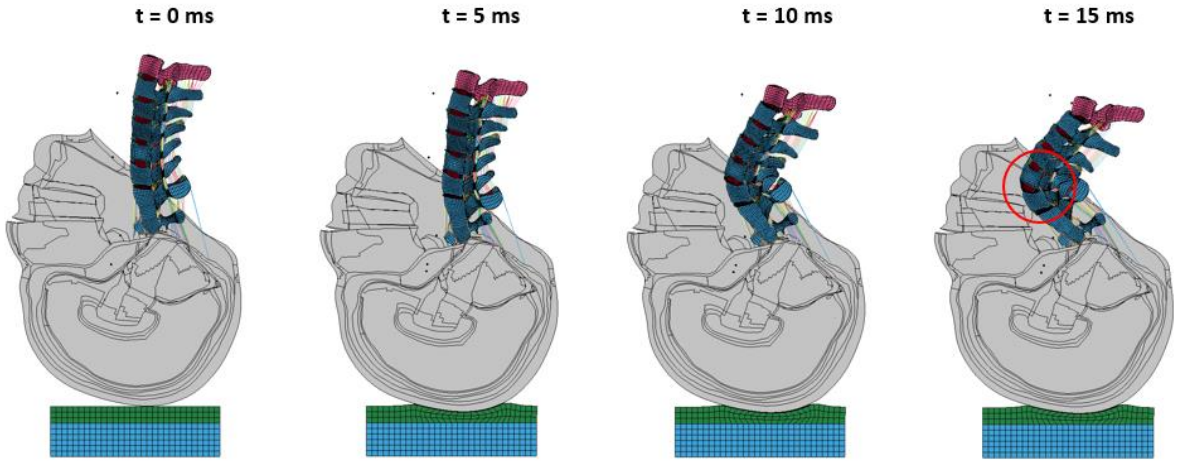

Figure 4-53: HFI progression from 0-7 ms of Head_angle_0° model with buckling transition point (C3) circled in red

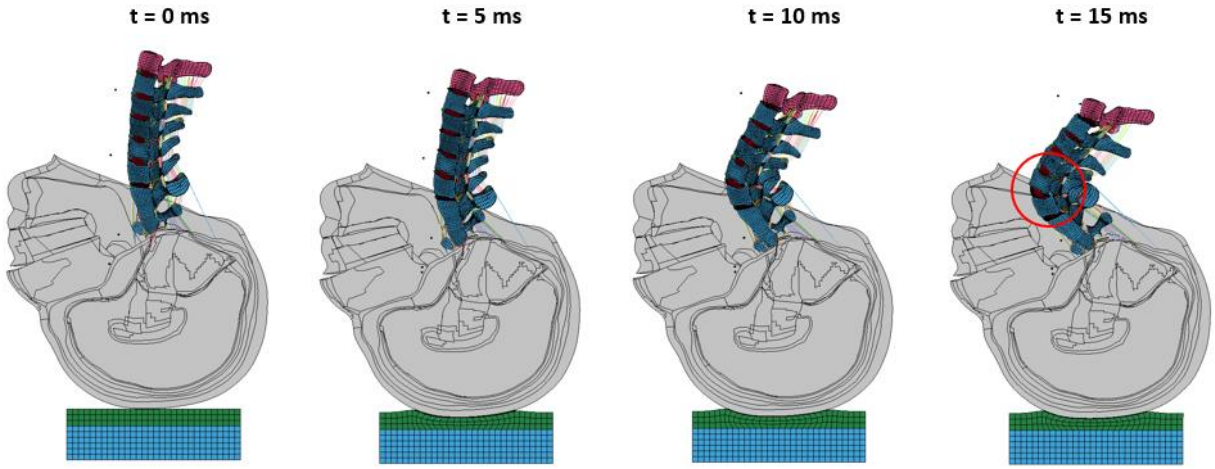

Figure 4-54: HFI progression from 0-7 ms of Head_angle_20° model with buckling transition point (C3) circled in red

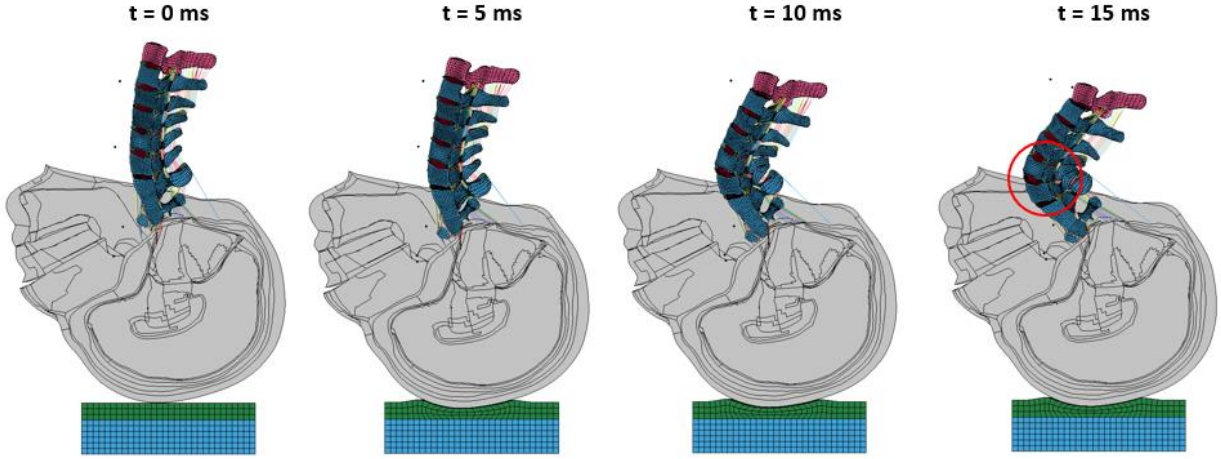

Figure 4-55: HFI progression from 0-7 ms of Head_angle_30° model with buckling transition point (C3) circled in red

Kinematic Results

Figure 4-56 shows the kinematic plots from 0-7 ms of the model cervical spines overlaid on top of the baseline cervical spine for comparison. Table 4-28 summarizes the kinematic data extracted from the aforementioned plots pertaining to the buckling parameter increase between every consecutive millisecond.

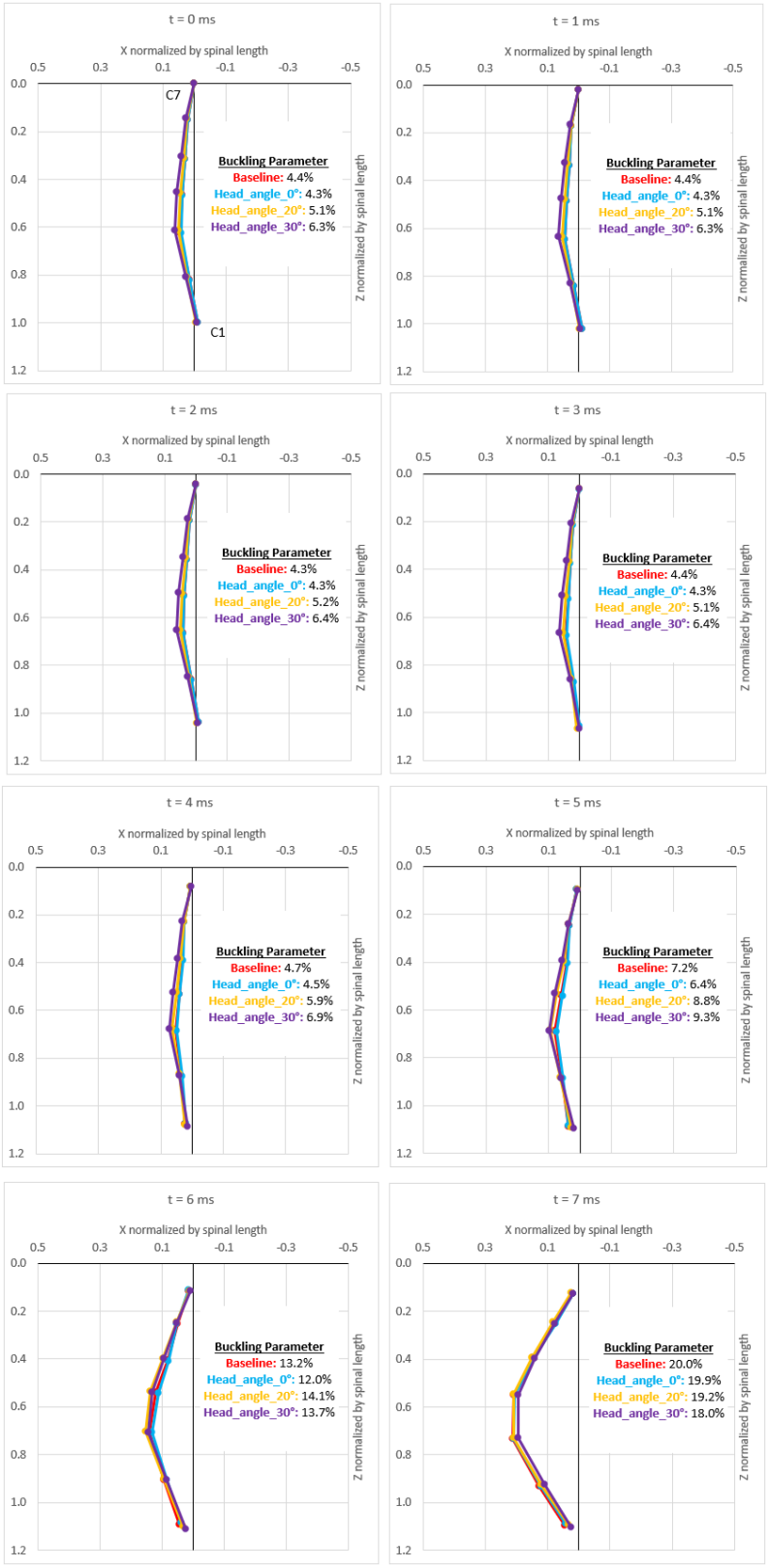

Figure 4-56: Kinematic plots from 0-7 ms for the baseline, Head_angle_0°, Head_angle_20°, and Head_angle_30° models

Table 4-28: Buckling parameter increase throughout the first 7 ms of loading for the baseline, Head_angle_0°, Head_angle_20°, and Head_angle_30° models

Buckling Parameter Increase Throughout First 7 ms of Loading			
Model	Average of buckling parameter increases (%)	Greatest buckling parameter increase (%)	Time interval corresponding to greatest increase (ms)
Baseline	2.2	6.8	6-7
Head_angle_0°	2.2	7.9	6-7
Head_angle_20°	2.0	5.3	5-6
Head_angle_30°	1.7	4.4	5-6

During the first 4 ms after head impact, the model cervical spines did not experience buckling (consistent with qualitative findings from HFI progressions). During the 4-7 ms interval where buckling occurred, the cervical spine of the Head_angle_30° model experienced the least amount of buckling relative to the other models, followed by the Head_angle_20°, baseline, and Head_angle_0° models (in that order). There was less buckling observed in the Head_angle_30° model due to the head in the Head_angle_0° and baseline models rotating in extension during the first 7 ms, which in turn increased the anterior displacement of the upper cervical spine and accentuated the overall buckling across the entire cervical spine. The head in the Head_angle_20° and Head_angle_30° models did not experience any rotation during the first 7 ms due to their initially rotated orientation, which resulted in less anterior displacement of the upper cervical spine relative to the other two models and less overall buckling. Moreover, the C2 in the Head_angle_30° model experienced less extension rotation than C2 in Head_angle_20°, which led to less buckling in the former. The time interval corresponding to the greatest buckling parameter increase was 6-7 ms for the baseline and Head_angle_0° models (lower head angles) and was 5-6 ms for the Head_angle_20° and Head_angle_30° models (greater head angles). These time intervals indicated that the increased curvature made the buckling more gradual over the span of 7 ms of loading. The buckling was more gradual because as the initial curvature increased with the head angle, (Head_angle_20° and Head_angle_30°) the buckling was more distributed across the cervical spine thereby not allowing for an abrupt initiation as was the case for the straighter cervical spines (Head_angle_0° and baseline).

Kinetic Results

Figure 4-57 and Figure 4-58 show the head contact force and axial neck compressive force history plots of the models, respectively. Table 4-29 and Table 4-30 summarize the extracted head contact force and axial neck compressive force metrics, respectively.

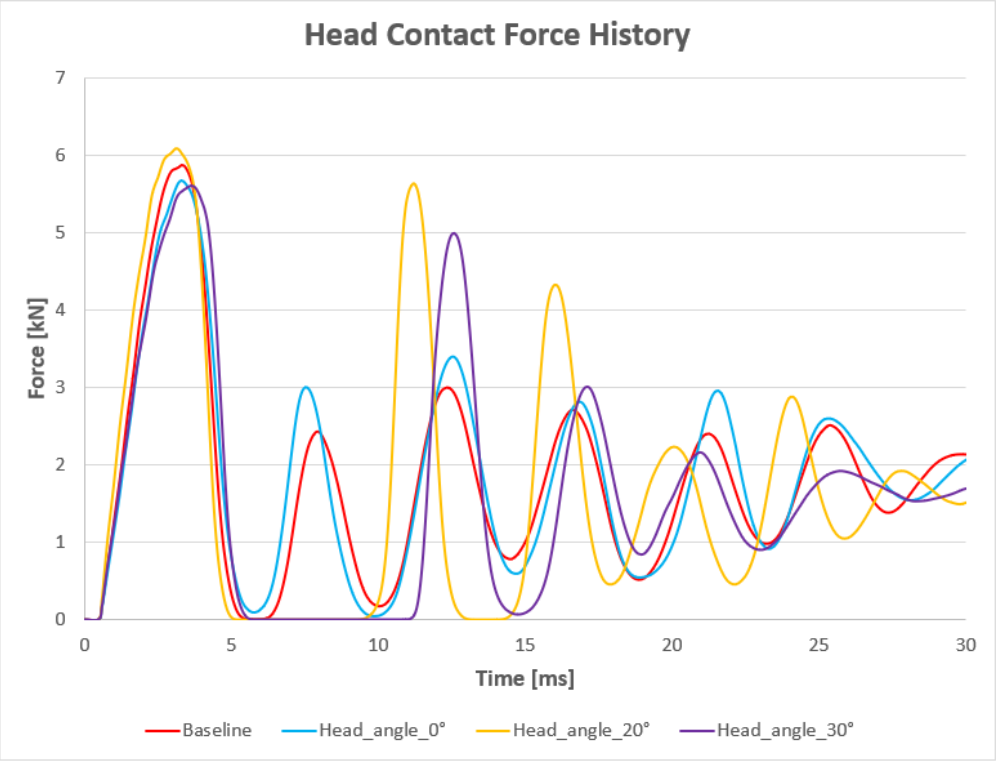

Figure 4-57: Head contact force history plots of baseline, Head_angle_0°, Head_angle_20°, and Head_angle_30° models

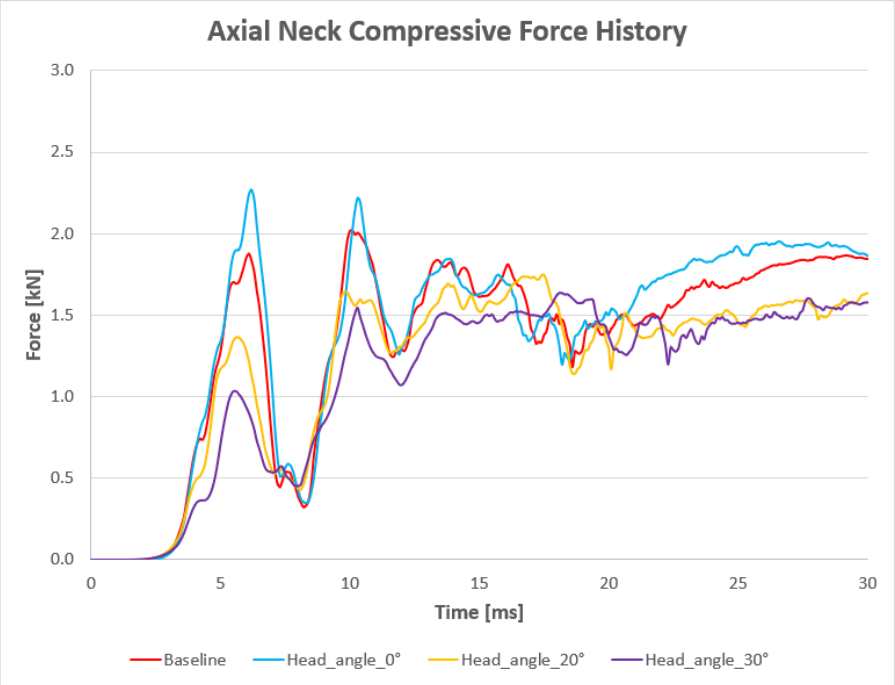

Figure 4-58: Axial neck compressive force history of baseline, Head_angle_0°, Head_angle_20°, and Head_angle_30° models

Table 4-29: Head contact force metrics of baseline, Head_angle_0°, Head_angle_20°, and Head_angle_30° models

Head Contact Force Metrics		
GHBMC Model	**Initial peak head contact force (kN)**	**Slope of initial head contact force rise time (kN/ms)**
Baseline	5.9	2.1
Head_angle_0°	5.7	2.0
Head_angle_20°	6.1	2.3
Head_angle_30°	5.6	1.8

Table 4-30: Axial neck compressive force metrics of baseline, Head_angle_0°, Head_angle_20°, and Head_angle_30° models

Axial Neck Compressive Force Metrics				
GHBMC Model	**Initial peak axial force (kN)**	**Slope of initial neck force rise time (kN/ms)**	**Time from head impact to initial peak axial neck force (ms)**	**Time from head impact to neck force rise time (ms)**
Baseline	1.9	0.5	5.6	2.1
Head_angle_0°	2.3	0.6	5.7	2.1
Head_angle_20°	1.4	0.4	5.2	1.8
Head_angle_30°	1.0	0.3	5.0	1.8

As the head angle increased, the centre of gravity of the head became more posterior relative to the centre of mass of T1 (where the effective torso mass was applied). The head centre of mass was more anterior than the centre of mass of T1 in all models except for Head_angle_30° (where the head was more posterior). The posterior orientation of the head in Head_angle_30° increased the extension rotation of C1 after 3 ms relative to the other three models, which provided more translational freedom for the head to rebound and thereby reduce the peak load. Moreover, the head rebound period corresponding to Head_angle_30° was the longest out of the models. For the remainder of the models where the head was more anterior than T1, the Head_angle_20° had the highest head contact force peak, followed by the baseline model and the Head_angle_0° model. The x (anteroposterior) offset between the centres of mass of T1 and the head for the Head_angle_20° model was the least out of the 3 remaining models, which led to a higher peak load and reduced head rebound period. The second greatest x offset corresponded to the baseline model, leading it to have the second highest peak force. The same applied to the Head_angle_0° model. The slopes of the initial head contact force rise time followed the same order as the aforementioned initial peak head contact force values.

As the head angle increased, the initial peak axial force decreased. Moreover, the slope of the initial neck force rise time in addition to the time from head impact to initial peak axial neck force decreased. This decrease was associated with the higher cervical spine curvature that was resultant from the increased head angle. Similar to the discussion for the C7 angle (subsection 4.3.1), as the initial cervical spine curvature increased, the axial stiffness of the cervical spine decreased, and the shear (anteroposterior) force increased. As a result, the initial peak axial force decreased as the head angle and cervical spine curvature increased. Moreover, unlike what was inferred from subsection 4.3.1, the slope of the initial neck force rise time decreased with the increasing head angle because the increase in curvature affected the entire cervical spine, which in turn reduced the axial load transmission. The time from head impact to neck force rise time corresponding to the baseline and Head_angle_0° models were equal (2.1 ms), and the same was predicted for the Head_angle_20° and Head_angle_30° models.

Hard Tissue Injury Risk

Figure 4-59 shows the effective plastic strain fringe plots of the cortical bone of C2 at the onset of injury of all model configurations alongside the baseline model for reference.

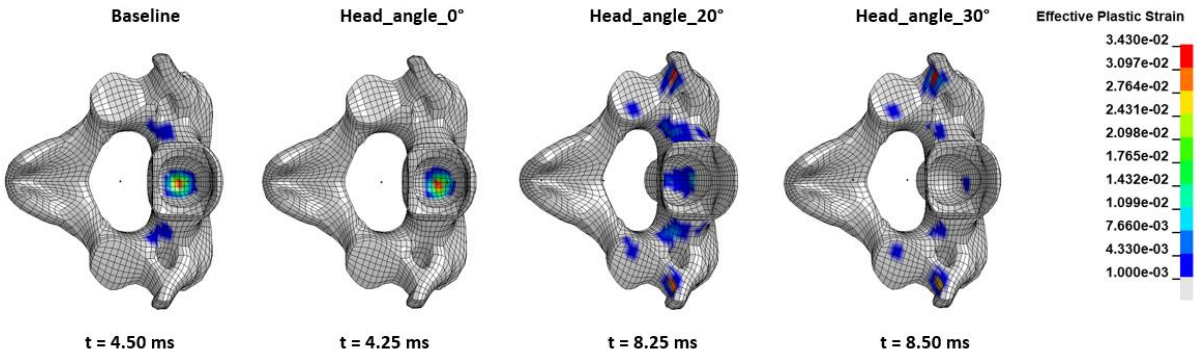

Figure 4-59: Effective plastic strain fringe plots (inferior view) of Baseline, Head_angle_0°, Head_angle_20°, and Head_angle_30° models

As the head angle increased, the onset time of hard tissue injury was delayed. The delay in injury was in part attributed to the reduced axial load on the cervical spine associated with greater head angles. The onset of hard tissue injury occurred at the tip of the dens for the Baseline and Head_angle_0° models due to the impact with the base of the skull following extension rotation of C2. As the head angle increased (i.e., head rotated in extension), the initial distance between the tip of the dens and the base of the skull increased, which reduced the impact force between the tip of the dens and the base of the skull. However, contact between the two surfaces still occurred due to the extension rotation of C2 (indicated by the blue regions in Head_angle_20° and Head_angle_30° in Figure 4-59). As a result of the reduced impact force at the dens-skull base interface in the Head_angle_20° and Head_angle_30° models, the onset of hard tissue injury occurred at the transverse processes instead (indicated by the red regions in Head_angle_20° and Head_angle_30° in Figure 4-59). Hard tissue failure occurred at the transverse processes due to the superior articular processes of C3 impacting the transverse processes of C2 later in the loading process (roughly 8.0-8.5 ms after head impact).

Soft Tissue Injury Risk

Figure 4-60 shows the onset times of ligament failure for all segment levels of the three models, and Table 4-31 identifies which ligaments failed at every segment level.

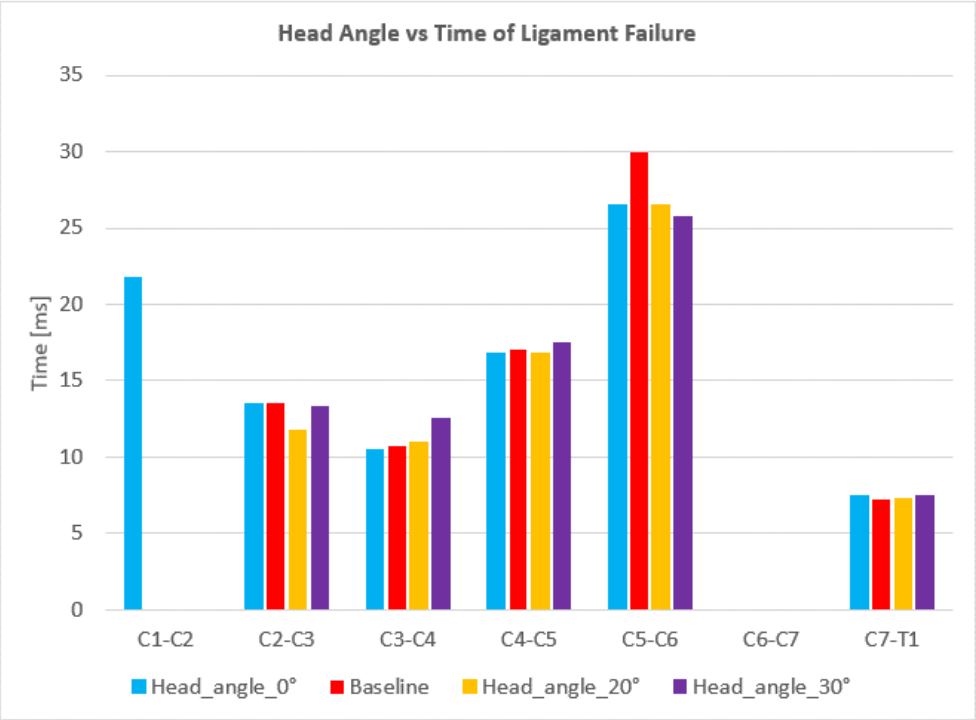

Figure 4-60: Onset times of ligament failure of all segment levels for baseline, Head_angle_0°, Head_angle_20°, and Head_angle_30° models

Table 4-31: Location of ligament failure at every segment level for baseline, Head_angle_0°, Head_angle_20°, and Head_angle_30° models

Ligament Failure				
Level	Baseline	Head_angle_0°	Head_angle_20°	Head_angle_30°
C1-C2		ISL		
C2-C3	CL	CL	ALL, CL	ALL, CL
C3-C4	ALL, CL	ALL, CL	ALL, CL	ALL, CL
C4-C5	ALL	ALL	ALL	ALL
C5-C6	ALL	ALL	ALL	ALL
C6-C7				
C7-T1	ISL, LF, CL, PLL	ISL, LF, CL, PLL	ISL, LF, CL, PLL	ISL, LF, CL, PLL

As the head angle increased, the onset time of ligament failure increased only for the C3-C4 and C4-C5 segment levels. Moreover, the soft tissue injury predictions at those segment levels were the same for all the models (ALL and CL for C3-C4, and ALL for C4-C5). Similar to hard tissue

injury, the Head_angle_0° model was the only one that predicted ligament failure at the C1-C2 segment level (ISL). Increasing the head angle did not have a clear effect on the onset time of ligament failure for the remainder of the segment levels. Moreover, all the models predicted the same ligaments to fail across the respective segment levels (e.g., all models predicted ALL failure for the C5-C6 segment level, etc.). All the models predicted disc avulsion at the C7-T1 segment level.

Summary of Results and Discussion for AP Head Angle Variation

As the head angle increased, cervical spine buckling decreased due to the reduced anterior displacement of the upper cervical spine. Additionally, the buckling associated with the greater head angles was more gradual due to the increased cervical spine curvature. Increasing the head angle increased the cervical spine curvature, which reduced the axial stiffness of the cervical spine, the initial peak axial load, as well as the slope of the initial neck force rise time. The head angle did not have a consistent effect on the initial peak head contact force: the Head_angle_20° had the highest peak head contact force because of the smallest x offset between the head and T1 (where the effective torso mass was applied). The reduced axial force associated with the increasing head angle delayed the onset of hard tissue injury and changed the location as well (from dens to transverse processes). Varying the head angle did not have a significant effect on the occurrence or onset of soft tissue injury, nor on disc avulsion at the C7-T1 segment level; all models predicted disc avulsion at that level.

4.3.7 Sensitivity Study of Head-First Impact Parameters: Summary and Discussion

The impact velocity had the greatest influence on the cervical spine response and injury during HFI loading, followed by the lateral impact plate angle, AP angle of the head, cervical spine curvature, AP impact plate angle, and the coefficient of friction at the impact interface (in that order). The impact velocity had the greatest influence on cervical spine response and injury as it was the only parameter that directly changed the input energy, thereby playing an important role in the resultant kinetic and kinematic response of the cervical spine. Varying the lateral plate angle influenced the kinematic behaviour of the head and introduced lateral deformation and loading into the model, which alleviated the buckling and axial loads, leading to fewer hard and soft tissue injuries. Changing the head AP angle had a strong effect on the cervical spine response during HFI

as it also changed the cervical spine curvature, and as a result affected the load transfer and injury occurrence. Changing the cervical spine curvature also had a notable effect on the response and injury risk of the cervical spine during loading. The AP plate angle slightly alleviated the axial load on the cervical spine and helped delay some hard and soft tissue injuries. Lastly, the friction at the interface was not predicted to have a significant effect on the response of the cervical spine during HFI loading. The fact that the interface friction was a significant factor like the remaining parameters was attributed to the significant plastic deformation of the leather-wood layer that restricted the relative motion of the head during impact.

Chapter 5: Conclusion and Recommendations

5.1 Conclusion

The GHBMC neck model was developed for occupant safety purposes and was successfully adapted for assessment of HFI in this study. Model validation against HFI required the removal of certain soft tissues (such as passive musculature and the spinal cord) in order to replicate the reported specimen setup details, as well as ensuring other initial and boundary conditions (such as initial cervical spine curvature and effective torso mass) were represented in the model. Hard tissue failure was defined through two options: failure on and failure off. The failure on option eroded solid and shell elements once they reached their respective failure effective plastic strain values, whereas the failure off option did not erode the elements upon reaching the threshold values. Both failure options were considered for model validation and only the failure off option was implemented in the sensitivity study. Ligament rupture was defined by the tensile displacement at failure and disc avulsion was defined by the ultimate stress at failure. The validation results indicated that the model was suitable in predicting response and injury risk due to HFI and the sensitivity study results identified factors that influenced the response and injury risk of the cervical spine during HFI loading (which addressed the limitation in previous experimental HFI studies). The analysis presented in this study also addressed the limitations in previous numerical HFI studies: soft tissue injuries were extracted and analyzed, and the kinematic response was quantitatively investigated using the buckling parameter and the sagittal cervical spine traces.

The model validation entailed result extraction and analysis of the models with hard tissue failure turned off (GHBMC_Saari and GHBMC_Nightingale) and hard tissue failure turned on (GHBMC_Saari_failON and GHBMC_Nightingale_failON). Both failure options were considered in order to bound hard tissue injury prediction (failure off was the upper bound and failure on was the lower bound (Chapter 3)), discuss the respective limitations, and subsequently select an appropriate failure option to apply for the sensitivity study simulations. The failure off option was ultimately selected for the sensitivity study. The key findings from the validation against experimental results from Saari and Nightingale as well as the sensitivity study are summarized below.

5.1.1 Computational Neck Model Validation Summary Using Experimental Data from Saari

Kinetics: Axial Neck Compressive Force

- **Good agreement was predicted** because the model and experimental traces had equal peak forces (1.9 kN) and comparable slopes of initial neck force rise time (0.5 kN/ms model slope vs. 0.8 kN/ms $\pm$ 0.4 kN/ms experimental slope), and comparable trends.

Kinetics: Head Contact Force

- **Poor agreement was predicted** because the model traces had lower peak head contact forces (more than 3,500 N) and lower slopes of the initial head contact force rise time.
- The lower force and slope of the models was attributed to the impact interface with the leather-wood layer (used to eliminate head rebound) which significantly dampened the impact force and consequently impeded the axial load transfer to the head from the cervical spine.

Kinematics

- **Good agreement was predicted** because the cervical spine of the models and experiment experienced first order buckling with a buckling transition point occurring at the middle cervical spine (C3-C4). However, the models experienced abrupt buckling (mostly during the 5-7 ms interval) compared to the more consistent experimental buckling (the buckling parameter increased at a near constant rate throughout the first 7 ms of loading).

Hard Tissue Injury Risk

- **Good agreement was predicted** because the model and experiment had comparable onset time of injury (4.0 ms model time vs. 4.9 ms $\pm$ 1.1 ms experimental time) and vertebral injury location (laminar and spinous process fractures of C3 and C4).

Soft Tissue Injury Risk

- **Good agreement was predicted** because the model and experiment had comparable ligament rupture location (ALL and ISL ruptures at the C3-C4 and C4-C5 segment levels).

5.1.2 Computational Neck Model Validation Summary Using Experimental Data from Nightingale

Kinetics: Axial Neck Compressive Force

- **Good agreement was predicted** because the model and experimental traces had comparable peak forces (2.1 kN model force vs. 2.6 kN $\pm$ 1.2 kN experimental force) and slopes of initial neck force rise time (1.6 kN/ms model slope vs. 1.5 kN/ms $\pm$ 0.5 kN/ms experimental slope).

Kinetics: Head Contact Force

- **Poor agreement was predicted** because the peak head contact force of the model was higher than the experimental peak force due to the head rebound that occurred in the model which indicated the presence of high elastic energy at the interface upon impact.

Kinematics (qualitative)

- **Poor agreement was predicted** because the model rebounded off the impact plate, whereas the experimental kinetic plots indicated that head rebound did not occur following impact with the plate.

Hard Tissue Injury Risk

- **Good agreement was predicted** because the model and experiment had comparable onset time of injury (3.0 ms model time vs. 4.4 $\pm$ 3.0 ms experimental time) and vertebral injury location.

Soft Tissue Injury Risk

- Analysis and comparison were not conducted because experimental soft tissue injuries were not reported.

5.1.3 Summary of Sensitivity Study Results

The order of HFI parameters from greatest to least influence on cervical spine response (with an elaboration of the top 3 parameters) is listed below.

1. Impact velocity
    - Increasing the impact velocity from 1 m/s to 5 m/s had the greatest influence as it was the only parameter that directly changed the input energy, thereby leading to higher loading and more hard and soft tissue injuries
    - Impact velocities up to 2 m/s were predicted to result in minimal hard and soft tissue injury during HFI loading
2. Lateral impact plate angle
    - Increasing the lateral angle of the impact plate (a factor which has not been assessed previously in experimental studies) from 0° to 30° introduced lateral (shear) deformation into the model which alleviated the buckling (in the sagittal plane) and axial load, leading to fewer hard and soft tissue injuries
    - Impacting a surface at a lateral angle greater than 15° (as opposed to vertex impact, for example) can reduce the risk of injury due to the lateral component of the load
3. AP head angle
    - Increasing the AP head angle (the influence of which has not been previously quantified) from 0° to -30° (negative sign indicating head extension) increased the cervical spine curvature as well, and as a result reduced the axial stiffness of the cervical spine and reduced the axial loading and amount of hard and soft tissue injury
    - Impacting a surface with the head pre-extended with Frankfort angle greater than 20° was predicted to reduce the risk of hard and soft tissue injury as well as the axial load across the cervical spine and the degree of buckling
    - Alternatively, impacting a surface with the head pre-flexed (Frankfort plane angle < 5°) was predicted to increase the risk of injury and loading on the cervical spine during HFI
4. Cervical spine curvature
5. AP impact plate angle
6. Coefficient of friction between the head and impact plate

HFI has been previously researched and investigated (both numerically and experimentally); however, there were associated limitations with these studies which have been addressed in this thesis. Important findings from the model validation and sensitivity study are summarized below. The findings can serve as additional foundational knowledge that can help characterize the complex kinematics of the cervical spine during HFI and inform further research in this field.

- The buckling parameter (percentage ratio of the sagitta to the chord length of the cervical spine) was a useful tool in quantifying and measuring the buckling of the cervical spine
    - It also provided understanding as to how abruptly or gradually the cervical spine experienced buckling
- There was a good correlation between the anterior velocity of the buckling transition point and the amount of buckling (quantified by the anterior displacement of the vertebrae and the value of the buckling parameter)
    - As the anterior velocity of the buckling transition point increased, the cervical vertebrae displaced more anterior and buckling increased
    - As the anterior velocity of the buckling transition point slowed down to a peak value (followed by a velocity decrease or plateau), the buckling decreased and slowed down and the cervical spine achieved an eventual transient 'locked state'
- Identifying when the buckling occurred (by observing the changes in the buckling parameter) helped explain trends in the axial neck compressive force plots
    - When the buckling increased, the axial force decreased (due to reduced axial stiffness of the cervical spine associated with the buckling)
    - When the buckling slowed down and the cervical spine reached an eventual locked state, the axial neck force trace simultaneously reached a peak value
- Overall, understanding the kinematic response by quantifying the buckling behaviour helped explain the kinetic response of the cervical spine which in turn facilitated understanding hard and soft tissue injury outcome
    - Moreover, the kinematic behaviour helped infer why certain ligaments ruptured (by observing and identifying the relative extension or flexion rotation of adjacent vertebrae)

- Contrary to a previous experimental study [Nusholtz et al., 1981], head motion was predicted to play an important role in the response of the cervical spine during HFI (as was shown for the lateral plate angle and AP head angle parameters)

5.2 Recommendations

Although this study provided additional information to better characterize the complex kinematic response of the cervical spine during HFI, there were model limitations that must be addressed and recommendations (based on the limitations) to be made.

The development of a failure model for predicting hard tissue failure, particularly for visualizing and representing vertebral fracture initiation and propagation, is recommended to extract hard tissue injury from numerical models and understand the overall hard tissue injury outcome during HFI loading. The development of such a failure model is important as the failure options implemented in this study had their respective limitations for accurately predicting hard tissue injury risk.

The GHBMC_Nightingale model predicted head rebound at the impact interface between the head and steel impact surface. The GHBMC_Saari model predicted significant plastic deformation (~ 6 mm) of the leather-wood layer that was modelled to eliminate head rebound. Therefore, investigation into controlling or dissipating the elastic energy at the interface that leads to head rebound without significantly dampening the impact is recommended.

The biggest discrepancy in the validation against the Saari experimental results was that the surrogate head used in the drop tests was not modelled. The surrogate head was not modelled because the full information/data required to do so was not available. The absence of the surrogate head in the model affected the impact at the interface and the resultant response of the cervical spine during HFI.

The effect of active and passive musculature should be investigated owing to their anatomical and structural importance and how that can play a role in affecting the response of the cervical spine

during HFI loading. Active and passive musculature were removed from the GHBMC model in accordance with the specimen preparation details reported in the experimental studies by Saari and Nightingale. However, the inclusion of active muscles changes the pre-impact cervical spine curvature [Newell et al. 2013]. Passive muscles, on the other hand, can play a role in stabilizing the cervical spine during HFI, which would in turn limit the buckling due to the tissue directly surrounding the vertebrae and consequently influence the kinetic response and injury outcome. The inclusion of muscles provides a more accurate representation of occupants in real-life HFI scenarios and can help explain the high incidence of injuries reported epidemiologically (such as fracture dislocations at the lower cervical spine) which have not been predicted numerically in this study [Sekhon et al., 2001].

In addition to the numerical recommendations, there are potential areas of further experimental research as well. Experimental studies always used a constant effective torso mass (e.g., 15 kg for Saari specimens) for all specimens regardless of anthropometrics (e.g., age, sex, etc.). It is therefore recommended, wherever possible, to vary the mass depending on the anthropometric properties of the specimens as this is predicted to have an effect on the response of the cervical spine due to the direct influence on compressive force.

Experimental studies usually constrain the motion of the T1 vertebra to vertical translation only (due to potting to the mount cup). This boundary condition is an important factor that significantly affected the response of the cervical spine. However, a HFI experimental study using full body cadavers performed by Roberts et al. suggests that the T1 vertebra experiences rotation and translation in other degrees of freedom. Therefore, in pursuit of better representing real-life HFI scenarios, modifying the T1 boundary condition such that the vertebra has more degrees of freedom is recommended.

The lateral angle of the impact plate is a factor that has not been previously varied or investigated experimentally. However, the work presented in this thesis indicated that the lateral angle of the impact plate is an important factor that has a significant influence on the response of the cervical spine during HFI. Therefore, further research and investigation pertaining to the lateral angle of the impact plate and how it influences the response and injury outcome of the cervical spine during HFI loading is recommended.

Letter of Copyright Permissions

Wolters Kluwer License Terms and Conditions

WOLTERS KLUWER HEALTH, INC. LICENSE
TERMS AND CONDITIONS
Dec 22, 2021

This Agreement between University of Waterloo -- Marwan Darweesh ("You") and Wolters Kluwer Health, Inc. ("Wolters Kluwer Health, Inc.") consists of your license details and the terms and conditions provided by Wolters Kluwer Health, Inc. and Copyright Clearance Center.

License Number	5213761424649
License date	Dec 21, 2021
Licensed Content Publisher	Wolters Kluwer Health, Inc.
Licensed Content Publication	WK Health Book
Licensed Content Title	Cervical Spine
Licensed Content Author	Edward C Benzel MD
Licensed Content Date	Mar 22, 2013
Type of Use	Dissertation/Thesis
Requestor type	University/College
Sponsorship	No Sponsorship
Format	Electronic
Will this be posted online?	Yes, on a secure website
Portion	Figures/tables/illustrations
Number of figures/tables/illustrations	2
Author of this Wolters Kluwer article	No
Will you be translating?	No
Intend to modify/change the content	No

Current or previous edition of book	Current edition
Title	Evaluating Cervical Spine Response and Potential for Injury During Head-First Impact Loading Using a Finite Element Head-Neck Model
Institution name	University of Waterloo
Expected presentation date	Jan 2022
Portions	Figure 1.4B (page 4) and Figure 1.5 (page 5)
Requestor Location	University of Waterloo 155 Highland Crescent B7 Kitchener, ON N2M 0A1 Canada Attn: University of Waterloo
Publisher Tax ID	895524239 RT0001
Total	0.00 CAD

Lippincott Williams and Wilkins License Terms and Conditions

This is a License Agreement between University of Waterloo ("User") and Copyright Clearance Center, Inc. ("CCC") on behalf of the Rightsholder identified in the order details below. The license consists of the order details, the CCC Terms and Conditions below, and any Rightsholder Terms and Conditions which are included below.

All payments must be made in full to CCC in accordance with the CCC Terms and Conditions below.

Order Date

17-Dec-2021

Order License ID

1169814-1

ISSN

0362-2436

Type of Use

Republish in a thesis/dissertation

Publisher

LIPPINCOTT WILLIAMS & WILKINS

Portion

Image/photo/illustration

LICENSED CONTENT

Publication Title

Spine

Article Title

A numerical investigation of factors affecting cervical spine injuries during rollover crashes.

Date

01/01/1976

Language

English, English

Country

United States of America

Rightsholder

Wolters Kluwer Health, Inc.

Publication Type

Journal

Start Page

2529

End Page

2535

Issue

23

Volume

33

REQUEST DETAILS

Portion Type

Image/photo/illustration

Number of images / photos / illustrations

1

Format (select all that apply)

Electronic

Who will republish the content?

Publisher, not-for-profit

Duration of Use

Life of current edition

Lifetime Unit Quantity

Up to 499

Rights Requested

Main product

Distribution

Worldwide

Translation

Original language of publication

Copies for the disabled?

No

Minor editing privileges?

No

Incidental promotional use?

No

Currency

CAD

NEW WORK DETAILS

Title

Evaluating Cervical Spine Injury and Response During Head-First Impact Loading Using a Finite Element Head-Neck Model

Instructor name

Duane Cronin

Institution name

University of Waterloo

Expected presentation date

2022-01-12

ADDITIONAL DETAILS

Order reference number

N/A

The requesting person / organization to appear on the license

University of Waterloo

REUSE CONTENT DETAILS

Title, description or numeric reference of the portion(s)

Figure 1

Editor of portion(s)

Hu, Jingwen; Yang, King H; Chou, Clifford C; King, Albert I

Volume of serial or monograph

33

Page or page range of portion

2529-2535

Title of the article/chapter the portion is from

A numerical investigation of factors affecting cervical spine injuries during rollover crashes.

Author of portion(s)

Hu, Jingwen; Yang, King H; Chou, Clifford C; King, Albert I

Issue, if republishing an article from a serial

23

Publication date of portion

2008-11-01

Pergamon License Terms and Conditions

This is a License Agreement between University of Waterloo ("User") and Copyright Clearance Center, Inc. ("CCC") on behalf of the Rightsholder identified in the order details below. The license consists of the order details, the CCC Terms and Conditions below, and any Rightsholder Terms and Conditions which are included below.

All payments must be made in full to CCC in accordance with the CCC Terms and Conditions below.

Order Date

13-Dec-2021

Order License ID

1168120-1

ISSN

0021-9290

Type of Use

Republish in a thesis/dissertation

Publisher

PERGAMON

Portion

Image/photo/illustration

LICENSED CONTENT

Publication Title

Journal of biomechanics

Article Title

Impact responses of the cervical spine: A computational study of the effects of muscle activity, torso constraint, and pre-flexion.

Author/Editor

UNIVERSITY OF MICHIGAN., AMERICAN SOCIETY OF BIOMECHANICS., EUROPEAN SOCIETY OF BIOMECHANICS.

Date

01/01/1968

Language

English

Country

United Kingdom of Great Britain and Northern Ireland

Rightsholder

Elsevier Science & Technology Journals

Publication Type

Journal

Start Page

558

End Page

564

Issue

4

Volume

49

REQUEST DETAILS

Portion Type

Image/photo/illustration

Number of images / photos / illustrations

1

Format (select all that apply)

Electronic

Who will republish the content?

Academic institution

Duration of Use

Life of current edition

Lifetime Unit Quantity

Up to 499

Rights Requested

Main product

Distribution

Worldwide

Translation

Original language of publication

Copies for the disabled?

No

Minor editing privileges?

No

Incidental promotional use?

No

Currency

CAD

NEW WORK DETAILS

Title

Evaluating Cervical Spine Injury and Response During Head-First Impact Loading Using a Finite Element Head-Neck Model

Instructor name

Duane Cronin

Institution name

University of Waterloo

Expected presentation date

2022-01-12

ADDITIONAL DETAILS

Order reference number

N/A

The requesting person / organization to appear on the license

University of Waterloo

REUSE CONTENT DETAILS

Title, description or numeric reference of the portion(s)

Figure 1

Editor of portion(s)

Nightingale, Roger W.; Sganga, Jake; Cutcliffe, Hattie; Bass, Cameron R. 'Dale'

Volume of serial or monograph

49

Page or page range of portion

558-564

Title of the article/chapter the portion is from

Impact responses of the cervical spine: A computational study of the effects of muscle activity, torso constraint, and pre-flexion.

Author of portion(s)

Nightingale, Roger W.; Sganga, Jake; Cutcliffe, Hattie; Bass, Cameron R. 'Dale'

Issue, if republishing an article from a serial

4

Publication date of portion

2016-02-29

SAE International License Terms and Conditions

This is a License Agreement between University of Waterloo ("User") and Copyright Clearance Center, Inc. ("CCC") on behalf of the Rightsholder identified in the order details below. The license consists of the order details, the CCC Terms and Conditions below, and any Rightsholder Terms and Conditions which are included below.

All payments must be made in full to CCC in accordance with the CCC Terms and Conditions below.

Order Date

13-Dec-2021

Order License ID

1168118-1

System ID

973345

Type of Use

Republish in a thesis/dissertation

Publisher

SAE International

Portion

Image/photo/illustration

LICENSED CONTENT

Publication Title

Experimental Flexibility Measurements for the Development of a Computational Head-Neck Model Validated for Near-Vertex Head Impact

Author/Editor

Camacho, Daniel L.

Date

01/01/1997

Country

United States of America

Rightsholder

SAE International

Publication Type

Report

REQUEST DETAILS

Portion Type

Image/photo/illustration

Number of images / photos / illustrations

1

Format (select all that apply)

Electronic

Who will republish the content?

Academic institution

Duration of Use

Life of current edition

Lifetime Unit Quantity

Up to 499

Rights Requested

Main product

Distribution

Worldwide

Translation

Original language of publication

Copies for the disabled?

No

Minor editing privileges?

No

Incidental promotional use?

No

Currency

CAD

NEW WORK DETAILS

Title

Evaluating Cervical Spine Injury and Response During Head-First Impact Loading Using a Finite Element Head-Neck Model

Instructor name

Duane Cronin

Institution name

University of Waterloo

Expected presentation date

2022-01-12

ADDITIONAL DETAILS

Order reference number

N/A

The requesting person / organization to appear on the license

University of Waterloo

REUSE CONTENT DETAILS

Title, description or numeric reference of the portion(s)

Figure 4

Editor of portion(s)

N/A

Volume of serial or monograph

N/A

Page or page range of portion

473-486

Title of the article/chapter the portion is from

N/A

Author of portion(s)

Camacho, Daniel L.

Issue, if republishing an article from a serial

N/A

Publication date of portion

1997-01-01

Pergamon License Terms and Conditions

This is a License Agreement between University of Waterloo ("User") and Copyright Clearance Center, Inc. ("CCC") on behalf of the Rightsholder identified in the order details below. The license consists of the order details, the CCC Terms and Conditions below, and any Rightsholder Terms and Conditions which are included below.

All payments must be made in full to CCC in accordance with the CCC Terms and Conditions below.

Order Date

13-Dec-2021

Order License ID

1168108-1

ISSN

0021-9290

Type of Use

Republish in a thesis/dissertation

Publisher

PERGAMON

Portion

Image/photo/illustration

LICENSED CONTENT

Publication Title

Journal of biomechanics

Article Title

Neck posture and muscle activity are different when upside down: a human volunteer study.

Author/Editor

UNIVERSITY OF MICHIGAN., AMERICAN SOCIETY OF BIOMECHANICS., EUROPEAN SOCIETY OF BIOMECHANICS.

Date

01/01/1968

Language

English

Country

United Kingdom of Great Britain and Northern Ireland

Rightsholder

Elsevier Science & Technology Journals

Publication Type

Journal

Start Page

2837

End Page

2843

Issue

16

Volume

46

REQUEST DETAILS

Portion Type

Image/photo/illustration

Number of images / photos / illustrations

1

Format (select all that apply)

Electronic

Who will republish the content?

Academic institution

Duration of Use

Life of current edition

Lifetime Unit Quantity

Up to 499

Rights Requested

Main product

Distribution

Worldwide

Translation

Original language of publication

Copies for the disabled?

No

Minor editing privileges?

No

Incidental promotional use?

No

Currency

CAD

NEW WORK DETAILS

Title

Evaluating Cervical Spine Injury and Response During Head-First Impact Loading Using a Finite Element Head-Neck Model

Instructor name

Duane Cronin

Institution name

University of Waterloo

Expected presentation date

2022-01-12

ADDITIONAL DETAILS

Order reference number

N/A

The requesting person / organization to appear on the license

University of Waterloo

REUSE CONTENT DETAILS

Title, description or numeric reference of the portion(s)

Figure 3

Editor of portion(s)

Newell, Robyn S.; Blouin, Jean-Sébastien; Street, John; Cripton, Peter A.; Siegmund, Gunter P.

Volume of serial or monograph

46

Page or page range of portion

2837-2843

Title of the article/chapter the portion is from

Neck posture and muscle activity are different when upside down: a human volunteer study.

Author of portion(s)

Newell, Robyn S.; Blouin, Jean-Sébastien; Street, John; Cripton, Peter A.; Siegmund, Gunter P.

Issue, if republishing an article from a serial

16

Publication date of portion

2013-11-15

Springer License Terms and Conditions

This is a License Agreement between University of Waterloo ("User") and Copyright Clearance Center, Inc. ("CCC") on behalf of the Rightsholder identified in the order details below. The license consists of the order details, the CCC Terms and Conditions below, and any Rightsholder Terms and Conditions which are included below.

All payments must be made in full to CCC in accordance with the CCC Terms and Conditions below.

Order Date

13-Dec-2021

Order License ID

1168090-1

ISBN-13

978-1-4939-1731-0

Type of Use

Republish in a thesis/dissertation

Publisher

Springer New York

Portion

Image/photo/illustration

LICENSED CONTENT

Publication Title

Accidental Injury

Article Title

Neck Injury Biomechanics. 11

Date

01/01/2015

Language

English

Country

United States of America

Rightsholder

Springer

Publication Type

Book

Start Page

259

End Page

308

URL

http://link.springer.com/10.1007/978-1-4939-1732-7

REQUEST DETAILS

Portion Type

Image/photo/illustration

Number of images / photos / illustrations

3

Format (select all that apply)

Electronic

Who will republish the content?

Academic institution

Duration of Use

Life of current edition

Lifetime Unit Quantity

Up to 499

Rights Requested

Main product

Distribution

Worldwide

Translation

Original language of publication

Copies for the disabled?

No

Minor editing privileges?

No

Incidental promotional use?

No

Currency

CAD

NEW WORK DETAILS

Title

Evaluating Cervical Spine Injury and Response During Head-First Impact Loading Using a Finite Element Head-Neck Model

Instructor name

Duane Cronin

Institution name

University of Waterloo

Expected presentation date

2022-01-12

ADDITIONAL DETAILS

Order reference number

N/A

The requesting person / organization to appear on the license

University of Waterloo

REUSE CONTENT DETAILS

Title, description or numeric reference of the portion(s)

Figures 5, 6, and 7

Editor of portion(s)

Nightingale, Roger W.; Yoganandan, Narayan; Myers, Barry S.

Volume of serial or monograph

N/A

Page or page range of portion

259-308

Title of the article/chapter the portion is from

Neck Injury Biomechanics. 11

Author of portion(s)

Nightingale, Roger W.; Yoganandan, Narayan; Myers, Barry S.

Issue, if republishing an article from a serial

N/A

Publication date of portion

2015-01-01

SAE International License Terms and Conditions

This is a License Agreement between University of Waterloo ("User") and Copyright Clearance Center, Inc. ("CCC") on behalf of the Rightsholder identified in the order details below. The license consists of the order details, the CCC Terms and Conditions below, and any Rightsholder Terms and Conditions which are included below.

All payments must be made in full to CCC in accordance with the CCC Terms and Conditions below.

Order Date

13-Dec-2021

Order License ID

1168050-1

System ID

973344

Type of Use

Republish in a thesis/dissertation

Publisher

SAE International

Portion

Image/photo/illustration

LICENSED CONTENT

Publication Title

The Dynamic Responses of the Cervical Spine: Buckling, End Conditions, and Tolerance in Compressive Impacts

Author/Editor

Nightingale, Roger W.

Date

01/01/1997

Country

United States of America

Rightsholder

SAE International

Publication Type

Report

REQUEST DETAILS

Portion Type

Image/photo/illustration

Number of images / photos / illustrations

3

Format (select all that apply)

Electronic

Who will republish the content?

Academic institution

Duration of Use

Life of current edition

Lifetime Unit Quantity

Up to 499

Rights Requested

Main product

Distribution

Worldwide

Translation

Original language of publication

Copies for the disabled?

No

Minor editing privileges?

No

Incidental promotional use?

No

Currency

CAD

NEW WORK DETAILS

Title

Evaluating Cervical Spine Injury and Response During Head-First Impact Loading Using a Finite Element Head-Neck Model

Instructor name

Duane Cronin

Institution name

University of Waterloo

Expected presentation date

2022-01-12

ADDITIONAL DETAILS

Order reference number

N/A

The requesting person / organization to appear on the license

University of Waterloo

REUSE CONTENT DETAILS

Title, description or numeric reference of the portion(s)

Figures 1, 6, and 7

Editor of portion(s)

N/A

Volume of serial or monograph

N/A

Page or page range of portion

451-457

Title of the article/chapter the portion is from

N/A

Author of portion(s)

Nightingale, Roger W.

Issue, if republishing an article from a serial

N/A

Publication date of portion

1997-01-01

Elsevier License Terms and Conditions

This is a License Agreement between University of Waterloo ("User") and Copyright Clearance Center, Inc. ("CCC") on behalf of the Rightsholder identified in the order details below. The license consists of the order details, the CCC Terms and Conditions below, and any Rightsholder Terms and Conditions which are included below.

All payments must be made in full to CCC in accordance with the CCC Terms and Conditions below.

Order Date

13-Dec-2021

Order License ID

1168035-1

ISBN-13

9780702031458

Type of Use

Republish in a thesis/dissertation

Publisher

Churchill Livingstone Elsevier

Portion

Image/photo/illustration

LICENSED CONTENT

Publication Title

A system of orthopaedic medicine

Article Title

Applied anatomy of the cervical spine

Author/Editor

Ombregt, Ludwig.

Date

01/01/2013

Language

English

Country

United Kingdom of Great Britain and Northern Ireland

Rightsholder

Elsevier Science & Technology Journals

Publication Type

Book

Start Page

e1

End Page

e12

REQUEST DETAILS

Portion Type

Image/photo/illustration

Number of images / photos / illustrations

3

Format (select all that apply)

Electronic

Who will republish the content?

Academic institution

Duration of Use

Life of current edition

Lifetime Unit Quantity

Up to 499

Rights Requested

Main product

Distribution

Worldwide

Translation

Original language of publication

Copies for the disabled?

No

Minor editing privileges?

No

Incidental promotional use?

No

Currency

CAD

NEW WORK DETAILS

Title

Evaluating Cervical Spine Injury and Response During Head-First Impact Loading Using a Finite Element Head-Neck Model

Instructor name

Duane Cronin

Institution name

University of Waterloo

Expected presentation date

2022-01-12

ADDITIONAL DETAILS

Order reference number

N/A

The requesting person / organization to appear on the license

University of Waterloo

REUSE CONTENT DETAILS

Title, description or numeric reference of the portion(s)

Figures 17, 18, and 19

Editor of portion(s)

N/A

Volume of serial or monograph

N/A

Page or page range of portion

e1-e12

Title of the article/chapter the portion is from

Applied anatomy of the cervical spine

Author of portion(s)

Ombregt, Ludwig.

Issue, if republishing an article from a serial

N/A

Publication date of portion

2013-01-01

IEEE License Terms and Conditions

Requirements to be followed when using any portion (e.g., figure, graph, table, or textual material) of an IEEE copyrighted paper in a thesis:

1) In the case of textual material (e.g., using short quotes or referring to the work within these papers) users must give full credit to the original source (author, paper, publication) followed by the IEEE copyright line © 2011 IEEE.
2) In the case of illustrations or tabular material, we require that the copyright line © [Year of original publication] IEEE appear prominently with each reprinted figure and/or table.
3) If a substantial portion of the original paper is to be used, and if you are not the senior author, also obtain the senior author's approval.

Requirements to be followed when using an entire IEEE copyrighted paper in a thesis:

1) The following IEEE copyright/ credit notice should be placed prominently in the references: © [year of original publication] IEEE. Reprinted, with permission, from [author names, paper title, IEEE publication title, and month/year of publication]
2) Only the accepted version of an IEEE copyrighted paper can be used when posting the paper or your thesis on-line.
3) In placing the thesis on the author's university website, please display the following message in a prominent place on the website: In reference to IEEE copyrighted material which is used with permission in this thesis, the IEEE does not endorse any of [university/educational entity's name goes here]'s products or services. Internal or personal use of this material is permitted. If interested in reprinting/republishing IEEE copyrighted material for advertising or promotional purposes or for creating new collective works for resale or redistribution, please go to http://www.ieee.org/publications_standards/publications/rights/rights_link.html to learn how to obtain a License from RightsLink.

Wolters Kluwer License Terms and Conditions

CCC Marketplace™

This is a License Agreement between University of Waterloo ("User") and Copyright Clearance Center, Inc. ("CCC") on behalf of the Rightsholder identified in the order details below. The license consists of the order details, the CCC Terms and Conditions below, and any Rightsholder Terms and Conditions which are included below.

All payments must be made in full to CCC in accordance with the CCC Terms and Conditions below.

Order Date	17-Dec-2021	Type of Use	Republish in a thesis/dissertation
Order License ID	1169814-2		
ISSN	0362-2436	Publisher	LIPPINCOTT WILLIAMS & WILKINS
		Portion	Image/photo/illustration

LICENSED CONTENT

Publication Title	Spine	Publication Type	Journal
Article Title	A mechanistic classification of closed, indirect fractures and dislocations of the lower cervical spine.	Start Page	1
		End Page	27
		Issue	1
Date	01/01/1976	Volume	7
Language	English, English		
Country	United States of America		
Rightsholder	Wolters Kluwer Health, Inc.		

REQUEST DETAILS

Portion Type	Image/photo/illustration	Distribution	Worldwide
Number of images / photos / illustrations	1	Translation	Original language of publication
Format (select all that apply)	Electronic	Copies for the disabled?	No
		Minor editing privileges?	No
Who will republish the content?	Publisher, not-for-profit	Incidental promotional use?	No
Duration of Use	Life of current edition	Currency	CAD
Lifetime Unit Quantity	Up to 499		
Rights Requested	Main product		

NEW WORK DETAILS

Title	Evaluating Cervical Spine Injury and Response During Head-First Impact Loading Using a Finite Element Head-Neck Model	Institution name	University of Waterloo
		Expected presentation date	2022-01-12
Instructor name	Duane Cronin		

ADDITIONAL DETAILS

REUSE CONTENT DETAILS

Title, description or numeric reference of the portion(s)	Figure 2A	Title of the article/chapter the portion is from	A mechanistic classification of closed, indirect fractures and dislocations of the lower cervical spine.
Editor of portion(s)	Allen, B L; Ferguson, R L; Lehmann, T R; O'Brien, R P	Author of portion(s)	Allen, B L; Ferguson, R L; Lehmann, T R; O'Brien, R P
Volume of serial or monograph	7	Issue, if republishing an article from a serial	1
Page or page range of portion	1-27	Publication date of portion	1982-01-01

ASME License Terms and Conditions

This is a License Agreement between Marwan Darweesh ("User") and Copyright Clearance Center, Inc. ("CCC") on behalf of the Rightsholder identified in the order details below. The license consists of the order details, the CCC Terms and Conditions below, and any Rightsholder Terms and Conditions which are included below.

All payments must be made in full to CCC in accordance with the CCC Terms and Conditions below.

Order Date

23-Dec-2021

Order License ID

1171548-1

ISSN

0148-0731

Type of Use

Republish in a thesis/dissertation

Publisher

AMERICAN SOCIETY OF MECHANICAL ENGINEERS,

Portion

Image/photo/illustration

LICENSED CONTENT

Publication Title

Journal of biomechanical engineering

Article Title

Compressive follower load influences cervical spine kinematics and kinetics during simulated head-first impact in an in vitro model.

Author/Editor

AMERICAN SOCIETY OF MECHANICAL ENGINEERS.

Date

01/01/1977

Language

English

Country

United States of America

Rightsholder

American Society of Mechanical Engineers ASME

Publication Type

Journal

Start Page

111003

Issue

11

Volume

135

REQUEST DETAILS

Portion Type

Image/photo/illustration

Number of images / photos / illustrations

1

Format (select all that apply)

Electronic

Who will republish the content?

Academic institution

Duration of Use

Life of current edition

Lifetime Unit Quantity

Up to 499

Rights Requested

Main product

Distribution

Worldwide

Translation

Original language of publication

Copies for the disabled?

No

Minor editing privileges?

No

Incidental promotional use?

No

Currency

CAD

NEW WORK DETAILS

Title

Evaluating Cervical Spine Response and Potential for Injury During Head-First Impact Loading Using a Finite Element Head-Neck Model

Instructor name

Duane Cronin

Institution name

University of Waterloo

Expected presentation date

2022-01-12

ADDITIONAL DETAILS

Order reference number

N/A

The requesting person / organization to appear on the license

Marwan Darweesh

REUSE CONTENT DETAILS

Title, description or numeric reference of the portion(s)

Figure 1a

Editor of portion(s)

Saari, Amy; Dennison, Christopher R; Zhu, Qingan; Nelson, Timothy S; Morley, Philip; Oxland, Thomas R; Cripton, Peter A; Itshayek, Eyal

Volume of serial or monograph

135

Page or page range of portion

111003

Title of the article/chapter the portion is from

Compressive follower load influences cervical spine kinematics and kinetics during simulated head-first impact in an in vitro model.

Author of portion(s)

Saari, Amy; Dennison, Christopher R; Zhu, Qingan; Nelson, Timothy S; Morley, Philip; Oxland, Thomas R; Cripton, Peter A; Itshayek, Eyal

Issue, if republishing an article from a serial

11

Publication date of portion

2013-11-01

SAE License Terms and Conditions

This is a License Agreement between Marwan Darweesh ("User") and Copyright Clearance Center, Inc. ("CCC") on behalf of the Rightsholder identified in the order details below. The license consists of the order details, the CCC Terms and Conditions below, and any Rightsholder Terms and Conditions which are included below.

All payments must be made in full to CCC in accordance with the CCC Terms and Conditions below.

Order Date

23-Dec-2021

Order License ID

1171614-1

ISSN

0148-7191

Type of Use

Republish in a thesis/dissertation

Publisher

SOCIETY OF AUTOMOTIVE ENGINEERS,

Portion

Image/photo/illustration

LICENSED CONTENT

Publication Title

SAE technical paper series

Author/Editor

SOCIETY OF AUTOMOTIVE ENGINEERS.

Date

01/01/1970

Language

English

Country

United States of America

Rightsholder

SAE International

Publication Type

Monographic Series

REQUEST DETAILS

Portion Type

Image/photo/illustration

Number of images / photos / illustrations

2

Format (select all that apply)

Electronic

Who will republish the content?

Academic institution

Duration of Use

Life of current edition

Lifetime Unit Quantity

Up to 499

Rights Requested

Main product

Distribution

Worldwide

Translation

Original language of publication

Copies for the disabled?

No

Minor editing privileges?

No

Incidental promotional use?

No

Currency

CAD

NEW WORK DETAILS

Title

Evaluating Cervical Spine Response and Potential for Injury During Head-First Impact Loading Using Finite Element Head-Neck Model

Instructor name

Duane Cronin

Institution name

University of Waterloo

Expected presentation date

2022-01-12

ADDITIONAL DETAILS

Order reference number

N/A

The requesting person / organization to appear on the license

Marwan Darweesh

REUSE CONTENT DETAILS

Title, description or numeric reference of the portion(s)

Figures 1 and 4a

Editor of portion(s)

N/A

Volume of serial or monograph

44

Page or page range of portion

362

Title of the article/chapter the portion is from

Investigation of Conditions that Affect Neck Compression-Flexion Injuries Using Numerical Techniques

Author of portion(s)

Peter Halldin, Karin Brolin

Issue, if republishing an article from a serial

N/A

Publication date of portion

1970-01-01

SAE License Terms and Conditions

This is a License Agreement between Marwan Darweesh ("User") and Copyright Clearance Center, Inc. ("CCC") on behalf of the Rightsholder identified in the order details below. The license consists of the order details, the CCC Terms and Conditions below, and any Rightsholder Terms and Conditions which are included below.

All payments must be made in full to CCC in accordance with the CCC Terms and Conditions below.

Order Date

19-Jan-2022

Order License ID

1179900-1

System ID

983157

Type of Use

Republish in a thesis/dissertation

Publisher

SAE International

Portion

Image/photo/illustration

LICENSED CONTENT

Publication Title

Development of a Finite Element Model of the Human Neck

Author/Editor

Yang, King H.

Date

01/01/1998

Country

United States of America

Rightsholder

SAE International

Publication Type

Report

REQUEST DETAILS

Portion Type

Image/photo/illustration

Number of images / photos / illustrations

1

Format (select all that apply)

Electronic

Who will republish the content?

Academic institution

Duration of Use

Life of current edition

Lifetime Unit Quantity

Up to 499

Rights Requested

Main product

Distribution

Worldwide

Translation

Original language of publication

Copies for the disabled?

No

Minor editing privileges?

No

Incidental promotional use?

No

Currency

CAD

NEW WORK DETAILS

Title

Evaluating Cervical Spine Response and Potential for Injury During Head-First Loading Using a Finite Element Head-Neck Model

Instructor name

Duane Cronin

Institution name

University of Waterloo

Expected presentation date

2022-01-31

ADDITIONAL DETAILS

Order reference number

N/A

The requesting person / organization to appear on the license

Marwan Darweesh

REUSE CONTENT DETAILS

Title, description or numeric reference of the portion(s)

Figure 6

Editor of portion(s)

N/A

Volume of serial or monograph

N/A

Page or page range of portion

337

Title of the article/chapter the portion is from

N/A

Author of portion(s)

Yang, King H.

Issue, if republishing an article from a serial

N/A

Publication date of portion

1998-01-01

Bibliography

Aito, S., D'Andrea, M., & Werhagen, L. (2005). Spinal cord injuries due to diving accidents. *Spinal Cord*, *43*(2), 109–116. https://doi.org/10.1038/sj.sc.3101695

Allen Jr., B. L., Ferguson, R. L., Lehmann, T. R., & O'Brien, R. P. (1982). A Mechanistic Classification of Closed Fractures and Dislocations of Lower Cervical Spine. *Spine*, *7*(1), 1–27.

Bahling, G. S., Bundorf, R. T., Kaspzyk, G. S., Moffatt, E. A., Orlowski, K. F., & Stocke, J. E. (1990). Rollover and drop tests - The influence of roof strength on injury mechanics using belted dummies. *SAE Technical Papers*. https://doi.org/10.4271/902314

Barker, J. B., Cronin, D. S., & Nightingale, R. W. (2017). Lower cervical spine motion segment computational model validation: Kinematic and kinetic response for quasistatic and dynamic loading. *Journal of Biomechanical Engineering*, *139*(6), 1–11. https://doi.org/10.1115/1.4036464

Barker, J. B., & Cronin, D. S. (2021). Multilevel Validation of a Male Neck Finite Element Model with Active Musculature. *Journal of Biomechanical Engineering*, *143*(1). https://doi.org/10.1115/1.4047866

Bedbrook, G. M. (1979). Spinal injuries with tetraplegia and paraplegia. *Journal of Bone and Joint Surgery - Series B*, *61*(3), 267–284. https://doi.org/10.1302/0301-620x.61b3.225332

Been, E., Shefi, S., & Soudack, M. (2017). Cervical lordosis: the effect of age and gender. *Spine Journal*, *17*(6), 880–888. https://doi.org/10.1016/j.spinee.2017.02.007

Benzel, E. C., Halliday, A. L., Dickman, C. A., & Yoganandan, N. (2005). Practical Anatomy and Fundamental Biomechanics. *Spine Surgery*, 109–135. https://doi.org/10.1016/b978-0-443-06616-0.50012-2

Benzel, E. C. (2012). The Cervical Spine. In *Wolters Kluwer Health.*

Camacho, D. L., Nightingale, R. W., Robinette, J. J., Vanguri, S. K., Coates, D. J., & Myers, B. S. (1997). Experimental flexibility measurements for the development of a computational head-neck model validated for near-vertex head impact. *SAE Technical Papers*. https://doi.org/10.4271/973345

Cheng, Y., Kheng Leow, W., & Chye Lim, T. (2012). Automatic identification of Frankfurt plane and mid-sagittal plane of skull. *Proceedings of IEEE Workshop on Applications of Computer Vision*, 233–238. https://doi.org/10.1109/WACV.2012.6162994

Clayton, J. L., Harris, M. B., Weintraub, S. L., Marr, A. B., Timmer, J., Stuke, L. E., McSwain, N. E., Duchesne, J. C., & Hunt, J. P. (2012). Risk factors for cervical spine injury. *Injury*, *43*(4), 431–435. https://doi.org/10.1016/j.injury.2011.06.022

Culver, R., Bender, M., & Melvin, J. (1978). *Mechanisms, Tolerences and Responses Obtained Under Dynamic Super-Inferior Head Impact, A Pilot Study* (Vol. 53, Issue 9).

Cusick, J. F., & Yoganandan, N. (2002). Biomechanics of the cervical spine 4: Major injuries. *Clinical Biomechanics*, *17*(1), 1–20. https://doi.org/10.1016/S0268-0033(01)00101-2

DeWit, J. A., & Cronin, D. S. (2012). Cervical spine segment finite element model for traumatic injury prediction. *Journal of the Mechanical Behavior of Biomedical Materials*, *10*, 138–150. https://doi.org/10.1016/j.jmbbm.2012.02.015

Ebara, S., Iatridis, J., Setton, L., Foster, R., Mow, V., & Weidenbaum, M. (1996). Tensile Properties of Nondegenerate Human Lumbar Annulus Fibrosus. *Spine*, *21*(4), 452–461.

Falavigna, A., Righesso, O., da Silva, P., Chavez, F. A. S., Sfreddo, E., de Almeida, L. P., Carrasco, M. J. V., & Joaquim, A. F. (2018). Epidemiology and Management of Spinal Trauma in Children and Adolescents <18 Years Old. *World Neurosurgery*, *110*, 479–483.

Foster, J. B., Kerrigan, J. R., Nightingale, R. W., Funk, J. R., Cormier, J. M., Bose, D., Sochor, M. R., Ridella, S. A., Ash, J. H., & Crandall, J. (2012). Analysis of cervical spine injuries and mechanisms for CIREN rollover crashes. *2012 IRCOBI Conference Proceedings - International Research Council on the Biomechanics of Injury*, 61–75.

Fredo, H. L., Rizvi, S. A. M., Lied, B., Rønning, P., & Helseth, E. (2012). The epidemiology of traumatic cervical spine fractures: A prospective population study from Norway. *Scandinavian Journal of Trauma, Resuscitation and Emergency Medicine*, *20*, 17–21. https://doi.org/10.1186/1757-7241-20-85

Fujita, Y., Duncan, N. A., & Lotz, J. C. (1997). Radial Tensile Properties. *Bioengineering*, 814–819.

Fuller, D. D. (1984). *Theory and practice of lubrication for engineers. Second Edition.*

Gayzik, F. S., Moreno, D. P., Vavalle, N. A., Rhyne, A. C., & Stitzel, J. D. (2011). Development of the Global Human Body Models Consortium mid-sized male full body model. *Injury Biomechanics Research*, 39–12.

Gray, H. (1918). Anatomy of the human body. Retrieved June, 2021, from http://www.bartleby.com/107/

Guo, G. M., Li, J., Diao, Q. X., Zhu, T. H., Song, Z. X., Guo, Y. Y., & Gao, Y. Z. (2018). Cervical lordosis in asymptomatic individuals: A meta-analysis. *Journal of Orthopaedic Surgery and Research*, *13*(1), 1–7. https://doi.org/10.1186/s13018-018-0854-6

Halldin, P., & Brolin, K. (2000). Investigation of Conditions That Affect Neck Compression-Flexion Injuries Using Numerical Techniques. *SAE Technical Papers*, *44*, 127–138. https://doi.org/10.4271/2000-01-SC10

Hasler, R. M., Exadaktylos, A. K., Bouamra, O., Benneker, L. M., Clancy, M., Sieber, R., Zimmermann, H., & Lecky, F. (2012). Epidemiology and predictors of cervical spine injury in adult major trauma patients: A multicenter cohort study. *Journal of Trauma and Acute Care Surgery*, *72*(4), 975–981. https://doi.org/10.1097/TA.0b013e31823f5e8e

Holzapfel, G. A., Schulze-Bauer, C. A. J., Feigl, G., & Regitnig, P. (2005). Single lamellar mechanics of the human lumbar anulus fibrosus. *Biomechanics and Modeling in Mechanobiology*, *3*(3), 125–140. https://doi.org/10.1007/s10237-004-0053-8

Hu, J., Yang, K. H., Chou, C. C., & King, A. I. (2008). A numerical investigation of factors affecting cervical spine injuries during rollover crashes. *Spine*, *33*(23), 2529–2535. https://doi.org/10.1097/BRS.0b013e318184aca0

Iatridis, J., Weidenbaum, M., Setton, L., & Mow, V. (1996). Is the nucleus a solid or a fluid?. *Spine*, *21*(10), 1174–1184.

Iencean, S. M. (2003). Classification of spinal injuries based on the essential traumatic spinal mechanisms. *Spinal Cord*, *41*(7), 385–396. https://doi.org/10.1038/sj.sc.3101468

Ivancic, P. C., Pearson, A. M., Tominaga, Y., Simpson, A. K., Yue, J. J., & Panjabi, M. M. (2008). Biomechanics of cervical facet dislocation. *Traffic Injury Prevention*, *9*(6), 606–611. https://doi.org/10.1080/15389580802344804

Kanagy, J. R., & Wallace, E. L. (1943). Density of leather and its significance. *Journal of Research of the National Bureau of Standards*, *31*(1), 169. https://doi.org/10.6028/jres.031.006

Kasra, M., Parnianpour, M., Shirazi-Adl, A., Wang, J. L., & Grynpas, M. D. (2004). Effect of strain rate on tensile properties of sheep disc anulus fibrosus. *Technology and Health Care*, *12*(4), 333–342. https://doi.org/10.3233/thc-2004-12405

Kennedy, E. I. (1965). Strength and Related Properties of Woods Grown in Canada. *Department of Forestry*, *1104*, 51. http://cfs.nrcan.gc.ca/pubwarehouse/pdfs/24694.pdf

Khor, F. (2018). *Computational Modeling of Hard Tissue Response and Fracture in the Lower Cervical Spine under Compression Including Age Effects (MASc thesis)*.

Koivikko, M. P., Myllynen, P., & Santavirta, S. (2004). Fracture dislocations of the cervical spine: A review of 106 conservatively and operatively treated patients. *European Spine Journal*, *13*(7), 610–616. https://doi.org/10.1007/s00586-004-0688-2

Kopperdahl, D. L., & Keaveny, T. M. (1998). Yield strain behavior of trabecular bone. *Journal of Biomechanics*, *31*(7), 601–608. https://doi.org/10.1016/S0021-9290(98)00057-8

Kretschmann, D. E. (2010). Chapter 5 - Mechanical Properties of Wood. *Wood Handbook - Wood as an Engineering Material*, 1–46.

Lascurain-Aguirrebeña, I., Newham, D. J., Galarraga-Gallastegui, B., & Critchley, D. J. (2018). Differences in neck surface electromyography, kinematics and pain occurrence during physiological neck movements between neck pain and asymptomatic participants. A cross-sectional study. *Clinical Biomechanics*, *57*, 1–9. https://doi.org/10.1016/j.clinbiomech.2018.05.010

Maiman, D., Pintar, F., Malik, W., & Yoganandan, N. (2018). AIS scores in spine and spinal cord trauma: Epidemiological considerations. *Traffic Injury Prevention*, *19*, 169–173. https://doi.org/10.1080/15389588.2017.1410144

Martínez-Pérez, R., Paredes, I., Cepeda, S., Ramos, A., Castaño-León, A. M., García-Fuentes, C., Lobato, R. D., Gómez, P. A., & Lagares, A. (2014). Spinal cord injury after blunt cervical spine trauma: Correlation of soft-tissue damage and extension of lesion. *American Journal of Neuroradiology*, *39*(5), 1029–1034. https://doi.org/10.3174/ajnr.A3812

Martini, F., Nath, J., & Bartholomew, E. (2017). Fundamentals of Anatomy and Physiology. In *Pearson*.

Mattucci, S. F. E., Moulton, J. A., Chandrashekar, N., & Cronin, D. S. (2012). Strain rate dependent properties of younger human cervical spine ligaments. *Journal of the Mechanical Behavior of Biomedical Materials*, *10*, 216–226. https://doi.org/10.1016/j.jmbbm.2012.02.004

Mattucci, S. F. E., & Cronin, D. S. (2015). A method to characterize average cervical spine ligament response based on raw data sets for implementation into injury biomechanics models. *Journal of the Mechanical Behavior of Biomedical Materials*, *41*, 251–260. https://doi.org/10.1016/j.jmbbm.2014.09.023

McElhaney, J., Snyder, R. G., States, J. D., & Gabrielsen, M. A. (1979). Biomechanical analysis of swimming pool neck injuries. *SAE Technical Papers*, 494–500. https://doi.org/10.4271/790137

Moore, K., Agur, A., & Dalley, A. (2015). Essential Clinical Anatomy. In *Wolters Kluwer*.

Nasim, M., Cernicchi, A., & Galvanetto, U. (2021). Development of a finite element neck model for head-first compressive impacts: Toward the assessment of motorcycle neck protective equipment. *Proceedings of the Institution of Mechanical Engineers, Part H: Journal of Engineering in Medicine*. https://doi.org/10.1177/09544119211018112

National Spinal Cord Injury Statistical Center (NSCISC) (2021). Spinal Cord Injury Facts and Figures at a Glance. https://www.nscisc.uab.edu/

Newell, R. S., Blouin, J. S., Street, J., Cripton, P. A., & Siegmund, G. P. (2013). Neck posture and muscle activity are different when upside down: A human volunteer study. *Journal of Biomechanics*, *46*(16), 2837–2843. https://doi.org/10.1016/j.jbiomech.2013.08.013

Nightingale, R. W., Myers, B. S., McElhaney, J. H., Doherty, B. J., & Richardson, W. J. (1991). The influence of end condition on human cervical spine injury mechanisms. *SAE Technical Papers*. https://doi.org/10.4271/912915

Nightingale, R. W., McElhaney, J. H., Camacho, D. L., Kleinberger, M., Winkelstein, B. A., & Myers, B. S. (1997). The dynamic responses of the cervical spine: Buckling, end conditions, and tolerance in compressive impacts. *SAE Technical Papers*, *106*, 3968–3988. https://doi.org/10.4271/973344

Nightingale, R. W., Richardson, W. J., & Myers, B. S. (1997). The effects of padded surfaces on the risk for cervical spine injury. *Spine*, *22*(20), 2380–2387. https://doi.org/10.1097/00007632-199710150-00012

Nightingale, R. W., Myers, B. S., & Yoganandan, N. (2015). Neck Injury Biomechanics. *Accidental Injury: Biomechanics and Prevention*. https://doi.org/10.1007/978-1-4939-1732-7

Nightingale, R. W., Sganga, J., Cutcliffe, H., & Bass, C. R. D. (2016). Impact responses of the cervical spine: A computational study of the effects of muscle activity, torso constraint, and pre-flexion. *Journal of Biomechanics*, *49*(4), 558–564. https://doi.org/10.1016/j.jbiomech.2016.01.006

Nusholtz, G. S., Melvin, J. W., Huelke, D. F., Alem, N. M., & Blank, J. G. (1981). Response of the cervical spine to superior-inferior head impact. *SAE Technical Papers*, 197–237. https://doi.org/10.4271/811005

Ombregt, L. (2013). Applied anatomy of the cervical spine. *A System of Orthopaedic Medicine*, e1–e12. https://doi.org/10.1016/b978-0-7020-3145-8.00060-0

Panjabi, M. M., Chen, N. C., Shin, E. K., & Wang, J. L. (2001). The cortical shell architecture of human cervical vertebral bodies. *Spine*, *26*(22), 2478–2484. https://doi.org/10.1097/00007632-200111150-00016

Peck, G. E., Shipway, D. J. H., Tsang, K., & Fertleman, M. (2018). Cervical spine immobilisation in the elderly: a literature review. *British Journal of Neurosurgery*, *32*(3), 286–290. https://doi.org/10.1080/02688697.2018.1445828

Pintar, F. A., Yoganandan, N., Voo, L., Cusick, J. F., Maiman, D. J., & Sances, A. (1995). Dynamic characteristics of the human cervical spine. *SAE Technical Papers*. https://doi.org/10.4271/952722

Rae, P. J., & Dattelbaum, D. M. (2004). The properties of poly(tetrafluoroethylene) (PTFE) in compression. *Polymer*, *45*(22), 7615–7625. https://doi.org/10.1016/j.polymer.2004.08.064

Ridella, S. A., & Eigen, A. M. (2008). Biomechanical investigation of injury mechanisms in rollover crashes from the CIREN database. *International Research Council on the Biomechanics*

of Injury - 2008 International IRCOBI Conference on the Biomechanics of Injury, Proceedings, September, 33–47.

Roberts, C., & Kerrigan, J. R. (2015). Injuries and Kinematics: Response of the Cervical Spine in Inverted Impacts. *Esv*, *15–0432*, 1–27.

Roberts, C. W., Toczyski, J., & Kerrigan, J. R. (2019). Cervical spine injury in rollover crashes: Anthropometry, excursion, roof deformation, and ATD prediction. *Clinical Biomechanics*, *64*, 42–48. https://doi.org/10.1016/j.clinbiomech.2018.04.004

Ryan, M. D., & Henderson, J. J. (1992). The epidemiology of fractures and fracture-dislocations of the cervical spine. *Injury*, *23*(1), 38–40. https://doi.org/10.1016/0020-1383(92)90123-A

Saari, A., Dennison, C. R., Zhu, Q., Nelson, T. S., Morley, P., Oxland, T. R., Cripton, P. A., & Itshayek, E. (2013). Compressive follower load influences cervical spine kinematics and kinetics during simulated head-first impact in an in vitro model. *Journal of Biomechanical Engineering*, *135*(11), 1–11. https://doi.org/10.1115/1.4024822

Salman, M. M., Muttar, A., & Mohammad, H. kareem. (2020). Correlation between Stress and Strain of wood used in construction. *IOP Conference Series: Materials Science and Engineering*, *870*(1). https://doi.org/10.1088/1757-899X/870/1/012070

Sekhon, L. H. S., & Fehlings, M. G. (2001). Epidemiology, demographics, and pathophysiology of acute spinal cord injury. *Spine*, *26*(24 SUPPL.), 2–12. https://doi.org/10.1097/00007632-200112151-00002

Swartz, E. E., Floyd, R. T., & Cendoma, M. (2005). Cervical spine functional anatomy and the biomechanics of injury due to compressive loading. *Journal of Athletic Training*, *40*(3), 155–161.

Thompson, W. L., Stiell, I. G., Clement, C. M., & Brison, R. J. (2009). Association of injury mechanism with the risk of cervical spine fractures. *Canadian Journal of Emergency Medicine*, *11*(1), 14–22. https://doi.org/10.1017/S1481803500010873

Torg, J. S., Vegso, J. J., & Sennett B. (1987). The National Football Head and Neck Injury Registry: 14-Year Report on Cervical Quadriplegia (1971-1984). *Clinics in Sports Medicine. 6(1)*, 61-72

Viano, D. C., & Parenteau, C. S. (2008). Analysis of head impacts causing neck compression injury. *Traffic Injury Prevention*, *9*(2), 144–152. https://doi.org/10.1080/15389580801894940

Winkelstein, B. A. (1997). The biomechanics of cervical spine injury and implications for injury prevention. *Medicine &Science in Sports & Exercise*, *29*(7), 246–255. https://journals.lww.com/acsm-msse/Fulltext/1997/07001/The_biomechanics_of_cervical_spine_injury_and.7.aspx

Yadollahi, M., Paydar, S., Ghaem, H., Ghorbani, M., Mousavi, S. M., Akerdi, A. T., Jalili, E., Niakan, M. H., Khalili, H. A., Haghnegahdar, A., & Bolandparvaz, S. (2016). Epidemiology of cervical spine fractures. *Trauma Monthly*, *21*(3), 6–10. https://doi.org/10.5812/traumamon.33608

Yang, K. H., Zhu, F., Luan, F., Zhao, L., & Begeman, P. C. (1998). Development of a finite element model of the human neck. *SAE Technical Papers*. https://doi.org/10.4271/983157

Yoganandan, N., Sances, A., Maiman, D. J., (1986). Experimental Spinal Injuries with Vertical Impact. *Spine, 11*(9), 855-860.

Yoganandan, N., Pintar, F. A., Haffner, M., Jentzen, J., Maiman, D. J., Weinshel, S. S., Larson, S. J., Nichols, H., & Sances, A. (1989). Epidemiology and injury biomechanics of motor vehicle related trauma to the human spine. *SAE Technical Papers*. https://doi.org/10.4271/892438

Yoganandan, N., Pintar, F. A., Sances, A., Reinartz, J., & Larson, S. J. (1991). Strength and Kinematic Response of Dynamic Cervical Spine Injuries.pdf. *Spine*, *16*, 511–517.

Yoganandan, N., Kumaresan, S., & Pintar, F. A. (2001). Biomechanics of the cervical spine. Part 2. Cervical spine soft tissue responses and biomechanical modeling. *Clinical Biomechanics*, *16*(1), 1–27. https://doi.org/10.1016/S0268-0033(00)00074-7

Yoganandan, N., Pintar, F. A., Humm, J. R., Maiman, D. J., Voo, L., & Merkle, A. (2016). Cervical spine injuries, mechanisms, stability and AIS scores from vertical loading applied to military environments. *European Spine Journal*, *25*(7), 2193–2201. https://doi.org/10.1007/s00586-016-4536-y

Yoganandan, N., Banerjee, A., DeVogel, N., Pintar, F. A., & Baisden, J. L. (2018). A Novel Competing Risk Analysis Model to Determine the Role of Cervical Lordosis in Bony and Ligamentous Injuries. *World Neurosurgery*, *119*, 962–967.

Young, D., Grzebieta, R., McIntosh, A., Bambach, M., & Frechede, B. (2007). Diving versus roof intrusion: A review of rollover injury causation. *International Journal of Crashworthiness*, *12*(6), 609–628. https://doi.org/10.1080/13588260701497946

Zhang, Q. H., Teo, E. C., & Ng, H. W. (2005). Development and validation of a C0-C7 FE complex for biomechanical study. *Journal of Biomechanical Engineering*, *127*(5), 729–735. https://doi.org/10.1115/1.1992527